Master of Science Thesis

Wind Gust Generation for Wind Turbine Testing via Numerical Methods

Ahmed Valentin Kassem

November 29, 2019

dynamics

TU Delft

Wind Gust Generation for Wind Turbine Testing via Numerical Methods

Master of Science Thesis

For obtaining the degree of Master of Science in Aerospace Engineering
at Delft University of Technology

Ahmed Valentin Kassem

November 29, 2019

Faculty of Aerospace Engineering · Delft University of Technology

Delft University of Technology

DELFT UNIVERSITY OF TECHNOLOGY
DEPARTMENT OF AERODYNAMICS

The undersigned hereby certify that they have read and recommend to the Faculty of Aerospace Engineering for acceptance the thesis entitled **"Wind Gust Generation for Wind Turbine Testing via Numerical Methods"** by **Ahmed Valentin Kassem** in fulfillment of the requirements for the degree of **Master of Science**.

Dated: November 29, 2019

Thesis Committee:

_____
Prof.dr.ir. C.J. Simão Ferreira

_____
Dr. A.C. Viré

_____
Dr.ir. W.A.A.M. Bierbooms

_____
Dr.ir. R. De Breuker

Preface

In loving memory of my grandmother.

The completion of this document marks the end in my journey of becoming an Aerospace Engineer, a period which has drastically shaped me into the person I am today. The thesis at hand proved to be a challenge and an eye opener, which put my resilience to test. Understanding the atmosphere and the formation of gusts was truly rewarding. At the same time, modelling the generation of these gusts, by what some might call low fidelity models, revealed to me their true potential and versatility.

I would like to thank my supervisor, Prof.dr.ir. Carlos J. Simão Ferreira, for giving me the opportunity of working on this topic as well as Dr. Axelle C. Viré for being involved in the thesis as my co-supervisor. Thank you both for your guidance, support, encouragement and understanding. I would also like to thank Dr.ir. Bas W. van Oudheusden, Dr.ir. Marc I. Gerritsma, ir. Nando W.A. Timmer and Dr.ir. Wim A.A.M. Bierbooms for engaging in open discussions, which helped me better understand my topic and results.

Furthermore, I would like to thank my friends, some of whom have assisted me in the completion of this thesis. Special thanks to Patryk and Yuyang for the countless discussions they engaged in, to Martina, Alex and Manuel for their help with proofreading, as well as other *residents of the basement* for advice that lead to *the path of least resistance*. Honourable mention to all my other friends for making my thesis life more bearable.

Lastly, and most importantly, I am thankful to my family, who has encouraged and supported me though my entire education process. I thank my partner, Kristel, for being patient and our son, Oskar Ali, for giving me a new perspective on life. Special thanks to my mother, who was always there for me and my father, who has always supported my decisions. *Mulţumesc nespus!*

Ahmed Valentin Kassem
November 29, 2019
Delft, The Netherlands

Summary

In 2017 there was 514 $[GW]$ of installed wind energy generating capacity. The growth rate of wind energy is apparent and advancements are required for longer lasting wind turbines that extract energy more efficiently. However, gusts pose a threat to their optimal performance and longevity. As such, improvements in load alleviation, controller strategies and more tolerant aerodynamics designs are required. To facilitate these advancements a controlled environment is needed, where concepts could be tested under in-field representative wind gusts, free of outside interference and experimental measurements could be generated for model validation. Current advancements in LiDAR technology and remote sensing will enable the prediction of such gusts, allowing the wind turbine to employ appropriate settings prior to the wind event arriving at the rotor plane. The current thesis aims to gain insight into the potential and limitations of in-field representative gust generation processes. The analysis is carried out by numerical methods. The considered wind tunnel is Delft University of Technology Open Jet Facility, which, currently, is capable of generating lateral sinusoidal gusts by means of twin, parallel, vertical oscillating vanes.

The research at hand has successfully identified gusts that horizontal axis wind turbines (HAWTs) are exposed to and their detrimental effects. These included: veer (turning of wind direction with height), wind gusts (temporal variation in direction/magnitude of the wind), low-level jets (peak in the vertical velocity profile of the wind) and shear. Their corresponding detrimental effects on HAWTs were identified to be significant differential loading between the top and bottom of the rotor, wake skewing, power delivery fluctuation, increased fatigue and unsteady loads.

Test set-ups capable of producing gusts in the wind tunnel setting have been classified, as well as their corresponding advantages and disadvantages. These include circulation control, introduction of secondary flow, wind tunnel fan control, array of oscillating vanes, active turbulence grid and boundary layer wind tunnels. The analysis was performed for a gust generator based on oscillating vanes, a choice encouraged by the current set-up. Furthermore, due to the limited test section length of the considered wind tunnel, only veer and wind gusts were targeted. Additionally, their corresponding scaling was established based on veer angle distribution over the rotor, tip-speed-ratio and Strouhal number matching. The numerical simulation of gust generation was conducted via potential flow, unsteady lifting-surface panel method with free vortex wake, due to lower computational cost than CFD methods. The model coupled the interaction of vanes as well as modelled the free stream produced by

the wind tunnel considered. Thorough verification, convergence, sensitivity and validation studies proved the validity of the model versus experimental measurements as limited by its assumptions. Errors of as low as 5% were observed when the model was used within its limitations. Maximum errors in gust reproduction were smaller than 14%. A limited validation case showed errors of up to 30%, however, still preserving general trends. Mass was conserved with maximum errors of 5% when compared to theoretical values.

Various gust generator vanes configurations were proposed and tested to produce veer and wind gusts. The generation of veer was strategized by means of vertically varying lateral momentum, via flow deflection by the vanes, and suppression of tip vortices, by stacking the vanes on top of each other. The conceptualised gust generator featured 9 static vanes in an array of 3 by 3. In-field veer profiles representative to a wind turbine with diameter of 128 $[m]$ were simulated. The veer profiles spanned all atmospheric stability conditions and the results, although noisy, showed good overall match to the scaled veer profiles. The loadings and corresponding orientations of each vane and for each veer profile have been documented. The model wind turbine diameter was discovered not to play an important role as long as the gust generator vanes were sized appropriately. It was concluded that the trailing vorticity directly influenced the resulting veer profile downstream. The analysis recommends the optimisation of spanwise twist distribution, and thus the spanwise circulation distribution, such that a desired trailing vorticity profile is obtained, allowing for better matching of a targeted veer profile. This would be implemented as continuous vanes with twist, leading to no tip vortices hitting the rotor and thus reducing the noisy behaviour seen in the current study. Lastly, a limiting case was showcased, showing the potential to achieve veer profiles with difference of up to 20 $[°]$ between the angle at the top and bottom of the rotor.

Gust generator configurations were tested by targeting a modified IEC standard extreme gust. The generation of unsteady streamwise velocity component is strategized based on local jet cross sectional area constriction by oppositely pitching vanes. A typical extreme operating gust was used to assess the effectiveness of the generated gusts. An increased number of vanes showed little improvement over the current twin, parallel vanes configuration. Furthermore, streamwise velocity component absolute variation of up to 28% is observed. The targeted profile, however, was not reproduced, with the simulated gust showing a larger lapse. The author recommends further investigation of the pitching protocol, in the context of an optimisation problem, minimising the difference between targeted gust profile and simulated one. Nevertheless, targeted gust profile features could clearly be distinguished in the simulated gusts. The time scaling, however, has been voided due to small gust length scale, not enabling the testing of larger model wind turbine diameters.

The study concludes that there is great potential at experimental testing of HAWTs under spatially and temporally varying wind conditions. The results supports the potential for veer/wind gust generation in the wind tunnel setting with some/no change to the current configuration. Furthermore, the method documented can be extended to vertical axis wind turbines, which, are an order of magnitude smaller in size than HAWTs. Assuming that the model wind turbine could be as large as half scale, wind tunnel tests would have the potential for aerodynamics load assessment and aeroelastic experimental simulations. Finally, the developed model could be used as input to higher fidelity CFD simulations with actuator line model to verify the obtained results or future gust generator vane configurations.

Table of Contents

List of Figures

List of Tables

Nomenclature

Abbreviations

ABL	Atmospheric Boundary Layer
BEM	Blade Element Method
CBL	Convective Boundary Layer
CCA	Circulation Controlled Airfoil
CFD	Computational Fluid Dynamics
ECD	Extreme Coherent Gust with Direction Change
EDC	Extreme Direction Change
EOG	Extreme Operating Gust
EWM	Extreme Wind Speed Model
EWS	Extreme Wind Shear
HAWT	Horizontal Axis Wind Turbine
IEC	International Electrotechnical Commission
IRENE	International Renewable Energy Agency
LE	Leading Edge
LES	Large Eddy Simulation
LiDAR	LIght Detection And Ranging of Laser Imaging Detection And Ranging
LLJ	Low Level Jet
NFAC	National Full-Scale Aerodynamics Complex
NREL	National Renewable Energy Laboratory
OJF	Open Jet Facility
PBL	Planetary Boundary Layer
PIV	Particle Image Velocimetry
RMS	Root Mean Square
RSC	Rotating Slotted Cylinder
SBL	Stable Boundary Layer
TE	Trailing Edge

URANS   Unsteady Reynolds Average Navier-Stokes

Greek Symbols

α	Angle of attack	$[°]$
α_{gust}	Gust angular magnitude	$[°]$
$\boldsymbol{\tau}$	Surface tangent unit vector	$[-]$
Γ	Circulation	$[m^2 s^{-1}]$
γ	Veer angle	$[°]$
κ	Von Kármán constant	$0.41 \ [-]$
λ	Tip-speed-ratio	$[-]$
μ	Dynamic viscosity	$[Nsm^{-2}]$
ν	Kinematic viscosity	$[m^2 s^{-1}]$
Ω	Rotational speed	$[rads^{-1}]$
ω	Angular frequency	$[rads^{-1}]$
$\overline{\Theta' w_0'}$	Surface virtual potential temperature flux	$[Jm^{-2}s^{-1}]$
Φ	Velocity potential	$[m^2 s]$
ϕ, θ, ψ	Body fixed coordinate system orientation	$[°]$
ϕ_m	Dimensionless shear	$[-]$
ρ	Fluid density	$[kgm^{-3}]$
Θ	Potential temperature	$[K]$
ζ	Vorticity	$[s^{-1}]$

Latin Symbols

A	Cross sectional area	$[m^2]$
$a_{i,j}$	Influence coefficient	$[m^{-1}]$
AR	Aspect ratio	$[-]$
b	Span length	$[m]$
c	Chold length	$[m]$
C_L	Lift coefficient of 3D surface	$[-]$
C_l	Lift coefficient of 2D airfoil	$[-]$
C_p	Pressure coefficient	$[-]$
c_p	Specific heat at constant pressure	$[Jg^{-1}K^{-1}]$
D	Wind turbine diameter	$[m]$
dh	Vane spacing	$[m]$
Eu	Euler number	$[-]$
$\mathbf{F}$	Resultant force vector	$[N]$
Fr	Froude number	$[-]$
g	Gravitational acceleration	$9.81 \ [ms^{-2}]$
h	Height above ground level	$[m]$
I	Turbulence intensity	$[-]$
k	Reduced frequency	$[-]$

K_M	Turbulent vertical exchange coefficient for momentum	$[m^2 s^{-1}]$
L_*	Obukhov length scale	$[-]$
$\dot{m}$	Mass flow	$[kgs^{-1}]$
M	Number of panels in the chordwise direction	$[-]$
$\mathbf{n}$	Surface normal unit vector	$[-]$
N	Number of panels in the spanwise direction	$[-]$
p	Pressure	$[Pa]$
$\mathbf{r}$	Position vector	$[m]$
R	Vortex core radius	$[m]$
Re	Reynolds number	$[-]$
S	Surface area	$[m^2]$
St	Strouhal number	$[-]$
T	Time period of process	$[s]$
Δt	Time step	$[s]$
t	Time	$[s]$
u, v, w	Velocity component in the x, y, z-directions	$[ms^{-1}]$
U_∞	Free stream velocity	$[ms^{-1}]$
u_*	Frictional velocity	$[ms^{-1}]$
X, Y, Z	Inertial frame Cartesian coordinates system directions	$[m]$
x, y, z	Body fixed Cartesian coordinates system directions	$[m]$

Superscripts

$'$	Perturbation from mean value of quantity
$*$	Non-dimensionalised quantity

Subscripts

1	At point 1
2	At point 2
∞	Free stream condition
g	Geostrophic wind quantity
l	Gust lapse quantity (time/speed)
m	Model wind turbine quantity
p	Physical wind turbine quantity
r	Gust rise quantity (time/speed)
w	Wall quantity

Chapter 1

Introduction

Wind energy has been exploited for thousands of years, starting with the simple, yet crucial, wind sail. Windmills followed, primarily for grinding grains and water pumping. This can be traced back to more than 3000 years Burton et al. (2011). The first direct current windmill was constructed in the late nineteenth century with much of the twentieth century not seeing interest in electricity generation. The industry peaked in the 1970s, when research was driven by a sudden increase in fossil fuel prices Burton et al. (2011). Today, it is common to see horizontal axis wind turbines (HAWTs) with diameters greater than 100 $[m]$; MHI Vestas V164-9.5MW (164 $[m]$), Siemens Gamesa SG 8.0-167 DD (167 $[m]$), Goldwind GW154 6.7MW (154 $[m]$) and the colossal GE Haliade-X 12 MW (220 $[m]$). The International Renewable Energy Agency (IRENE) reported a worldwide total installed capacity of 514 $[GW]$ (0.8% in the Netherlands) at the end of 2017 IRENA (2018). There is clear potential in the industry for generating a large percentage of the consumed electricity. As the trend grows towards ever larger and taller wind turbines, so does the demand of longer operational life and decreased maintenance. Ideally, one would want a wind turbine to operate in a uniform free stream of air. However, due to complex flow within the atmospheric boundary layer (ABL), this is not the case. In its life time, a wind turbine will encounter unsteady winds with temporal and spatial variation in magnitude and/or direction. These rapidly changing flow fields, referred to as gusts, introduce detrimental aerodynamic loads on the wind turbine which have to be taken into account in the design process Burton et al. (2011). Currently, the International Electrotechnical Commission (IEC) stipulates design load calculation requirements via a variety of models IEC (2005). Stochastic models have been developed such as NewGust Bierbooms et al. (2000) for long term fatigue calculations. Furthermore, high fidelity computational fluid dynamics (CFD), particularly large eddy simulations (LES) have been used to determine extreme loads Storey et al. (2014). Additionally, other various lower fidelity models have been developed for this purpose such as free vortex methods Jeong et al. (2014) Qiu et al. (2014) Kim et al. (2014).

The experimental simulation of gusts has proven difficult and test campaigns have been few in number. This has been attributed to various reasons such as: highly mixed out resulting flow

field, slow ramp up/down speeds Snel and Schepers (1995). Experimental simulation of gusts will enable the validation of existing models. Furthermore, this will also allow for better wind turbine controller designs, enabling testing of concepts in representative field conditions. The undertaken project aims to study the experimental generation of gusts by numerical methods. This is to seek understanding of gust generation aerodynamics processes in the aims of setting the ground work for future test set-up designs of wind tunnel gust generators, particularly for Delft's University of Technology Open Jet Facility (OJF). The focus of the project is limited to HAWTs relevance.

1.1 Problem Definition

Interest in the generation of more in-field representative gusts exists, however, the current OJF set-up is only capable of sinusoidal gust generation. This is achieved by a pair of vertical vanes, that are able to oscillate independently. Modelling their flow field is problematic from two aspects; i.e. moving solid walls and unsteady flow field downstream. Traditional methods, such as CFD, are computationally expensive due to the need of a moving mesh and transient solver. Furthermore, the phrase "in-field representative gusts" needs to be defined in terms of realistic wind conditions that wind turbines are exposed to and their relevant scaling for wind tunnel simulation. Therefore two areas in the field of wind turbines where a contribution can be made are identified:

1. The need to identify relevant wind gusts and their appropriate scaling for wind tunnel simulations.

2. The development of a computationally efficient tool that can model the generation of such wind gusts within a wind tunnel, particularly the OJF, enabling the design of test set-ups.

The study hence aims to analyse the potential of generating more in-field representative gusts in the OJF; it is intended to model the gust generation in the OJF via a computationally efficient model such as vortex methods. Given the validation of the model with existing measurements, the model can be used to explore the potential of achieving more in-field representative gusts in the OJF and give insight to future experimental set-ups design. The model will be assessed for its validity using experimental measurements from the current wind tunnel gust generator. Requirements and limitations of future gust generators in the OJF will therefore be derived in the project.

1.2 Research Questions and Objectives

This section will present the project's research questions together with relevant sub-questions. The derived objectives and sub-goals are presented subsequently.The main research question is stated as follows:

R.Q. - *What is the potential and limitations of in-field representative gust generation at Delft University of Technology Open Jet Facility wind tunnel for horizontal axis wind turbine experimental testing?*

To answer the above question, the following sub-questions need answering first:

R.Q. 1 What are the gusts HAWTs are exposed to?

R.Q. 2 What are the detrimental effects on HAWTs due to the identified gusts?

R.Q. 3 What experimental set-ups are used for gust generation in wind tunnels?

R.Q. 4 What are the relevant similarity parameters for scaling in-field wind gusts to the OJF?

R.Q. 5 How can gust generation in the OJF be modelled by a computationally efficient simulation?

R.Q. 6 What is the validity of the aforementioned model when compared to existing experimental measurements and previously performed CFD simulations?

R.Q. 7 Which gust generator experimental set-up parameters are of importance?

Having posed the research questions, the following main objective and sub-goals are set:

The derivation of experimental gust generator conceptual configurations for generation of in-field representative wind gusts by numerical simulation.

1. Identify relevant/important gusts HAWTs experience.

2. Identify the detrimental effects to HAWTs under wind gusts.

3. Identify relevant experimental set-ups for gust generation.

4. Develop a computationally efficient model via vortex theory modelling the empty OJF.

5. Extend the model to include the current gust generator.

6. Validate the open OJF and sinusoidal gust results by comparing to existing measurements.

7. Compare the computationally efficient model and previously performed CFD simulations; quantify the relevance of higher computational cost in relation to validity with the experimental measurements.

8. Simulate the identified relevant gusts.

9. Provide limitations and requirements of future experimental set-ups.

1.3   Document Structure

The remaining of this text is split into two parts:

  I. A research paper is attached that describes the thesis carried out. All relevant results are presented here. The reader is advised to first go through this part.

 II. Supporting chapters documenting additional information, which, are organised as described below:

A literature survey is carried out and findings are documented in Chapter 2. Chapter 3 discusses the processes occurring inside the ABL and presents resulting velocity profiles of wind gusts. The experimental generation of gusts is presented in Chapter 4. Furthermore, flow governing theory is discussed in Chapter 5. Lastly, the results of a convergence and sensitivity analysis on the developed model are documented in Chapter 6.

The reader is advised to read the document in full colour for interpretation ease.

Part I

Research Paper

Wind Gust Generation for Wind Turbine Testing via Numerical Methods

A. V. Kassem

Delft University of Technology, Kluyverweg 1, 2629HS, Delft, The Netherlands

Prof.dr.ir. C.J. Simão Ferreira∗, Dr. A.C. Viré†

Delft University of Technology, Kluyverweg 1, 2629HS, Delft, The Netherlands

The modelling of gust generation by an array of oscillating vanes at Delft's University of Technology Open Jet Facility is proposed. Focus is placed on identifying relevant in-field gusts that horizontal axis wind turbines are exposed to and reproduction via numerical methods in the wind tunnel setting. A computationally efficient model is developed based on potential flow theory. The model validation showed good results overall, preserving general trends. Several vane configurations are proposed. Veer profiles representative of all atmospheric stability conditions are simulated as well as a maximum profile with veer angle difference between the top and bottom of the rotor of up to $20°$. A coupling between the trailing vorticity of the vanes and achieved veer profile is identified. Temporal variation of the streamwise velocity component is achieved, however, not following the intended gust profile. Peak to trough velocity variation of up to 28% of the free stream value is observed. Furthermore, gust length scale was linked to vane spacing, limiting the possibility of small geometric scale testing.

I. Introduction

In its lifetime, a wind turbine will encounter winds with temporal and spatial variation in magnitude and/or direction. These rapidly changing flow fields, referred to as gusts, introduce detrimental effects posing a threat to the longevity and operation of wind turbines. Significant differential loading between the top and bottom of the rotor, wake skewing, power delivery fluctuation, increased fatigue and unsteady loads can be observed in the presence of various gusts [1–3]. Mitigation by appropriate aerodynamic design, load alleviation and new control strategies that can cope with in-field gusts are requirements in the long term. As advancements in remote sensing and load alleviation are made, the need for experimental testing in a controlled environment arises [4, 5]. This paper therefore addresses the feasibility for in-field representative wind gust generation in the wind tunnel setting. The work is aimed for Delft's University of Technology Open Jet Facility (OJF) wind tunnel. The focus of the project is limited to gusts relevant to horizontal axis wind turbines (HAWT).

The experimental simulation of wind gusts has made use of various test set-ups: rotating slotted cylinders [6], introduction of a secondary flow [7], wind tunnel fan control [8], array of oscillating vanes [9, 10], active turbulence grid [11, 12] and boundary layer wind tunnels [13, 14]. Promising results have been achieved by active turbulence grids and boundary layer wind tunnels at the expense of a complex mechanical system and long test sections respectively. The current paper seeks to determine the feasibility of wind turbine relevant wind gust generation by an array of oscillating vanes. The choice was encouraged by the current OJF gust generator configuration, twin parallel vanes capable of producing lateral sinusoidal gusts. The analysis is done numerically with priority towards the model's computational efficiency. Understanding of gust generation processes is sought and linked to gust generator parameters, in the aim of setting the ground work for future test set-up designs.

The remainder of this paper will identify and describe relevant in-field gusts in Section II as well as present the OJF and chosen gust generator type. The methodology of the study is discussed in Section IV, followed by the steps taken to develop the computational model in Section V. The model's validation is documented in Section VI. The conceptualised gust generator configurations and corresponding achieved gusts are presented and discussed in Section VII. Finally, conclusions and recommendations for future work are drawn in Section VIII.

∗Thesis supervisor
†Thesis co-supervisor

II. In-Field Gusts

Various gust types are identified based on the definition that gusts are a temporal and/or spatial variation of the velocity vector (magnitude and/or direction). These are: (1) veer, (2) wind gusts (speed/direction change), (3) shear and (4) low-level jets. This paper will focus on the first two cases, however, all the aforementioned gusts have been characterised during the study. The choice of only considering veer and wind gusts is limited by the chosen wind tunnel; the experimental simulation of shear flows requires specialised wind tunnels known as boundary layer wind tunnels, characterised by a very long testing section. The OJF does not satisfy this requirement.

A. Veer

Veering is the clockwise turning of the wind vector with height in the northern hemisphere. Its formation is linked to the influence of Coriolis force [15]. Theoretical veer profiles can be computed from Ekman theory, which predicts veer of up to $45 \, [°]$. In reality, however, the extent of veer is affected by atmospheric stability and horizontal temperature gradients [1, 3]. Additionally, the surface roughness plays a role in the resulting veer profile. Similarly to vertical wind shear, the presence of veer leads to an increase in differential loading on the wind turbine [1]. This results in increased fatigue loads and therefore puts the operational longevity of the wind turbine at risk. Measurements have shown that veering can lead up to a difference of $2.6 \, [ms^{-1}]$ between the top and bottom of the rotor [1]. Furthermore, veering has been linked to wake skewing, which in the wind farm setting, can be detrimental for downstream turbines [2, 15, 16].

Various in-field measurements campaigns have been carried out to quantify veering profiles. Instruments such as sonic anemometers and LiDAR were used. Measurements have been carried out on mostly flat plains [17], forested canopy [18], off-shore [1] and in complex terrain characterised by ridges/valleys [19]. A campaign carried out at the Høvsøre site, located in Denmark is chosen as reference. The site is characterised by mostly flat lands, with a southern fjord, $800 \, [m]$ away. Measurements have been conducted for three atmospheric stability conditions: stable, neutral and unstable. The profiles are shown in Figure 1. For the convective (unstable) atmospheric boundary layer (ABL), the veering with height is considerably lower than in stable conditions as several studies have concluded [1, 3, 18]. Furthermore, the extent of veer is greater at slow wind speeds and in stable conditions, exceeding $40 \, [°]$. The shown veering profiles will be utilised as target profiles for derived conceptual gust generator configurations. Only the faster wind speed bins are considered (8-$10 \, [ms^{-1}]$).
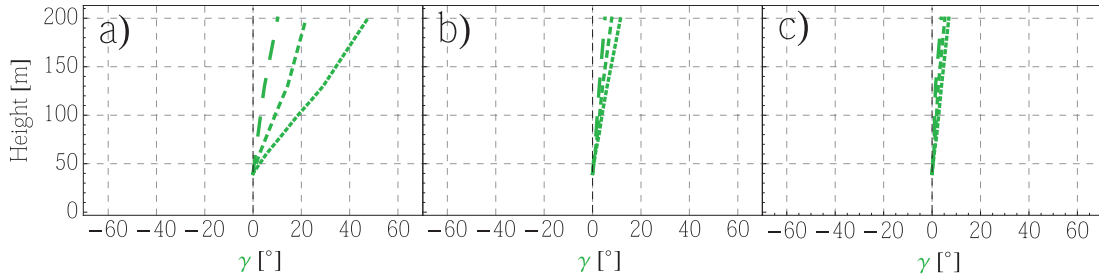
Fig. 1   Vertical profile of veer angle based on 30-min averages in a) stable, b) neutral and c) unstable atmospheric conditions. Line type represents wind speed bins; dotted: 4-6, short dash: 6-8 and long dash: 8-10 $[ms^{-1}]$. The veer angle is relative to the $40 \, [m]$ level. Adapted from [17].

B. Wind Gusts: Speed Variation

Wind gusts manifest themselves as variations in wind magnitude and/or direction. The passage of fronts, formation of thunderstorms due to moist convection or the perturbations in stability leading to downward momentum mixing are primary mechanisms in their formation [1]. For off-shore/coastal locations, the onset of local circulation will also lead to wind gusts. Their time scales vary from hours to a few seconds. An example of detrimental loading and power generation fluctuation was determined from measurements at the Eolos research facility 2.5 MW Clipper Liberty C96 wind turbine during a gust event. The response of the wind turbine was recorded in terms of blade pitch and output power [20]. A peak in output power was observed, despite a decrease in blade pitch. This is harmful to the power grid, which requires a steady, fluctuation free generation of power. Power fluctuations are further amplified when large wind farms are considered.

Wind gusts tend to have a chaotic profile, however, systematic classification has been achieved by parametric models

[21, 22]. The International Electrotechnical Commission (IEC) standards stipulate extreme design loads based on modelled gust profiles. The extreme operation gust (EOG) is considered in the current study. The gust varies in time over a period of $T = 10.5\ [s]$ as described by (1). The gust magnitude (u_{gust}) is based on the turbine class and turbulence scale parameter (constant for hub heights $\geq 60\ [m]$) [21]. An example profile is shown in Figure 2 for a class I_A wind turbine with hub speed of $25\ [ms^{-1}]$ and $D = 42\ [m]$.

$$u(t) = \begin{cases} U_\infty - 0.37 u_{gust} \sin\left(\frac{3\pi t}{T}\right)\left[1 - \cos\left(\frac{2\pi t}{T}\right)\right] & 0 \leq t \leq T \\ U_\infty & \text{otherwise} \end{cases} \tag{1}$$
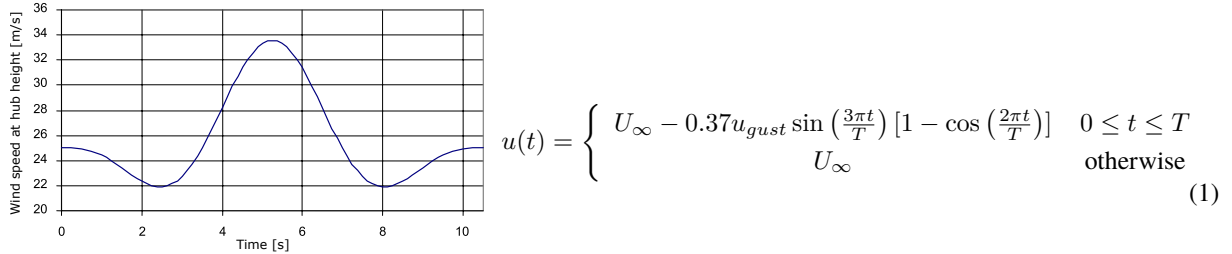
Fig. 2   Example of EOG. Adapted from [21].

Hu et al. have defined the gust asymmetric factor (GAF) as (2), where (u_r), (t_r), (u_l) and (t_l) are the rise/lapse magnitude/time. The nomenclature is shown for an in-field measured gust in Figure 3. The profile resembles an asymmetric EOG.

$$GAF = \frac{u_r/t_r}{u_l/t_l} \tag{2}$$
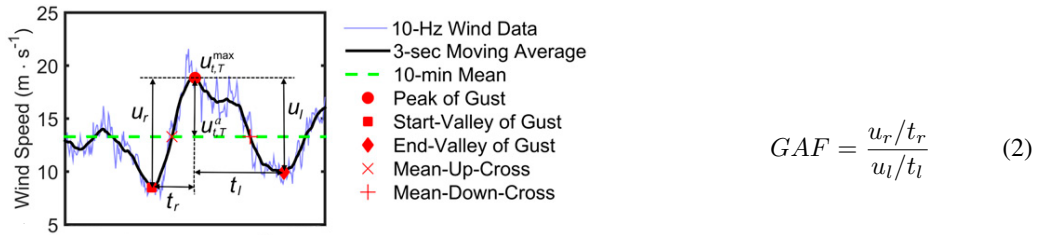
Fig. 3   In-field asymmetric wind gust event with duration $T = 15.5$ $[s]$. Adapted from [22].

Wind data from the test site at Thyborøn, Denmark shows the true extent of wind gusts variability [23]. Time series recorded at 21 and 85 $[m]$ altitude are shown in Figure 4. Two wind ramps can be identified:

1) At $80 \leq t \leq 89\ [s]$ with an increase from 15 to 20 $[ms^{-1}]$.
2) At $108 \leq t \leq 111\ [s]$, with an increase from 13.6 to 23.3 $[ms^{-1}]$.

The former ramp is targeted, by considering the wind series at 85 $[m]$ for $0 \leq t \leq 100\ [s]$.
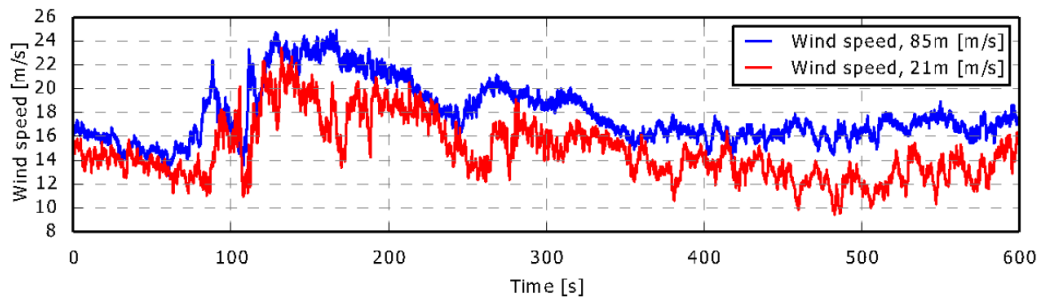
Fig. 4   Wind data from the Thyborøn, Denmark test site on 24 October, 2013. Adapted from [23].

Note that direction change wind gusts are not considered, since the current test set-up is capable of producing these.

3

III. Open Jet Facility - Oscillating Vanes Gust Generator

The controlled generation of wind gusts is a multi-disciplinary problem. It applies to many systems other than wind turbines, such as unmanned aerial vehicles (UAVs) [8], aircrafts [9] and trucks [7]. Six gust generators types are identified, although the study solely focuses on gust generation via oscillating vanes. The OJF and its current gust generator set-up are described below.

1) circulation control [6, 24]
2) introduction of secondary flow [7]
3) wind tunnel fan control [8]
4) oscillating vanes array [9, 10]
5) active turbulence grid [11, 12, 25]
6) boundary layer wind tunnels [13, 14].

The OJF is a closed-loop, open test section wind tunnel driven by a $500 \, [kW]$ fan that can achieve free stream speeds of up to $35 \, [ms^{-1}]$. The contraction ratio is 3:1, ending into an octagonal nozzle of $2.85 \times 2.85 \, [m]$, feeding a jet flow into the test section, a room of $8.2 \times 6.6 \, [m]$. At the end of the test section a $350 \, [kW]$ cooler is present. This keeps the flow at a temperature of $20 \, [°C]$ ($293.15 \, [K]$); corresponding to a density $\rho = 1.204 \, [kgm^{-3}]$ and kinematic viscosity $\nu = 1.516 \times 10^{-5} \, [m^2 s^{-1}]$. The turbulence intensity at $1 \, [m]$ and $6 \, [m]$ downstream of the nozzle are lower than 0.5% and 2% respectively [26]. A technical drawing of the settling chamber, contraction and test section is shown in Figure 5, complemented by a 3D schematic of the entire OJF in Figure 6. Note than the shown inertial coordinate system will be used for the remainder of this paper, with (x): streamwise, (y) horizontal and (z) vertical.
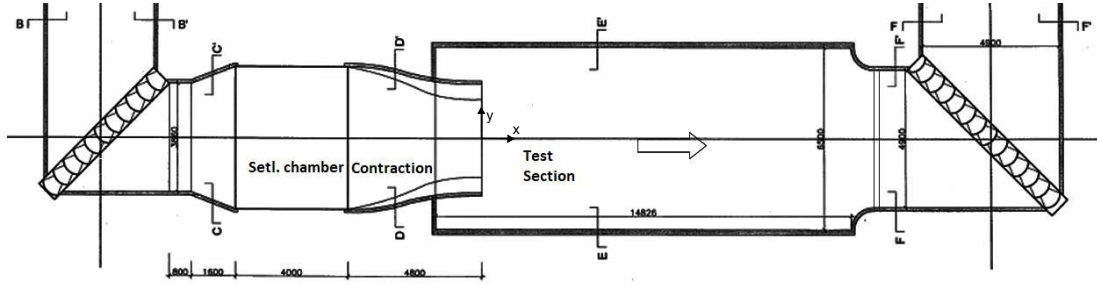
Fig. 5   Technical drawing of the Open Jet Facility. Dimensions in millimetres.
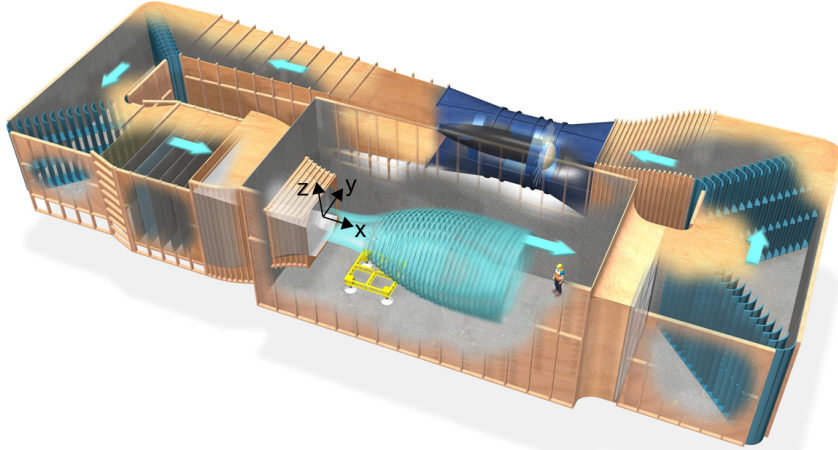
Fig. 6   3D schematic of the Open Jet Facility. Adapted from [27]

The uniformity of the jet has previously been characterised, namely the mean flow speed, turbulence intensity and shear layer aperture angle. A constant temperature hot wire anemometer was used together with a static Pitot tube. The aperture angle was found to be $9.5 \, [°]$, resulting in a free-stream reduction of $16.7 \, [cmm^{-1}]$. This corresponds to a uniform area of $2 \times 2 \, [m^2]$ at a downstream location of $6 \, [m]$ [28]. The downstream mean speed uniformity maintains well with variations of 1% and 3% at $1 \, [m]$ and $6 \, [m]$ respectively.

4

The OJF implements a gust generator based on a pair of vertical oscillating vanes. Undisturbed fluid flows past the vanes, which vary their angle of attack in time (i.e. pitch angle). This results in the flow downstream being deflected in relation to the reduced frequency of oscillation and vane deflection angle. The vanes employ a NACA0012 airfoil profile with $c = 0.3 \, [m]$ and aspect ratio $AR = 9.6 \, [-]$. The gust generator is shown in Figure 7.
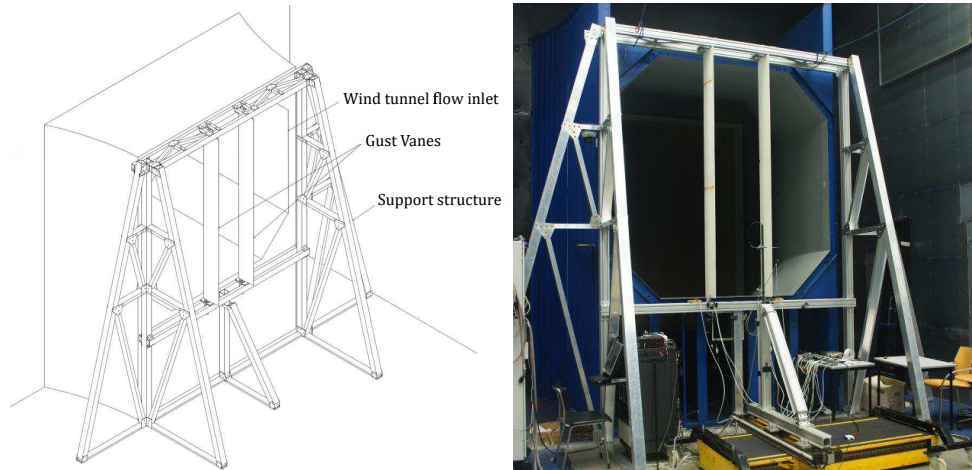
Fig. 7   Delft University of Technology Open-Jet Facility with the gust generator installed. Adapted from [9].

The current configuration is capable of generating sinusoidal and $1 - \cos$ lateral gusts. Studies have characterised the gust amplitude (maximum flow deflection angle) to be linear in vane chord length and maximum vane deflection angle. The reduced frequency of oscillation did not have first order effects on the gust amplitude [9]. The generated gusts were laterally uniform in between the vane spacing [29]. Spacing equal to the chord length showed vane interaction. This paper aims to extend this functionality by altering the configuration; the number of vanes, orientation and oscillation protocol.

IV. Methodology

The study aims to numerically analyse the potential and limits of wind gusts generation relevant to HAWTs. To do this, the following steps are followed:

1) Identification of relevant in-field gusts, as described in Section II.
2) Setting scaling rules for wind tunnel equivalence.
3) Development of a relatively efficient simulation model via potential flow theory.
4) Performing configuration search for targeted wind gusts.
5) Qualitative description of each gust generation's aerodynamics.

In the process, requirements are to be drawn for future gust generators. The remaining for this section will describe the scaling, flow governing theory and gust generator parameters.

A. Wind Gusts Scaling

The experimentally simulated wind gusts need to be representative of the in-field gusts described in Section II. Their effects will vary based on the considered physical wind turbine geometric and performance parameter. To establish a systematic approach in proposing gust generator configurations, a choice of physical wind turbine is made ahead. The scaling is based on the legacy model (Siemens) Gamesa G128-5.0 MW HAWT. Its characteristics are summarised in Table 1. The choice is made arbitrarily, however, its low tip-speed-ratio (λ) of $5.7 \, [-]$ was a desirable feature. Furthermore, a model wind turbine is assumed with diameter limited to $0.6 \leq D_m \leq 1.8 \, [m]$. The constraint is enforced to avoid wind tunnel blockage and unrealistic rotational speeds. The wind tunnel free stream is limited to $5 \leq U_{\infty,m} \leq 25 \, [ms^{-1}]$, ensuring reasonable Reynolds numbers, manageable structural loads and enough flow momentum for good deflection.

Table 1 (Siemens) Gamesa G128-5.0MW wind turbine characteristics.

U_{cut-in}	U_{rated}	$U_{cut-out}$	D	Ω_{max}	U_{tip}	H_{hub}
2 $[ms^{-1}]$	14 $[ms^{-1}]$	27 $[ms^{-1}]$	128 $[m]$	12 $[rpm]$	80 $[ms^{-1}]$	120 $[m]$

The temporal/spacial wind variations the model wind turbine feels are prioritised in the scaling. The considered properties to maintain are as follow:

1) Aerodynamic kinetics: tip-speed-ratio.
2) Gust characteristics:
   - Veer: the veering angle distribution along the diameter, or veer gradient across the rotor diameter; i.e. $\frac{\Delta\gamma}{D}$, where the difference in veer angle at the top and bottom of the rotor is represented by ($\Delta\gamma$).
   - Wind gusts: gust Strouhal number; $St = \frac{D}{TU_\infty}$, where (T) is the gust time period and (U_∞) is the freestream velocity.

The above considerations lead to the matching of tip sped ratio, veering angle distribution over the diameter and time scales. The veer angle distribution is ensured by appropriate vane deflection angles. The matching of tip-speed-ratio in relation to the chosen physical wind turbine and simulation set-up is governed by (3). Figure 8 shows the possible design space (choice of ($U_{\infty,m}$), (D_m) and corresponding (Ω_m)) that satisfies tip-speed-ratio matching. Note is made that the highest possible model wind turbine diameter is desirable such that the gradient of veer angle with height is minimised; i.e. the distribution of veer is across a larger length.
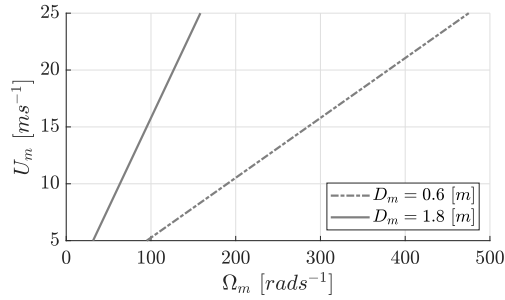
$$\lambda_p = \lambda_m$$
$$\lambda_p = \frac{R_m \Omega_m}{U_{\infty,m}}$$
$$2\lambda_p = \frac{D_m \Omega_m}{U_{\infty,m}} \quad (3)$$
$$\therefore U_{\infty,m} = \frac{D_m}{2\lambda_p}\Omega_m$$

Fig. 8 Relation between wind tunnel free stream and model wind turbine rotational speed for $\lambda_p = 5.7\,[-]$.

Analogously, Strouhal number matching is described by (4) and the design space is shown in Figure 9. It is preferred to choose the largest possible time scale, such that the oscillation frequency of the gust generator vanes can stay relatively low.
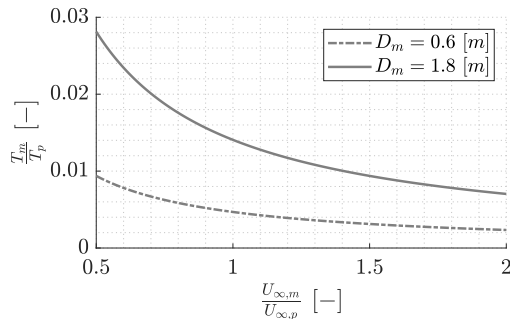
$$St_p = St_m$$
$$\frac{D_p}{T_p U_{\infty,p}} = \frac{D_m}{T_m U_{\infty,m}} \quad (4)$$
$$\therefore \frac{T_m}{T_p} = \frac{D_m U_{\infty,p}}{D_p U_{\infty,m}}$$

Fig. 9 Relation between time scales ratio and wind tunnel free stream to physical free stream ratio for $D_p = 128\,[m]$.

B. Flow Governing Theory

The presence of oscillating vanes in the flow field introduce unsteady effects governed by the full Navier-Stokes equations. Their numerical modelling is computationally expensive and not justified in the conceptual phase of aerodynamic bodies. As such, the developed model is implemented by means of potential flow theory. The main assumptions applied in simplifying the Navier-Stokes equations are:

1) Effect of viscosity is neglected.
2) The flow is incompressible (low speed) and irrotational; vorticity is confined to the boundary layer and thin wakes.

Applying the above stated assumptions leads to the Laplace equation (5), which can be solved for known boundary conditions resulting in a known velocity potential (Φ). The derivation is not shown, however, the reader can refer to texts such as [30–32]. The pressure (p) is then obtained from the unsteady Bernoulli's equation (6). The unsteady behaviour of the flow is introduced by corresponding unsteady boundary conditions. Since the fluid is assumed to be incompressible (infinite speed of sound) the instantaneous solution is independent of time derivatives; the entire fluid domain will feel the influence of a momentary boundary condition [30].

$$\nabla^2\Phi = 0$$
$$\frac{\partial\Phi}{\partial n} = \mathbf{n} \cdot \mathbf{u}_B \quad \text{on body} \qquad (5) \qquad \qquad \frac{p_\infty - p}{\rho} = \frac{u^2}{2} - \frac{U_\infty^2}{2} + \frac{\partial\Phi}{\partial t} \qquad (6)$$
$$\nabla\Phi \to 0 \quad \text{at} \quad r \to \infty$$

The principle of superposition is employed, allowing for the flow field to be described by a linear combination of flow singularities; vortex filaments of constant strength. The problem is solved numerically, obtaining the vortex filaments strengths, and thus the velocity field (Biot-Savart law). Smoothing techniques such as a Rankine vortex core is implemented for the purpose of a numerical solution [33]. Combined, the induced velocity at an arbitrary point in the flow field due to a vortex filament is given by (7); where (R) denoted the chosen vortex core size.

$$\mathbf{u}_{induced1,2} = \begin{cases} \frac{\Gamma}{4\pi} \frac{\mathbf{r}_1 \times \mathbf{r}_2}{|\mathbf{r}_1 \times \mathbf{r}_2|^2} \mathbf{r}_0 \cdot \left(\frac{\mathbf{r}_1}{|\mathbf{r}_1|} - \frac{\mathbf{r}_2}{|\mathbf{r}_2|} \right) & \mathbf{r}_1, \mathbf{r}_2, \mathbf{r}_1 \times \mathbf{r}_2 > R \\ \frac{\Gamma}{4\pi} \frac{\mathbf{r}_1 \times \mathbf{r}_2}{R^2|\mathbf{r}_0|^2} \mathbf{r}_0 \cdot \left(\frac{\mathbf{r}_1}{|\mathbf{r}_1|} - \frac{\mathbf{r}_2}{|\mathbf{r}_2|} \right) & \mathbf{r}_1, \mathbf{r}_2, \mathbf{r}_1 \times \mathbf{r}_2 \leq R \end{cases} \qquad (7)$$

The pressure on the body surface can be directly linked to the body's local circulation. Section V will guide the reader through the numerical implementation of the model.

C. Gust Generator Description

Gust generator configurations will be described by vanes geometry location, orientation and pitching protocol. The four factors are dependent on the targeted gust. The following guidelines will be followed for conceptualisation of veer generator:

- The vanes are set at a fixed pitch angle.
- Their corresponding pitch angle is proportional to the targeted veer angle distribution.
- Vanes are distributed in three rows. The middle vanes will have span equal to $\frac{D_m}{3}$. The top and bottom vanes will have span $\geq \frac{D_m}{3}$ such that their tip vortices are away from the rotor disc.

Furthermore, two configurations for the generation of wind gusts will be considered, employing two and four vanes, spanning the entire OJF nozzle length. The main guideline considered are:

- The vanes will be spaced at $\frac{D_m}{3}$ and placed symmetrically about the centreline.
- The vanes on either side of the nozzle's centreline will pitch opposite to each other.
- The pitch angle of the vanes varies proportionally to the gust profile.

The opposite pitching of the vanes will produce an effective reduction of jet cross sectional area, resulting in the speeding up of the flow and vice versa. Furthermore, to obtained the pitching protocol ($\psi(t)$), the targeted gust profile is normalised and scaled by a maximum pitch angle (ψ_{max}) as shown in (8). The method is advantageous in its simplicity and offers a clearly defined upper limit of the pitch angle such that stall is not approached.

$$\psi(t) = \psi_{max} \frac{u_{gust}(t) - \overline{u_{gust}(t)}}{\max\left(u_{gust}(t)\right)} \qquad (8)$$

Figure 10 provides a schematic of the considered configurations. The distributed overlapping configuration will extend the span of the middle vanes by 25, 50 and 75% of $\frac{D_m}{3}$, resulting in a total of 8 configurations to be tested, 6 for veer and 2 for wind gusts.
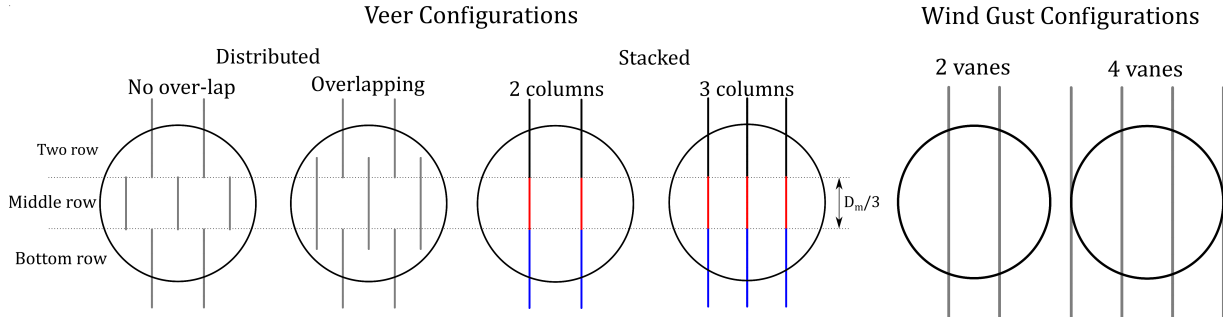
Fig. 10   Schematic of vane configuration for simulating a veer angle distribution across a model wind turbine.

V. Model Development

This section will present the methodology and development process of the computational model; describing the approach used and giving insight into the numerical implementation. The top level flow chart of the model is shown in Figure 11. The green box termed as OJF velocity will be explained in details in Section V.A while the blue dotted box termed as the time loop is detailed in Section V.B.
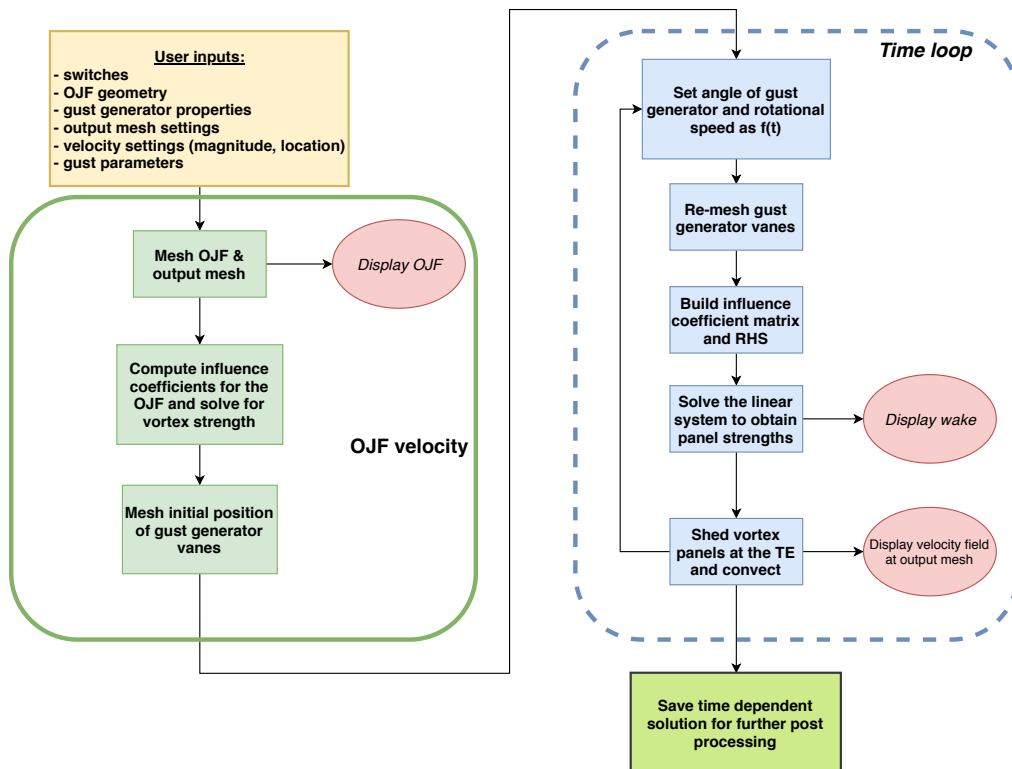
Fig. 11   Computational model flow chart.

A. Free Stream Modelling

The OJF model is approached by representing the flow through vortex filaments. The boundary of the solid walls and the jet flow are represented via closed vortex rings; squares in the settling chamber and octagons in the contraction/test section's jet. This choice of flow singularity stems from the requirement of low computational cost and the relative ease of algorithm implementation. Wind tunnels have previously been modelled using panel methods, such as the VSAERO and PMARC codes [34] [35]. These codes represent the wind tunnel by panelling solid walls with vortex rings/sources/doublets. Their corresponding strengths are governed by a linear system of size $n \times n$, where n is the number of panels used. This is significantly faster than CFD methods, however, when outputting the velocity at a point in the flow field, n vortex rings' influence should be taken into account. In such an implementation Equation 7 needs to be called for each vortex filament. Figure 12 shows an example of such panelling of the National Full-Scale Aerodynamics Complex (NFAC) wind tunnel. The proposed model aims to further improve the computational efficiency of internal flows by using vortex rings to represent the surface instead of panels; i.e. the streamwise vortex filaments would be omitted. Figure 13 shows an example of the OJF discretisation by vortex rings.
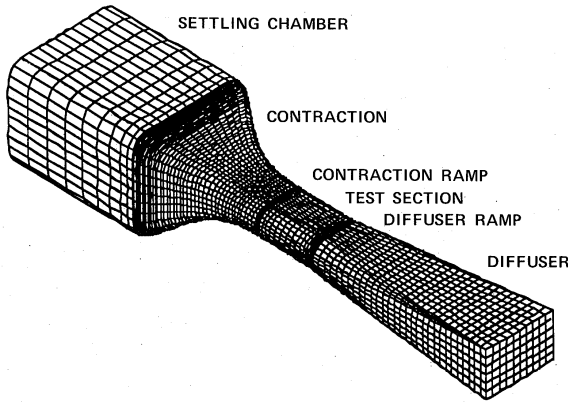
Fig. 12 The panelling of the NFAC wind tunnel via PMARC code. Adapted from [35].
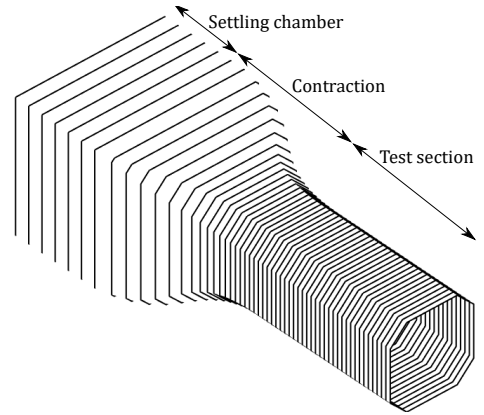
Fig. 13 Representation of the OJF using vortex rings on the surface and jet boundaries.

It becomes apparent that the flow field will be dependent on the vortex rings distribution and their strength. The following is proposed: the vortex ring spacing shall be such that the resulting velocity field conserves mass. Table 2 describes the dimensions of each wind tunnel area, the vortex ring spacing and their circulation.

Table 2 Settings of the free stream model vortex ring distribution and circulations.

Section	Settling chamber	Contraction	Test section
Domain	$-16.9 \leq x < -4.9 \, [m]$	$-4.9 \leq x < 0 \, [m]$	$0 \leq x \leq 13 \, [m]$
Vortex ring spacing	Varying (user defined)	Decreasing according to (9)	Constant
Vortex ring circulation	Constant	Varying	Constant

The algorithm places vortex rings within the settling chamber with variable spacing. The spacing distribution is described by a fitted spline to ten user input values; such that spacing changes smoothly. At $x_1 = -4.9 \, [m]$, the algorithm will compute the spacing based on relation (9), where (dx_0) is a user input spacing at the start of the contraction.

$$dx = dx_0 \frac{A_{\text{local}}}{A_{\text{setl. chamber}}} \tag{9}$$

The jet boundary is then further discretised using octagonal vortex rings, spaced by the last computed vortex ring spacing in the contraction. The resulting vortex ring distribution is shown in Figure 14. As can be seen, the settling chamber and jet boundary extend past the real dimensions of the OJF (Figure 5). This is to avoid entry effects and obtain a smooth flow in the region of importance; i.e. $-8.9 \leq x \leq 6 \, [m]$. Furthermore, several collocation points and corresponding unit vectors are defined

9
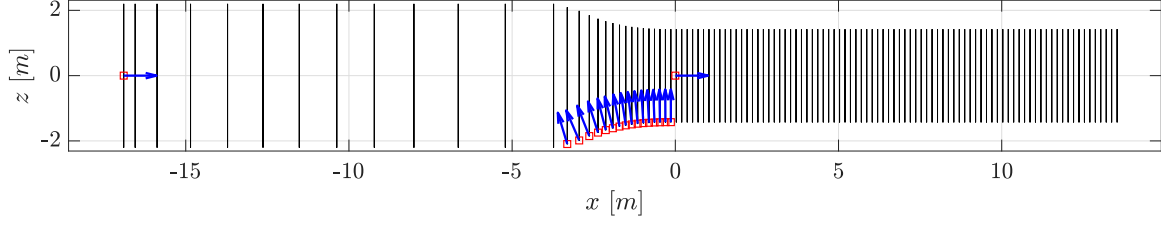
Fig. 14   Vortex ring distribution of the OJF. Red squares represent collocation points, blue arrows are their corresponding unit vectors in the appropriate direction. Side view projection.

To solve for the vortex strengths a linear system can be set up, governed by a square matrix of influence coefficients with size $n + 2$, where n is number of vortex rings representing the contraction. The linear system is composed of $n + 2$ appropriate boundary conditions at the collocation points. The general expression is shown in (10), where (U_i) is the induced velocity at collocation point i by all vortex filaments and subscripts 1 through n represent the contraction elements, subscript 0 the settling chamber and subscript $n + 1$ the test section. The full linear system is shown in (11). The coefficients of the matrix are obtained from (12), where Ω_j is the set representing all the vortex filaments of the ith vortex ring. When $i = 0$ or $n + 1$, all the vortex rings representing the settling chamber or test section are considered. The subscripts $st.$ and $en.$ represent the position vector of the start and end of the kth vortex filament.

$$\mathbf{U}_i \cdot \mathbf{n}_i = a_{i,0}\Gamma_0 + a_{i,1}\Gamma_1 + \cdots + a_{i,n}\Gamma_n + a_{i,n+1}\Gamma_{n+1} = U_{BC,i} \tag{10}$$

$$
\begin{bmatrix}
a_{0,0} & a_{0,1} & a_{0,2} & \cdots & a_{0,n} & a_{0,n+1} \\
a_{1,0} & a_{1,1} & a_{1,2} & \cdots & \cdots & a_{1,n+1} \\
a_{2,0} & a_{2,1} & a_{2,2} & \cdots & \cdots & a_{2,n+1} \\
\vdots & & & \ddots & & \vdots \\
a_{n,0} & \cdots & & \cdots & a_{n,n} & a_{n,n+1} \\
a_{n+1,0} & a_{n+1,1} & \cdots & & \cdots & a_{n+1,n+1}
\end{bmatrix}
\begin{bmatrix}
\Gamma_0 \\ \Gamma_1 \\ \Gamma_2 \\ \vdots \\ \Gamma_n \\ \Gamma_{n+1}
\end{bmatrix}
=
\begin{bmatrix}
U_0 \\ 0 \\ 0 \\ \vdots \\ 0 \\ U_\infty
\end{bmatrix}
\tag{11}
$$

$$a_{i,j} = \sum_{k \in \Omega_j} \left[\frac{1}{4\pi} \frac{\mathbf{r}_{k,st.} \times \mathbf{r}_{k,en.}}{|\mathbf{r}_{k,st.} \times \mathbf{r}_{k,en.}|^2} \mathbf{r}_i \cdot \left(\frac{\mathbf{r}_{k,st.}}{|\mathbf{r}_{k,st.}|} - \frac{\mathbf{r}_{k,en.}}{|\mathbf{r}_{k,en.}|} \right) \right] \cdot \mathbf{n}_i \quad i,j = 0,1,2,...,n,n+1 \tag{12}$$

Solving for the state vector provides the circulation of all vortex filaments, which enables the computation of the flow field within the OJF at a user specified mesh.

Lastly, once the circulation vector is established, the volumetric flow rate is calculated numerically at four stations; settling chamber entry ($x = -8.9$) [m], contraction entry ($x = -4.9$) [m], nozzle ($x = 0$) [m] and jet cross sections at ($x = 1, x = 6$) [m]. This is achieved by determining the cross sectional velocity field projection in the x-direction at each station. The volumetric flow rate is then obtained from (13).

$$\frac{\dot{m}}{\rho} = \sum_{y,z} u(y,z)dA(y,z) \tag{13}$$

B. Gust Generator Modelling

The gust generator comprises one or more vanes oscillating independently such that appropriate flow conditions are achieved in their wakes. The vanes have a symmetrical airfoil, pitching about their quarter chord point. Their LE coincides with the end of the OJF nozzle when at zero pitch angle. Figure 15 provides the reader with the model representation of the current OJF gust generator configuration (corresponding to Figure 7). The vanes are modelled as flat lifting-surfaces. The fluid is assumed incompressible, inviscid and irrotational. The flow field is governed by Equation 5. A solution is obtained numerically through the method of unsteady lifting-surface represented by vortex rings. The model is implemented by aid of its description from [30].
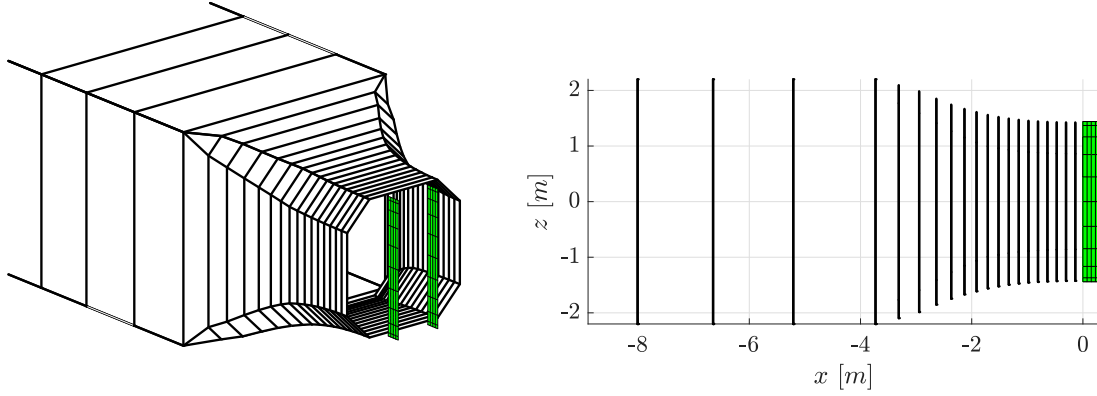
Fig. 15 The current OJF gust generator setup as discretised by the developed model. Vanes shown in green with $b = 2.88 \, [m]$, $c = 0.3 \, [m]$, spaced $0.7 \, [m]$ apart and centred at $y = 0 \, [m]$.

To model the kinematics of the vanes, two coordinates systems are defined; an inertial frame of reference and a body-fixed coordinate system with origin at the quarter chord mid-span of each vane. Therefore, for $t > 0$, the location and orientation of the body-fixed coordinate system can be described by (14). The transformation used is shown in (15), where (ϕ), (θ) and (ψ) are the angles describing the orientation of the x, y and z axes respectively. Figure 16 shows the explained nomenclature.

$$(X_0, Y_0, Z_0) = \mathbf{R}_0(t) \qquad (\phi, \theta, \psi) = \mathbf{\Theta}(t) \tag{14}$$

$$
\begin{pmatrix} x \\ y \\ z \end{pmatrix} = \begin{pmatrix} 1 & 0 & 0 \\ 0 & \cos\phi(t) & \sin\phi(t) \\ 0 & -\sin\phi(t) & \cos\phi(t) \end{pmatrix} \begin{pmatrix} \cos\theta(t) & 0 & -\sin\theta(t) \\ 0 & 1 & 0 \\ \sin\theta(t) & 0 & \cos\theta(t) \end{pmatrix}
$$
$$
\times \begin{pmatrix} \cos\psi(t) & \sin\psi(t) & 0 \\ -\sin\psi(t) & \cos\psi(t) & 0 \\ 0 & 0 & 1 \end{pmatrix} \begin{pmatrix} X - X_0 \\ Y - Y_0 \\ Z - Z_0 \end{pmatrix} \tag{15}
$$
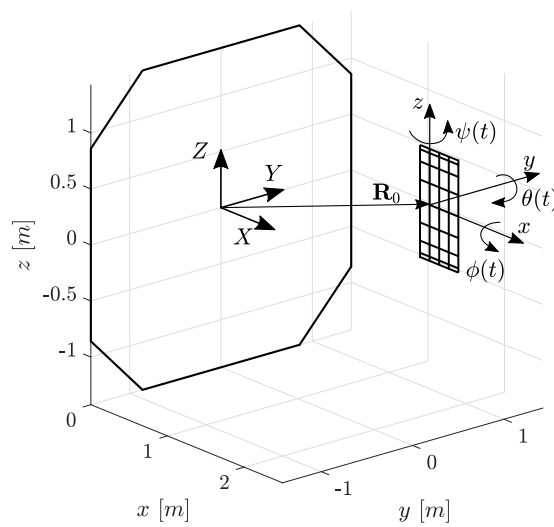
Fig. 16 Representation of the inertial frame of reference (X, Y, Z) and body-fixed coordinate system (x, y, z). The location of the vane is an exaggeration for clear depiction.

11

Using this, the zero normal flow boundary condition on the surface can be expressed as a time varying function in the body fixed frame as shown by (16). Here, ($\mathbf{v}$) is the velocity vector at collocation points at the solid surface due to its motion and (Φ) is the total potential. The kinematic velocity is evaluated by (17), where ($\mathbf{U}_0$) is the body-fixed coordinate system translational velocity, ($\mathbf{r}$) and ($\mathbf{\Omega}$) are the position and rate of rotation vectors in the body-fixed coordinate system.

$$(\nabla\Phi + \mathbf{v}(t)) \cdot \mathbf{n}(t) = 0 \tag{16}$$

$$\mathbf{v} = -\left[\mathbf{U}_0 + \mathbf{\Omega} \times \mathbf{r}\right] \qquad \mathbf{U}_0 = \left(\dot{X}_0, \dot{Y}_0, \dot{Z}_0\right) \qquad \mathbf{\Omega} = (\dot{\phi}, \dot{\theta}, \dot{\psi}) = (p, q, r) \tag{17}$$

Lastly, the pressure can be obtained from the unsteady Bernoulli equation (18). The pressure coefficient is further obtained from (19). The reference velocity in both equations is the surface kinematic velocity as shown by (17).

$$\frac{p_{\,\text{ref}} - p}{\rho} = \frac{u^2}{2} - \frac{v_{\text{ref}}^2}{2} + \frac{\partial\Phi}{\partial t} \tag{18}$$

$$C_p = \frac{p - p_{\text{ref}}}{(1/2)\rho v_{\text{ref}}^2} = 1 - \frac{u^2}{v_{\text{ref}}^2} - \frac{2}{v_{\text{ref}}^2}\frac{\partial\Phi}{\partial t} \tag{19}$$

Finally, the resultant force increment for the k_{th} panel on the lifting-surface follows from (20).

$$\Delta\mathbf{F}_k = -C_{p_k}\left(\frac{1}{2}\rho v_{\text{ref}}^2\right)_k \Delta S_k \mathbf{n}_k \tag{20}$$

Discretisation

The lifting-surface is discretised into quadrilaterals with cosine spacing in the spanwise direction. The mesh is generated with equal spacing in the chordwise direction. At each panel, the leading vortex filament of a vortex ring is placed at the panel's quarter chord. Similarly, a collocation point is defined at $3/4$ of its chord (Δc). Additionally, a local right hand coordinate system is defined at each collocation point with unit directions pointing in the normal ($\mathbf{n}$), spanwise ($\boldsymbol{\tau}_b$) and chordwise direction ($\boldsymbol{\tau}_c$). This is illustrated in Figure 17. Additionally, the area (ΔS), the spanwise (Δb) and chordwise (Δc) lengths of the panel are computed and stored for later use.
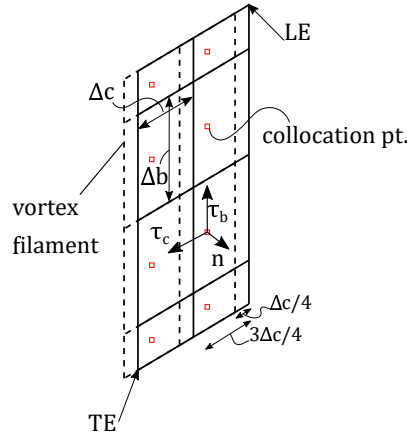
Fig. 17 Example of gust generator vane discretisation into panels (solid lines) by vortex rings (dotted lines). Red squares represent collocation points.

Kinematics

The gust vanes follow a predefined motion (user input), which needs to be taken into account in the simulation. The velocity of the surface at each collocation point can be determined from the vane's motion. Note is made that this computation needs to be done in the body-fixed coordinate system defined above. Equation 21 then provides the surface

velocity at each collocation point, where $(\mathbf{U}_0)$ is the transformed translational velocity to the body-fixed frame. The term $(\frac{\partial \eta}{\partial t})$ accounts for the deformation of the surface. Since the gust generator vanes are assumed rigid and are fixed at the tips, their only motion will be pitching; i.e. $\frac{\partial \eta}{\partial t} = 0$, $\phi(t), \theta(t) = const.$ and $p, q = 0$. Additionally, the vanes feel an oncoming free stream; the jet flow of the OJF.

$$
\begin{pmatrix} U(t) \\ V(t) \\ W(t) \end{pmatrix} = \begin{pmatrix} U_0 \\ V_0 \\ W_0 \end{pmatrix} + \begin{pmatrix} -qz + ry \\ -rx + pz \\ -py + qx - \frac{\partial \eta}{\partial t} \end{pmatrix} = \begin{pmatrix} U_\infty + (r\sin\phi(z - Z_0) + r\sin\phi\,(y - Y_0)) \\ V_\infty - (r\cos\phi(x - X_0)) \\ W_\infty - (r\sin\phi(x - X_0)) \end{pmatrix} \tag{21}
$$

Linear System

Subsequently, the influence coefficient matrix can be build. This works similarly to the system build in Equation 11. Since the model is to account for more than one vane, their interaction needs to be included in the influence coefficient matrix. An example is provided for a system of two vane, discretised by a grid of 2×2 panels (Figure 18).
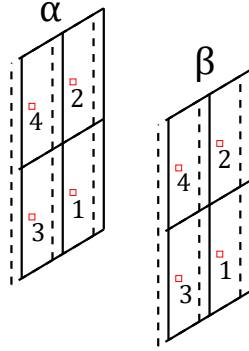
Fig. 18   Numbering of a two vanes (vane α and β) system discretised each by 4 panels.

The resulting matrix will be of size 8×8, since there are a total of 8 collocation points where the zero normal boundary condition (16) needs to be prescribed. Expanding (16) such that the velocity potential is written in terms of vortex rings influence coefficients and their corresponding circulation and noting that additionally to the velocity components described in (21), the wakes in the flow field also induce a velocity component at collocation points, (16) reads:

$$
\sum_j a_{i,j}\Gamma_i = - \left[U(t) + \left(\sum_k u_{\mathrm{w}} \right), V(t) + \left(\sum_k v_{\mathrm{w}} \right), W(t) + \left(\sum_k w_{\mathrm{w}} \right) \right]_i \cdot \mathbf{n}_i = RHS_i \tag{22}
$$

Equation 23 shows the resulting linear system for the two vane system depicted in Figure 18.

$$
\begin{bmatrix}
a_{\alpha1,\alpha1} & a_{\alpha1,\alpha2} & a_{\alpha1,\alpha3} & a_{\alpha1,\alpha4} & a_{\alpha1,\beta1} & a_{\alpha1,\beta2} & a_{\alpha1,\beta3} & a_{\alpha1,\beta4} \\
a_{\alpha2,\alpha1} & a_{\alpha2,\alpha2} & a_{\alpha2,\alpha3} & a_{\alpha2,\alpha4} & a_{\alpha2,\beta1} & a_{\alpha2,\beta2} & a_{\alpha2,\beta3} & a_{\alpha2,\beta4} \\
a_{\alpha3,\alpha1} & a_{\alpha3,\alpha2} & a_{\alpha3,\alpha3} & a_{\alpha3,\alpha4} & a_{\alpha3,\beta1} & a_{\alpha3,\beta2} & a_{\alpha3,\beta3} & a_{\alpha3,\beta4} \\
a_{\alpha4,\alpha1} & a_{\alpha4,\alpha2} & a_{\alpha4,\alpha3} & a_{\alpha4,\alpha4} & a_{\alpha4,\beta1} & a_{\alpha4,\beta2} & a_{\alpha4,\beta3} & a_{\alpha4,\beta4} \\
a_{\beta1,\alpha1} & a_{\beta1,\alpha2} & a_{\beta1,\alpha3} & a_{\beta1,\alpha4} & a_{\beta1,\beta1} & a_{\beta1,\beta2} & a_{\beta,\beta3} & a_{\beta1,\beta4} \\
a_{\beta2,\alpha1} & a_{\beta2,\alpha2} & a_{\beta2,\alpha3} & a_{\beta2,\alpha4} & a_{\beta2,\beta1} & a_{\beta2,\beta2} & a_{\beta,\beta3} & a_{\beta2,\beta4} \\
a_{\beta3,\alpha1} & a_{\beta3,\alpha2} & a_{\beta3,\alpha3} & a_{\beta3,\alpha4} & a_{\beta3,\beta1} & a_{\beta3,\beta2} & a_{\beta,\beta3} & a_{\beta3,\beta4} \\
a_{\beta4,\alpha1} & a_{\beta4,\alpha2} & a_{\beta4,\alpha3} & a_{\beta4,\alpha4} & a_{\beta4,\beta1} & a_{\beta4,\beta2} & a_{\beta,\beta3} & a_{\beta4,\beta4}
\end{bmatrix}
\begin{bmatrix} \Gamma_{\alpha1} \\ \Gamma_{\alpha2} \\ \Gamma_{\alpha3} \\ \Gamma_{\alpha4} \\ \Gamma_{\beta1} \\ \Gamma_{\beta2} \\ \Gamma_{\beta3} \\ \Gamma_{\beta4} \end{bmatrix}
=
\begin{bmatrix} RHS_{\alpha1} \\ RHS_{\alpha2} \\ RHS_{\alpha3} \\ RHS_{\alpha4} \\ RHS_{\beta1} \\ RHS_{\beta2} \\ RHS_{\beta3} \\ RHS_{\beta4} \end{bmatrix} \tag{23}
$$

The coefficient are given by (24), where (Ω_j) represents the set of vortex filaments of the jth panel. The right hand side

of the system is built from Equation 22.

$$a_{i,j} = \sum_{k \in \Omega_j} \left[\frac{1}{4\pi} \frac{\mathbf{r}_{k,st.} \times \mathbf{r}_{k,en.}}{|\mathbf{r}_{k,st.} \times \mathbf{r}_{k,en.}|^2} \mathbf{r}_i \cdot \left(\frac{\mathbf{r}_{k,st.}}{|\mathbf{r}_{k,st.}|} - \frac{\mathbf{r}_{k,en.}}{|\mathbf{r}_{k,en.}|} \right) \right] \cdot \mathbf{n}_i \quad i,j = \alpha1, \alpha2, ..., \alpha4, \beta1, \beta2, ..., \beta4 \quad (24)$$

Simplified, one can see that the matrix in (23) is made up of 4 separate matrices; namely each vane's self influence matrices, the influence of vane α on vane β and vice versa as shown in (25). This trend holds for n number of vanes.

$$\begin{bmatrix} A_{\alpha,\alpha} & A_{\alpha,\beta} \\ A_{\beta,\alpha} & A_{\beta,\beta} \end{bmatrix} \begin{bmatrix} \mathbf{\Gamma}_\alpha \\ \mathbf{\Gamma}_\beta \end{bmatrix} = \begin{bmatrix} \mathbf{RHS}_\alpha \\ \mathbf{RHS}_\beta \end{bmatrix} \quad (25)$$

Proceeding, the system is solved for the circulation vector, which will allow the computation of the velocity field, local pressure and forces. Discretizing Equation 18 results in (26), where subscripts i, j refer to the spanwise and chordwise panel per each vane.

$$\begin{aligned} \Delta p_{ij} = \rho \Big\{ & [U(t) + u_W, V(t) + v_W, W(t) + w_W]_{ij} \cdot \tau_c \frac{\Gamma_{i,j} - \Gamma_{i-1,j}}{\Delta c_{ij}} \\ & + [U(t) + u_W, V(t) + v_W, W(t) + w_W]_{ij} \cdot \tau_b \frac{\Gamma_{i,j} - \Gamma_{i,j-1}}{\Delta b_{ij}} + \frac{\partial}{\partial t} \Gamma_{ij} \Big\} \end{aligned} \quad (26)$$

Finally, the incremental resultant force per panel is obtained from (27).

$$\Delta \mathbf{F} = -(\Delta p \Delta S)_{ij} \mathbf{n}_{ij} \quad (27)$$

The final step in the time loop (per time step) is to shed a row of vortices at the TE with circulation equal to that of the TE panel. Placing the leading filament of the vortex ring at the panel's quarter chord and shedding a wake element with equal circulation as the TE panel results in them cancelling each other out and thus satisfying $\Gamma_{TE} = 0$ (Kutta condition). As new wake elements are shed into the flow field, the existing elements are convected with the local velocity that accounts for the induced velocity by the wake itself, the OJF flow and the vanes (three induced velocities). It is worth noting that this results in an algorithm with computational effort that scales with the square of the wake elements; i.e. quadratically increasing computational effort as the simulation progresses. To address this, the wake in the near field is allowed to deform freely up to a certain distance downstream (the far region), where the wake is frozen and is only convected by the free stream velocity; i.e. only one induced velocity is accounted for (that of the OJF). Implementing a frozen wake scales down the algorithm's computational cost. An illustration of the shedding at each time step is shown in Figure 19. Note is made that for the first iteration ($t = 0$), only the leading filaments of the first wake panels row are present in the simulation.
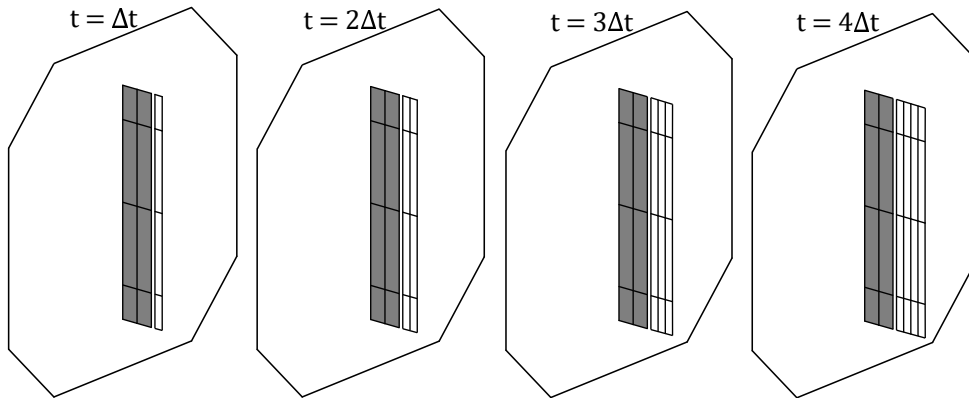
Fig. 19   Illustration of wake shedding for the first through forth time step.

VI. Validation

Prior to carrying out the validation process, the model is subjected to a unit test verification procedure on the essential subroutines and a convergence study, where the time step (Δt), panel density (N, M), vortex core size (R) and free wake length are characterised. Analytical solution such as the Wagner and Theodorsen lift were used as reference in the analysis [36]. The results are summarised in Table 3. Furthermore, the model's sensitivity to gust generator parameters is tested and compared to results from an analogous study carried out by means of 2D, transient CFD with moving meshes [9]. Additionally, conversation of mass was checked versus theoretical values. Volumetric flow rate errors smaller than 2% were identified within the settling chamber and contraction, which grew at the jet flow boundary, where differences were smaller than 5%.

Table 3   Recommended model parameter practices derived from the converge analysis.

Parameter	Recommendation
N	20
M	9
R	$0.005\,[m]$ or $\mathcal{O}\left(\min(\Delta b)\right) - 1$
Δt	$\mathcal{O}(\frac{c}{4U\infty})$ or s.t. $\Delta\psi \le 0.3\,[°]$
Wake	$\mathcal{O}(b/2)$ or s.t. $b/2$ length past region of interest in the domain

The results of the developed tool are compared to experimental measurements from various studies [28, 29, 37]. The analysis was split into three components; evaluation of the resulting free stream uniformity, the modelling of symmetric airfoil lift curves and gust generation. A list of model assumptions, the reason why they are made and their effects is provided below.

1) Incompressible flow:
   - Application: The wind tunnel is run at low speeds.
   - Effect: This results in higher-order density errors, which at an engineering level can be neglected.
2) Inviscid, irrotational flow:
   - Application: The flow is at rather high Reynolds numbers. Furthermore, drag forces are not of primary importance. Vorticity is confined to a thin wake sheet.
   - Effect: Viscous drag is not predicted.
3) The gust generator vanes are represented via flat lifting surfaces.
   - Application: The vanes have symmetrical airfoil.
   - Effect: Loss of LE suction peak.
4) The gust generator vanes are assumed rigid.
   - Application: The original OJF gust generator is made of ROHACELL 31IGF foam, undergone aeroelastic analysis and was deemed rigid enough not to interact with the flow [9].
   - Effect: Potential for deformations occurrence due to oscillations of higher frequency than the original gust generator. Additionally, for larger planforms, the forces acting on the vanes will be similarly larger, therefore deformations could occur, interacting with the flow field.
5) The flow stays attached to the surface.
   - Application: The vanes will not be used at high angles of attack; i.e. at angles lower than the stall angle.
   - Effect: The oscillation motion could induce early separation, which is not accounted for.
6) The model does not consider strong vortex stretching
   - Application: The wake elements can not undergo large amount of stretching due to interaction with other wake elements.
   - Effect: In the case of strong stretching, the circulation of wake elements need to be decreased proportionally to the stretching such to preserve angular momentum [30]. This is not done and hence unrealistic induced velocities will be observed in the case of strong stretching.

A. OJF Uniformity

The resulting flow field at three downstream locations are validated against measurements from [28] in Figure 20. It is noted that uniformity is maintained along $\approx 86\%$ of the nozzle width. The model follows the measurements closely in

this area, however, at the jet boundaries differences are seen. Firstly, the model predicts an acceleration close to the jet boundary at $1.5\,[m]$ downstream of the nozzle. This is physically contradicting since the flow slows down in that region due to the formation of shear layers. The influence of the upstream vortex rings (making up the contraction) dictate this behaviour. As velocity is sampled further downstream, where, the vortex rings maintain a constant circulation, the velocity behaviour approaches the measurements for a wider portion of the jet width. The validity of the region of interest, where models are usually tested in the OJF $-1.2 \leq y \leq 1.2\,[m]$ is achieved, deeming the success of correctly simulating the free stream flow.
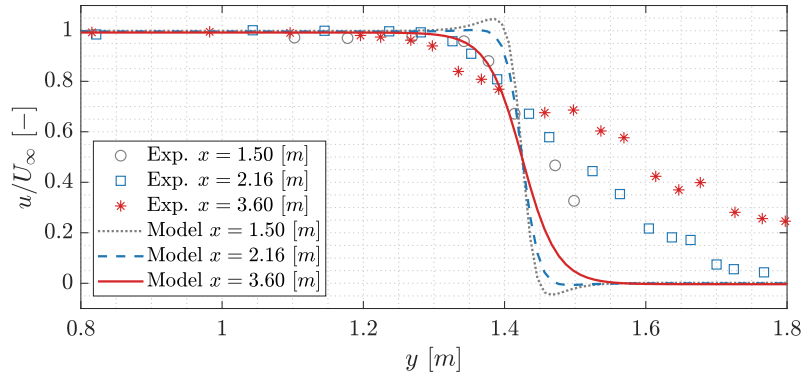
Fig. 20 Comparison of the uniformity in the OJF at 1.5, 2.16 and 3.6 $[m]$ downstream of the nozzle. Data points from [28] versus the developed model.

B. Steady-State Lift Curves

The validity of representing a symmetrical airfoil, the NACA0012, by a flat lifting-surface is checked. Airfoil measurements from [37] are used for comparison. The Reynolds number is varied in the simulation via the free stream velocity. The lift curves at $Re = 1.44 \times 10^6$ ($U_\infty = 28.7$) and 2.88×10^6 ($U_\infty = 57.4$) as well as the pressure coefficient distribution at $\alpha = 6, 14\,[°]$ are shown in Figure 21.
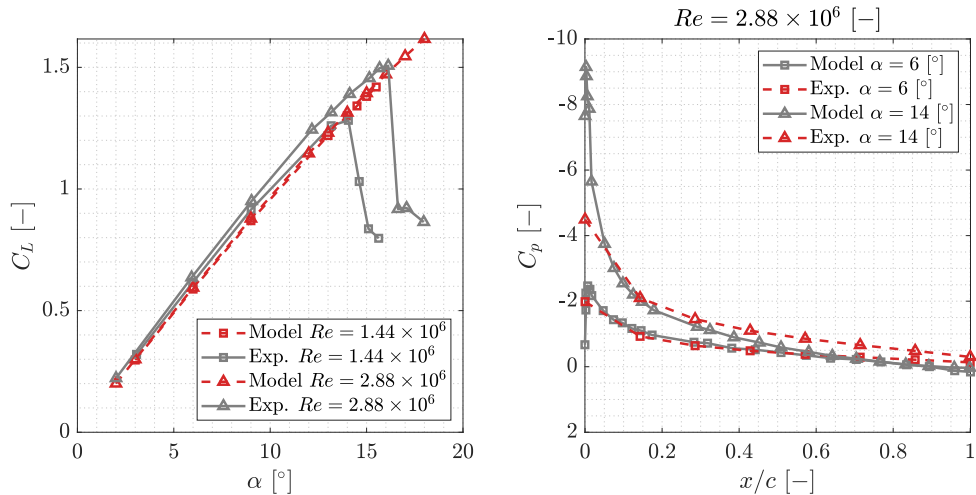
Fig. 21 Lift curves and pressure distributions of the NACA0012 at $Re = 1.44 \times 10^6$ and $2.88 \times 10^6\,[-]$. Experimental measurements from [37]. Model pressure sampled at mid-span.

The model approximates the lift curve well, with negligible differences for low angle of attack; i.e. $\alpha \leq \approx 5\,[°]$. As the angle of attack increases so do the differences, which trend towards under predicting the experimental measurements.

As expected, the model does not predict stall. The effect of Reynolds number is small, with the two sets of model results being virtually identical at low angles of attack and marginally different for angles of attack greater than 10 [°]. The pressure distribution at relatively low angle of attack, matches the measurements well close to the LE, however, the predictions deteriorate near the TE. Overall, the pressure distribution at low angles of attack is simulated well. As angle of attack is increased, the model struggles approximating the suction peak; expected behaviour due to the draw backs of thin lifting surface modelling. The results show large differences at the LE, explained by the lack of LE radius, leading to the under-prediction of the suction peak pressure. Towards the quarter chord point the results converge to experimental measurements. The trend is not maintained, as further towards the TE the model over-predicts suction.

C. OJF Gust Generator

The current configuration of the OJF gust generator has been analysed by means of PIV measurements of the achieved flow field in [29]. The vanes followed a $1 - \cos$ motion as described by (28), where (ψ_{max}) was the gust vanes' maximum pitch angle and (ω) was the oscillation frequency. The results have been documented in terms of flow field gust angle as defined by Equation 29. The velocity components have been sampled at various downstream and vertical locations. Furthermore, different reduced frequencies of oscillation (as defined by (30)) have been tested. A schematic of the vane configuration is shown in Figure 22.

$$\psi(t) = \psi_{max}[1 - \cos(\omega t)] \tag{28}$$
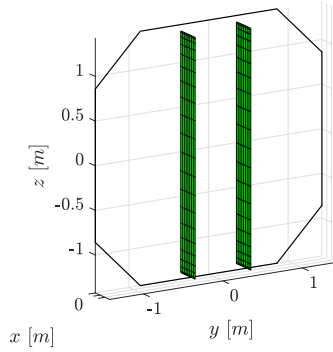
$$\alpha_{gust} = \tan^{-1}\left(\frac{v}{u}\right) \tag{29}$$

$$k = \frac{\omega c}{2U_\infty} \tag{30}$$

Fig. 22   Schematic of OJF gust generator configuration used for validation.

The achieved gust angle at $\mathbf{x} = (1.5, 0, 0)$, or $3c$ $[m]$ downstream as a function of time for one period of the gust is shown in Figure 23. The results match the experimental measurements well, with a discrepancy of ≈ 0.4 [°] (4.3%) at the peak of the gust. The upstroke and downstroke match to a better degree. Good match is seen in terms of lateral uniformity, while vertical uniformity is not preserved with differences up to $\approx 15\%$ (≈ 0.8 [°]) when comparing centreline gust angle to a vertical offset of 1 $[m]$. Additional results can be viewed in the appendix.

The behaviour of the model to downstream gust uniformity, maximum pitching angle and reduced frequency of oscillation is summarised in Figure 24 in terms of peak gust angle.

The maximum gust amplitude generally increases downstream for low and moderate reduced frequency of oscillation. This is not seen for the highest reduced frequency where the maximum gust amplitude downstream stays constant. The model follows this trend with an error of ≤ 0.5 [°]. The error increases to ≈ 1 [°] for large maximum vane deflection angle at larger downstream locations.

As expected, the maximum gust amplitude scales with the maximum vane deflection angle. The model clearly captures this trend, as can be seen by the grouping of curves in Figure 24. It is noted that the model generally under-predicts the maximum gust amplitude for smaller maximum vane deflection angles. The opposite is true for large maximum vane deflection angles and large reduced frequency of oscillation. This points towards difficulties in predicting vane effectiveness loss, highlighting the limitations introduced by the model's assumptions.

The effect of reduced frequency at a given downstream location and maximum vane deflection angle is relatively limited. However, the measurements at a further downstream location from the vanes point towards loss of vane effectiveness as reduced frequency increases past 0.1 $[-]$. This is not captured by the model, which generally shows an increase in maximum gust amplitude with increasing reduced frequency.
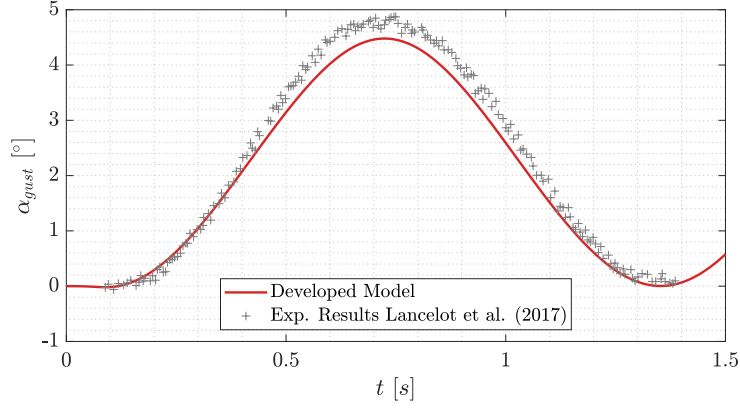
Fig. 23 Gust angle at $\mathbf{x} = (1.5, 0, 0)\ [m]$ of the developed model vs experimental measurements from [29]. Simulation carried out for 2 vanes with $c = 0.3\ [m]$, $b = 2.7\ [m]$, $U_\infty = 15\ [ms^{-1}]$, $\psi(t) = 10[1 - \cos(5t)]\ [°]$ and $k = 0.05\ [-]$.
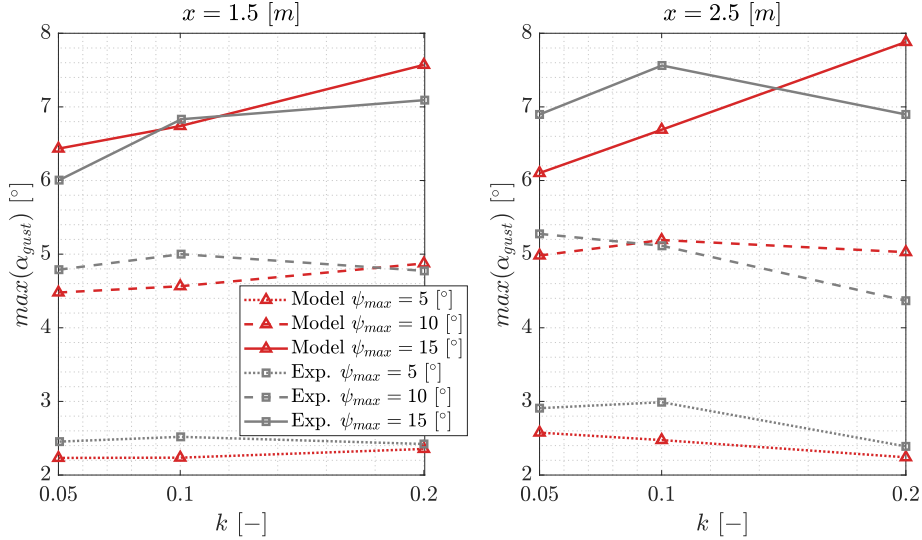
Fig. 24 Maximum gust angle for varying downstream location, reduced frequency, and maximum pitching angle: $x = 1.5, 2.5\ [m]$; $k = 0.05, 0.1, 0.2$ and $\psi_{max} = 5, 10, 15\ [°]$. Simulation carried out for 2 vanes with $c = 0.3\ [m]$, $b = 2.7\ [m]$, $U_\infty = 15\ [ms^{-1}]$.

In summary, results match well close to the vanes ($x = 1.5\ [m]$) and for smaller maximum pitching angle ($\psi_{max} = 5, 10$ [°]). Larger discrepancies are observed further downstream, for large reduced frequency and large maximum pitching angle; i.e. $x = 2.5\ [m]$, $k = 0.2\ [-]$ and $\psi_{max} = 15\ [°]$. However, general trends are captured well, with the maximum errors of $\approx 1\ [°]$ ($\approx 14\%$).

D. Cranfield Gust Generator

An analogous analysis is performed for the Cranfield gust generator set-up. The facility employs 6 horizontal vanes of $c = 0.114\ [m]$ and $AR = 10\ [-]$ spaced $0.254\ [m]$ from each other. The vanes followed a sinusoidal pitching motion described by (31). The experimental measurements were conducted with a cross hot-wire-anemometer at $U_\infty = 7.5\ [ms^{-1}]$ [10]. The velocity components were measured at two locations, $7c$ downstream ($x = 0.8128\ [m]$) at $z = -0.127$ and $0\ [m]$; the latter location corresponds to halfway between the middle vanes, while the former coincides with the location of the TE of the third vane counting from bottom. The maximum gust angle is compared, as computed

18

from (32). The vanes are scaled to match the OJF nozzle width, while maintaining $AR = 10 \, [-]$ and the experimental reduced frequency is maintained by scaling the free stream velocity. A schematic of the test set-up is shown in Figure 25.
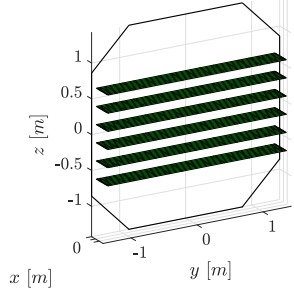
$$\psi(t) = \psi_{max} \sin(\omega t) \qquad (31)$$

$$\alpha_{gust} = \tan^{-1}\left(\frac{w}{u}\right) \qquad (32)$$

Fig. 25 Schematic of the Cranfield gust generator facility as used in the developed model.

The time series of a sinusoidal gust at two vertical locations is shown in 26. It is interesting to point out that the lower vertical location results match the experimental measurements better than the centreline results.
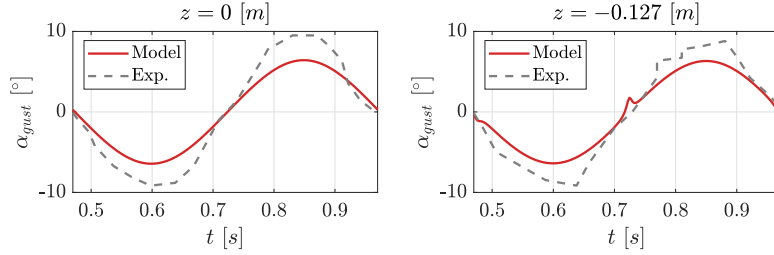
Fig. 26 Gust angle for the developed model and experimental measurements at two vertical locations; $x = 0.8128$ and $z = 0, -0.127 \, [m]$ for $\psi(t) = 8\sin(4\pi t) \, [°]$ and $k = 0.1 \, [-]$.

The effects of reduced frequency, maximum pitch angle and vertical location are summarised in Figure 27. The maximum gust angle is compared. Similar trends are seen; i.e. the centreline predictions differing to a higher extent. Very good matching is seen for low reduced frequency at a higher maximum pitch angle with errors $\leq 8\%$ and $\leq 4\%$ at the centreline and lower vertical position, respectively. For increased reduced frequency and decreased maximum pitch angle, the predictions deteriorate. The general trend is captured, however, maximum gust angle is under predicted by up to 30%. This behaviour is opposite to the OJF test case, which featured only two vanes. The mismatch suggests that the model has a stronger relation between achieved maximum gust angle and maximum pitch angle in the presence of a large number of vanes; i.e. $\frac{\partial \alpha_{gust}}{\partial \psi}|_{exp} < \frac{\partial \alpha_{gust}}{\partial \psi}|_{model}$.
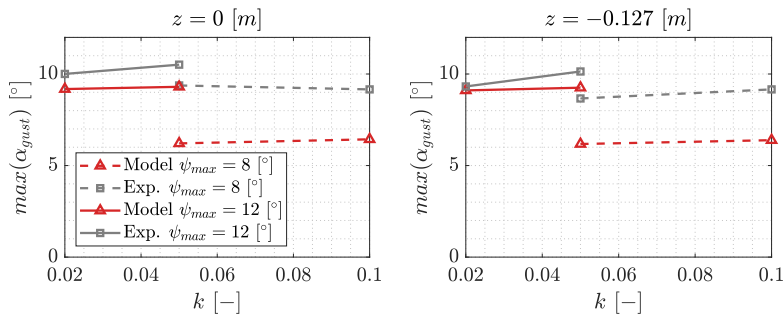
Fig. 27 Maximum gust angle for the developed model and experimental measurements at various reduced frequencies, maximum pitch angle and vertical location; $k = 0.02, 0.05, 0.1 \, [-]$; $\psi_{max} = 8, 12 \, [°]$ and $z = 0, -0.127 \, [m]$.

19

VII. Gust Generator - Results and Discussion

The derived model is used in assessing conceptualised gust generator configurations. Two gusts types are considered; veer and speed wind gusts as introduced in Section II. Per gust type, a configuration search is performed considering the guidelines described in Section IV. The results can be found in the appendix. A total of eight configurations are tested, six for veer and two for wind gusts. A candidate is chosen per gust type that best matched the targeted gust profile. The remainder of this section will describe the results obtained by the chosen configurations.

Note is made that the analysis has been performed assuming a model wind turbine diameter of $D_m = 1.8\,[m]$, with hub at OJF centreline and $2\,[m]$ downstream of the nozzle. All gust generator vanes had chord length $c = 0.4\,[m]$. This choice is made for maximum vane effectiveness.

A. Veer

The veer case demonstrated the generation of a steady, spatially varying gust. Veering profiles from [17] are digitised, sampled for the chosen physical wind turbine and scaled for wind tunnel simulation. The wind profiles for three atmospheric stabilities are shown in Figure 28. The mean in-field free stream speed was $9\,[ms^{-1}]$.
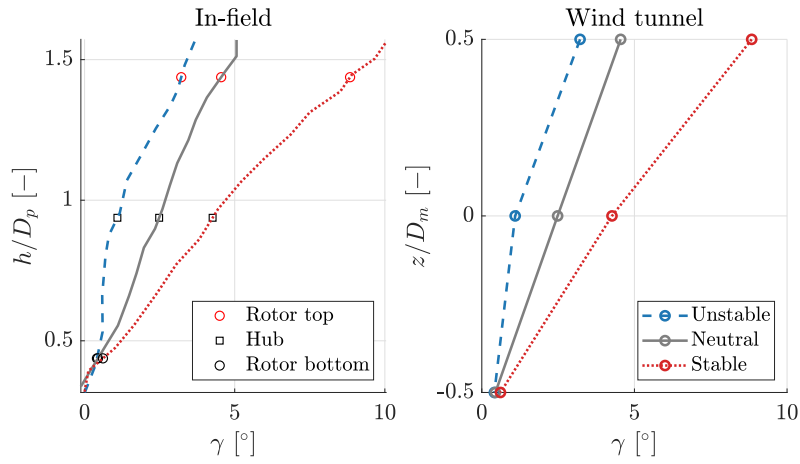
Fig. 28 Veer profiles for stable, neutral and unstable atmospheric conditions. In-field measurements from [17] and sampled for $D_p = 128\,[m]$.

The neutral veer profile was targeted in the configuration search. The results revealed a noisy veer distribution for the distributed vanes configurations. The peaks in veer angle were linked to the location of vane tip vortices. As overlap was increased the influence of tip vortices damped out. The stacked vanes configurations further smoothed out the effects of tip vortices. Furthermore, as supported in [10], a larger number of vanes resulted in better lateral uniformity. Therefore, the stacked, 3 columns configuration was chosen for veer generation. The simulated neutral veer profile over the rotor disc and corresponding horizontally averaged (y-direction) profile are shown in Figure 29.
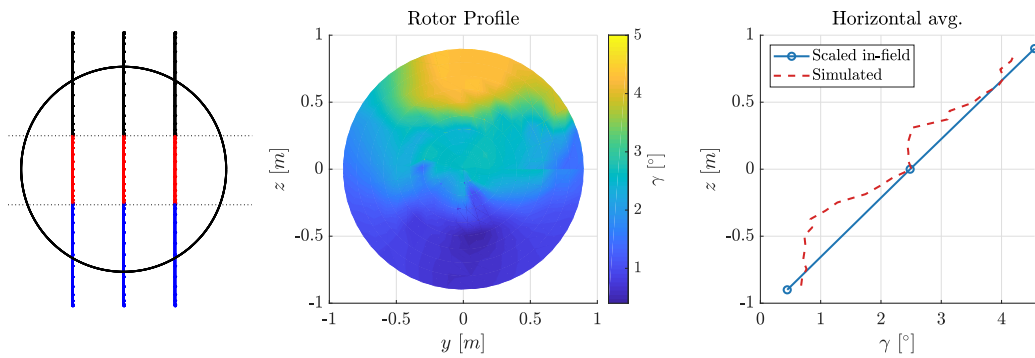
Fig. 29 Surface contour across rotor disc and horizontally averaged (y-direction) veer profile for neutral conditions.

The stable condition veer profile is further targeted while seeking flow features, since the effects are accentuated with increased veer distribution, enabling for easier interpretation.

From the performed configuration search, it became apparent that the flow is governed by lateral momentum change as well as the shed tip vortices of the vanes. Although the stacked configuration provides somewhat of a barrier for fluid particles to circulate from the pressure side to the suction side, tip vortices still develop and interact together downstream. Streamlines seeded from the TE tips of the vanes are generated up to and past the model rotor. Side and front views are shown in Figure 30. The flow is from left to right when viewed from the side or out of the page when viewed from the front. The vanes are deflected to the right in the front view. Tip vortices are clearly identified by the helix shape of the streamlines. The streamlines released from location (A) do not only follow the path of the tip vortices but also a larger scale rotation, showing a positive rotation about the x-axis when following the right hand rule. The same behaviour is mirrored by the streamlines released from locations (B) and (C) (negative rotation about x-axis). As the vane deflection angle decreases for the bottom row vanes, the strength of the tip vortices and the larger scale rotation decreases; as supported by the decreased deflection of the streamlines in the yz-plane at location (D).
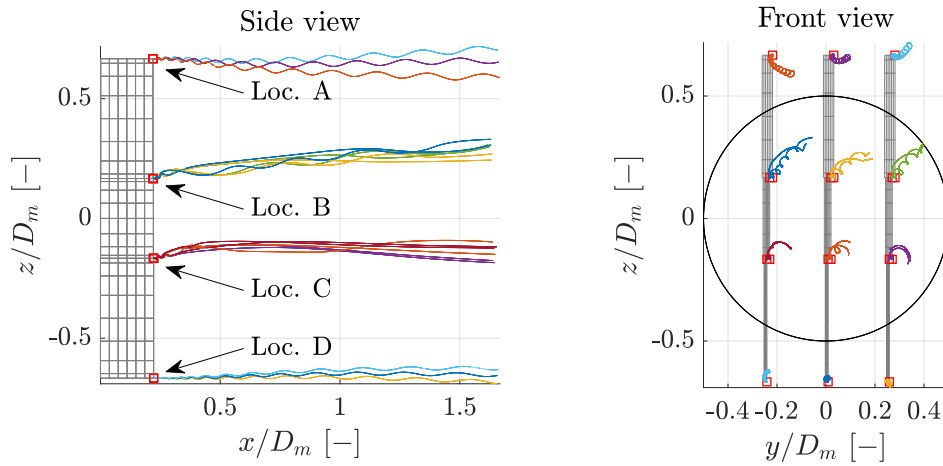
Fig. 30 Side and front view of streamlines seeded from the TE tips of the gust generator vanes. Configuration set-up targetting the stable atmospheric veer distribution of Figure 28. Figure to scale.

To verify the above trends, normalised x-direction vorticity (ζ_x) contours at various yz-planes are shown in Figure 31, where the x-axis was stretched for easier visualisation. The same streamlines are overlaid. It is confirmed that the streamlines indeed follow the tip vortices; they intersect the concentrations of vorticity in the the yz-planes. Additionally, the horizontally averaged, normalised vorticity and achieved veer profiles for each plane are shown in Figure 32.
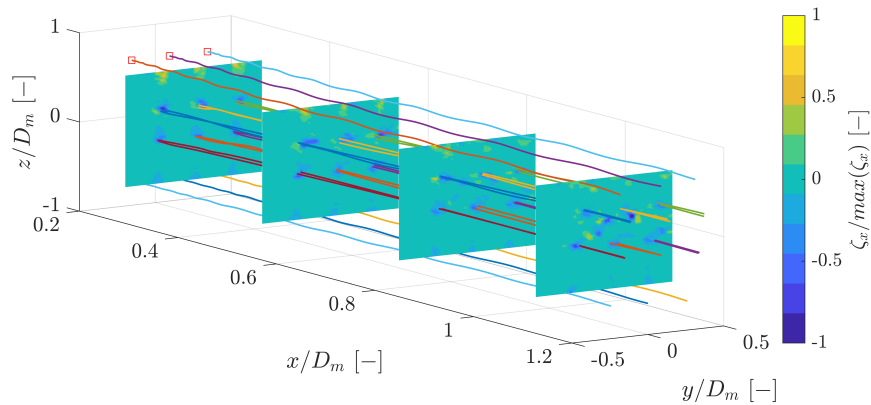
Fig. 31 Streamwise vorticity (ζ_x) contours at various streamwise locations and rotor plane. Streamlines seeded from the TE tips of the gust generator vanes are overlaid.

21
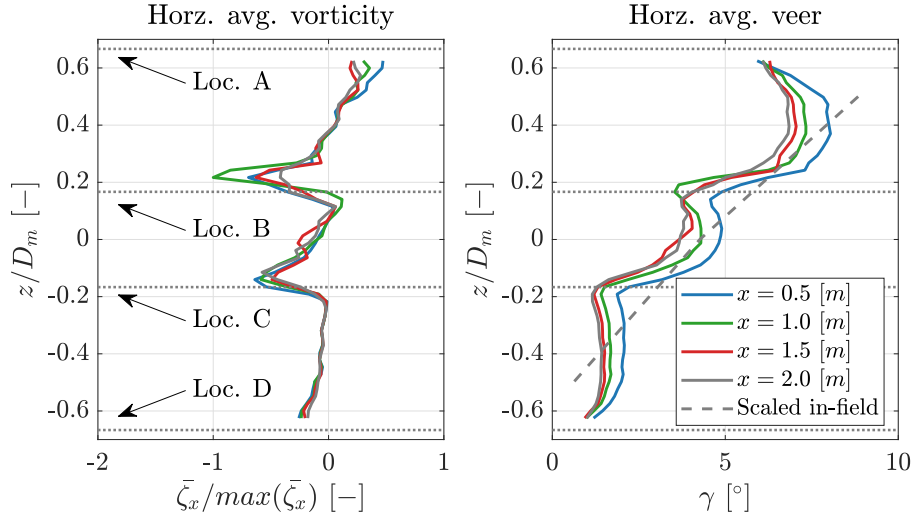
Fig. 32 Horizontally averaged normalised vorticity and veer profiles at various streamwise planes. In-field scaled veer overlaid for comparison.

The vorticity profiles follow the same trend for all yz-planes, with small differences. This is as expected since vorticity is conserved. The profiles begin with positive x-direction vorticity at location (A), decreasing towards (B). A minimum is reached just ahead of (B), with magnitude approximately equal to that at location (A). The trend resembles the spanwise trailing vorticity distribution of a lifting-surface (as consequence of spanwise circulation gradient). The vorticity quickly returns to a small positive value past location (B). The blend in vorticity on either side of (B) is the result of two counter rotating tip vortices; i.e. that of the top row vanes with the middle row vanes. The same is repeated at location (C), however, to a lesser extent since the bottom row vanes are deflected by a small pitch angle. Vorticity value crossing locations (B) and (C) are negative and equal, since the difference in vane deflection angles between the top/middle vanes and middle/bottom vanes was the same ($\Delta\psi = 4\,[°]$); i.e. the difference in tip vortices strengths of the top/bottom vanes was the same as the middle/bottom vanes.

The veering profile is plotted analogously. Veer profiles are marginally larger close to the vanes, and approach the same trend further downstream; virtually identical profiles for $x = 1.5$ and $2\,[m]$. A maximum in veer angle is obtained as the mid span of the top row vanes is approached ($\approx x/D_m = 0.4\,[-]$). As seen from Figure 30, at locations (A) and (B) two large scale rotations of the fluid form (counter rotating). The veer maximum coincides with the location halfway in between them. As such, two contributions in lateral flow component are present and responsible for the veer maximum. Furthermore, the location of the veer maximum also coincides with the saddle point of the trailing vorticity in between locations (A) and (B). As location (B) is approached, veer angle rapidly decreases as a consequence of shorter moment arm from the large scale rotation at (B). Past (B), a secondary veer maximum is achieved, repeating the formerly explained trend to a lesser extent. Segment (CD) shows the same behaviour.

As saddle points in the vorticity profile coincide to maxima in veer profile and steep vorticity gradients coincide with steep veer profile gradients, the two quantities are linked. Furthermore, a correlation between their gradients is also expected; i.e. $\frac{\partial\zeta_x}{\partial z^*} \propto \frac{\partial\gamma}{\partial z^*}$, where $z^* = z/D_m$.

In summary, the vanes' trailing vorticity convects downstream leading to the profiles presented in Figure 32. Since vorticity is conserved, the same result can be concluded by considering that the trailing vorticity is equal to minus the spanwise circulation gradient of the vane; i.e. $\zeta_x = -\frac{\partial\Gamma(z)}{\partial z}$. Furthermore, as seen from the results, a gradient in (ζ_x) gives rise to a veer angle gradient. This leads to the conclusion that the second spanwise derivative of circulation is correlated to the veer gradient; i.e. $-\frac{\partial^2\Gamma(z)}{\partial z^2} \propto \frac{\partial\gamma}{\partial z}$. It is common to implement twist to a lifting surface such that the spanwise circulation is varied. The conclusion can be used to derive the optimal twist distribution for a given targeted veer profile, therefore, fully excluding tip vortices across the tested rotor disc, resulting in smooth veer profiles.

22

General Case

The deflection angles of the vanes are tuned to match each atmospheric condition as presented in Figure 28. A 2D viscous analysis was performed via XFOIL, identifying the stall angle of a NACA0012 airfoil at $Re = 237,467 \ [-]$ to be 12 $[°]$. A maximum pitch angle of 11 $[°]$ is opted for providing some margin against stall. Furthermore, the 3D vane will stall at a higher angle of attack, further increasing the margin taken. It is noted that the maximum pitch angle can be increased for increasing Reynolds number as long as the tested wind turbine's rotational speed is increased proportionally, satisfying tip-speed-ratio matching.

An additional case is added; i.e. the limiting case. The strategy of deriving set veering profile was increasing the veer gradient across the rotor diameter. This meant having the largest possible difference between the veer angle at the top and bottom of the rotor. The vanes at the top and bottom were deflected in opposite directions. The middle vanes are still kept in the simulation to provide a constraint to the development of tip vortices. The tuned deflection angles are summarised in Table 4. Furthermore, each vane loading in terms of lift coefficient is summarised in Figure 33.

Table 4 Vane deflection angles distribution the unstable, neutral, stable and limit veer profile. Values in degrees.

Case	Unstable	Neutral	Stable	Limit
Top	4°	6°	11°	11°
Middle	2°	4°	7°	0°
Bottom	1°	2°	3°	−11°
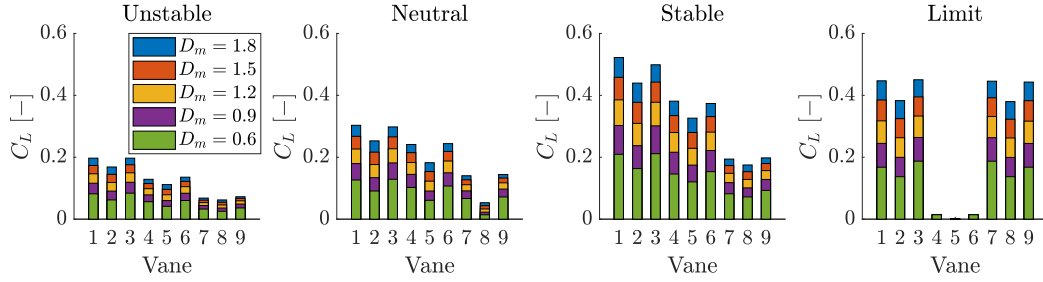
Fig. 33 Corresponding vane loading for vane deflection angles from Table 4. Vanes 1-3 represent the top row, 4-6 middle and 7-9 the bottom.

The achieved veering profiles as a function of veer condition and model wind turbine diameter are shown in Figure 34.
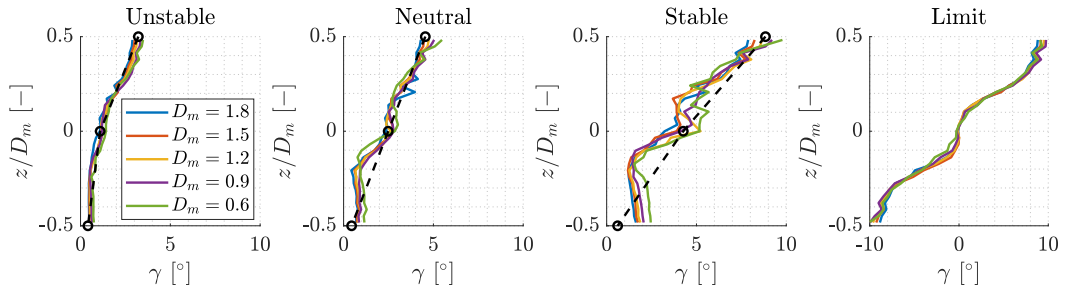
Fig. 34 Horizontally averaged veering profiles as a function of atmospheric stability and model wind turbine diameter. A limiting case is included showing the maximum veering gradient.

As can be seen, veer profiles are independent of model wind turbine diameter. The three atmospheric conditions veer profiles are approximated well at the upper half diameter of the rotor. The results show zero veer gradient across the bottom third of the model wind turbine diameter for the neutral and stable cases; i.e. $-0.5 \leq z/D_m \leq -0.1$. Furthermore, for the limiting case, a difference between veer at the rotor top and bottom of 20 $[°]$ is achieved.

B. Velocity Gust

Unsteady streamwise velocity component variation is demonstrated. Two gust generator configuration are assessed by targeting a modified EOG gust as described by Figure 35. The gust profile is computed with physical wind turbine properties from Table 1. The gust magnitude is lowered by as much as 50% and its time period increased by a factor of 4, providing a range of target gusts, since the original extreme gust might be unrealistic for the wind tunnel setting. The gust is scaled based on a velocity ratio of $\frac{U_{\infty,m}}{U_{\infty,p}} = 0.5\ [-]$. This lead to time scale of $\frac{t_m}{t_p} = 0.0281\ [-]$.
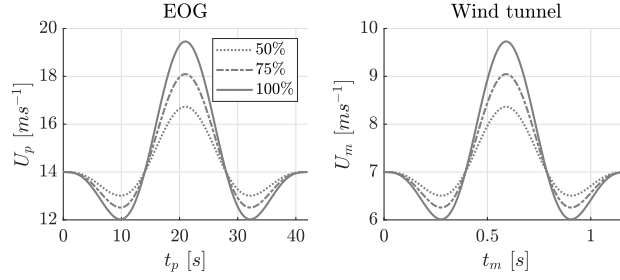
Fig. 35 EOG profiles at various magnitudes for the chosen physical wind turbine and corresponding scaled wind tunnel gust. Gust generated with $I_{ref} = 0.16\ [-]$, $U_{\infty,p} = 14\ [ms^{-1}]$, $h_{hub} = 120\ [m]$ and $D_p = 128\ [m]$.

The maximum vane deflection angle is set to 10 [°]. Figure 36 shows the pitching motion followed by the vanes, as well as a top view of the vanes location for the two vanes configuration. Initially, the vanes are at zero pitch angle for $0.05\ [s]$. Subsequently, the vanes on the positive side of the y-axis deflect in the positive direction (right hand rule about z-axis) and vice-versa. This creates an effective increase in nozzle area. Since the flow is incompressible, conservation of mass predicts that the flow will decelerate. The vanes then change deflection angles in the opposite direction, which creates an effective decrease in local area, accelerating the flow. Once the pitching motion completes, the vanes are held at zero deflection angle such that the created gust can convect past the rotor, which has been assumed to be $1.8\ [m]$ in diameter and $2\ [m]$ downstream of the OJF nozzle. The same motion applied to the configuration with four vanes. Note is made that the motion corresponds to a reduced frequency of $k \approx 0.15\ [-]$, a value well within the capabilities of the developed model as supported by validation results.
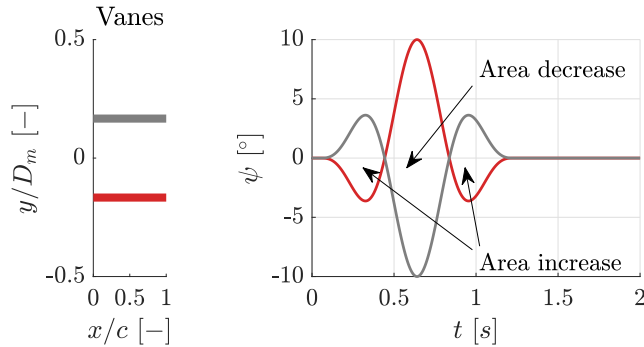
Fig. 36 Left: top view of 2 vanes configuration placement. Right: pitching motion followed by the vanes. Pitch angle (ψ) defined positive about the z-axis (out of page) according to the right hand rule.

The point corresponding to the hub location is sampled for the streamwise velocity component. The results are presented in Figure 37, where both considered configurations are shown. The results are identical, with the exception of the velocity peak; the four vane configuration achieving a slightly larger peak. A 3% decrease in velocity is seen at $t = 0.45$ [s], corresponding to the first jet area increase by the vanes. As they start pitching in the opposite direction, a sharp increase in velocity is observed. The streamwise component increases by $\approx 14\%$ (18%) in $0.27\ [s]$ for the two (four) vanes configuration. At the peak, the velocity decreases sharply, by $\approx 23\%$ (28%) in $\approx 0.3\ [s]$ for the two (four) vane configuration. This is linked to the time at which the vanes complete pitching towards each other plus the convection time of the wake to the rotor plane: $0.64 + \frac{1.6}{7} \approx 0.9\ [s]$, where $0.64\ [s]$ is the time at which the vanes reach their

maximum deflection angles, 1.6 $[m]$ is the distance between the vanes' TE and the rotor plane and 7 $[ms^{-1}]$ is the average free stream velocity. The hub velocity then recovers to free stream value mirroring the gust profile of the first half time period.
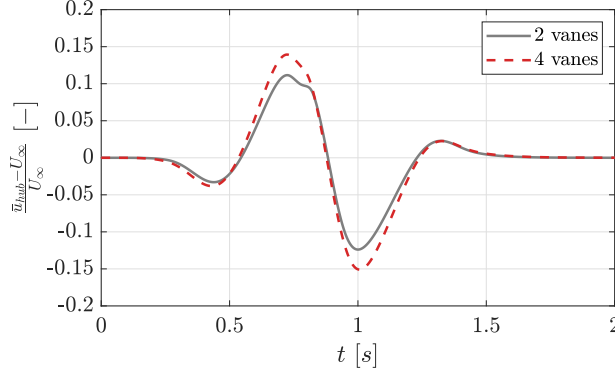
Fig. 37   Hub normalised streamwise velocity component sampled at $\mathbf{x} = (2, 0, 0)\ [m]$ for 2 and 4 vanes configurations.

Furthermore, the streamwise and lateral velocity components are sampled and vertically averaged across the rotor disc as a function of time. Contour plots are presented in Figures 38 and 39, respectively.

The two configurations are marginally different in the centre third of the rotor achieving a reasonable speed up, followed by a slow down. On either side of this area, the streamwise velocity component behaves opposite. The four vanes configuration maintains a smaller difference between the inner region and outer edge. Additionally, an equal and opposite (on either side of the y-axis) lateral velocity component is introduced (Fig. 39).

(a) Two vanes

(b) Four vanes
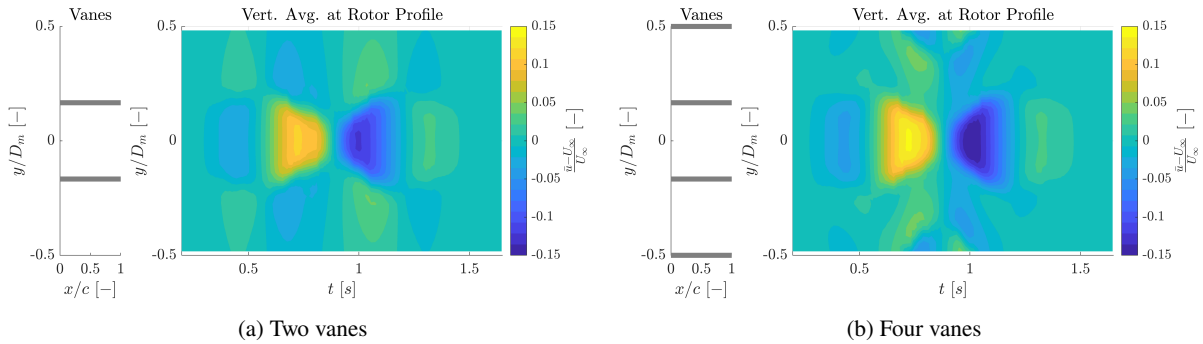
Fig. 38   Normalised vertically averaged streamwise velocity component ($\frac{u - U_\infty}{U_\infty}$) along the rotor profile.

(a) Two vanes

(b) Four vanes
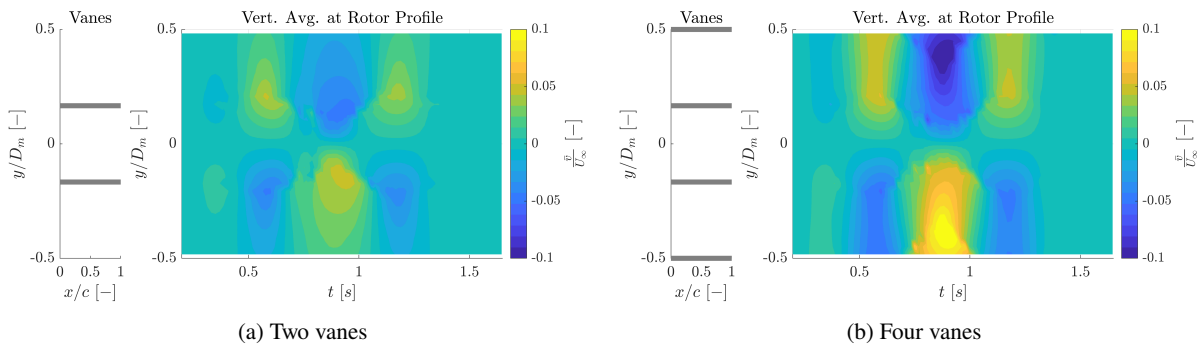
Fig. 39   Normalised vertically averaged lateral velocity component ($\frac{v}{U_\infty}$) along the rotor profile.

25

Reflecting on the initial EOG scaling, the targeted gust has not been achieved in terms of length scale and gust shape. The simulated gust length scale was equal to the centre vanes spacing. Adjusting the model wind turbine diameter such that the created gust would span its entire rotor results in time scaling of $\frac{t_m}{t_p} \approx 0.01\,[-]$, requiring high reduced frequencies of $k \approx 0.4\,[-]$.

Additionally, the two vanes configuration is tested at increasing vane spacing: $\frac{D_m}{2}$, $\frac{2D_m}{3}$ and D_m. The trend with increasing vane spacing shows decreased velocity peak and gust uniformity in between the vanes. A compromise is identified between gust magnitude and length scale.

(a) $\frac{D_m}{2}$ (b) $\frac{2D_m}{3}$ (c) D_m
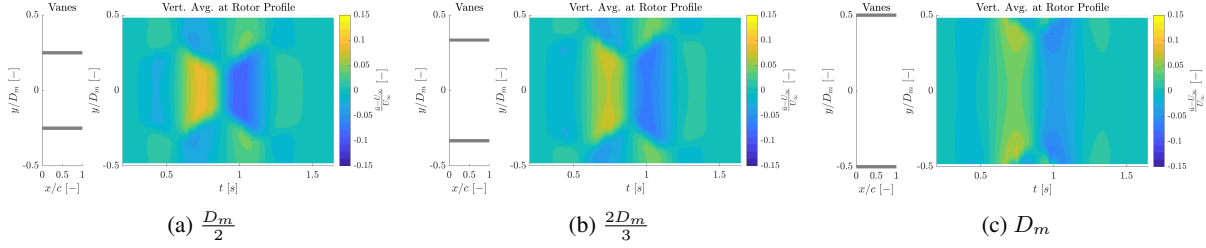
Fig. 40 Normalised vertically averaged streamwise velocity component ($\frac{u-U_\infty}{U_\infty}$) along the rotor profile for varying vane spacing.

The presented strategy could be used successfully for small physical wind turbine diameters (larger geometric scaling). Application of the derived gust generation methodology can be relevant to vertical wind axis wind turbines, which are orders of magnitude smaller in size [38]. Tests would be performed on models ranging from half scale to quarter scale, allowing for better matching of non-dimensional parameters.

In-field Gust Replication

Lastly, two scaled in-field wind histories are replicated by the two vanes configuration with vane spacing of $\frac{D_m}{3}$. The results are shown in Figure 41 in terms of velocity at the hub; i.e. OJF centreline. The gust shown in Figure 41a and 41b correspond to reduced frequency of oscillation of $k = 0.27$ and $0.16\,[-]$, respectively.

(a) Asymmetric gust [22].   (b) Wind time series at Thyborøn, Denmark [23].
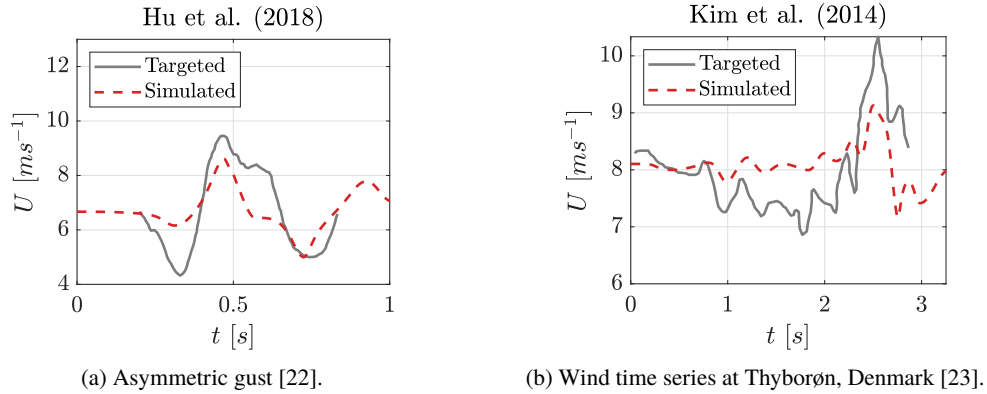
Fig. 41 Simulated in-field gusts.

Trends similar to the simulated EOG profiles are observed. The velocity past peak values decreases sharply, not retaining the targeted gust profile. The targeted asymmetric gust in Figure 41a is characterised by $GAF = 2.31\,[-]$, while the simulate gust achieves $GAF = 1.11\,[-]$. Furthermore, simulating a wind time series displays target gust features, however, centred about the free stream velocity as can be seen in Figure 41b for $1 \leq t \leq 2\,[s]$. The peak at $t = 2.5\,[s]$ achieves only half the targeted peak, however, the absolute velocity variation considering peak to trough is $\approx 70\%$ of the targeted gust rise magnitude. The configuration and pitching protocol are deemed capable of achieving tailored velocity maximum, followed by an equal minimum, before returning to free stream values.

26

VIII. Conclusions

The presence of veer and wind gusts introduce detrimental effects affecting wind turbine longevity, power grid and efficiency of wind farms. Counteractive measures such as active control strategies, remote sensing and load alleviation are becoming available and the need to test them in a controlled environment arises. As such, this text has explored the feasibility of wind tunnel gust generation relevant to wind turbines by an array of oscillating vanes.

Potential flow theory has been successfully implemented in the development of a computationally efficient model, enabling prompt results to unsteady flows. Validation by PIV measurements showed errors of maximum 14% for high frequency gusts ($k = 0.2 \, [-]$), while less unsteady gusts were modelled with 5% accuracy ($k = 0.1 \, [-]$). An isolated case showed error of up to 30%, however, preserving general trends.

New gust generator configurations were proposed for the generation of veer and wind gusts. In-field veer profiles representative of unstable, neutral and stable atmospheric conditions were successfully simulated. A limit case with veer differential of $20 \, [°]$ was demonstrated. Veer profile gradient was linked to the trailing vorticity of the vanes, and thus the vanes' spanwise circulation. As such, the implementation of twist can be exploited for tailoring user defined veer profiles.

The generation of unsteady wind gusts (speed variation) was demonstrated by a slightly altered set-up from the current OJF gust generator, in terms of number of vanes and their spacing. The target gust was not achieved in terms of length scale. A compromise is identified between gust length and time scales. The application to large scale wind turbines proves difficult for unsteady non-dimensional parameter matching. The methodology, however, can apply to smaller wind turbines. Meaningful velocity variations of up to 28% of free stream values are simulated within $0.3 \, [s]$, corresponding to vane reduced frequency $k \approx 0.15 \, [-]$. A validation campaign is recommended on the current gust generator to validate the produced results. Furthermore, obtained results can be coupled to a URANS CFD simulation with an actuator line model to verify the obtained results at higher fidelity.

References

[1] Kalverla, P. C., Steeneveld, G. J., Ronda, R. J., and Holtslag, A. A., "An observational climatology of anomalous wind events at offshore meteomast IJmuiden (North Sea)," *Journal of Wind Engineering and Industrial Aerodynamics*, Vol. 165, 2017, pp. 86–99. https://doi.org/10.1016/j.jweia.2017.03.008.

[2] Van Der Laan, M. P., and Sørensen, N. N., "Why the Coriolis force turns a wind farm wake to the right in the Northern Hemisphere," *Journal of Physics: Conference Series*, Vol. 2, 2017, pp. 285–294. https://doi.org/10.5194/wes-2-285-2017, URL www.wind-energ-sci.net/2/285/2017/.

[3] Brown, A. R., Beljaars, A. C., Hersbach, H., Hollingsworth, A., Miller, M., and Vasiljevic, D., "Wind turning across the marine atmospheric boundary layer," *Quarterly Journal of the Royal Meteorological Society*, Vol. 131, No. 607, 2005, pp. 1233–1250. https://doi.org/10.1256/qj.04.163.

[4] Bos, R., Giyanani, A., and Bierbooms, W., "Assessing the Severity of Wind Gusts with Lidar," *Remote Sensing*, Vol. 8, No. 9, 2016. https://doi.org/10.3390/rs8090758.

[5] Van Wingerden, J. W., Hulskamp, A. W., Barlas, T., Marrant, B., Van Kuik, G. A., Molenaar, D. P., and Verhaegen, M., "On the proof of concept of a 'smart' wind turbine rotor blade for load alleviation," *Wind Energy*, Vol. 11, No. 3, 2008, pp. 265–280. https://doi.org/10.1002/we.264.

[6] Ham, N. D., Bauer, P. H., and Lawrence, T. L., "WIND TUNNEL GENERATION OF SINUSOIDAL LATERAL AND LONGITUDINAL GUSTS BY CIRCULATION CONTROL," Tech. rep., NASA, 1974.

[7] Volpe, R., Da Silva, A., Ferrand, V., and Le Moyne, L., "Experimental and Numerical Validation of a Wind Gust Facility," *Journal of Fluids Engineering*, Vol. 135, No. 1, 2013, p. 011106. https://doi.org/10.1115/1.4023194, URL http://fluidsengineering. asmedigitalcollection.asme.org/article.aspx?doi=10.1115/1.4023194.

[8] Castellani, F., Astolfi, D., Becchetti, M., and Berno, F., "Experimental and Numerical Analysis of the Dynamical Behavior of a Small Horizontal-Axis Wind Turbine under Unsteady Conditions: Part I," *Machines*, Vol. 6, No. 4, 2018, p. 52. https://doi.org/10.3390/machines6040052, URL http://www.mdpi.com/2075-1702/6/4/52.

[9] Lancelot, P., Sodja, J., Werter, N., and Breuker, R., "DESIGN AND TESTING OF A LOW SUBSONIC WIND TUNNEL GUST GENERATOR," *International Forum on Aeroelasticity and Structural Dynamics*, 2015.

[10] Saddington, A. J., Finnis, M. V., and Knowles, K., "The characterisation of a gust generator for aerodynamic testing," *Proceedings of the Institution of Mechanical Engineers, Part G: Journal of Aerospace Engineering*, Vol. 229, No. 7, 2015, pp. 1214–1225. https://doi.org/10.1177/0954410014548237.

[11] Kröger, L., Frederik, J., Van Wingerden, J. W., Peinke, J., and Hölling, M., "Generation of user defined turbulent inflow conditions by an active grid for validation experiments," *Journal of Physics: Conference Series*, Vol. 1037, 2018, p. 052002. https://doi.org/10.1088/1742-6596/1037/5/052002, URL https://doi.org/10.1088/1742-6596/1037/5/052002.

[12] Cordes, U., Lambie, B., Hufnagel, K., Spiegelberg, H., Kampers, G., and Tropea, C., "The Adaptive Camber Concept—A passive approach for gust load alleviation on wind turbines," *Wind Energy*, Vol. 21, No. 9, 2018, pp. 732–744. https://doi.org/10.1002/we.2190.

[13] Cal, R. B., Lebrón, J., Castillo, L., Kang, H. S., and Meneveau, C., "Experimental study of the horizontally averaged flow structure in a model wind-turbine array boundary layer," *Journal of Renewable and Sustainable Energy*, Vol. 2, No. 1, 2010. https://doi.org/10.1063/1.3289735.

[14] Ohya, Y., Nakamura, R., and Uchida, T., "Intermittent Bursting of Turbulence in a Stable Boundary Layer with Low-level Jet," *Boundary-Layer Meteorology*, Vol. 126, No. 3, 2008, pp. 349–363. https://doi.org/10.1007/s10546-007-9245-y.

[15] Churchfield, M. J., and Sirnivas, S., "On the Effects of Wind Turbine Wake Skew Caused by Wind Veer," *American Institute of Aeronautics and Astronautics SciTech*, National Renewable Energy Laboratory, Kissimmee, 2018. https://doi.org/10.2514/6.2018-0755, URL https://arc.aiaa.org/doi/10.2514/6.2018-0755.

[16] Abkar, M., Sørensen, J. N., and Porté-Agel, F., "An Analytical Model for the Effect of Vertical Wind Veer on Wind Turbine Wakes," *Energies*, Vol. 11, No. 7, 2018, pp. 1–10. https://doi.org/10.3390/en11071838.

[17] Berg, J., Mann, J., and Patton, E. G., "Lidar-observed stress vectors and veer in the atmospheric boundary layer," *Journal of Atmospheric and Oceanic Technology*, Vol. 30, No. 9, 2013, pp. 1961–1969. https://doi.org/10.1175/JTECH-D-12-00266.1.

[18] Arnqvist, J., Segalini, A., Dellwik, E., and Bergström, H., "Wind Statistics from a Forested Landscape," *Boundary-Layer Meteorology*, Vol. 156, No. 1, 2015, pp. 53–71. https://doi.org/10.1007/s10546-015-0016-x, URL http://dx.doi.org/10.1007/s10546-015-0016-x.

[19] Bell, T., Klein, P., Wildmann, N., and Menke, R., "Analysis of Flow in Complex Terrain Using Multi-Doppler Lidar Retrievals," *Atmospheric Measurement Techniques Discussions*, , No. January, 2019, pp. 1–21. https://doi.org/10.5194/amt-2018-417, URL https://www.atmos-meas-tech-discuss.net/amt-2018-417/.

[20] Howard, K. B., and Guala, M., "Upwind preview to a horizontal axis wind turbine: a wind tunnel and field-scale study," *Wind Energy*, Vol. 19, 2016, pp. 1371–1389.

[21] IEC, "Wind turbines - Part 1: Design requirements," International standard, International Electrotechnical Commission, Geneva, 2005.

[22] Hu, W., Letson, F., Barthelmie, R. J., and Pryor, S. C., "Wind Gust Characterization at Wind Turbine Relevant Heights in Moderately Complex Terrain," *Journal of Applied Meteorology and Climatology*, Vol. 57, No. 7, 2018, pp. 1459–1476. https://doi.org/10.1175/JAMC-D-18-0040.1, URL https://doi.org/10.1175/JAMC-D-18-0040.1.

[23] Kim, T., Petersen, M. M., and Larsen, T. J., "A comparison study of the two-bladed partial pitch turbine during normal operation and an extreme gust conditions," *Journal of Physics: Conference Series (Online)*, Vol. 524, No. 1, 2014, p. 012065. https://doi.org/10.1088/1742-6596/524/1/012065, URL https://doi.org/10.1088/1742-6596/524/1/012065.

[24] Tang, D. M., Cizmas, P. G. A., and Dowell, E. H., "Experiments and analysis for a gust generator in a wind tunnel," *Journal of Aircraft*, Vol. 33, No. 1, 1996, pp. 139–148. https://doi.org/10.2514/3.46914, URL http://arc.aiaa.org/doi/10.2514/3.46914.

[25] Makita, H., "Realization of a large-scale turbulence field in a small wind tunnel," *Fluid Dynamics Research*, Vol. 8, No. 1-4, 1991, pp. 53–64. https://doi.org/10.1016/0169-5983(91)90030-M.

[26] Lignarolo, L. E., Ragni, D., Krishnaswami, C., Chen, Q., Simão Ferreira, C. J., and van Bussel, G. J., "Experimental analysis of the wake of a horizontal-axis wind-turbine model," *Renewable Energy*, Vol. 70, 2014, pp. 31–46. https://doi.org/10.1016/j.renene.2014.01.020, URL http://dx.doi.org/10.1016/j.renene.2014.01.020.

[27] TU Delft, "Open Jet Facility," , 2019. URL https://www.tudelft.nl/lr/organisatie/afdelingen/aerodynamics-wind-energy-flight-performance-and-propulsion/facilities/low-speed-wind-tunnels/open-jet-facility/.

[28] Lignarolo, L. E., "ON THE TURBULENT MIXING IN HORIZONTAL AXIS WIND TURBINE WAKES," Ph.D. thesis, Delft University of Technology, 2016. https://doi.org/10.4233/uuid:057fa33f-82a3-4139-beb8-53f184cd1d57, URL https://doi.org/10.4233/uuid:057fa33f-82a3-4139-beb8-53f184cd1d57.

[29] Lancelot, P., Sodja, J., and De Breuker, R., "Investigation of the Unsteady Flow Over a Wing Under Gust Excitation," *International Forum on Aeroelasticity and Structural Dynamics*, 2017.

[30] Katz, J., and Plotkin, A., *Low-Speed Aerodynamics*, 2nd ed., Cambridge University Press, 2001.

[31] Pope, S. B., *Turbulent Flows*, Cambridge University Press, 2000. URL https://books.google.nl/books?id=HZsTw9SMx-0C.

[32] van Kuik, G., *The Fluid Dynamic Basis for Actuator Disc and Rotor Theories*, IOS Press BV, Delft, 2018. https://doi.org/10.3233/978-1-61499-866-2-i.

[33] Sarpkaya, T., "Computational Methods With Vortices — The 1988 Freeman Scholar Lecture," *Journal of Fluids Engineering*, Vol. 111, No. 1, 1989, pp. 5–52.

[34] Maskew, B., "Program VSAERO Theory Document," Tech. Rep. CR 4023, NASA, 1987.

[35] Ashby, D., Dudley, M., and Iguchi, S., "Development and Validation of an Advanced Low-Order Panel Method," Tech. Rep. TM 101024, NASA, 1988.

[36] Gordon Leishman, J., *Principles of Helicopter Aerodynamics*, 2nd ed., Cambridge University Press, 2006.

[37] Gregory, N., and O'Reilly, C., "Low-Speed Aerodynamic Characteristics of NACA 0012 Aerofoil Section, including the Effects of Upper-Surface Roughness Simulating Hoar Frost," *Reports and Memoranda*, Vol. 3726, 1970.

[38] Bertényi, T., Wickins, C., and McIntosh, S., "Enhanced Energy Capture Through Gust-Tracking in the Urban Wind Environment," *48th AIAA Aerospace Sciences Meeting Including the New Horizons Forum and Aerospace Exposition*, American Institute of Aeronautics and Astronautics, Orlando, FL, 2010.

Appendix

Veer Configuration Analysis

The afore mentioned gust generator vanes configurations for veering are analysed by reproduction of the neutral veer profile. Each vane's deflection angle is tuned manually, in proportion to the targeted veer profile. Increments of 1 [°] are used. Figures A.1 through A.6 present the achieved veering profiles by the six considered gust generator configurations.

The veer distributions over the rotor as well as the horizontally averaged (y-direction) veer profiles are shown. The targeted profile is overlaid for comparison. The analysis has been done for a model wind turbine diameter of $D_m = 1.8$ [m], with hub at the centreline and 2 [m] downstream of the OJF nozzle. The distributed vanes configurations (Figures A.1 through A.4) show a noisy veer distribution. The peaks can be correlated to the location of the tip vortices of the vanes. As overlap is increased the influence of tip vortices is damped out. The stacked vanes configurations (Figures A.5 and A.6) further smooths out the effects of tip vortices.

Configuration 6: stacked vanes with 3 columns is deemed to best fit the targeted veer profile. This choice is purely made on the basis of best achieved matching of the targeted profile; i.e. least interference from tip vortices.
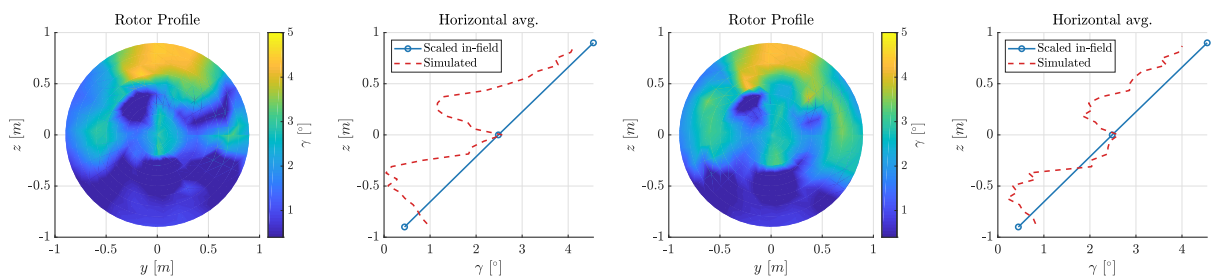
Fig. A.1   Configuration 1: Distributed no overlap

Fig. A.2   Configuration 2: Distributed 25% overlap.
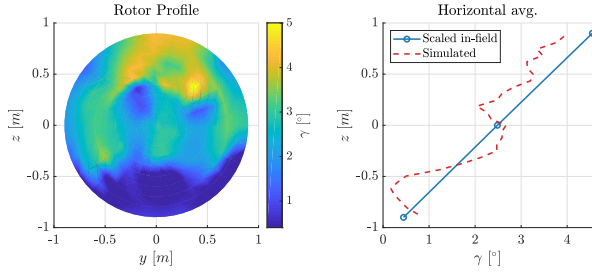
Fig. A.3   Configuration 3: Distributed 50% overlap.
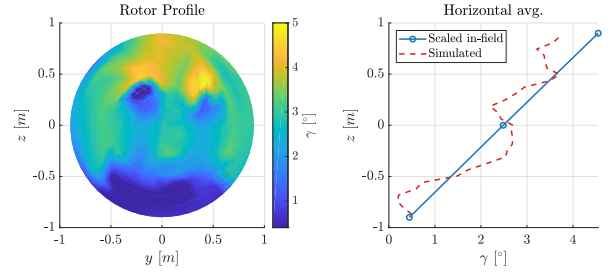
Fig. A.4   Configuration 4: Distributed 75% overlap.
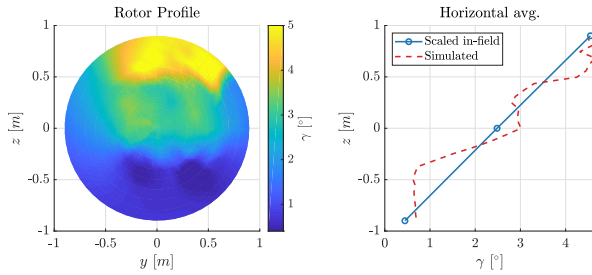
Fig. A.5   Configuration 5: Stacked 2 columns.
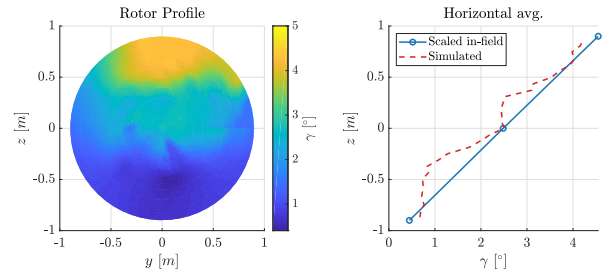
Fig. A.6   Configuration 6: Stacked 3 columns.

Additional Validation Results

Figures A.7 and A.8 shows the lateral and vertical gust uniformity, respectively.
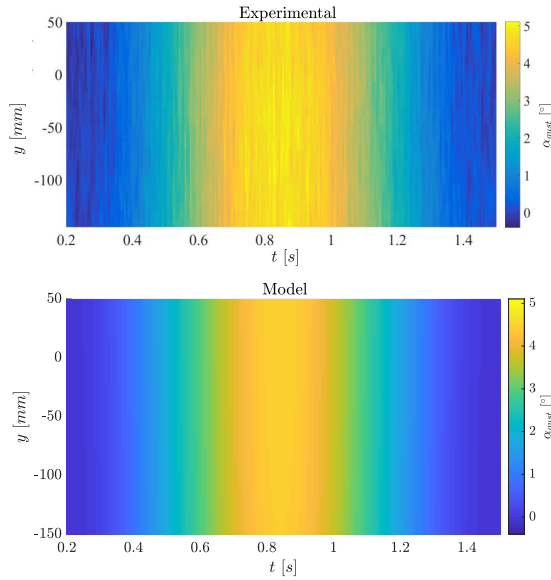
Fig. A.7   Gust angle along a line at $x = 1.5$, $z = 0$ and $-0.15 \leq y \leq 0.05$ $[m]$ of the developed model vs experimental measurements from [29]. Simulation carried out for 2 vanes with $c = 0.3$ $[m]$, $b = 2.7$ $[m]$, $U_\infty = 15$ $[ms^{-1}]$, $\psi(t) = 10[1 - \cos(5t)]$ $[°]$ and $k = 0.05$ $[-]$.
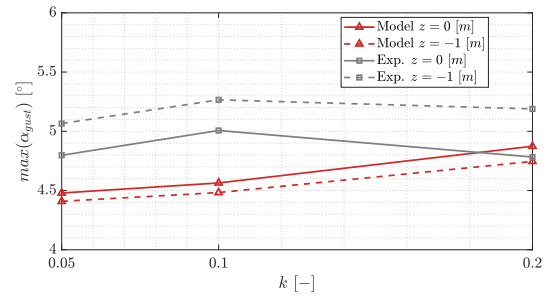
Fig. A.8   Maximum gust angle for varying reduced frequency and vertical location: $k = 0.05, 0.1, 0.2$ and $z = 0, -1$ and $x = 1.5$ $[m]$. Simulation carried out for 2 vanes with $c = 0.3$ $[m]$, $b = 2.7$ $[m]$, $U_\infty = 15$ $[ms^{-1}]$, $\psi_{max} = 10$ $[°]$.

Part II

Supporting Chapters

Chapter 2

Literature Survey

The performed literature review was split based on several criteria. First, the origin of gusts was sought out and explained by phenomena in the atmospheric boundary layer. Secondly, in-field measurements of such gusts are studied and the industry characterisation is given. Their impact on wind turbines is presented as found from in-field measurements and numerical simulations. Furthermore, the current industry practices for experimental gust generation are presented. Lastly, the knowledge gap and intent of thesis research is explored.

Wind turbines operate inside the ABL. As a result, wind turbines experience gusts that manifest themselves as spatial and temporal velocity changes with time scales of minutes or less Burton et al. (2011). Furthermore, due to turbulence production within the ABL, wind gusts also have a stochastic nature with varying time/length scale, intensity and intermittency Wächter et al. (2012). The intermittency refers to an irregular alteration of the flow from turbulent to non-turbulent Pope (2000). The presence of turbulence and temporal/spatial variation in the flow field will have detrimental effects on the wind turbine; its design, performance and power delivery to the grid Burton et al. (2011).

The flow of air over the surface of the earth develops into a boundary layer flow termed as the planetary boundary layer (PBL) or ABL. Due to surface (terrain) roughness, atmospheric stability (thermal effects), Coriolis effect (latitude based) and the strength of geostrophic wind (wind speed outside the ABL) turbulent production will undergo inside the ABL Burton et al. (2011). The listed phenomena are interconnected in turbulence production. Turbulence manifests itself as large-scale eddies, which, wind turbines feel as gusts, with variable occurrence periods and strength (velocity variation). This is dependent on turbulent intensity, length-scale and power spectra Burton et al. (2011).

In-field measurements have been performed at onshore and offshore locations which have identified relevant wind gusts. Pulsed wind light detection and ranging of laser imaging detection and ranging (LiDAR) has been used to measure the wind turning or veering in the stable, unstable and neutral ABL at Høvsøre, Denmark Berg et al. (2013). The results showed

the highest veer angle in stable conditions. Stability has been evaluated based on Obukhov length. An experimental campaign has been conducted at Ryningsnäs, Sweden, which, focused on identifying the wind field characteristics above a forested landscape Arnqvist et al. (2015). The results showed significant wind veer for stable ABL. Furthermore, it was showed that derived dimensionless gradients followed theoretical curves up to heights of 100 $[m]$. The results have been obtained by six sonic anemometers. Shear assessment studies have been conducted using LiDAR and sonic 3D anemometer concluding that stability corrections should be taken into account for better power generation estimates Sakagami et al. (2014). The consequence of a wind gust (speed variation) has been recorded at the Eolos wind research facility showing a spike in power generation during the wind event Howard and Guala (2016). The study further concluded that velocity sampled above the hub height is statistically most relevant to turbine operation and control. An extensive study at the Høvsøre site, analysed wind recorded data from 2005-2013 period Peña et al. (2016). It found similar results to the precedently mentioned studies; accentuated veer can be observed under stable ABL conditions. Furthermore, low-level jets have been measured and deemed of interest due to their impact on the turbine loading. These flows manifest as high vertical wind shear and wind turning over the rotor. Studies have also been done at offshore locations such as the meteomast IJmuiden in the North Sea Kalverla et al. (2017). The findings of the study point towards the need of better understanding gusts which would lead to reduction in design cost and risk of failure. Furthermore, the study characterised six "anomalous wind events"; low-level jets, extreme wind speeds, shear, veer, turbulence and wind ramps. The need of understanding wind conditions at sites is of utmost importance and advancements are clearly made as measurement techniques evolve, however, to achieve further improvements, the understanding of their effects on wind turbines needs to be validated as well. Studies support the idea of LiDAR application in detecting the severity of a wind gust before the event arrives at the turbine Bos et al. (2016). Such applications can be coupled with active turbine control to alleviate loading while maintaining efficient power extraction, such as adaptive camber Cordes et al. (2018).

Based on measurements and theory, standardised descriptions of gusts have been implemented. For engineering purposes, these wind events, have been translated into velocity profiles. Such profiles are described by IEC (2005). Studies have been performed to quantify the detrimental effects that gusts pose to wind turbines. Numerical studies are large in number while meaningful experimental simulations are few. This has been a challenge due to the difficulty of recreating comparable conditions in the wind tunnel. Numerous numerical studies have been performed on extreme wind condition stipulated by IEC; via 3D unsteady Reynolds Average Navier-Stokes (URANS) with moving meshes Menegozzo et al. (2018), LES Norris et al. (2012) Storey et al. (2014), blade element method (BEM) and free vortex methods Jeong et al. (2014). Studies, however, also define gusts in numerical studies based on in-field measurements, such as the ones derived from Thyborøn, Denmark; a ramp up of 10 $[ms^{-1}]$ in 3 $[s]$ Kim et al. (2014). LES simulations under ramp up gust found an increase in rotor speed and power generated in a modelled NREL 5 $[MW]$ variable-speed, variable-pitch controlled HAWT Norris et al. (2012). URANS simulations with moving meshing done in Menegozzo et al. (2018), have shown a clear trend of aerodynamic torque acting on a blade to increase as an extreme event arrived at the turbine. The study, however, lacks validation of the turbine response under the gust, and only validates the results using normal wind condition measurements from the NREL Phase IV campaign Hand et al. (2001) Menegozzo et al. (2018).

This is predominant in most the numerical gust studies to the knowledge of the author. An exception is the comparison made in Kim et al. (2014), where simulations performed by the HAWC2 code are compared to in-field measurements during an in-field measured ramp up. The study concludes that the rotor speed and blade loads do not react quickly enough to the wind gust, pointing to the need of appropriate turbine and controller design.

The generation of gusts in wind tunnels is not a new topic and attempts have been made in the past. The initial implementations have been intended for aircraft application studies, however, interest is peaking in wind turbine application. Several methods of gust generation can be distinguished. Rotating slotted cylinders have been used to generate longitudinal or lateral sinusoidal gusts by circulation control Ham et al. (1974). It has also been shown that gusts of multiple harmonics can be achieved for a relatively low cost Tang et al. (1996). Although the cost is low, the system has a rather simple configuration and low torque is needed for the cylinder rotation, these methods result in low gust amplitude, with deflection angles in the order of a few degrees. The authors, however, claim that the gust strength can be varied via geometrical cylinder parameters Tang et al. (1996). The injection of a secondary flow into the test section has also been used to create gusts Volpe et al. (2013), however, this requires a separate fluid source or a dual wind tunnel depending on the magnitude of the gust. Deflecting vanes that oscillate perpendicular to the free stream flow are another way of generating gusts Saddington et al. (2015). There is an almost linear relation between the maximum/minimum gust vane angle of attack deflection and the resulting gust strength (direction) Saddington et al. (2015) Lancelot et al. (2015) Lancelot et al. (2017). The flow deflection can be further developed into an active turbulence grid, which is capable of tailoring desired turbulence properties Makita (1991). The advantage of this is that large-scales can be created with large turbulence Reynolds numbers. The method has been implemented in a 2D wind tunnel Kobayahi and Hatanaka (1992). More recent studies have implemented the active turbulence grid in 3D, with promising results Mydlarski (2017) Cordes et al. (2018) Kröger et al. (2018). Lastly, velocity ramp up/down has been attempted in the past; via providing blockage to the flow with gauzes which were operated manually to open or close Snel and Schepers (1995) and via wind tunnel fan control Castellani et al. (2018). The former study was deemed inconclusive due to slow ramp up/down times and highly distorted flow field, while the latter achieved gust period of 10 $[s]$ with a relatively low gust amplitude of 1.3 $[ms^{-1}]$ (15% of free stream).

The trend is towards designing experimental set-ups where gusts can be generated in a controlled manner to enable further understanding of their interaction with wind turbines and testing of new control strategies. A current state-of-the-art facility is the Oldenburg active turbulence grid generator, which, is capable of generating stochastic gusts reproduced from LiDAR measurements Kröger et al. (2018). This has already enabled the validation of a new control algorithm called subspace predictive repetitive control (SPRC), with promising results Kröger et al. (2018). Delft University of Technology Open Jet Facility (OJF) has developed a gust generator Lancelot et al. (2015) that has been tested by hot-wire anemometry, particle image velocimetry (PIV) Lancelot et al. (2017) and wind tufts confirming the generation of sinusoidal lateral gusts. The expansion of this capability to wind turbines relevant gust generation is therefore explored in the current thesis.

Chapter 3

Atmospheric Boundary Layer

The global flow of air is the result of surface terrain and energy imbalance caused by the difference in surface heating latitude-wise. The system that governs the global circulation is split into three main cells; Hadley cell around the equator, Ferrel cell at higher latitudes (35-60 [°]) and the polar cell, which, result in a north-south circulation Emeis (2018). The rotation of the Earth adds a meridional (east-west) component to the circulation by the Coriolis force. To satisfy the no-slip condition the velocity at the surface of the Earth needs to vanish, which develops the flow into a boundary layer flow. The presence of vertical temperature gradient leads to three main states of the ABL. To classify the three states, the first order accurate potential temperature (Θ) is introduced by Equation 3.1 Kaimal and Finnigan (1994). The subscript $1bar$ refers to the height level of 1 $[bar]$ pressure.

$$\Theta = T + \frac{g}{c_p}\Delta z \qquad \Delta z = z - z_{1bar} \tag{3.1}$$

Differentiating with respect to (z), results in the potential temperature gradient (3.2).

$$\frac{\partial \Theta}{\partial z} = \frac{\partial T}{\partial z} + \frac{g}{c_p} \tag{3.2}$$

Based on the potential temperature gradient, the ABL can undertaken three states:

1. Convective (unstable) boundary layer (CBL): $\frac{\partial \Theta}{\partial z} < 0$; i.e. $\frac{\partial T}{\partial z} < -\frac{g}{c_p}$

2. Stable boundary layer (SBL): $\frac{\partial \Theta}{\partial z} > 0$; i.e. $\frac{\partial T}{\partial z} > -\frac{g}{c_p}$

3. Neutral (dynamical) boundary layer: $\frac{\partial \Theta}{\partial z} = 0$; i.e. $\frac{\partial T}{\partial z} = -\frac{g}{c_p}$

The ratio $\left(\frac{g}{c_p}\right)$ is the adiabatic lapse rate, where, (g) is the gravitational acceleration and (c_p) is the specific heat of air at constant pressure. Assuming no moisture or other contaminants in the air the lapse rate is ≈ 0.01 $[^\circ C/m]$. The depth of the layer is on the order of ≈ 1 $[km]$, with various sub-layers that are explored in Section 3.1. Section 3.2 will describe gusts mathematically, while Section 3.3 will go on documenting various gusts and present in-field wind measurements from literature.

3.1 ABL Sub-layers

The ABL is composed of three sub-layers; a very thin laminar layer very close to the surface (few $[mm]$), the surface layer ($\approx 10\%$ of the ABL) and the Ekman layer, which extends to encapsulate the remain 90% of the ABL Emeis (2018). The first layer is not considered since the wind turbine does not interact with it. The surface layer is known to affect all wind turbines and in addition, large rotor wind turbines can extend into the Ekman layer as well. The two layers are further discussed in Sections 3.1.1 and 3.1.2.

Due to the dependence of vertical temperature gradient, the ABL varies throughout the day as the Sun heats the ground unevenly. Figure 3.1 gives an idea of the depth growth throughout the day. As the Sun rises, the ground temperature increases and the air near the surface moves upwards. This gives rise to a negative vertical temperature gradient leading to the development of a CBL. As the ground continues to warm up, the CBL grows in depth, attaining its maximum at mid-day (≈ 1-2 $[km]$). The CBL is constrained by an inversion layer (capping inversion in Figure 3.1); an area where the potential temperature gradient inverses leading to a stable layer. The mean profile of speed, direction and potential temperature of a typical CBL can be seen in Figure 3.2. As the sun starts to set, the surface cools due to dissipation of energy via radiation. Shallow inversion layers grow close to the ground and the SBL develops as the surface continues to cool. The mean profiles of a SBL are shown in Figure 3.3. The neutral state is not as persistent as the CBL and SBL since a thermal stratification equal to the lapse rate is usually transient Kaimal and Finnigan (1994).
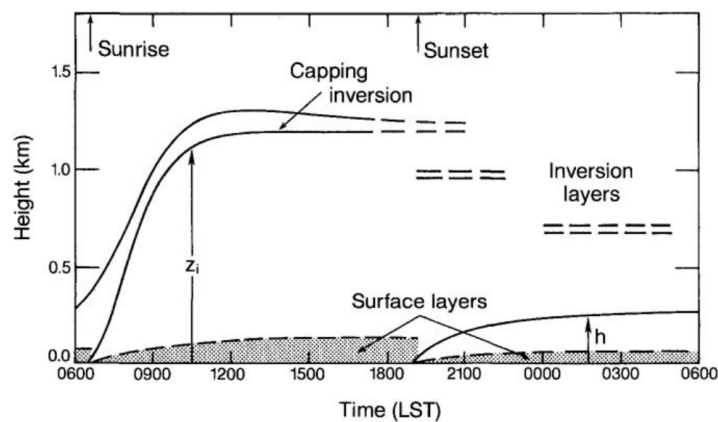
Figure 3.1: Schematic of the day evolution of the CBL and SBL. The horizontal axis refers to local standard time. Adapted from Kaimal and Finnigan (1994)
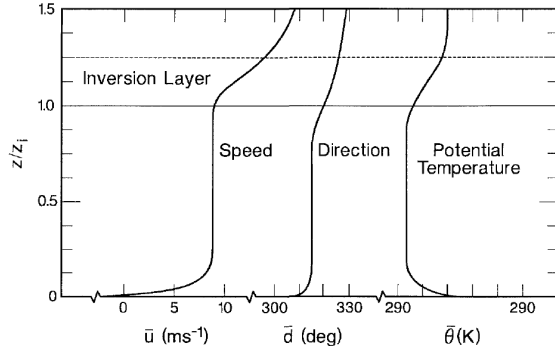
Figure 3.2: Mean speed, direction and potential temperature profiles of the CBL Kaimal and Finnigan (1994).
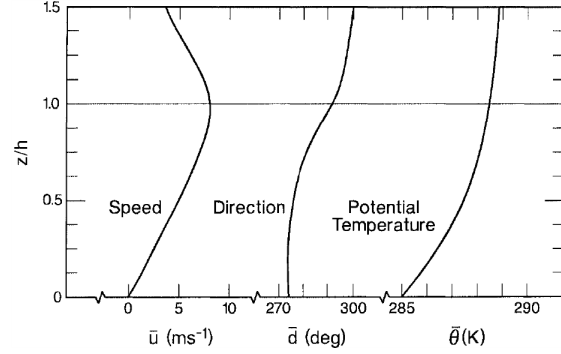
Figure 3.3: Mean speed, direction and potential temperature profiles of the SBL Kaimal and Finnigan (1994).

3.1.1   Surface Layer

The surface layer develops close to the ground. It contains the highest velocity gradients and meteorologically speaking is defined to encapsulate the potion of the ABL where the turbulent vertical fluxes of momentum, heat and moisture do not deviate by more than 10% of the surface values. It comprises roughly 10% of the entire ABL depth Emeis (2018). Within the surface layer the Coriolis force is negligible and the flow structure is mainly dictated by surface roughness and vertical thermal gradient Kaimal and Finnigan (1994). Assuming horizontal homogeneity and stationarity, the neutral condition, one-dimensional, mean vertical velocity profile can be represented by the logarithmic law (3.3).

$$\overline{u}(z) = \frac{u_*}{\kappa} \ln\left(\frac{z}{z_0}\right) \qquad u_* = \sqrt{\frac{\tau_w}{\rho}} = \sqrt{\overline{u'w'}_0} \qquad (3.3)$$

The frictional velocity (u_*) is a scaling parameter in the surface layer. It is dependent on the mean flow and the ground topology and evaluated from the wall shear stress (τ_w) or Reynold stress ($\overline{u'w'}_0$) near the surface. The surface roughness (z_0) is the resulting integration constant; physically it represents the height at which the mean velocity extrapolated downwards would vanish. The typical height of the surface layer can be approximated from a scale analysis and gives a layer height of 50 [m] Emeis (2018). The logarithmic law can be adapted for validity in the stable and unstable conditions. To do this, the Monin–Obukhov length needs to be evaluated from (3.4).

$$L_* = \frac{\Theta}{\kappa g} \frac{u_*^3}{\overline{\Theta' w'}_0} \qquad (3.4)$$

The ratio (z/L_*) is used to quantify deviations from the neutral conditions: i.e. $z/L_* > 0$

for stable state, < 0 for unstable ($= 0$ for neutral conditions). The ratio of the two scaling lengths accounts for the small deviation from neutral conditions Paulson (1970). Since the neutral stratification is for the most time transient, it is rare that perfectly neutral conditions are found in-field. Correction functions can be introduced for unstable (3.5) and for stable stratification (3.6) Holtslag and De Bruin (1988), varying with the ratio of (z/L_*).

$$\Psi_m = 2\ln\left(\frac{1 + z/L_*}{2}\right) + \ln\left[\frac{1 + (z/L_*)^2}{2}\right] - 2\tan^{-1}(z/L_*) + \frac{\pi}{2} \tag{3.5}$$

$$\Psi_m = \begin{cases} -a\frac{z}{L_*} & \text{for } 0 < \frac{z}{L_*} \leq 0.5 \\ A\frac{z}{L_*} + B\left(\frac{z}{L_*} - \frac{C}{D}\right)\exp\left(-D\frac{z}{L_*}\right) + B\frac{C}{D} & \text{for } 0.5 \leq \frac{z}{L_*} \leq 7 \end{cases} \tag{3.6}$$

The resulting velocity profile is then given by (3.7). The constant in (3.6) are: $a = 5$, $A = 1$, $B = 2/3$, $C = 5$ and $D = 0.35$.

$$\overline{u}(z) = \frac{u_*}{\kappa}\left(\ln\left(\frac{z}{z_0}\right) - \Psi_m\left(\frac{z}{L_*}\right)\right) \tag{3.7}$$

3.1.2 Ekman Layer

Above the surface layer, the Ekman layer lies, where the surface friction, the pressure gradient and Coriolis force are driving parameters. Since the Coriolis force influences the Ekman layer, wind turning with height is expected; i.e. wind veering. The Ekman layer extends above the surface layer, i.e. $> 100 \ [m]$. As modern wind turbines have diameters greater than 100 m, the influence of the Ekman layer is of importance to wind turbines' aerodynamic loading. The governing equations in the Ekman layer are given by (3.8); i.e. the defect laws.

$$-f(u_\mathrm{g} - u) - \frac{\partial\left(K_\mathrm{M}\frac{\partial v}{\partial z}\right)}{\partial z} = 0 \qquad f(v_g - v) - \frac{\partial\left(K_\mathrm{M}\frac{\partial u}{\partial z}\right)}{\partial z} = 0 \tag{3.8}$$

Assuming a constant value of the turbulent vertical exchange coefficient for momentum, the vertical mean velocity profile is given by (3.9) Emeis (2018). The top of the Ekman is approximated from (3.10). The inverse length scale (ξ) is introduced and depends on the Coriolis parameter (f) and turbulence vertical exchange coefficient for momentum; i.e. eddy viscosity (K_M). The subscript g refers to the outer flow; i.e. the geostrophic wind. Table 3.1 provides values of the Coriolis parameter latitude-wise.

$$\overline{u}(z) = u_\mathrm{g}\left(1 - \mathrm{e}^{-\xi z}\right) \qquad \xi = \sqrt{\frac{f}{2K_\mathrm{M}}} \tag{3.9}$$

$$z_g = \frac{\pi}{\xi} \tag{3.10}$$

The eddy viscosity (K_M) can be modelled via K-theory. Within the surface layer, K_M can be assumed to be linear in height, as (3.11) Kaimal and Finnigan (1994) and constant within the Ekman layer.

$$K_\mathrm{M} = \kappa u_* z \tag{3.11}$$

Table 3.1: Coriolis parameter for the northern hemisphere. The values for the southern hemisphere are opposite in sign. Adapted from Emeis (2018).

Latitude [°]	Coriolis parameter [s^{-1}]
30	0.727×10^{-4}
40	0.935×10^{-4}
50	1.114×10^{-4}
60	1.260×10^{-4}

The profile given by Equation 3.9 shows the mean horizontal velocity and does not provide any information on the wind turning with height. Models have been developed to compute the entire profile Svensson and Holtslag (2009). Holtslag analysed wind measurements from a 213 $[m]$ high meteorological towel and derived empirical relations for the wind turning with height Holtslag (1984). The site of sampling was Cabauw, the Netherlands, a relatively flat area with occasional lines of trees, river dikes and small villages. The relations are valid for diabatic wind profiles of various stability conditions (based on Obukhov length scale). Equation 3.12 describes the difference in wind direction between two heights Holtslag (1985).

$$D(z)/D(h) = d_1 \left[1 - \exp\left(-d_2 z/h\right) \right] \tag{3.12}$$

In Equation 3.12, (d_1) and (d_2) are empirical coefficients with values of 1.58 and 1.0 respectively. The left hand side is the ratio of the wind direction at heights (z) and (h). Assuming knowledge of the wind direction close to the ground, the relation provides the wind direction up to heights relevant to modern wind turbines.

3.2   Gust Description

The definition of a gust can be rather arbitrary. Generally, the event when the wind speed attains a maximum from its mean value is a gust. Gusts can manifest as increase/decrease in velocity magnitude and direction. For the purpose of this thesis, spatially varying velocity distributions are considered as gusts too; i.e. change of wind direction with height. The international standards define a gust as "*temporary change in the wind speed*" IEC (2005). This section will present mathematical formulations that describe gusts based on relevant

parameters. Section 3.2.1 will present the general gust description, while Section 3.2.2 will provide the IEC extreme gust profiles.

3.2.1 Gust Model

Hu et al. have analysed data from a moderately complex terrain and defined 10 parameters that describe gusts. The identification of a gust was based on the recommendation provided by the World Meteorological Organization; maximum 3 [s] moving average during each 10 [min] period. Therefore, the so-called peak wind gust ($u_{t,T}^{max}$) is defined as this maximum. The subscripts t, T refer to the moving average duration and the sampling duration, which are 3 [s] and 10 [min] Hu et al. (2018). From this, the gust amplitude definitions follows, as (3.13). The amplitude is simply the increase in wind speed from the mean observed speed over period (T); i.e. the increase from (U_T).

$$u_{t,T}^a = u_{t,T}^{\max} - U_T \tag{3.13}$$

The ratio between ($u_{t,T}^{\max}$) and (U_T) is called the gust factor ($G_{t,T}$) as shown by Equation 3.14.

$$G_{t,T} = \frac{u_{t,T}^{\max}}{U_T} \tag{3.14}$$

Defining the peak factor ($k_{t,T}$) as in (3.15), allows for the expression of ($G_{t,T}$) as a function of peak factor and turbulence intensity (I_T). In Equation 3.15, (σ_T), is the standard deviation in wind speed during the sampling period.

$$k_{t,T} = \frac{u_{t,T}^a}{\sigma_T} \qquad G_{t,T} = 1 + k_{t,T}I_T \tag{3.15}$$

Furthermore, the asymmetry of a gust can be characterised by the gust asymmetric factor (GAF). It is defined as (3.16) with (u_r), (t_r), (u_l) and (t_l) being the rise/lapse magnitude/time. Figure 3.4 shows their definition graphically from an in-field recorded wind gust Hu et al. (2018).

$$\mathrm{GAF} = \frac{u_r/t_r}{u_l/t_l} \tag{3.16}$$

Lastly, the gust length scale (L_g) is defined as (3.17). The subscripts sv and ev refer to the

start-valley of gust and end-valley of gust as shown in Figure 3.4.

$$L_g = \int_{t_{\text{sv}}}^{t_{\text{ev}}} u_{t,T}(t)dt \tag{3.17}$$
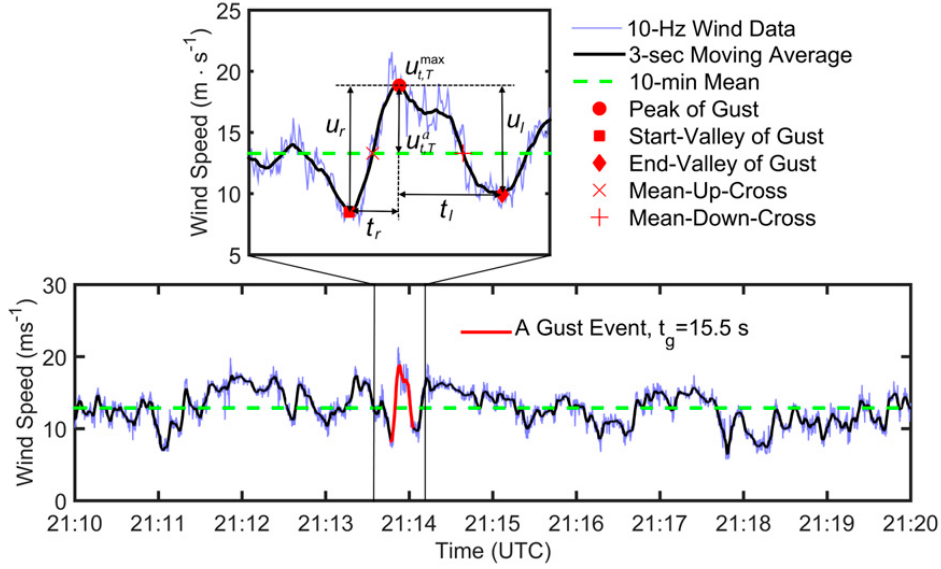
Figure 3.4: In-field recorded asymmetric wind gust event based on 3 s moving average in a period of 10 min. Adapted from Hu et al. (2018).

3.2.2 IEC Extreme Gusts

The IEC standards define several extreme gusts as time varying profiles IEC (2005). The gusts are described as deviation from the normal wind conditions, provided by the power law (3.18).

$$\overline{u}(z) = \overline{u}_{hub}\left(\frac{z}{z_{hub}}\right)^{\alpha} \qquad \alpha = 0.2 \tag{3.18}$$

The normal wind profile is accompanied by the normal turbulence model described by Equation 3.19. The value of (I_{ref}) is wind turbine dependent and provided by Table 3.2.

$$\sigma_1 = I_{ref}\left(0,75\overline{u}_{hub} + b\right) \qquad b = 5.6\ [ms^{-1}] \tag{3.19}$$

Table 3.2: Reference speed and turbulence intensity for wind turbine classes. Adapted from IEC (2005).

Wind turbine class	I	II	III
$\overline{u}_{ref}$ $[m/s]$	50	42.5	37.5
A I_{ref} $[-]$		0.16	
B I_{ref} $[-]$		0.14	
C I_{ref} $[-]$		0.12	

Extreme wind speed model (EWM)

The model is expressed as the extreme velocity profile attainable with repeat period of 50 years ($\overline{u}_{e50}$) and 1 year ($\overline{u}_{e1}$) as in (3.20).

$$\overline{u}_{e50}(z) = 1.4\overline{u}_{ref}\left(\frac{z}{z_{hub}}\right)^{0.11} \qquad \overline{u}_{e1}(z) = 0.8\overline{u}_{e50}(z) \qquad (3.20)$$

Extreme operating gust (EOG)

The gust magnitude is based on the turbine class and is given by (3.21); (D) is the turbine diameter and (Λ_1) is the turbulence scale parameter given by (3.22).

$$u_{gust} = \text{Min}\left\{1.35\left(\overline{u}_{e1} - \overline{u}_{hub}\right); \quad 3.3\left[\frac{\sigma_1}{1 + 0.1\left(\frac{D}{\Lambda_1}\right)}\right]\right\} \qquad (3.21)$$

$$\Lambda_1 = \begin{cases} 0.7z & z \leq 60 \ [ms^{-1}] \\ 42 & z \geq 60 \ [ms^{-1}] \end{cases} \qquad (3.22)$$

The gust varies in time over a period of $T = 10.5$ $[s]$ as described by (3.23). An example profile is shown in Figure 3.5.

$$\overline{u}(z,t) = \begin{cases} \overline{u}(z) - 0.37u_{gust}\sin\left(\frac{3\pi t}{T}\right)\left[1 - \cos\left(\frac{2\pi t}{T}\right)\right] & \text{for } 0 \leq t \leq T \\ \overline{u}(z) & \text{otherwise} \end{cases} \qquad (3.23)$$
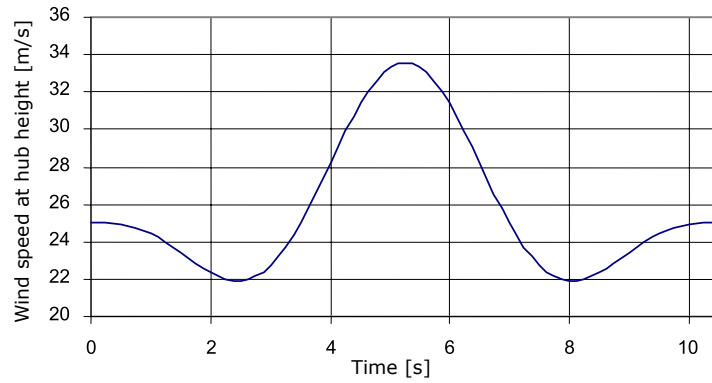
Figure 3.5: Example of EOG. Adapted from IEC (2005).

Extreme direction change (EDC)

An EDC is analogous to the EOG, but with respect to direction and a lower period of $T = 6$ [s]. The magnitude of the wind profile turning (θ_e) is given by Equation 3.24. The magnitude is limited to ± 180 [°].

$$\theta_e = \pm 4 \arctan \left(\frac{\sigma_1}{V_{hub} \left[1 + 0.1 \left(\frac{D}{\Lambda_1} \right) \right]} \right) \tag{3.24}$$

The transient direction change then follows the profile (3.25) and is shown in Figure 3.6

$$\theta(t) = \begin{cases} 0 & \text{for} \quad t < 0 \\ \pm 0.5 \theta_e \left[1 - \cos \left(\frac{\pi t}{T} \right) \right] & \text{for} \ 0 \le t \le T \\ \theta_e & \text{for} \quad t > T \end{cases} \tag{3.25}$$
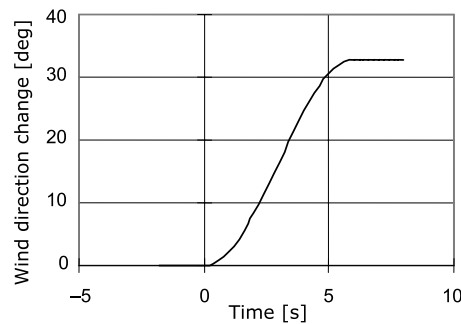
Figure 3.6: Example of EDC. Adapted from IEC (2005).

Extreme coherent gust with direction change (ECD)

The ECD combines a ramp up and direction change over a period $T = 6$ [s]. The speed

and direction transients are given by (3.26) and (3.28) respectively. The magnitude of the coherent gust magnitude is $u_{cg} = 15 \ [ms^{-1}]$. The direction magnitude is described by (3.27).

$$\overline{u}(z,t) = \begin{cases} \overline{u}(z) & \text{for } t \leq 0 \\ \overline{u}(z) + 0.5 u_{cg}[1 - \cos\left(\frac{\pi t}{T}\right)] & \text{for } 0 \leq t \leq T \\ \overline{u}(z) + u_{cg} & \text{for } t \geq T \end{cases} \tag{3.26}$$

$$\theta_{cg}\left(\overline{u}_{hub}\right) = \begin{cases} 180 \ [°] & \text{for } \overline{u}_{hub} < 4 \ [ms^{-1}] \\ \frac{720 \ [°] \ [ms^{-1}]}{\overline{u}_{hub}} & \text{for } 4 \ [ms^{-1}] < \overline{u}_{hub} < \overline{u}_{ref} \end{cases} \tag{3.27}$$

$$\theta(t) = \begin{cases} 0 \ [°] & \text{for } t < 0 \\ \pm 0.5 \theta_{\text{cg}}[1 - \cos\left(\frac{\pi t}{T}\right)] & \text{for } 0 \leq t \leq T \\ \pm \theta_{\text{cg}} & \text{for } t > T \end{cases} \tag{3.28}$$

Extreme wind shear (EWS)
The velocity gradient is increased/decreased over a period of $T = 12 \ [s]$. Parameters that calculate the time varying velocity profiles are wind turbine dependent. The vertical and horizontal shear profiles are given by (3.29) and (3.30) respectively with $\beta = 6.4$. An example is shown in Figure 3.7

$$\overline{u}(z,t) = \begin{cases} \overline{u}_{hub}\left(\frac{z}{z_{hub}}\right)^{\alpha} \pm \left(\frac{z-z_{hub}}{D}\right)\left[2.5 + 0.2\beta\sigma_1\left(\frac{D}{\Lambda_1}\right)^{1/4}\right]\left[1 - \cos\left(\frac{2\pi t}{T}\right)\right] & \text{for } 0 \leq t \leq T \\ \overline{u}_{hub}\left(\frac{z}{z_{hub}}\right)^{\alpha} & \text{otherwise} \end{cases} \tag{3.29}$$

$$\overline{u}(y,z,t) = \begin{cases} \overline{u}_{hub}\left(\frac{z}{z_{hub}}\right)^{\alpha} \pm \left(\frac{y}{D}\right)\left[2.5 + 0.2\beta\sigma_1\left(\frac{D}{\Lambda_1}\right)^{1/4}\right]\left[1 - \cos\left(\frac{2\pi t}{T}\right)\right] & \text{for } 0 \leq t \leq T \\ \overline{u}_{hub}\left(\frac{z}{z_{hub}}\right)^{\alpha} & \text{otherwise} \end{cases} \tag{3.30}$$
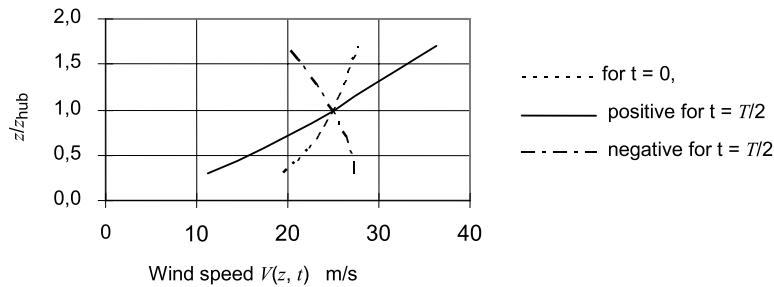
Figure 3.7: Example of EWS. Adapted from IEC (2005).

3.3   In-field Gusts

Various gusts types will be identified based on the idea that a gusts can be defined as a temporally and/or spatially varying change in the velocity vector (magnitude and/or direction). Four in-field recorded categories are presented: (1) veer, (2) wind gusts, (3) shear and (4) low-level jets. Furthermore, note is made that the time scale of these gusts are small, in the order of seconds/minutes. The spacial scale of the gusts is in the order of the rotor diameter.

To emphasize the wind variability with time, the recorded wind history at the Høvsøre, Denmark site is shown in Figure 3.8. The data has been collected between 2005 and 2013 and averaged per hour, day, month and year Peña et al. (2016). An almost constant yearly average is seen, with hourly variations in the range of $\pm 10 \ [ms^{-1}]$.
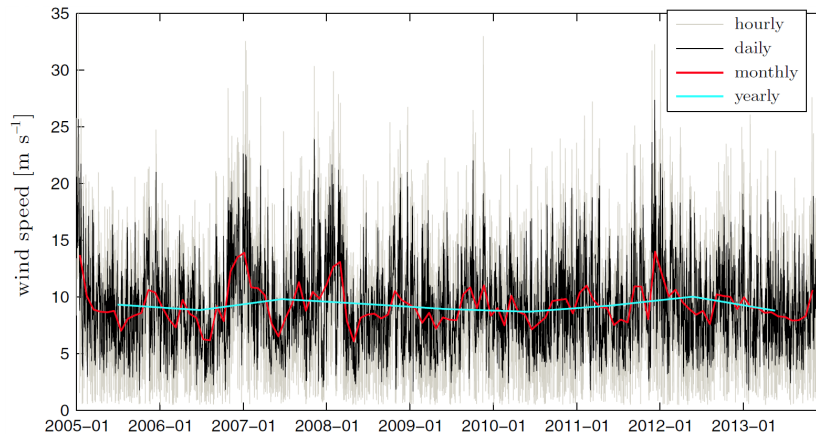
Figure 3.8: Time-series of the hourly, daily, monthly and yearly mean 100 $[m]$ velocity at the Høvsøre site. Adapted from Peña et al. (2016).

The wind variation over a day or the diurnal cycle at a coastal location (Pedra do Sal, Brazil) is shown in Figures 3.9. The velocity vector changes as a function of local time as explained in Section 3.1. Peaks are seen in the direction measurements, which are attributed to gusts.
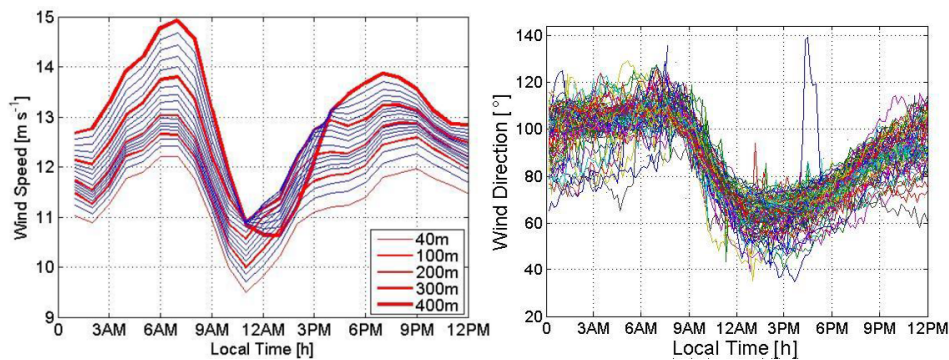
Figure 3.9: Wind speed and direction diurnal cycle recorded at Pedra do Sal, Brazil. Adapted from Sakagami et al. (2014).

Furthermore, the diurnal cycle for various flow homogeneity measured in a relatively complex terrain at Perdigão, Portugal, is presented in Figure 3.10. The measurements provide an idea of the possible flow complexity in a parallel double ridge topology; Figure 3.22 provides a terrain map of site. The results have been obtained via a new measurement technique involving the creation of virtual measurements towers by a number of LiDARs Bell et al. (2019). The results show the variability of flow complexity between three different days. Veer and significant vertical velocity gradient are observed as shown by Figures 3.10-d and 3.10-g. The envelope of flow complexity should be accounted for in wind turbine design and placement. It is noted that the following gusts are dependent on terrain and atmospheric stability. Additionally, as supported by Kalverla et al. (2017), the wind events can happen simultaneously. Figure 3.11 shows a Venn diagram for low-level jets, shear, veer and extreme wind speeds.
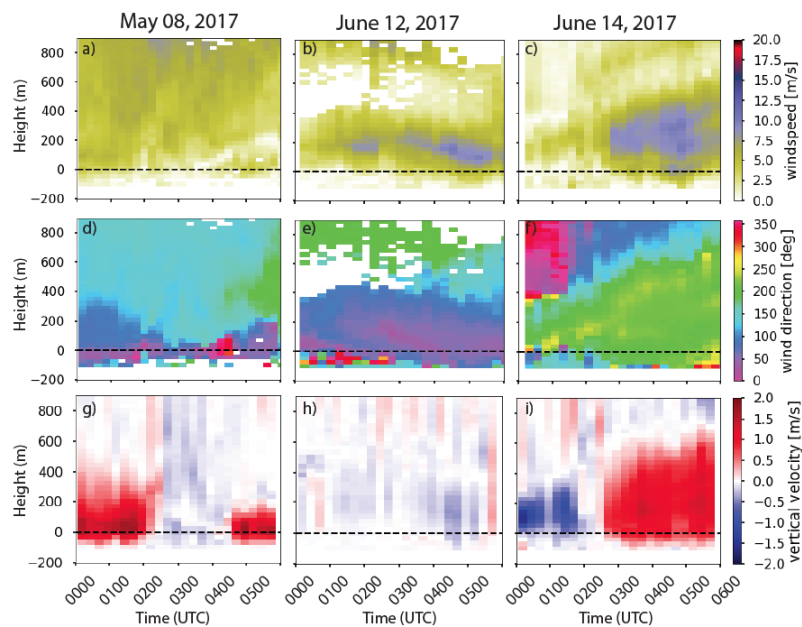
Figure 3.10: Diurnal cycle of wind speed, direction and vertical wind speed measured at the Perdigão, Portugal site. The dotted line corresponds to the base of a wind turbine installed at top of one of the ridges. Adapted from Bell et al. (2019).
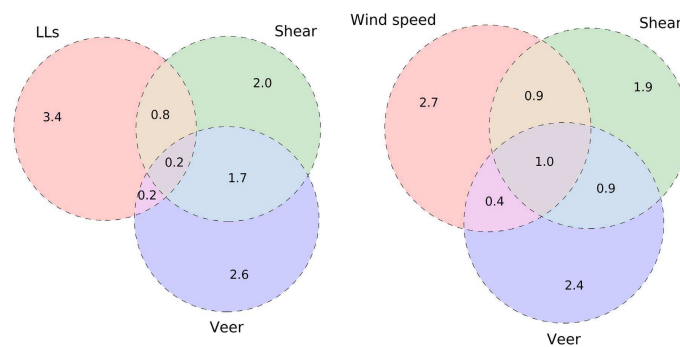
Figure 3.11: Venn diagrams relating wind gust events. Values refer to percent of total data collected in the study. Adapted from Kalverla et al. (2017).

3.3.1 Veer

Veering is the clockwise turning of the wind vector with height in the Northern hemisphere. It is a direct result of the Coriolis force Churchfield and Sirnivas (2018). Furthermore, the extent of veering is affected by the stability of the atmosphere. Based on Ekman theory, the ABL can veer up to 45 [°]. However, depending on stability and horizontal temperature gradient the veering can be lower in reality than Ekman predictions Kalverla et al. (2017). An illustration of a typical Ekman wind profile showing veering is presented in Figure 3.12.
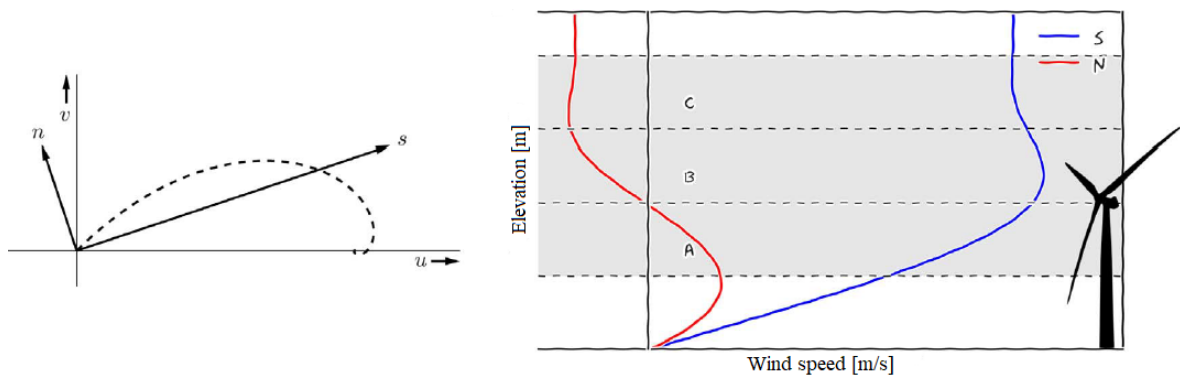
Figure 3.12: Right: illustrative hodograph of an Ekman layer wind profile. Left: Wind profile of wind aligned component at hub height (s) and perpendicular component (n). Adapted from Kalverla et al. (2017).

Measurements have been conducted at the Høvsøre site for three stability conditions based on Obukhov length; stable: $10 \leq L_* \leq 500$, neutral: $500 < L_*$ or $L_* < -1500$, and unstable: $-1500 \leq L_* \leq -10$. The profiles are shown in Figure 3.13. As the ABL becomes neutrally stratified, the veering with height is considerably lower than in stable conditions. At slow wind speeds and in stable conditions the veering is most severe, exceeding angles of 40 [°].
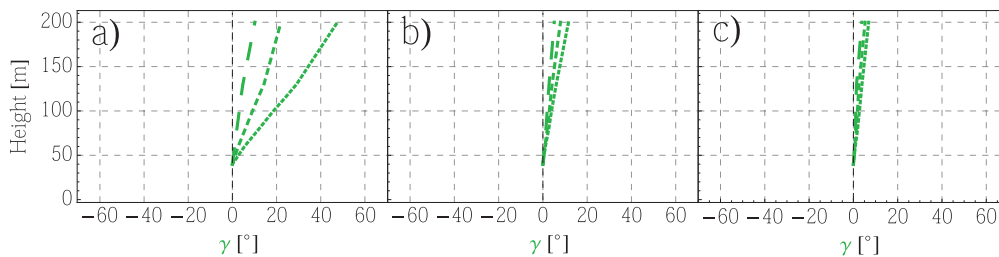
Figure 3.13: Vertical profile of veer angle based on 30-min averages in a) stable, b) neutral and c) unstable. Line type represents wind speed bins; dotted: 4-6, short dash: 6-8 and long dash: 8-10 m/s. The veer angle is relative to the 40 m level. Adapted from Berg et al. (2013).

The site at Høvsøre is characterised by mostly flat lands, with a southern fjord, 800 m away. In contrast, measurements were performed in Ryningsnäs, Sweden, a forested area with a mean canopy height $h_c = 20$ [m] Arnqvist et al. (2015). Similarly, veering profiles were derived based on stability. The results of the study are shown in Figure 3.14, agreeing that the highest veering is observed in stable conditions.
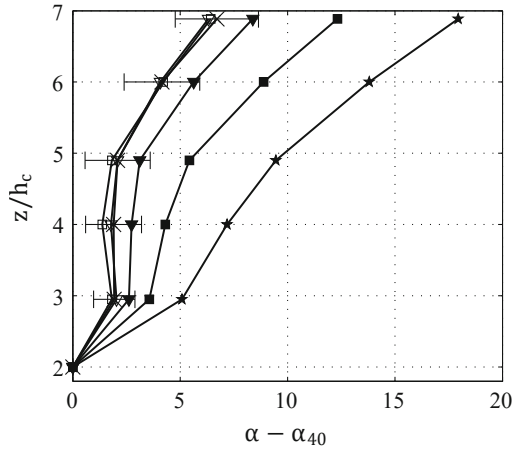
Table 3.3: Stability categories from Arnqvist et al. (2015).

Diabatic Stability
$L_*/h_c < 5$, ($\bigstar$)
$5 < L_*/h_c < 20$, ($\blacksquare$)
$20 < L_*/h_c < 50$, ($\blacktriangledown$)
$|L_*/h_c| > 50$, ($\times$)
$-50 < L_*/h_c < -20$, ($\triangledown$)
$-20 < L_*/h_c < -5$, ($\square$)

Figure 3.14: Vertical profile of veer angle. The veer angle is relative to the 40 $[m]$ level. The symbols stability conditions are given by Table 3.3. Adapted from Arnqvist et al. (2015).

Furthermore, veer measurements have been conducted at Perdigão, Portugal. Figure 3.15 shows the vertical profiles measured via various methods. The reader is referred to Bell et al. (2019) for details on the measurement techniques. It is noted that the vertical profiles match instantaneous time from Figure 3.10 and are representative of moderate flow complexity. Measurements are relative to the base of a wind turbine installed at the top of one of the ridges (refer to Figure 3.22). Veer at rotor relevant heights (above the ridges) in the order of ≈ 25 [°] is observed. Furthermore, highly varying wind direction and gradient are seen within the valley (height ≤ 0 $[m]$).
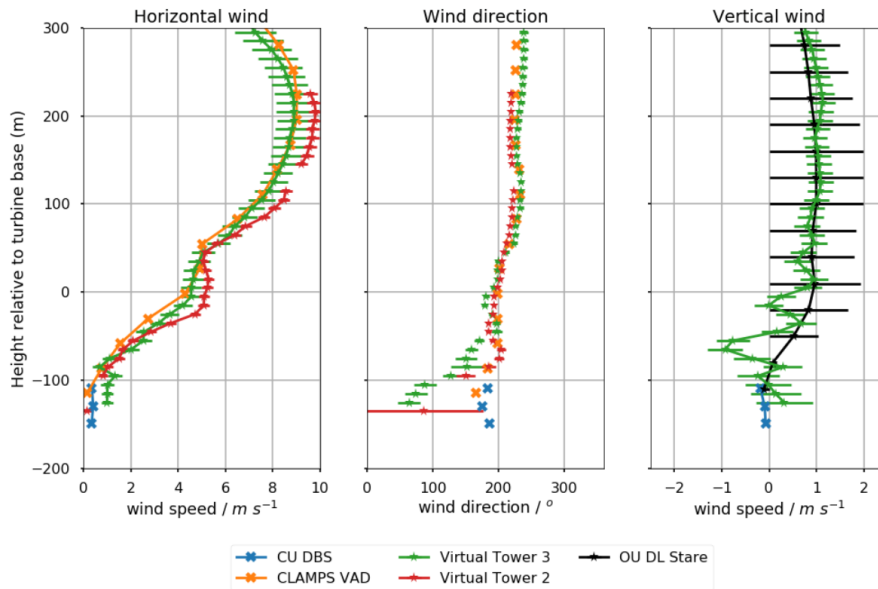
Figure 3.15: Vertical profiles of horizontal wind speed, direction and vertical wind speed. The profiles were recorded on June 12, 2017 at 2:58 UTC and match the second column in Figure 3.10. Adapted from Bell et al. (2019).

Lastly, veering has also been analysed via LES. The ABL was allowed to develop naturally in the simulation with the inclusion of Coriolis force in the momentum balance Abkar et al. (2018); Churchfield and Sirnivas (2018). Figures 3.16 and 3.17 show the resulting veer profiles for Coriolis force representation of the northern hemisphere at a latitude of 73 [°] and 57.5 [°], respectively.
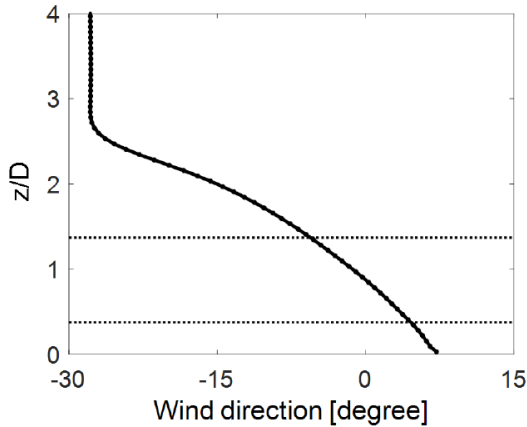
Figure 3.16: LES veer at latitude of 73 [°]. Adapted from Abkar et al. (2018).
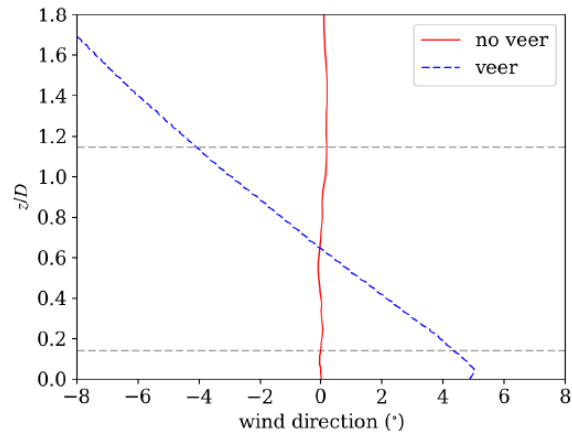
Figure 3.17: LES veer at latitude of 57.5 [°]. Adapted from Churchfield and Sirnivas (2018).

3.3.2 Wind Gusts

Wind gusts manifest themselves as variation in wind magnitude and/or change of direction. The EOG, EDG and ECG are wind gusts. Note is made on wind ramps, which, for the purpose of this thesis are defined as the portion of a wind gust showing strictly an increase/decrease in magnitude/direction. They develop from various mechanisms that have varying time scales. The passage of fronts, formation of thunderstorms due to moist convection or the perturbations in stability leading to downward momentum mixing are some of the mechanisms Kalverla et al. (2017). For off-shore/coastal wind turbines, the onset of local circulation will also lead to wind ramps. Their time scales vary from hours to a few seconds. Suomi et al. have documented the probability of cross flow at the Høvsøre site. The results, Figure 3.18, show that the probability of cross flow is low; implying that a velocity ramp can occur in the absence of veer, as supported by the Venn diagram shown in Figure 3.11 Kalverla et al. (2017). The text further documents the gust factor profile with height in Figure 3.19 Suomi et al. (2015). The measurements identified a decreasing trend in gust factor with heigh. Furthermore, the stable conditions exhibited lower gust factors. Additionally, Figure 3.20 shows the maximum/minimum mean vertical velocity profile during maxima/minima gusts. The negative values of (w_{max}) indicate down-draughts for maximum gusts and vice-versa. This points to a correlation between up/down-draughts and gusts.
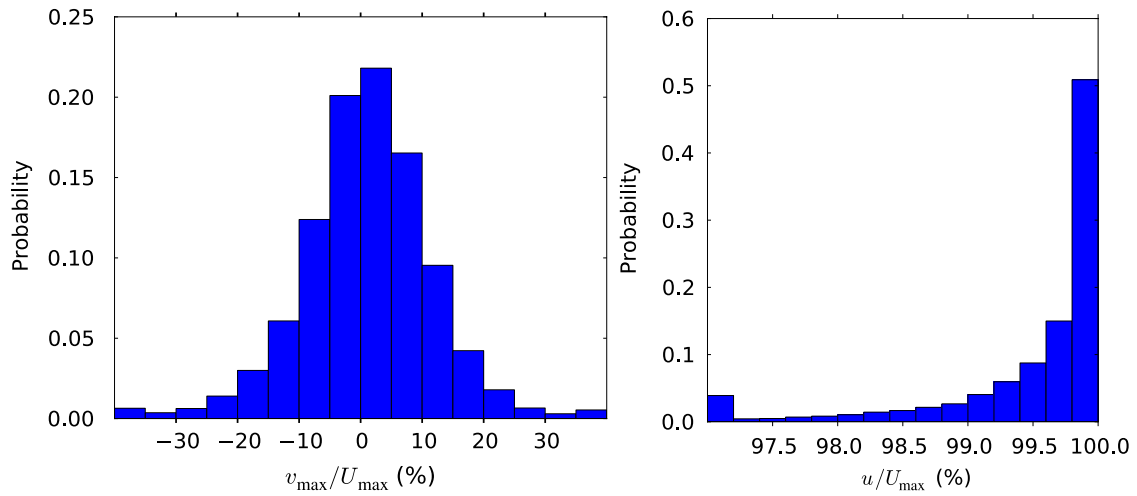
Figure 3.18: Probability distribution of mean cross and along wind velocity components averaged over duration of maximum gust; i.e. $t_g = 3$s within a measurement period of $T = 10$ min. Measurements have been carried out at a height of 10 m. Adapted from Suomi et al. (2015).
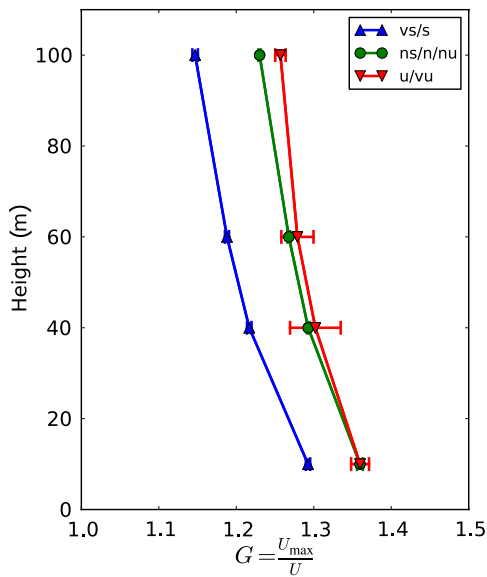
Figure 3.19: Median values of vertical profile of gust factor for various stability conditions. Abbreviations vs/s refer to very stable/stable, ns/n/nu refer to neutrally stable/neutral/neutrally unstable and vu/u refer to very unstable/unstable. Adapted from Suomi et al. (2015).
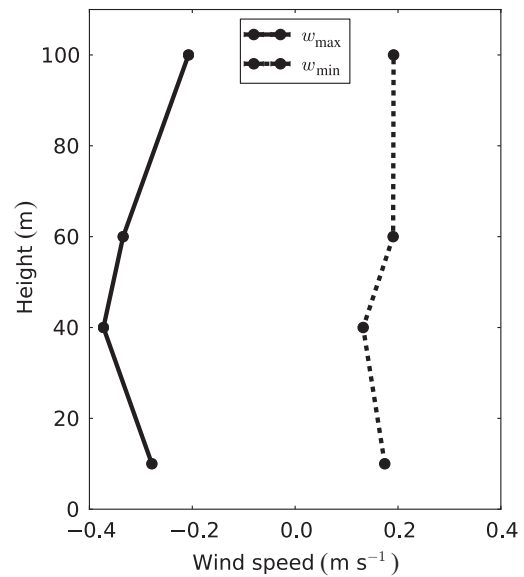
Figure 3.20: Median values of vertical wind velocity component profile for maximum and minimum gusts with period of $t_g = 3$s. Adapted from Suomi et al. (2015).

The vertical gust factor profile at Høvsøre was compared with the Perdigão site, confirming the increase in gust factor with terrain complexity as seen in Figure 3.21.
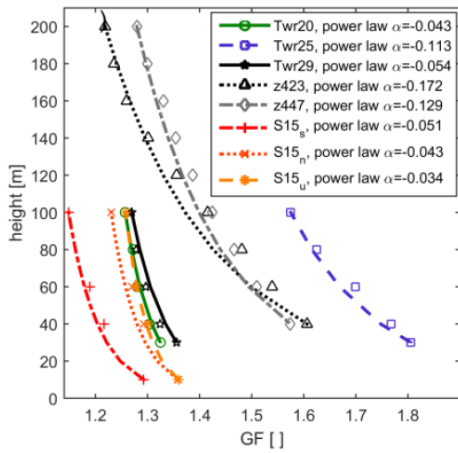
Figure 3.21: Power law fit to gust factor measurements at Perdigão. Tower locations are given in Figure 3.22. Data series labelled S15 refer to data from Suomi et al. (2015) (Figure 3.19). Adapted from Letson et al. (2018).
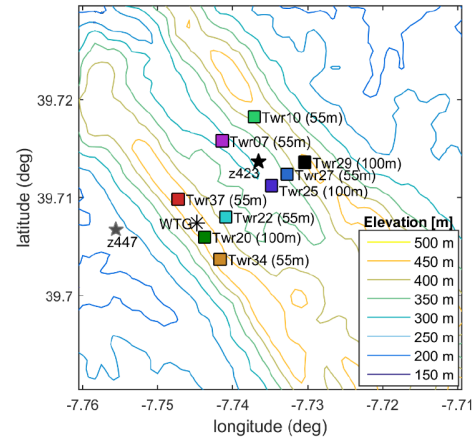
Figure 3.22: Perdigão site tower locations. Adapted from Letson et al. (2018).

Measurements have been done at the Eolos research facility 2.5 MW Clipper Liberty C96 wind turbine during a gust event. The response of the wind turbine has been recorded in terms of blade pitch and output power Howard and Guala (2016), shown in Figure 3.23. A peak in output power is observed, despite a decrease in blade pitch. This is detrimental to the power grid as previously explained Burton et al. (2011). Furthermore, when considering the power output of a large wind farm, the formerly mentioned power fluctuation is accentuated.
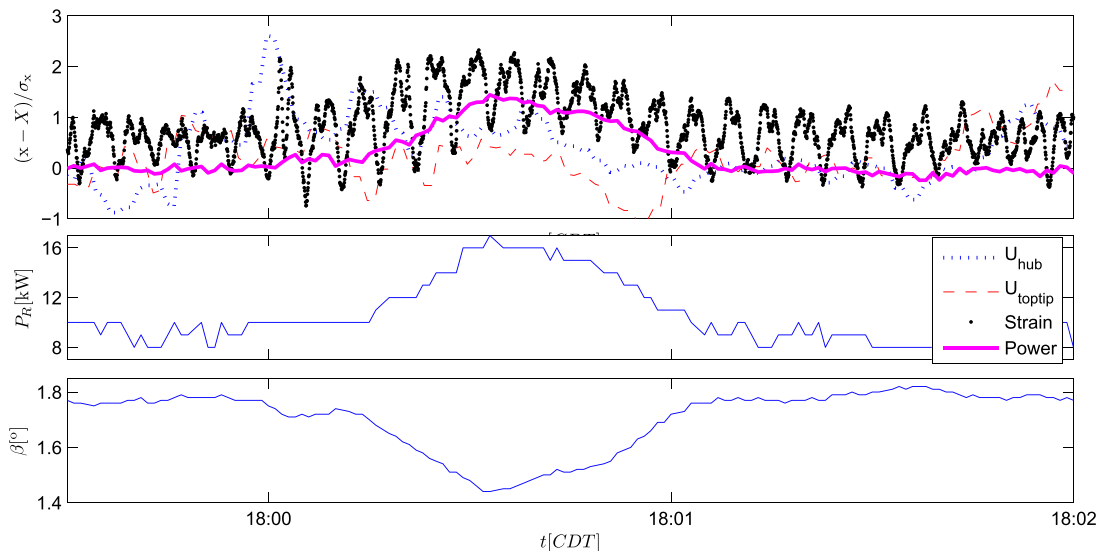
Figure 3.23: Gust event wind turbine response. Top plot is expressed as time signal minus mean value divided by the standard deviation. Adapted from Howard and Guala (2016).

Wind data from the Thyborøn, Denmark test site has been document by Kim et al., identifying a wind ramp-up from 13.6 to 23.3 $[ms^{-1}]$ within 3 $[s]$. The wind direction changes by 25 $[°]$ (240 to 265 $[°]$) within 10 $[s]$. The wind ramp-up can be identified in Figure 3.24 between 108 $[s]$ and 111 $[s]$. Similar variability can be seen in the wind direction.
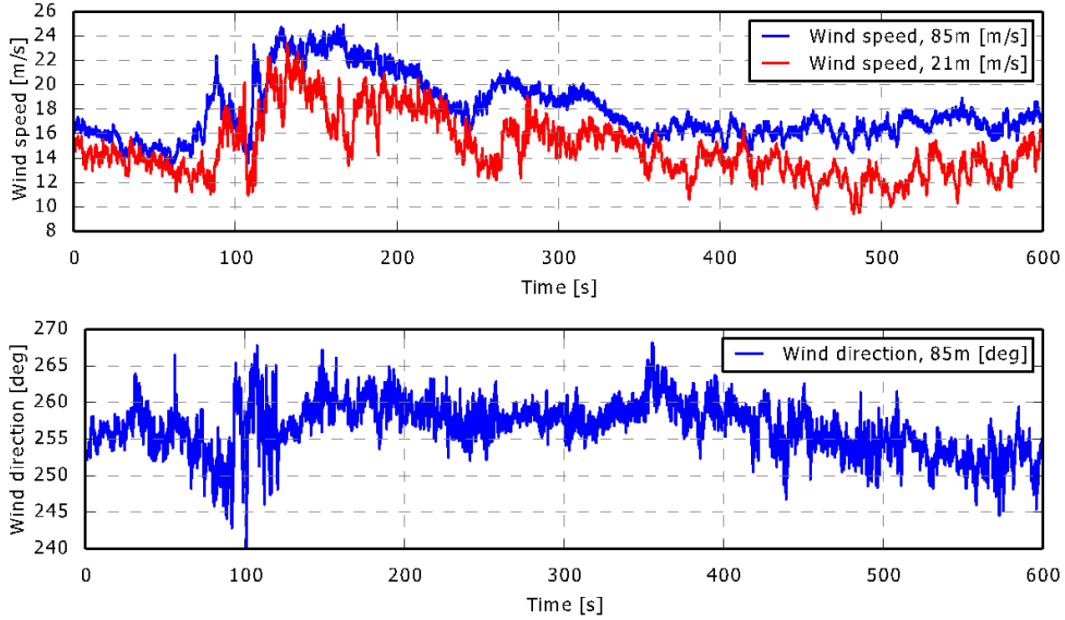
Figure 3.24: Wind data from the Thyborøn, Denmark test site on 24 October, 2013. Adapted from Kim et al. (2014).

Probability distributions have been fitted to in-field measurements for the gust descriptors presented in Section 3.2.1. The measurements were performed in complex (Letson et al., 2018, Fig. 3, page 9) and moderately complex terrain (Hu et al., 2018, Fig. 5, page 1469). Table 3.4 summaries the mode values from the two topologies. Values are comparable with the exception of $(u_{t,T}^a)$, which, was twice as high for the valley towers in complex terrain. Furthermore, gusts in complex terrain show a higher lapse time as well as shorter length scales.

Table 3.4: Summary of mode values of gust parameters in moderate Hu et al. (2018) and complex Letson et al. (2018) terrain topology. Values for complex topology are given a range based on the location of the measurement tower; italics - ridge towers, normal - valley towers.

Parameter	Moderate	Complex
U_T $[ms^{-1}]$	≥ 3	3.50
$u_{t,T}^{max}$ $[ms^{-1}]$	7	*6 - 7*
$G_{t,T}$ $[-]$	1.30	*1 - 3*
$u_{t,T}^a$ $[ms^{-1}]$	1.27	*1.55 - 3*
$k_{t,T}$ $[-]$	2.23	2.30
t_r $[s]$	11.2	12
t_l $[s]$	12.6	15.90
L_g $[m]$	224.8	*230 - 260*

3.3.3 Shear

Shear can be defined as the variation in speed with height. The no-slip condition has to be satisfied at the ground, where the velocity vanishes. This results in the flow adjusting and approaching zero velocity at the ground. Close to the ground the highest velocity gradients are observed, which lead to considerable differential loading on wind turbines Burton et al. (2011). Shear profiles have been measured extensively. Furthermore, logarithmic or power law profiles have been successfully been fit to measurements. This section will present two sets of shear profile measurements in flat and forested terrain. Velocity profiles for various normal planes in front of the Eolos research facility wind turbine are shown in Figure 3.25. The velocity profile for various stability classes (Table 3.3) are shown in Figure 3.26, showcasing the highest shear in stable conditions.
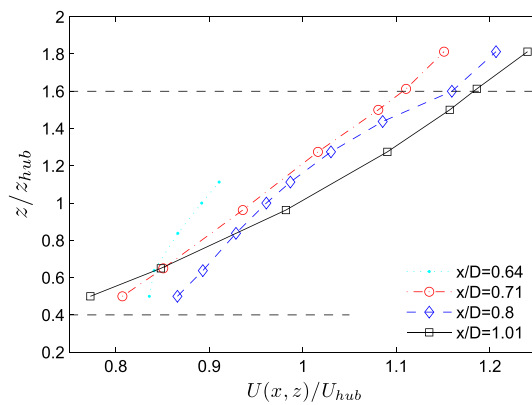
Figure 3.25: Mean velocity profile at varying x/D. Adapted from Howard and Guala (2016).
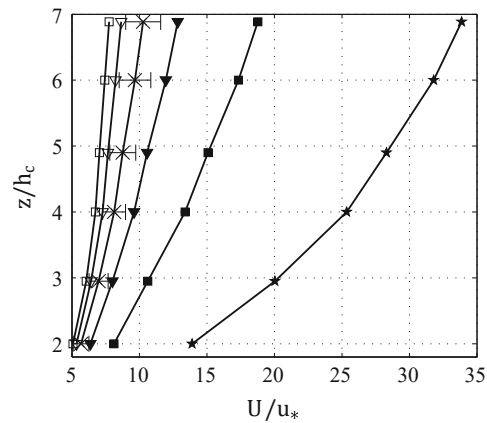
Figure 3.26: Mean velocity profiles for varying stability classes (Table 3.3). Adapted from Arnqvist et al. (2015).

3.3.4 Low-Level Jet

Low-level jet (LLJ) are a feature of the SBL and manifest as a wind speed maxima. Also known as "nocturnal low-level jets" due to their occurrence only at night time, when the SBL develops under surface cooling Emeis (2018). The jets form above ground level between 150-500 $[m]$ resulting in interaction with modern large rotor diameter wind turbines. Locations where LLJs develop are favourable for wind energy production due to an increase in wind speed, however, care is needed in the design of the rotor since LLJ significantly increase the shear of the inflow conditions Storm et al. (2009), leading to increased differential loading. A National Renewable Energy Laboratory (NREL) report found that LLJs can significantly influence vertical shear as well as producing intense coherent turbulence, depending on wind conditions Kelley et al. (2004). The occurrence of LLJ has been thoroughly documented by Baas et al., concluding they occur mostly in summer and in the months before/after. A variety of physical mechanisms lead to their formation:

1. Diurnal variation in eddy viscosity; as stable stratification develops, turbulence is damped out, decoupling the upper Ekman layer from the surface layer. This leaves the upper layer free of surface influence and it accelerates being unaffected by surface friction Blackadar (1957) Storm et al. (2009).

2. Large-scale baroclinicity; as the geostrophic wind decreases sharply with height, a LLJ (or maxima in vertical velocity profile) is likely to occur Kotroni and Lagouvardos (1993) Baas et al. (2009).

3. Slopping terrain that leads to diurnal cycle in horizontal temperature gradient. Changes in surface characteristics resulting in differential heating, such as coastal areas (water transition to sand/land) Hotlon (1967) Baas et al. (2009).

Measurements derived from a 7 years database at the Cabauw, Netherlands site are used to characterise LLJs in flat terrain Baas et al. (2009). Average wind profiles of 9 classes of LLJs are shown in Figure 3.27. The classes are based on the geostrophic wind speed (V_g) and isothermal long-wave radiative cooling (ΔT_{iso}). The results show a substantial LLJ at high radiative cooling and moderate geostrophic wind.
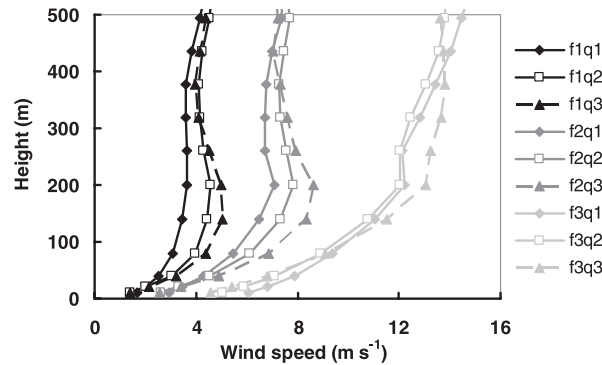
Figure 3.27: Mean wind profiles for nine LLJs classes. Classes f1,f2 and f3 refer to $V_g \leq 5$ [ms^{-1}], $5 < V_g \leq 10$ [ms^{-1}], and $V_g > 10$ [ms^{-1}] Classes q1, q2, q3 correspond to $\Delta T_{\text{iso}} \leq 3$ [K], $3 < \Delta T_{\text{iso}} \leq 6$ [K], and $\Delta T_{\text{iso}} > 6$ [K]. Adapted from Baas et al. (2009).

The histogram of LLJs heigh is shown in Figure 3.28-a, the relation between LLJ height and the height of the inversion layer in 3.28-b, the relation between LLJs height and speed in 3.28-c and the turning of the jet with respect to the wind at 10 [m] in 3.28-d. The majority of the population occurs at turbine relevant heights. Furthermore, the height of the jet core lies mostly along the inversion layer, which is at considerably lower heights during the night in stable conditions. Lastly, veering is expected to occur simultaneously with LLJ as supported by Kalverla et al. (2017).
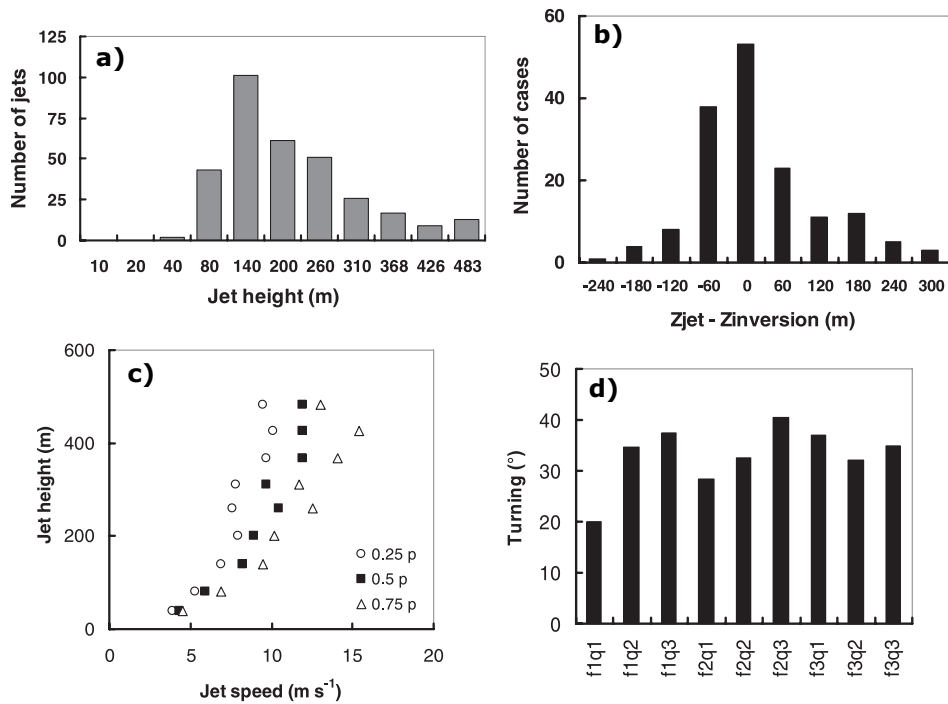
Figure 3.28: a) Histogram of LLJs height, b) histogram of difference in jet height and inversion layer heigh, c) LLJ speed-heigh relation; circles show 25th percentile, triangles 75th percentile and squares show the median, d) jet core turning with respect to the 10 m wind. Adapted from Baas et al. (2009).

Chapter 4

Gust Generators

The controlled generation of gusts is a multi-disciplinary problem. It applies to many systems other than wind turbines, such as, unmanned aerial vehicles (UAVs) Castellani et al. (2018), aircrafts Lancelot et al. (2015) and ground vehicles Volpe et al. (2013). The author has identified six gust generators that will be discussed in details in the following sections. Additionally, Section 4.6 discusses a special branch of wind tunnels, able to develop thermally stratified shear flows.

4.1 Circulation Control

One of the oldest ways of disturbing uniform flow in a wind tunnel to generate gusts normal/parallel to the mean flow is circulation control. This is achieved by circulation-controlled airfoils (CCAs); rotating slotted cylinders (RSC) installed at the training edge (TE) of airfoils Ham et al. (1974). A twin parallel configuration is shown in Figure 4.1. The airfoil contains an air plenum, which discharges into the rotating cylinder. Based on the orientation of the slot, fluid will mix into the main flow and induce vortices. This method of generating gusts is able of operate at high frequencies, it is mechanically simple due to only one moving part (the cylinder) and is capable of producing a high lift coefficient for rather low jet momentum coefficient. The two cylinders can rotate in-phase resulting in lateral (normal to mean flow) gusts or out-of-phase to produce longitudinal gusts (parallel to mean flow). The lateral and longitudinal root mean square (RMS) gusts are recorded versus reduced frequency for various mean speeds and shown in Figure 4.2. Reduced frequency is defined by Equation 4.1, where (c) is the chord length, (ω) is the circular velocity and $(\overline{u})$ is the mean flow velocity.

$$k = \frac{\omega c}{2\overline{u}} \tag{4.1}$$
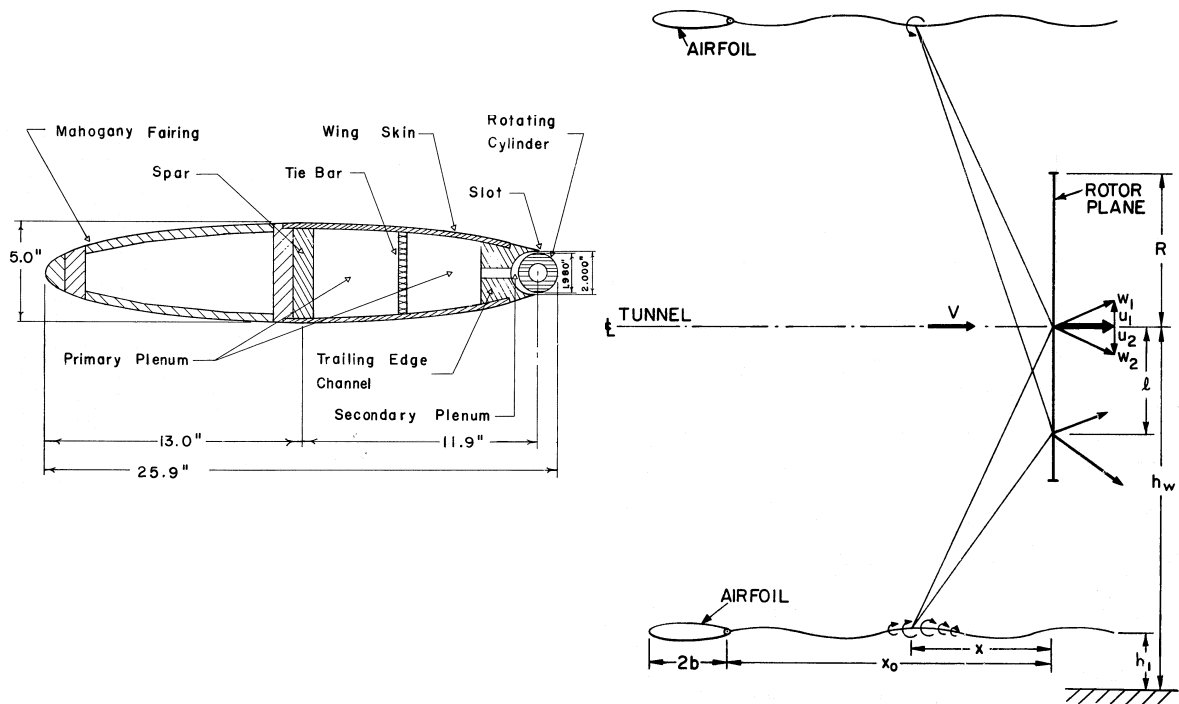
Figure 4.1: Left: cross section of the airfoil-RSC. Right: Twin parallel airfoils-RSC configuration. Adapted from Ham et al. (1974).
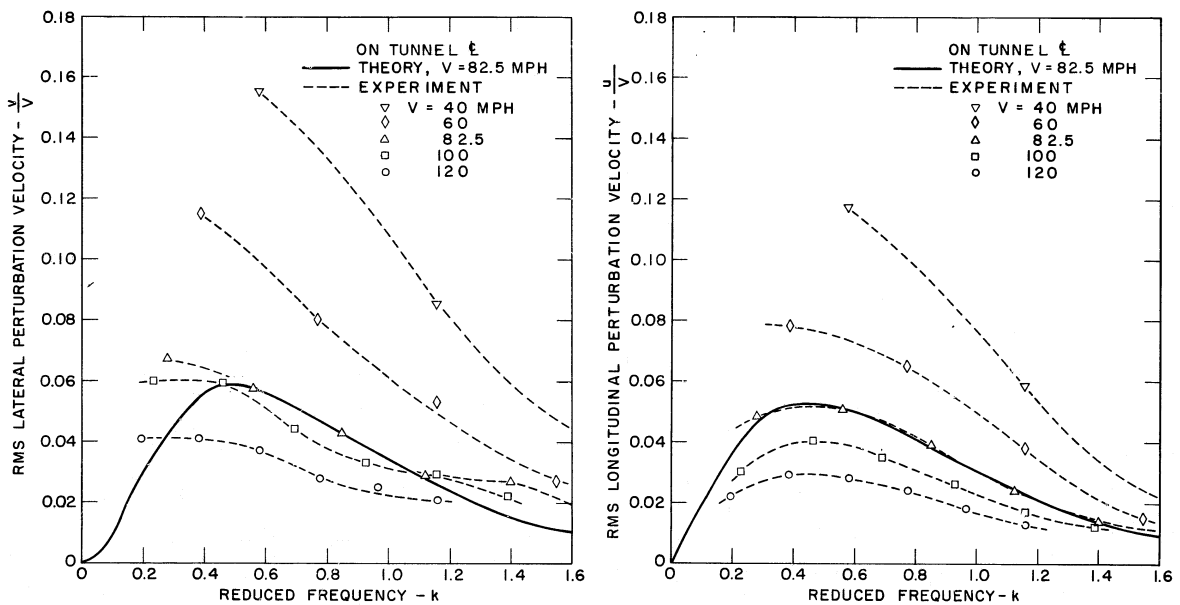
Figure 4.2: RMS lateral/longitudinal gusts produced by the twin parallel airfoils configuration versus reduced frequency. Measurements done at wind tunnel centre-line. Adapted from Ham et al. (1974).

RSCs have also been implemented to produce multi harmonic longitudinal/lateral gusts Tang et al. (1996). The set-up involved four airfoil-RSCs system with a phase lag in the rotation of adjacent cylinders. A recorded gust time series is shown in Figure 4.3 together with the frequency spectrum of the recorded gust.
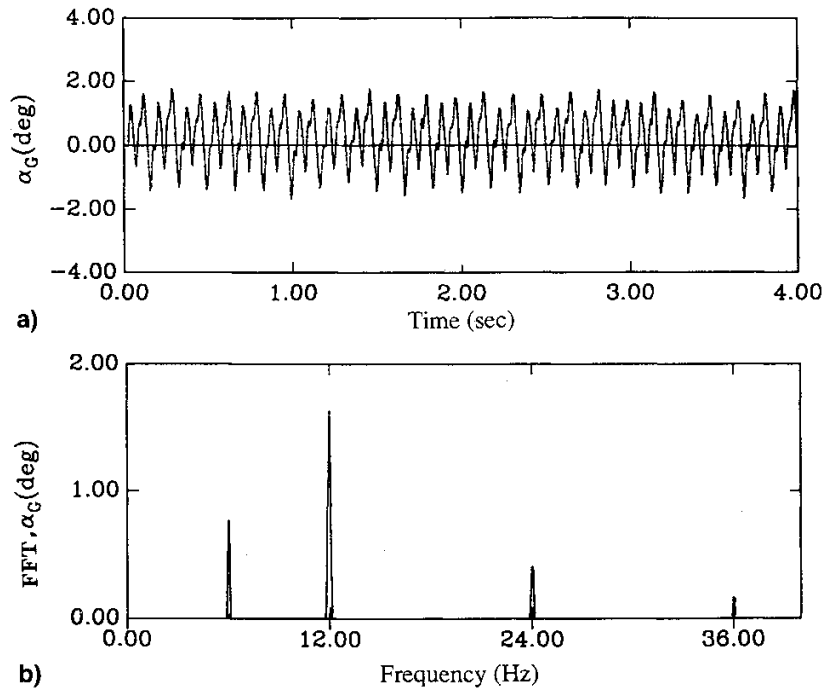
Figure 4.3: a) Recorded gust time series b) Fast Fourier transform of the time series. Adapted from Tang et al. (1996).

The absolute value of the gust angle is just under 2 [°], a relatively small angle, specially for wind turbine application, however, the authors support the ability of scaling up the gust amplitude by up-scaling the RSCs geometrically.

4.2   Secondary Flow

The injection of a secondary flow at an angle to the main flow can be used to generate lateral gusts. Volpe et al. have used this technique to simulate lateral gusts on ground vehicles. The set-up of the wind tunnel, measured and simulated unsteady gust at a point along the centre-line, aft of the auxiliary wind tunnel inflow are shown in Figure 4.4. As can be seen, the auxiliary inflow angle is reached within a relatively small rise time. Note is made that a specialised opening sequence was required, details given in Volpe et al. (2013). This method results in highly controllable gusts with large magnitudes, 30 [°]. The drawback is, however, the implementation of an auxiliary wind tunnel and a specialised opening sequence of the secondary flow.
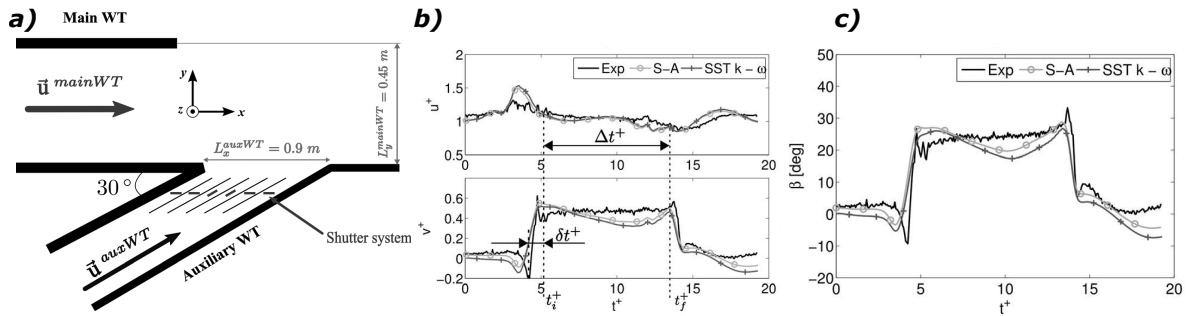
Figure 4.4: a) Wind tunnel set-up with auxiliary inflow that produce unsteady lateral gusts. b) Velocity profile at a point along the centre-line and just aft of the auxiliary inflow, c) yaw angle measured at the same point. CFD results are also shown with two turbulence models. Adapted from Volpe et al. (2013).

4.3 Fan Control

The equivalent of ramp up/down has been achieved via fan control of the wind tunnel of University of Perugia Castellani et al. (2018). The gusts were of sinusoidal nature in the longitudinal direction as shown by Figure 4.5. The fan of the wind tunnel was controlled by an inverter.
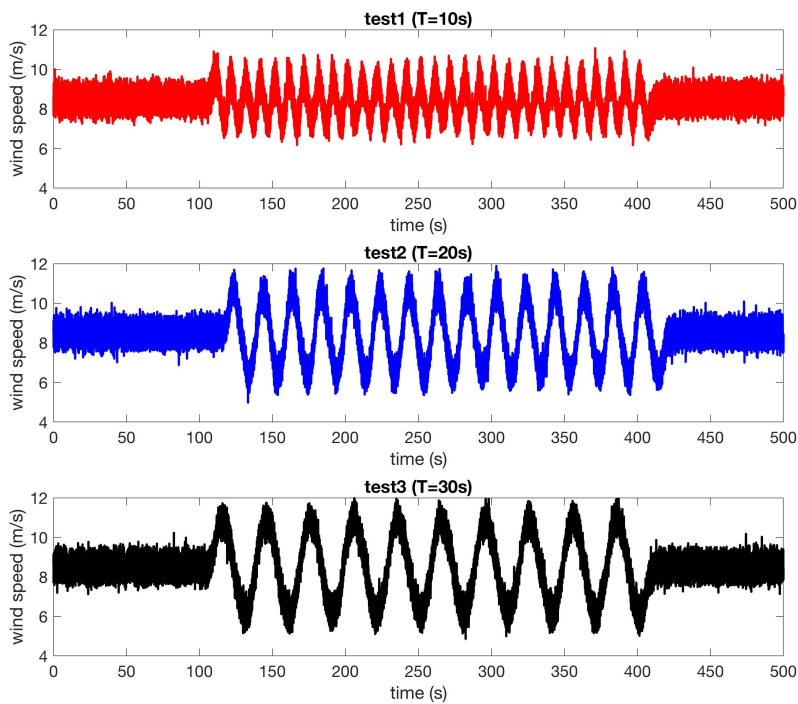
Figure 4.5: Time series of sinusoidal longitudinal gusts created by fan control. Three different time periods were achieved, 10, 20 and 30 s. The gust amplitude was 1.3 m/s from the base flow of 8.5 m/s. Adapted from Castellani et al. (2018).

It can be observed that for the higher frequency the gust amplitude is slightly smaller than the other measurements. This is attributed to an upper limit by the flow and wind tunnel inertia. The test campaign included a model HAWT characterised by: 3 $[kW]$ rated maximum power, 2 $[m]$ rotor diameter, 3 blade with fixed pitch angle and a fully electric load control through a pulse width modulation on a resistive load. Its response to the longitudinal gusts with time period of 10 and 30 $[s]$ in terms of power versus rotations per minute (rpm) is shown in Figure 4.6. This highlights the variability in power production under unsteady flow, which, if not properly mitigated via control system can affect the power grid Burton et al. (2011).
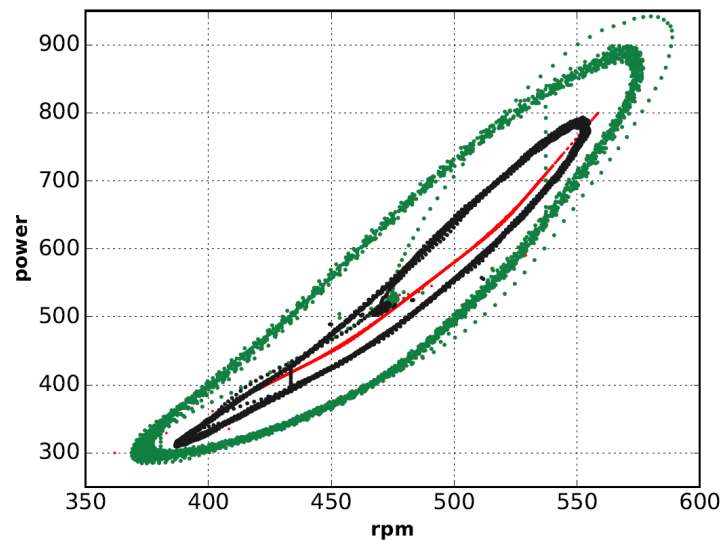
Figure 4.6: Wind turbine response to longitudinal sinusoidal gusts with time period 10 (green dots) and 30 s (black dots) in comparison to numerical simulation (red line). Adapted from Castellani et al. (2018).

The wider spread of the shorter time period gusts points towards the slow response of the wind turbine controller. Adjusting the controller could lead to improved behaviour in the presence of unsteady gusts Castellani et al. (2018). This further highlights the motive of this thesis; the need of gust generation in a controlled environment to test new control strategies.

4.4   Oscillating Vanes

Oscillating vanes are the most common way of producing angled gusts. Undisturbed fluid flows past an array of vanes (two or more) which can vary their angle of attack in time. This results of the flow downstream being deflected in relation to the frequency of oscillating, often expressed as reduced frequency and vane deflection angle. An example from the Cranfield University open jet, closed-circuit wind tunnel is presented in Saddington et al. (2015). The set-up employed 6 NACA0015 airfoils with chord length $c = 0.114$ $[m]$ and aspect ratio $AR = 10$ $[-]$. The setup is shown in Figure 4.7. A cross-wire anemometer was used to measure the longitudinal (u') and lateral (v') velocity fluctuations behind the TE of one of the vanes and at half pitch between the adjacent vane. Figure 4.8 shows the results for an

oscillation frequency of 1 $[Hz]$ and vane deflection angles of ± 8 and 12 $[°]$. The corresponding measured longitudinal and lateral turbulence intensity is shown in Figure 4.9.
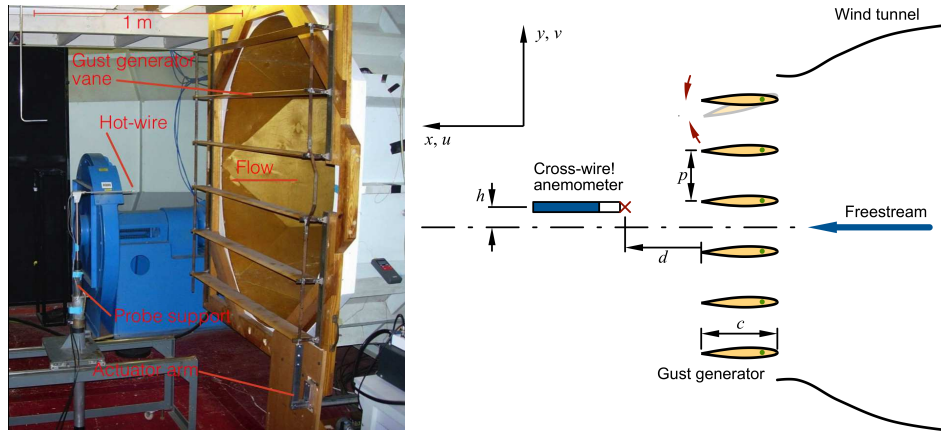
Figure 4.7: Gust generator set-up at the Cranfield University wind tunnel. Adapted from Saddington et al. (2015).
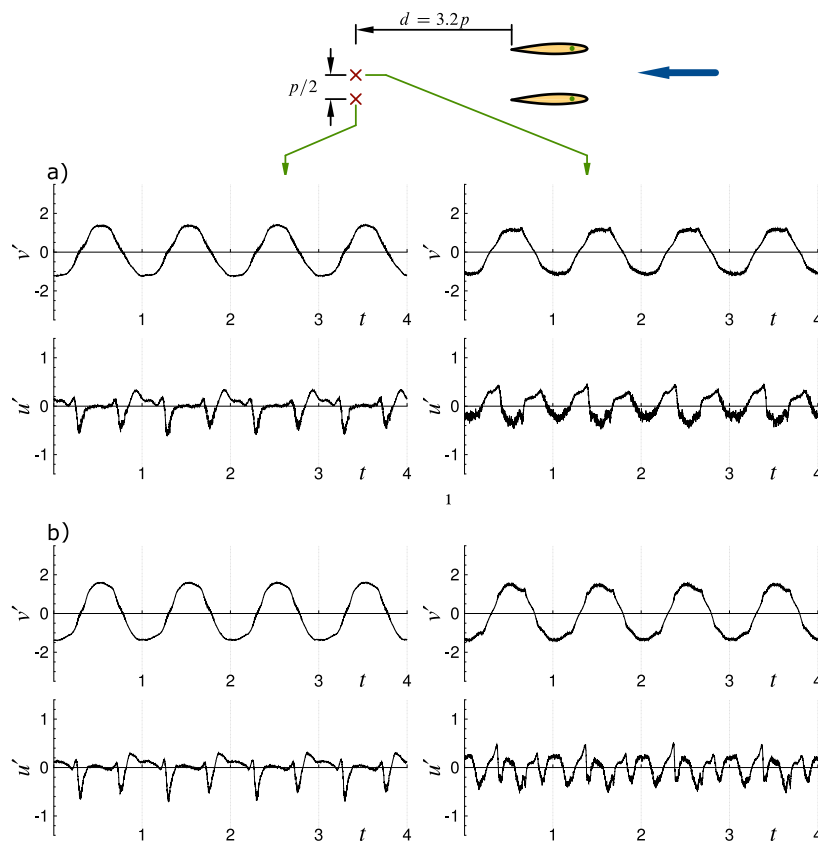
Figure 4.8: Hot-wire measurements at two points behind the gust generator for free stream velocity of 7.5 $[ms^{-1}]$ and flapping frequency of 1.0 $[Hz]$. a) gust vane angle of ± 8 $[°]$ b) 12 $[°]$. Adapted from Saddington et al. (2015).
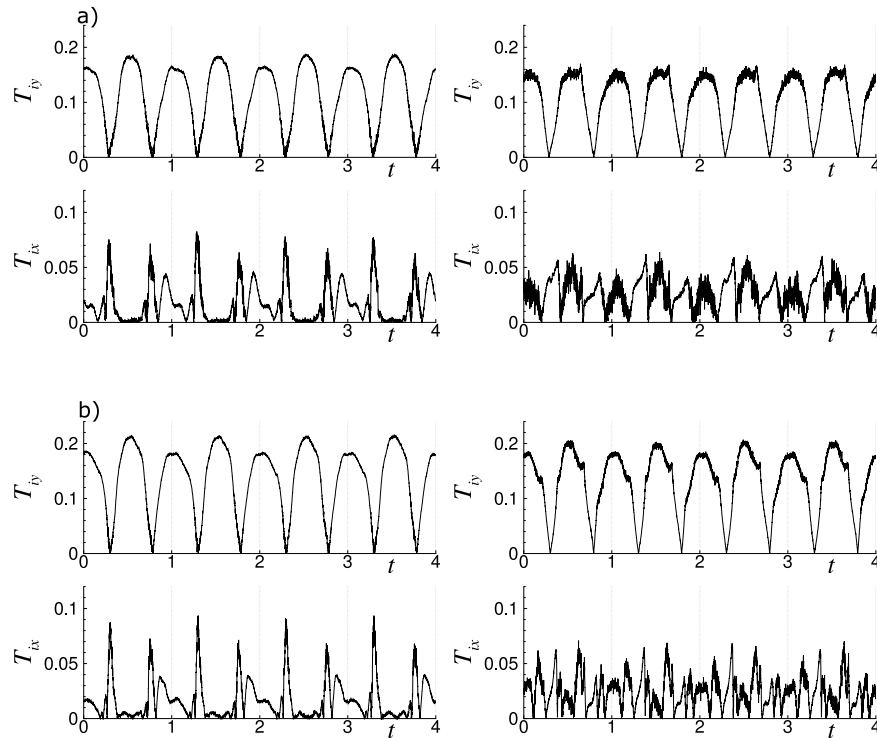
Figure 4.9: Longitudinal (T_{ix}) and lateral (T_{iy}) turbulence intensity at two points behind the gust generator for free stream velocity of 7.5 [ms^{-1}] and flapping frequency of 1.0 [Hz]. a) gust vane angle of ± 8 [°] b) 12 [°]. Adapted from Saddington et al. (2015).

Similarly to the velocity fluctuations, the turbulence intensity follows the oscillation of the gust vane in the lateral direction. Furthermore, the value of the lateral velocity fluctuations and turbulent intensity vary slightly for the two ranges of gust vane angles. The streamwise turbulence intensity generated is considerably lower than cross stream turbulence intensity Saddington et al. (2015).

The second example of oscillating vane gust generator is the focus of this thesis, the OJF lateral sinusoidal gust generator. The current configuration employs 2 vertical vanes capable of individual actuation. The airfoil profile used is the NACA0012 with $c = 0.3$ [m] and $AR = 9.6$ [$-$]. The gust generator is shown in Figure 4.10. Two sets of test campaigns have been carried out to validate the design and implementation of the gust generator. Emphasis is placed on the available measurements since the author intends to use these for validation purposes of the be developed models. Tufts and smoke were used initially to give a qualitative idea of the flow deflection, as well as a single hot-wire Lancelot et al. (2015). A second investigation campaign was conducted where particle image velocimetry (PIV) was used to measure the velocity profiles at two horizontal planes. Additionally, a semi-infinite NACA0012 airfoil was attached to a force balance which was used to compute lift coefficients of the semi-infinite wing under generated gusts Lancelot et al. (2017). The measurement locations are shown in Figure 4.11.
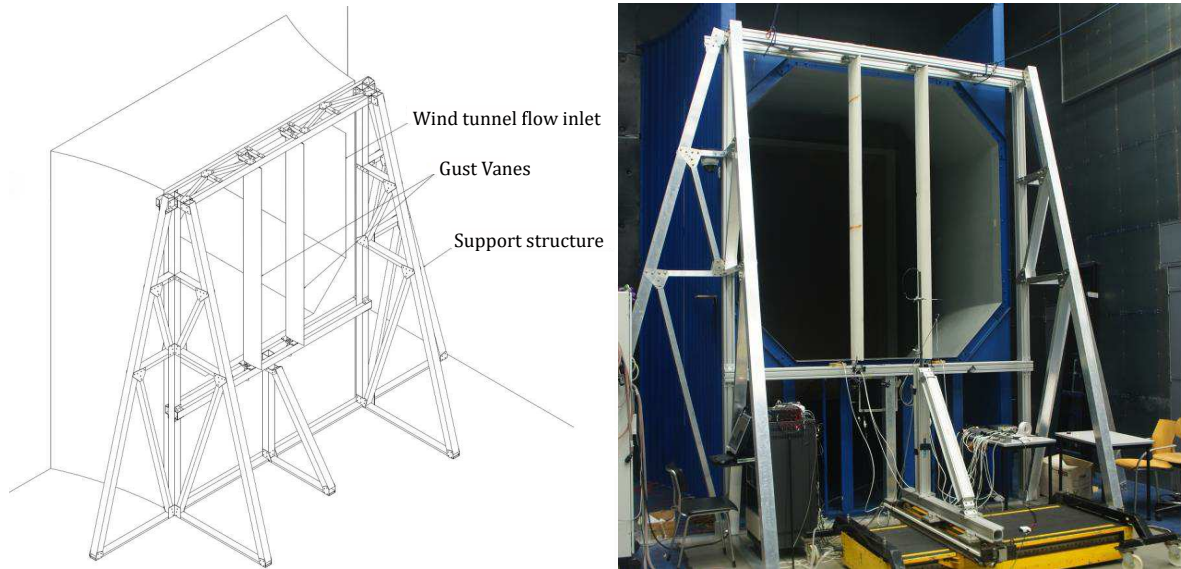
Figure 4.10: Delft University of Technology Open-Jet Facility with the gust generator installed. Adapted from Lancelot et al. (2015).
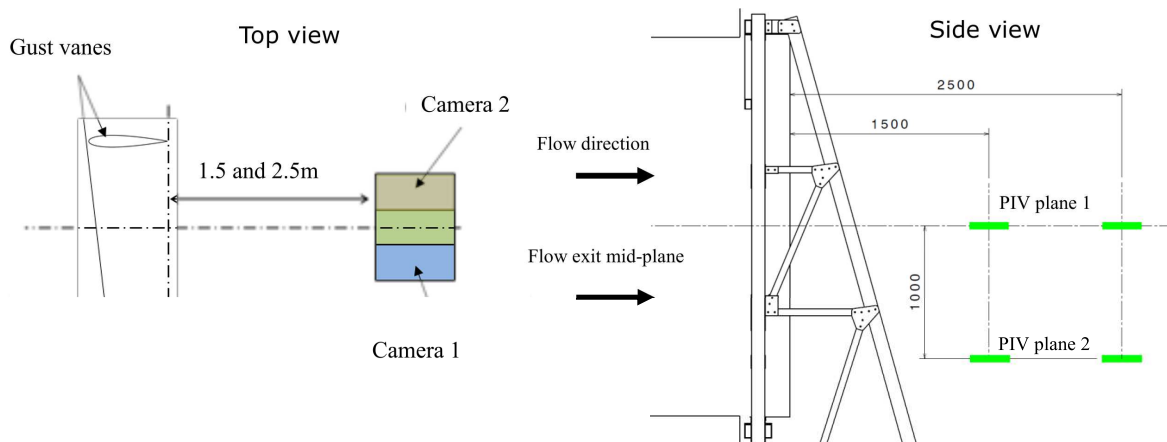
Figure 4.11: Measurement locations for the OJF gust generator. Adapted from Lancelot et al. (2017).

The test campaign firstly confirms the achievement of sinusoidal gusts at various reduced frequencies and a $1 - \cos$ gust is shown in Figure 4.12.
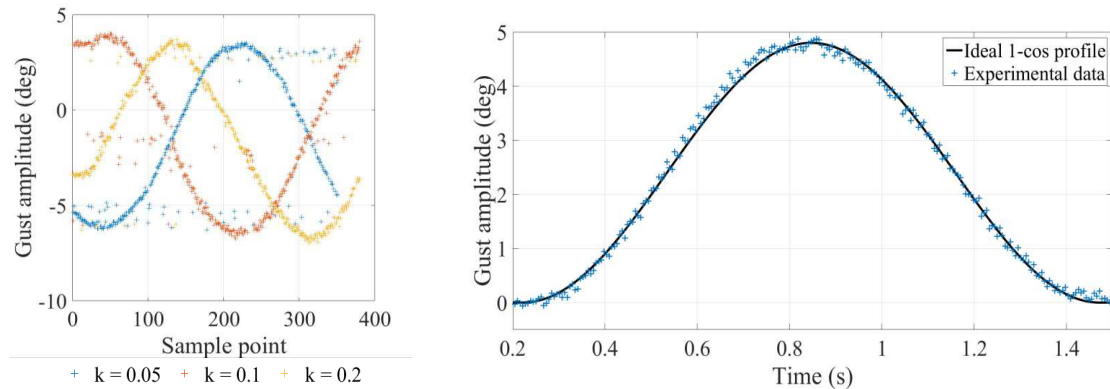
Figure 4.12: Left: sinusoidal gust expressed as gust angle in the horizontal plane for varying (k), right: $1-\cos$ gust expressed as gust angle in the horizontal plane for $k = 0.05$ [-]. Measurements conducted at $U_\infty = 15$ [ms^{-1}] and maximum gust vane pitching angle $\psi_{max} = \pm 10$ [°]. Adapted from Lancelot et al. (2017).

The horizontal homogeneity of the produced $1 - \cos$ gust is shown in Figure 4.13. Good homogeneity is recorded for the measured 200 [mm] span.
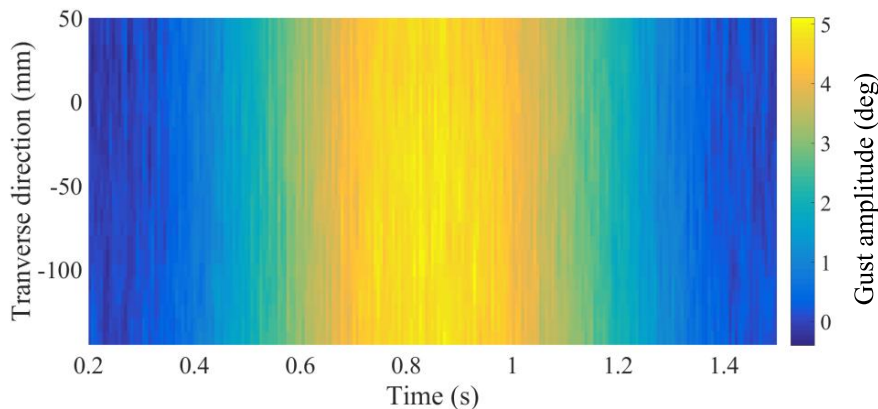
Figure 4.13: $1 - \cos$ gust expressed as gust angle in the horizontal plane for $k = 0.05$ [-], $U_\infty = 15$ [ms^{-1}], $\psi_{max} = \pm 10$ [°]. Measurements conducted along horizontal centre plane, with the transverse direction at 0 [mm] corresponding to the centre-line. 1.5 [m] downstream of the OJF nozzle. Adapted from Lancelot et al. (2017).

Finally, the influence of reduced frequency of oscillation (k), maximum vane pitching angle (ψ_{max}), downstream location and height are synthesised in Figure 4.14. The gust angle is not highly influenced by reduced frequency, which is also backed up by the conclusions drawn in Saddington et al. (2015). Furthermore, the two studies agree that gust angle mostly depends on the gust vane deflection angle (proportional). The downstream location of measuring affects the gust angle more at lower reduced frequencies. As the measuring plane approaches the tips of the gust vane (lower height) the gust angle decreases, which could be explained by 3D effects of the gust vanes. The trend with reduced frequency is however preserved.
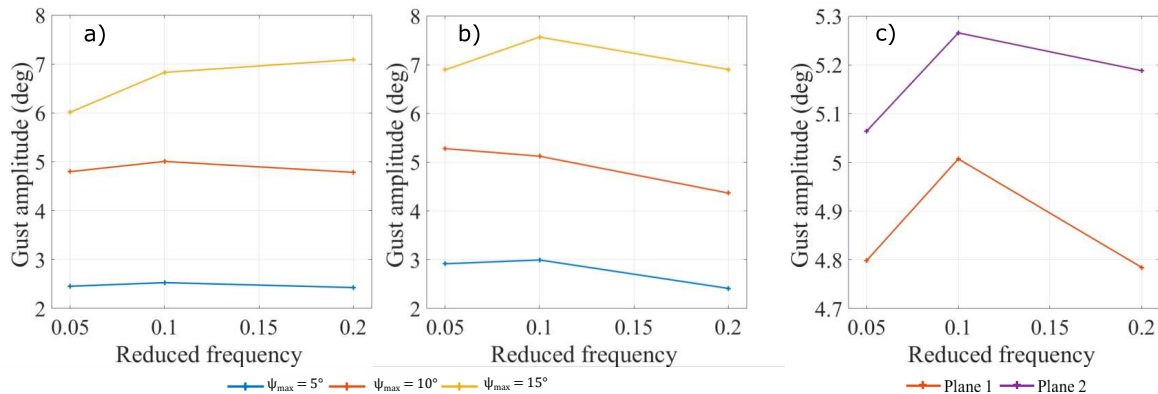
Figure 4.14: a) Gust angle for various (k) and (ψ_{max}) measured within plane 1 (Figure 4.11) at 1.5 $[m]$ downstream of the gust vanes, b) at 2.5 $[m]$ c) gust angle for various (k), $\psi_{max} = \pm 10$ [°] measured at plane 1 and 2. All measurements conducted at $U_\infty = 15$ [ms^{-1}]. Adapted from Lancelot et al. (2017).

4.5 Active Turbulence Grid

The concept of an active turbulence grid was first introduced by Makita. The original intent was realising better turbulence properties in the wind tunnel; large turbulent Reynolds numbers. Since, various changes have been implemented successfully Mydlarski (2017). Today, one state-of-the art active turbulent grid consists of 80 by 80 axes capable of individual actuation, resulting in a test section of 3×3 [m] and a mesh width of 0.14 [m] Kröger et al. (2018). Figure 4.15 shows the described facility.
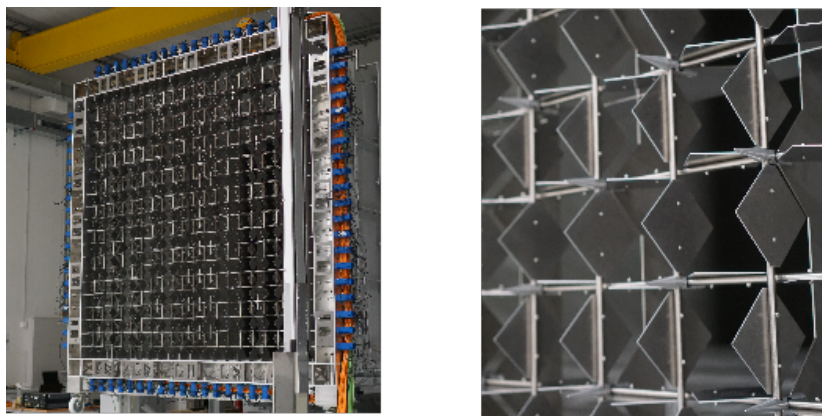
Figure 4.15: Active turbulence grid at the WindLab wind tunnel of the University of Oldenburg. Adapted from Kröger et al. (2018).

The grid is able to realise gusts from LiDAR measurements capturing the intermittent properties of the atmospheric flow. The grid's axes can be actuated independently and programmed via a so-called excitation protocol to produce desired flows. Two wind speed time series from

the Oldenburg facility are shown in Figure 4.16. Good repeatability of the experiment is seen. Furthermore, the gust generator achieves a similar wind speed time series compared to the ones measured at Thyborøn (Figure 3.24), however, with smaller deviations from the mean velocity; i.e. $\approx 20\%$
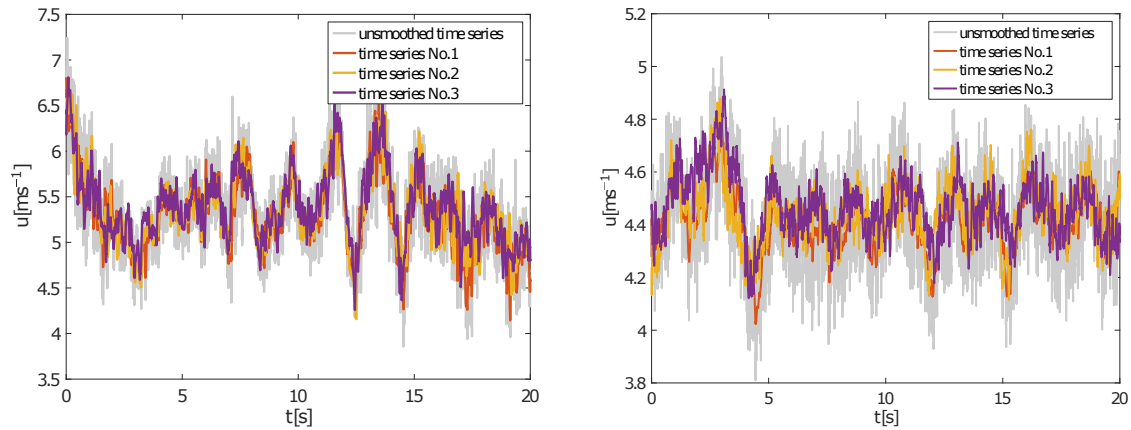
Figure 4.16: Left: wind speed time series generated using LiDAR excitation protocol, right: gust excitation protocol. Adapted from Kröger et al. (2018).

The study further tests the model TU Delft wind turbine ($D = 1.6$ [m]) under open grid (blockage of 21%) and under the LiDAR time series from Figure 4.16. The blade root bending moment of both blades are shown in Figure 4.17 for the controlled and uncontrolled wind turbine. No emphasis is placed on the control strategy, however, the author highlights the minimisation of root bending moments in the presence of the controlled wind turbine. Furthermore, the unsteady aerodynamic loads are clearly present and need to be mitigated to decrease fatigue. Additionally, the implementation of the suggested control strategy was enabled by the active grid configuration, the same intent of the undertaken thesis.
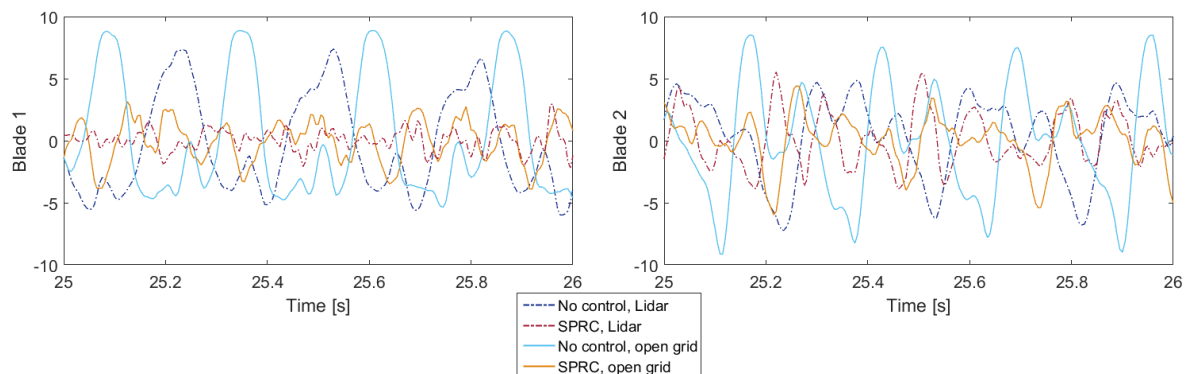
Figure 4.17: Blades root bending moment in presence and absence of control strategy. Adapted from Kröger et al. (2018).

Another recent application of the active turbulence grid was creating a sinusoidal gust similar to the ones described in Section 4.4 Cordes et al. (2018). The study focused on gust load

alleviation via adaptive camber of the 2D airfoil. The variation of the velocity vector due to the cyclic passage of the turbine blades through the ABL was related to the change in angle of attack of the 2D airfoil. This was translated to a sinusoidal wind gust in the wind tunnel. The achieved wind gust is shown in Figure 4.18.
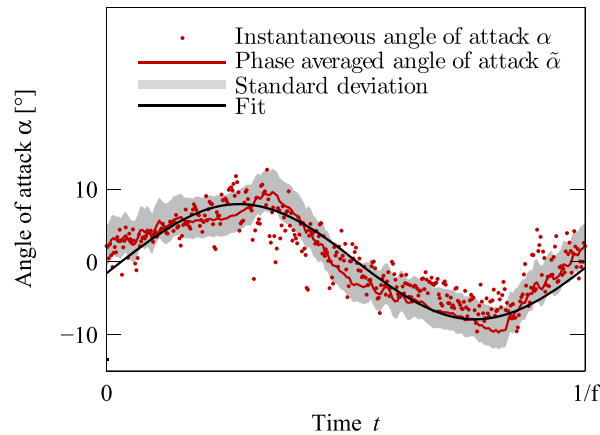
Figure 4.18: Sinusoidal wind gust expressed as flow angle of attack. Data measured by a hot-wire and phase-averaged. Adapted from Cordes et al. (2018).

4.6 Boundary Layer Wind Tunnels

Boundary layer wind tunnel are characterised by their extensive length. This is to allow a proper boundary layer to form in the presence of surface roughness Cal et al. (2010) or thermal stratification Ohya et al. (2008). The resulting inflow represents shear layers as found in the ABL. The author briefly will touch upon the topic. The description is not extensive since the undertaken thesis is to focus on OJF application. Such tunnels can adapt a combination of gust generators, such as surface roughness elements and an active turbulence grid to achieve the right atmospheric conditions Cal et al. (2010). An illustration of the used set-up as well as the achieved inflow profile is shown in Figure 4.19.
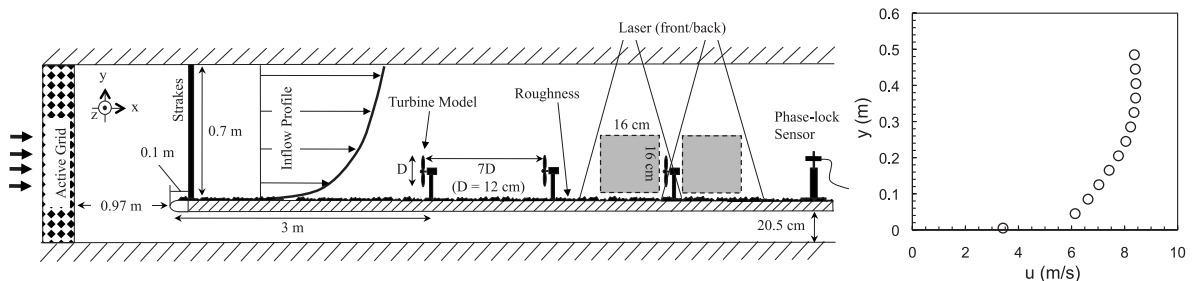
Figure 4.19: Illustration of test set-up from Cal et al. (2010) and achieved mean velocity profile at inflow.

A thermally stratified wind tunnel involves the surface being heated/cooled such that a desired temperature gradient is achieved. A SBL with a LLJ was created in such a wind tunnel. A schematic illustration is shown in Figure 4.20 together with the achieved mean velocity profile.
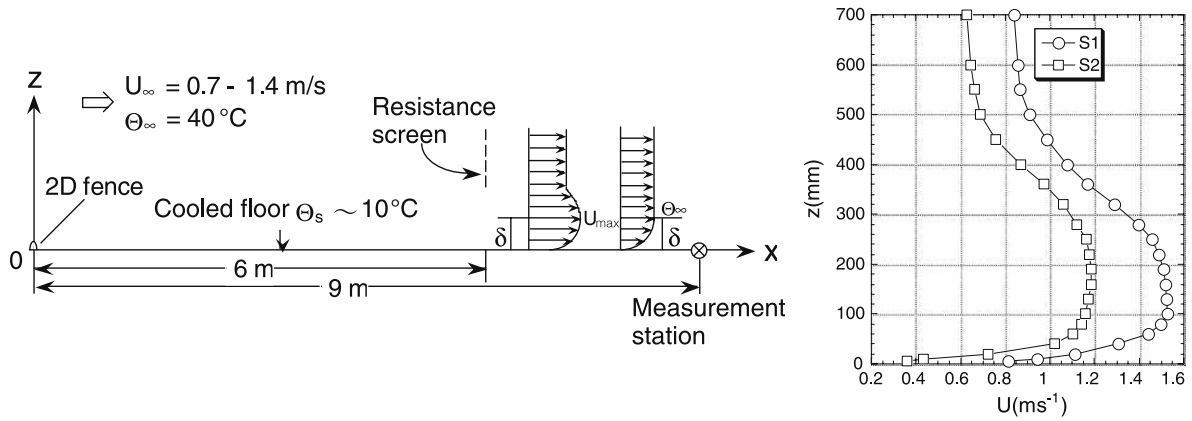
Figure 4.20: Illustration of test set-up from Ohya et al. (2008) and achieved mean velocity profile at inflow, showcasing a LLJ. S1/S2 correspond to two values of maxima.

Chapter 5

Flow Theory

This chapter will describe the theory required in carrying out the numerical simulations. The governing equations are derived and potential flow singularities used in flow models are presented in Section 5.1. Section 5.2 will discuss unsteady aerodynamics as well as provide analytical solutions for select airfoil motions.

5.1 Potential Flow Theory

Potential flow modelling together with boundary layer equations have been widely used in the design of low speed aerodynamic bodies Katz and Plotkin (2001). This is due to the low computational cost which allowed for fast optimisation problems. It is a powerful tool for preliminary insight of flow problems. The main assumptions of these models are:

1. Effects of viscosity are confined to the boundary layer and thin wakes and therefore the flow of interest is inviscid.

2. The flow is incompressible (low speed) and irrotational; vorticity is confined to the boundary layer and thin wakes.

With the above assumptions in mind, the derivation of inviscid, incompressible and irrotational flow is described. The derivation that follows will assume an Eulerian description and a Cartesian coordinate system. The differential conservation laws for mass and momentum are shown in (5.1) and (5.2) respectively.

$$\frac{D\rho}{Dt} + \rho \frac{\partial u_i}{\partial x_i} = 0 \quad i = 1, 2, 3 \tag{5.1}$$

$$\rho \left(\frac{\partial u_i}{\partial t} + u_j \frac{\partial u_i}{\partial x_j} \right) = \rho f_i - \frac{\partial}{\partial x_i} \left(p + \frac{2}{3} \mu \frac{\partial u_j}{\partial x_j} \right) + \frac{\partial}{\partial x_j} \mu \left(\frac{\partial u_i}{\partial x_j} + \frac{\partial u_j}{\partial x_i} \right) \quad i = 1, 2, 3 \quad (5.2)$$

For an incompressible flow, the density is constant in space and time. This leads to the first term of (5.1) to be dropped; i.e. $\frac{D\rho}{Dt} = 0$. The incompressible mass equation is then described by (5.3). Substituting this into (5.2) reduced the momentum equation to (5.4). Equations (5.3) and (5.4) are the governing over incompressible flows.

$$\frac{\partial u_i}{\partial x_i} = 0 \quad i = 1, 2, 3 \quad (5.3)$$

$$\rho \left(\frac{\partial u_i}{\partial t} + u_j \frac{\partial u_i}{\partial x_j} \right) = \rho f_i - \frac{\partial p}{\partial x_i} + \mu \frac{\partial^2 u_i}{\partial x_j^2} \quad i = 1, 2, 3 \quad (5.4)$$

A dimensional analysis can be conducted on (5.3) and (5.4) by non-dimensionalising the variables with characteristic quantities:

- Length Scale: L - chord length

- Reference speed: U - the free stream speed

- Characteristic time: T - time period of periodic processes, convection time past length scale; i.e. $\frac{1}{\omega}$ or $\frac{L}{U}$

- Reference pressure: p_0 - the free stream pressure

- Body forces: f_0 - Gravitational acceleration; i.e. g

The non-dimensional mass and momentum equations are then described by (5.5) and (5.6); with $*$ representing the non-dimentionalised variable.

$$\frac{\partial u_i^*}{\partial x_i^*} = 0 \quad i = 1, 2, 3 \quad (5.5)$$

$$\left(\frac{L}{TU} \right) \frac{\partial u_i^*}{\partial t^*} + u_j^* \frac{\partial u_i^*}{\partial x_j^*} = \left(\frac{L f_0}{U^2} \right) f_i^* - \left(\frac{p_0}{\rho U^2} \right) \frac{\partial p^*}{\partial x_i^*} + \left(\frac{\mu}{\rho U L} \right) \frac{\partial^2 u_i^*}{\partial x_j^{*2}} \quad i = 1, 2, 3 \quad (5.6)$$

Four non-dimensional parameters are identified:

1. $\frac{L}{TU}$: time constant or Strouhal number; $St = \frac{\omega L}{U}$, describing the importance of unsteadiness for a given flow.

2. $\frac{Lf_0}{U^2}$: body to inertial forces ratio or Froude number; $Fr = \frac{U}{\sqrt{Lf_0}}$, describing the importance of body forces for a given flow.

3. $\frac{p_0}{\rho U^2}$: pressure to inertial forces ratio or Euler number; $Eu = \frac{p_0}{\rho U^2}$, describing the dominances of the flow by pressure forces.

4. $\frac{\mu}{\rho UL}$: viscous to inertial forces ratio or inverse of Reynolds number; $Re = \frac{\rho u L}{\mu}$, describing the importance of viscosity for a given flow.

In the case of high Reynolds number flows, the viscous term in (5.4) can be neglected. It is noted however that in the region near solid boundaries, a strong shear layer develops where viscosity cannot be neglected. To account for this, an inner-outer layer methodology can be applied. This consists of describing the inner layer by simplified momentum conversation equations which assume axisymmetric and steady flow. Applying the latter assumptions to (5.4) leads to the boundary-layer equation (5.7).

$$\rho \left(u\frac{\partial u}{\partial x} + w\frac{\partial u}{\partial z} \right) = -\frac{\partial p}{\partial x} + \mu \frac{\partial^2 u}{\partial z^2} \tag{5.7}$$

At high Reynolds number the viscous term will have a small contribution in the outer region where the flow is mainly governed by inertial forces. Neglecting the viscous term in (5.4) leads to the governing equations for incompressible and inviscid flow; i.e. the Euler equations as shown by (5.8) and (5.9).

$$\frac{\partial u_i}{\partial x_i} = 0 \quad i = 1, 2, 3 \tag{5.8}$$

$$\frac{\partial u_i}{\partial t} + u_j \frac{\partial u_i}{\partial x_j} = f_i - \frac{\partial p}{\partial x_i} \quad i = 1, 2, 3 \tag{5.9}$$

The Euler equation is a first order differential equation requiring one velocity component at solid boundaries as boundary condition. To satisfy the no-slip condition, zero normal velocity is used. Prior to discussing the validity of the final assumption, irrotational flow, the vorticity is introduced as in (5.10).

$$\boldsymbol{\zeta} = \nabla \times \mathbf{u} \tag{5.10}$$

Next, the transport of vorticity equation for incompressible flows is sought. This is derived from (5.4) by taking the curl of the entire equation and applying the vector identity in (5.11), resulting in (5.12)

$$\mathbf{u} \cdot \nabla \mathbf{u} = \nabla \frac{||\mathbf{u}||^2}{2} - \mathbf{u} \times \boldsymbol{\zeta} \tag{5.11}$$

$$\frac{\partial \boldsymbol{\zeta}}{\partial t} - \nabla \times (\mathbf{u} \times \boldsymbol{\zeta}) = \nabla \times \mathbf{f} + \nu \nabla^2 \boldsymbol{\zeta} \tag{5.12}$$

Furthermore, rewriting using vector identity (5.13) and assuming body force are conservative; i.e. $\nabla \times \mathbf{f} = 0$ the rate of change of vorticity is obtained in (5.14).

$$\nabla \times (\mathbf{u} \times \boldsymbol{\zeta}) = \mathbf{u}\nabla \cdot \boldsymbol{\zeta} - \mathbf{u} \cdot \nabla \boldsymbol{\zeta} + \boldsymbol{\zeta} \cdot \nabla \mathbf{u} - \boldsymbol{\zeta}\nabla \cdot \mathbf{u} \tag{5.13}$$

$$\frac{D\boldsymbol{\zeta}}{Dt} = \frac{\partial \boldsymbol{\zeta}}{\partial t} + \mathbf{u} \cdot \nabla \boldsymbol{\zeta} = \boldsymbol{\zeta} \cdot \nabla \mathbf{u} + \nu \nabla^2 \boldsymbol{\zeta} \tag{5.14}$$

A similar dimensional analysis as performed on the conservation of momentum equations can be carried out on Equation 5.14. In the limit of high Reynolds number, the rate of change of vorticity reduces to (5.15), governing the vorticity for incompressible, inviscid flows. This states that the time rate of change of vorticity is equal to the change in vorticity due to stretching and tilting of existing vortex filaments in the flow field.

$$\frac{D\boldsymbol{\zeta}}{Dt} = \boldsymbol{\zeta} \cdot \nabla \mathbf{u} \tag{5.15}$$

The assumption of irrotational flow derives from the assuming inviscid flow. In Figure 5.1, two fluid motions are shown. For large viscous forces, the neighbouring fluid particles exert shear force on the fluid particle considered, causing it to rotate as it follows its path. However, as shown in Figure 5.1-b, if the viscous forces are negligible the fluid particle will continue its path without feeling any shear forces and thus will not rotate. It is noted that vorticity is still generated and confined near solid boundaries and in thin wakes Katz and Plotkin (2001). Given the flow is irrotational; i.e. $\boldsymbol{\zeta} = \mathbf{0}$, reduces (5.10) to (5.16).
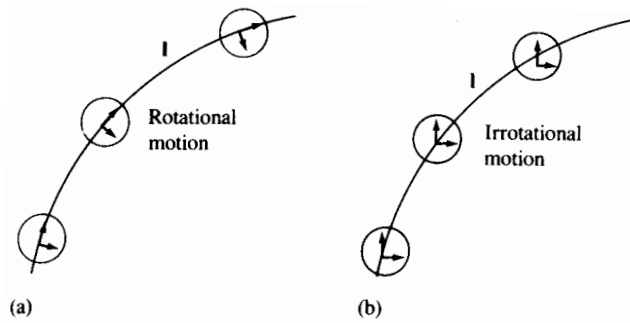
Figure 5.1: Schematic of rotational and irrotational flow. Adapted from Katz and Plotkin (2001)

$$\frac{\partial w}{\partial y} = \frac{\partial v}{\partial z} \quad \frac{\partial u}{\partial z} = \frac{\partial w}{\partial x} \quad \frac{\partial v}{\partial x} = \frac{\partial u}{\partial y} \tag{5.16}$$

A final step in deriving the governing equation for potential flow is introducing circulation. The definition of circulation derives from applying Stokes' theorem to a surface of vorticity. The general 3D case is showcased in Equation 5.17.

$$\Gamma = \oint_C \mathbf{u} \cdot d\mathbf{l} = \int_S \nabla \times \mathbf{u} \cdot \mathbf{n} dS = \int_S \boldsymbol{\zeta} \cdot \mathbf{n} dS \tag{5.17}$$

Given that the flow is irrotational; i.e. (5.16) applies, the line integral from (5.17) equals:

$$\int_C \mathbf{u} \cdot d\mathbf{l} = \int_C u dx + v dy + w dz$$

The integrand is an exact differential of a potential independent of the path of integration. The velocity potential can then be introduced (Φ) as a function of a point in space:

$$\Phi(x, y, z) = \int_{P_0}^{P} u dx + v dy + w dz \tag{5.18}$$

The velocity can then be obtained from its gradient:

$$\mathbf{u} = \nabla \Phi \tag{5.19}$$

Plugging (5.19) into the continuity equation results in the Laplace equation (5.20). This can be solved for known boundary conditions resulting in a known velocity potential. The pressure is then obtained from the unsteady Bernoulli equation (5.21).

$$\nabla \cdot (\nabla \Phi) = \nabla^2 \Phi = 0 \tag{5.20}$$

$$\frac{p_\infty - p}{\rho} = \frac{u^2}{2} - \frac{U_\infty^2}{2} + \frac{\partial \Phi}{\partial t} \tag{5.21}$$

The Laplace Equation is governing to incompressible, inviscid, irrotational flows. An additional consideration is made; i.e. the rate of change of circulation in the flow domain. Taking the time rate of change of Equation 5.17 and applying the chain rule results in:

$$\frac{D\Gamma}{Dt} = \frac{D}{Dt} \oint_C \mathbf{u} \cdot d\mathbf{l} = \oint_C \frac{D\mathbf{u}}{Dt} \cdot d\mathbf{l} + \oint_C \mathbf{u} \cdot \frac{D}{Dt} d\mathbf{l} \tag{5.22}$$

The integrals are taken around a fluid curve; i.e. the substantial derivative of the velocity field is equal to the acceleration, $\frac{D\mathbf{u}}{Dt} = \mathbf{a}$ and $\frac{D}{Dt}d\mathbf{l} = d\mathbf{u}$. This leads to:

$$\frac{D\Gamma}{Dt} = \oint_C \mathbf{a} \cdot d\mathbf{l} + \oint_C \mathbf{u} \cdot d\mathbf{u} = \oint_C \left(-\nabla\left(\frac{p}{\rho}\right) + \mathbf{f} \right) \cdot d\mathbf{l} + 0$$

The first term is obtained from Equation 5.9, representing the acceleration along a closed fluid curve. The second term is identical to zero; closed integral of an exact differential that is only a function of coordinates and time. Furthermore, considering a conservative force and that the integral of a perfect differential ($\oint_C d\left(\frac{p}{\rho}\right)$) is zero it is obtained that the circulation of a fluid curve remains constant in time. An elegant way of stating the above is Kelvin's theorem: "*the time rate of change of circulation around a closed curve consisting of the same fluid elements is zero*" Katz and Plotkin (2001). However, an airfoil suddenly set into motion, will develop a circulation around it. To comply with Kelvin's theorem an equal and opposite circulation must exist such that the net value is zero; i.e. a wake forms with circulation in the opposite direction. This translates to Equations 5.23:

$$\frac{D\Gamma}{Dt} = \frac{\Gamma_{airfoil} + \Gamma_{wake}}{\Delta t} = 0 \tag{5.23}$$

The assumption of body force being conservative has been used throughout literature and has no precise definition besides that its curl is null. The derivation of (5.15) has been approached differently by van Kuik using the following definition van Kuik (2018):

"*A force field distribution integrated on a surface S or a volume V with finite dimensions is non-conservative when it releases vorticity into the flow. It is conservative when this is not done. In an inertial frame of reference non-conservative forces perform work, while conservative forces act perpendicular to the local velocity vector, so do not perform work.*"

Retaining the curl of the force in (5.12), omitting viscosity and rewriting one obtains (5.24).

$$\frac{1}{\rho}\boldsymbol{\nabla} \times \boldsymbol{f} = \frac{D\boldsymbol{\zeta}}{Dt} - (\boldsymbol{\zeta} \cdot \nabla)\boldsymbol{u} \tag{5.24}$$

When the force field is distributed on a surface across a thickness (ϵ), the integration of (5.24) while taking the limit $\epsilon \to 0$ results in (5.25), where ($\mathbf{F}$) is the force field acting on the fluid and (γ) is the vortex sheet strength across the distribution of ($\mathbf{f}$).

$$\frac{1}{\rho}\boldsymbol{\nabla} \times \boldsymbol{F} = \frac{D\boldsymbol{\gamma}}{Dt} - (\gamma \cdot \boldsymbol{\nabla})\boldsymbol{u} \tag{5.25}$$

For the 2D case the closed curve integral left hand side vanishes and thus no vorticity is produced by the force field, therefore, by the above definition the force field of a 2D airfoil

is conservative. For the 3D case, the closed curve integral left hand side is not zero due to presence of spanwise force gradients in a lifting surface; i.e. such as effects of tip vortices, sweep. Therefore, force field of a 3D lifting surface is not conservative by the above definition. However, when taking the surface integral of the left hand side over the entire lifting surface it is equal to zero, implying no net vorticity is produced. Considering this, and the fact that the force field of a 3D lifting surface is non-conservative, it can be explained that locally a lifting surface produces vorticity while at a different location an equal and opposite in sign amount of vorticity is produced. Resulting in zero net vorticity over the entire surface. The above result will be used to model the generation of vorticity in wakes. The model approaches this by concentrating vorticity to a thin vortex sheet. The vortex sheet can be represented by various potential flow singularities as introduced in the following section.

5.1.1 Flow Singularities

The flow field can be modelled by various singularities that have an induced velocity effect. From potential flow, one can compute the induced velocity at arbitrary points. The singularities can be, sources/sinks, doublets and vortex filaments. Additionally, other structures can be formed from vortex filaments, such as vortex rings or horse shoe vortices. Given the principle of superposition, the solution of the velocity potential of singularities can be superimposed resulting in complex flow fields described by a linear combination of each singularity's velocity potential. This section will describe the flow field of the three main singularities.

Source/Sink

Trivially, a source/sink radiates in all directions. Its influence decreases with the inverse of squared distance to its centre. The derivation of the velocity potential solution is outside the scope of this thesis and is omitted. Interested readers are referred to (Katz and Plotkin, 2001, Section 3.4). Given the source strength (σ), the induced velocity by a source/sink at a point ($\mathbf{x}_0$) is given by (5.26).

$$
\begin{aligned}
u(x,y,z) &= \frac{\sigma\,(x - x_0)}{4\pi \left[(x - x_0)^2 + (y - y_0)^2 + (z - z_0)^2 \right]^{3/2}} \\[2mm]
v(x,y,z) &= \frac{\sigma\,(y - y_0)}{4\pi \left[(x - x_0)^2 + (y - y_0)^2 + (z - z_0)^2 \right]^{3/2}} \\[2mm]
w(x,y,z) &= \frac{\sigma\,(z - z_0)}{4\pi \left[(x - x_0)^2 + (y - y_0)^2 + (z - z_0)^2 \right]^{3/2}}
\end{aligned}
\tag{5.26}
$$

Doublet

The doubles is formed of a sink and a source. The derivation of the induced flow field due to a doublet can be found in (Katz and Plotkin, 2001, Section 3.5). Given a doublet strength (μ), the induced velocity field at $(\mathbf{x}_0)$ is given by (5.27).

$$
\begin{aligned}
u(x, y, z) &= -\frac{\mu}{4\pi} \frac{(y - y_0)^2 + (z - z_0)^2 - 2(x - x_0)^2}{\left[(x - x_0)^2 + (y - y_0)^2 + (z - z_0)^2\right]^{5/2}} \\
v(x, y, z) &= \frac{3\mu}{4\pi} \frac{(x - x_0)(y - y_0)}{\left[(x - x_0)^2 + (y - y_0)^2 + (z - z_0)^2\right]^{5/2}} \\
w(x, y, z) &= \frac{3\mu}{4\pi} \frac{(x - x_0)(z - z_0)}{\left[(x - x_0)^2 + (y - y_0)^2 + (z - z_0)^2\right]^{5/2}}
\end{aligned}
\tag{5.27}
$$

Vortex Filament

A vortex filament can be prescribed a certain circulation (Γ), which, affects the magnitude of induced velocity $(\mathbf{u}_{induced})$. This is shown schematically in Figure 5.2.
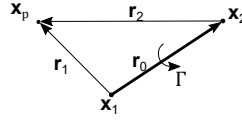
Figure 5.2: Vortex filament nomenclature in 3D space. Vectors $(\mathbf{x})$ depict position vectors.

The induced velocity by a vortex filament segment 1,2 of constant circulation can be derived from the Biot-Savart law (5.28). Discretely, this is shown by Equation 5.29, where $(\mathbf{r}_1)$, $(\mathbf{r}_2)$ are the vectors from the ends of the vortex filament to the point of interest and $(\mathbf{r}_0)$ is the vector from the start of the filament (pt. 1) to its end (pt. 2).

$$
\mathbf{u}_{induced} = \frac{\Gamma}{4\pi} \int \frac{d\mathbf{l} \times (\mathbf{r}_0 - \mathbf{r}_1)}{|\mathbf{r}_0 - \mathbf{r}_1|^3}
\tag{5.28}
$$

$$
\mathbf{u}_{induced 1,2} = \frac{\Gamma}{4\pi} \frac{\mathbf{r}_1 \times \mathbf{r}_2}{|\mathbf{r}_1 \times \mathbf{r}_2|^2} \mathbf{r}_0 \cdot \left(\frac{\mathbf{r}_1}{|\mathbf{r}_1|} - \frac{\mathbf{r}_2}{|\mathbf{r}_2|} \right)
\tag{5.29}
$$

Note is made that Equation 5.29 has a singular behaviour as $(\mathbf{r}_1)$, $(\mathbf{r}_2)$ or $(\mathbf{r}_1 \times \mathbf{r}_2)$ approach zero; i.e. as the sampling point gets closer to the vortex filament. A simple way of resolving this behaviour is to impose zero induced velocity past a certain threshold. This however does lead to non-smooth behaviour, particularly when unsteady algorithms are implemented with small time steps, resulting in vortex filaments stretching excessively. Many smoothing

techniques have been developed in addition to the former Sarpkaya (1989). A relatively simple method is modelling the vortex core by solid rotation. This means, that at a certain distance from the vortex filament, a vortex core radius is defined, inside which, the induced velocity is governed by solid rotation principle; i.e. the induced velocity would drop linearly to zero at the vortex filament. This is depicted in Figure 5.3. Equation 5.30 incorporates this numerically.
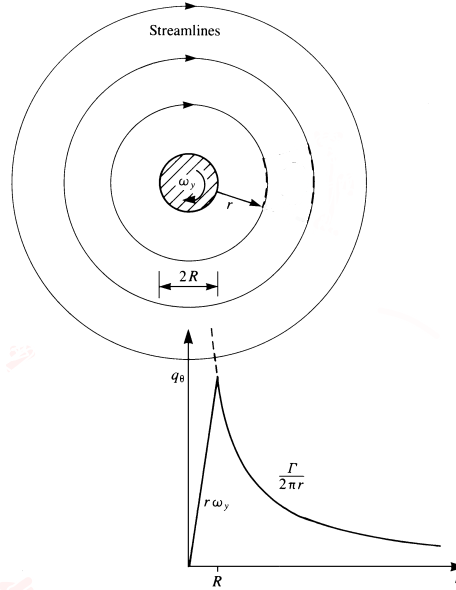
Figure 5.3: Vortex core modelled by solid body rotation. Adapted from Katz and Plotkin (2001).

$$
\mathbf{u}_{induced1,2} = \begin{cases} \frac{\Gamma}{4\pi} \frac{\mathbf{r}_1 \times \mathbf{r}_2}{|\mathbf{r}_1 \times \mathbf{r}_2|^2} \mathbf{r}_0 \cdot \left(\frac{\mathbf{r}_1}{|\mathbf{r}_1|} - \frac{\mathbf{r}_2}{|\mathbf{r}_2|} \right) & \mathbf{r}_1, \mathbf{r}_2, \mathbf{r}_1 \times \mathbf{r}_2 > R \\ \frac{\Gamma}{4\pi} \frac{\mathbf{r}_1 \times \mathbf{r}_2}{R^2 |\mathbf{r}_0|^2} \mathbf{r}_0 \cdot \left(\frac{\mathbf{r}_1}{|\mathbf{r}_1|} - \frac{\mathbf{r}_2}{|\mathbf{r}_2|} \right) & \mathbf{r}_1, \mathbf{r}_2, \mathbf{r}_1 \times \mathbf{r}_2 \leq R \end{cases} \tag{5.30}
$$

Figure 5.4 shows this behaviour for various core radii, for a 1 $[m]$ long filament with unit circulation placed along the z-axis. The velocity in the y-direction is sampled along the x-axis.
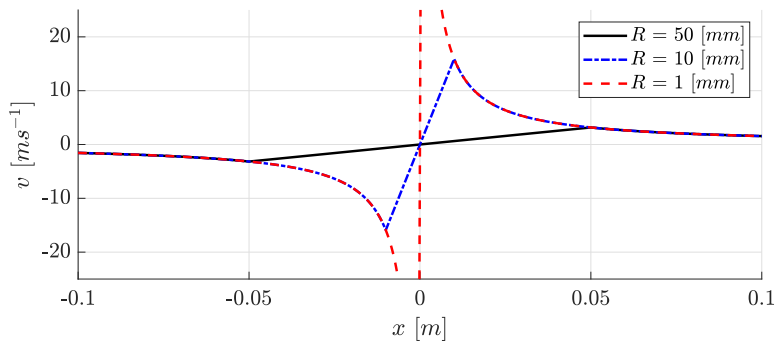
Figure 5.4: The velocity in the y-direction induced due to a vortex filament along the z-axis with unit circulation and vortex core size of 1, 10, and 50 $[mm]$.

A system of linear equations can be set up to produce a desired velocity field, which can be spatially and temporally variant. Furthermore, a free vortex methodology can be implemented, which at each time step updates the location of the vortex filaments which are convected by the flow field. This allows to view the spacial time evolution of wakes and jets Katz and Plotkin (2001). Note is made that the Kutta condition shall be satisfied at the trailing edge; the shed vortex emanates parallel to the trailing edge. Additionally, considerations to Helmholtz theorems should be made Katz and Plotkin (2001):

1. *"The strength of a vortex filament is constant along its length."*

2. *"A vortex filament cannot start or end in a fluid; it should form a closed path or extend to infinity."*

3. *"The fluid that forms a vortex tube continues to form a vortex tube and the strength of the vortex tube remains constant as the tube convects. Therefore, vortex elements such as lines, rings will remain vortex elements in time."*

5.2   Unsteady Aerodynamics

The topic of unsteady aerodynamics is key to the thesis at hand due to the need of modelling the flow field generated by pitching vanes; i.e. the gust generator. The flow is modelled numerically through the method of unsteady lifting-surface represented by vortex rings. Considerations from Section 5.1 are part of the model, such as implementing flow singularities in modelling solid walls and shedding trailing vorticity into the flow domain by means of a vortex sheet. This section will discuss two key airfoil unsteady motions and their corresponding analytical solutions.

5.2.1   Step Change in Angle of Attack

The step change in angle of attack is described such that:

$$\alpha = \left\{ \begin{array}{cc} 0 & t < 0 \\ const. & t \geq 0 \end{array} \right.$$

At $t = 0$ a wake forms and convects downstream. The lift coefficient of the airfoil is transient and reaches a steady value in the limit $t \to \infty$. The transient response of the lift coefficient is given by (5.31). The Wagner function is described by $(\phi(s))$, which takes as argument (s); the distance travelled by the airfoil in semi-chords. The first term represents the added mass contribution, while the second term is a result of circulatory effects caused by the shedding of the wake. The Wagner term can be obtained analytically or numerically from the Duhamel integral resulting from setting up the equation. This can be cumbersome and it is common to

use approximations for the function, which are within 1% accuracy Gordon Leishman (2006).
A common approximation by R.T. Jones is shown in (5.32).

$$C_l(t) = \frac{\pi c}{2U_\infty}\delta(t) + 2\pi\alpha\phi(s) \tag{5.31}$$

$$\phi(s) \approx 1.0 - 0.165e^{-0.0455s} - 0.335e^{-0.3s} \qquad s = \frac{2U_\infty t}{c} \tag{5.32}$$

5.2.2 Sinusoidal Pitching

The sinusoidal pitching motion of an airfoil results in a phase shift of the lift coefficient from
the steady state case. The motion is described by (5.33). Theodorsen provides an analytical
solution to the problem as a function of reduced frequency of the oscillation motion. The lift
coefficient is described by (5.34) Gordon Leishman (2006).

$$\begin{aligned}\alpha &= \bar{\alpha}\sin(\omega t) \\ \dot{\alpha} &= \omega\bar{\alpha}\cos(\omega t) \\ \ddot{\alpha} &= -\omega^2\bar{\alpha}\sin(\omega t)\end{aligned} \tag{5.33}$$

$$C_l = \pi b\left(\frac{\dot{\alpha}}{U_\infty} + \frac{\ddot{h}}{U_\infty^2} - \frac{ba\ddot{\alpha}}{U_\infty^2}\right) + 2\pi C(k)\left[\frac{h}{U_\infty} + \alpha + b\left(\frac{1}{2} - a\right)\frac{\dot{\alpha}}{U_\infty}\right] \tag{5.34}$$

Here, (b) is the semi-chord, (a) is the pitching axis relative to the mid-chord expressed in
semi-chord lengths, $\alpha, \dot{\alpha}, \ddot{\alpha}$ are the angle of attack, pitching speed and acceleration and $h, \dot{h}, \ddot{h}$
are the plunge distance, speed and acceleration. Considering a purely oscillatory motion, the
expression reduces to (5.35).

$$C_l = \pi b\left(\frac{\dot{\alpha}}{U_\infty} - \frac{ba\ddot{\alpha}}{U_\infty^2}\right) + 2\pi C(k)\left[\alpha + b\left(\frac{1}{2} - a\right)\frac{\dot{\alpha}}{U_\infty}\right] \tag{5.35}$$

The first term describes non-circulatory effects; i.e. the apparent mass effect. The second
term describes circulatory effects arising from the influence of the shed wake on the unsteady
aerodynamic loads. The Theodorsen function $(C(k))$ is described in (5.36), where the Hankel
functions H are given by Bessel functions of the first (J_v) and second (Y_v) kind; i.e. $H_v^{(2)} = J_v - iY_v$

$$C(k) = F(k) + iG(k) = \frac{H_1^{(2)}(k)}{H_1^{(2)}(k) + iH_0^{(2)}(k)} \tag{5.36}$$

Chapter 6

Model Analysis

The developed model is subjected to a verification, convergence and sensitivity analysis. The interested reader can find the verification procedure in Appendix A. A list of model inputs are provided in Table 6.1. The analysis is split into two parts; a convergence study on the model parameters and sensitivity analysis on the vane parameters. The convergence study is carried out on the panel resolution, vortex core size, time step and free wake length as presented in Section 6.1. Subsequently, the sensitivity analysis is carried out on the vane's chord length, spacing, reduced frequency of oscillation and maximum pitching angle. This is documented in Section 6.2, where results generated by the developed model are compared to numerical results (CFD) from Lancelot et al. (2015).

Table 6.1: List of inputs to the developed model and considered range for the convergence and sensitivity analysis.

Input	Description	Range
N	Panel resolution in spanwise direction	10, 20, 30, 40 $[-]$
M	Panel resolution in chordwise direction	4, 8, 16, 24 $[-]$
R	Vortex core size	0.001 0.005 0.01 $[m]$
Δt	Time step	$\frac{c}{2U_\infty}$, $\frac{c}{4U_\infty}$, $\frac{c}{8U_\infty}$, $\frac{c}{16U_\infty}$ $[s]$
Wake	Free wake length	$b/2$, b, $2b$ $[m]$
c	Vane chord length	0.2, 0.3, 0.4 $[m]$
dh	Vanes spacing	0.3, 0.5, 0.7 $[m]$
k	Reduced frequency of pitching motion	0.0377, 0.1131, 0.1885 $[-]$
ψ_{max}	Maximum pitching angle	2.5, 5, 10 $[°]$

6.1 Convergence Study

A convergence study is carried out to determine panel mesh independency, vortex core size, length of the free wake (the near region) and the appropriate time step. The analysis is

carried out with a single and dual vertical vanes configurations. Three motions are employed; step in pitch angle, ramp up and hold, sinusoidal motion ($k = 0.13 \; [-]$) as depicted in Figures 6.1 and 6.2 respectively. The step in pitch angle was simulated for $0.5 \; [s]$, while the ramp and sinusoidal motions had a duration of $1 \; [s]$. The tested combinations (number of vanes and vane motion) are summarised in Table 6.2. The free stream speed is set to $15 \; [ms^{-1}]$, corresponding to $Re = 296,833 \; [-]$. The chord and span of the vane were 0.3 and $2.7 \; [m]$ respectively; representing 95% of the nozzle height. This is done such that the tip vortices of the vane do not interact with the vortex filament elements representing the jet flow of the OJF. Figures 6.3 and 6.4 depict the vane set-ups of the tested configurations relative to the OJF nozzle. The free stream direction is out of the page, and the sign of the pitching angle is given by the right hand rule with axis pointing in the z-direction (vertical). This results in a negative lift coefficient for a positive pitch angle. The lift coefficient is described by (6.1). The end of the section summarises the findings as model parameter recommendations in Table 6.8.
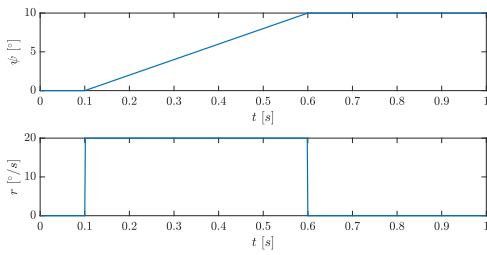
Figure 6.1: Pitching angle and angular speed as function of time for the ramp up and hold pitching motion: $\psi_{max} = 10 \; [°]$ and $r = 20 \; [°s^{-1}]$.
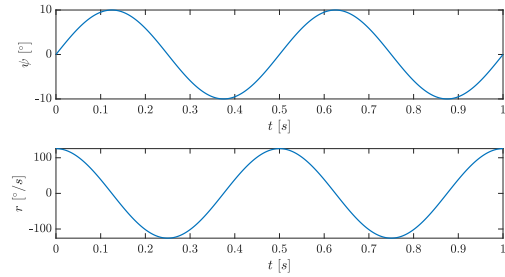
Figure 6.2: Pitching angle and angular speed as function of time for the sinusoidal motion: $\psi_{max} = 10 \; [°]$, $\omega = 4\pi \; [rads^{-1}]$; i.e. $\psi(t) = 10\sin(4\pi t) \; [°]$.
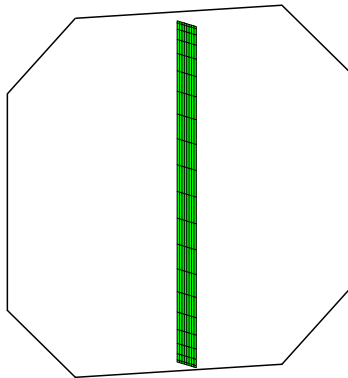
Figure 6.3: Single vane configuration. Mid span LE at nozzle centreline.
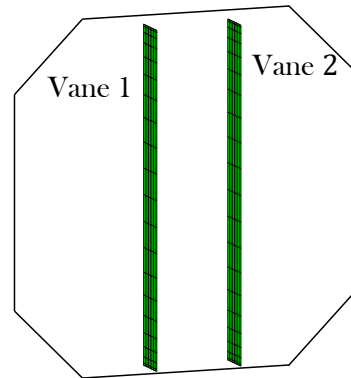
Figure 6.4: Two vanes configuration. Vanes about the centre line, spaced $0.7 \; [m]$ apart.

Table 6.2: Convergence study cases description.

Parameter	Vanes	Motion
N, M	1	**step** ($\psi = 10$ [°]), **sin** ($\psi(t) = 10\sin(4\pi t)$ [°])
R	1	**step** ($\psi = 10$ [°])
Δt	1	**ramp** ($\psi_{max} = 10$ [°], $r = 20$ [°s^{-1}]) , **sin** ($\psi(t) = 10\sin(4\pi t)$ [°])
Wake	1, 2	**step** ($\psi = 10$ [°]), **sin** ($\psi(t) = 10\sin(4\pi t)$ [°])

$$C_L = \frac{F_Y}{0.5\rho U_\infty^2 S} \tag{6.1}$$

6.1.1 Panel Resolution

The resolution of the panels is tested for three levels; coarse ($N = 10$, $M = 4$), medium ($N = 20$, $M = 8$) and fine ($N = 30$, $M = 16$). The vortex core size is set to 0.005 [m]. The wake is allowed to deform freely. The lift coefficient of the vane and the flow field velocity components at $\mathbf{x} = (1.5, 0, 0)$ [m] are monitored. The vertical velocity component is omitted since its equal to zero at the centreline.

Single Vane, Step Motion:

A step change in angle of attack is simulated. This is described by the vane being at zero angle of attack for $t < 0$. At $t = 0$ the angle of attack, i.e. pitch angle is set to 10 [°]. The time step is set to $\Delta t = \frac{c}{4U_\infty} = 0.005$ [s]. Although a positive pitch angle results in a negative lift coefficient, the result is inverted for easier interpretation. The simulations are terminated when the lift coefficient reaches a steady value to two decimal places. This behaviour is seen due to the growth of the wake and should provide an indication of the appropriate wake length. The mentioned consideration resulted in a simulation time of ≈ 0.5 [s]. The results are shown in Figure 6.5. The mid span wake sheet line at the end of the simulation is shown in Figure 6.6. The analytical solution for a step change in angle of attack of an airfoil by Wagner is overlaid for comparison Gordon Leishman (2006). The 2D lift coefficient is scaled by the DATCOM method to match the 3D wing with $AR = 9$ [$-$]. A number of observation are pointed out:

1. As the panel resolution is refined, the increase of (C_L) with wake growth is more gradual. The fine panel resolution initial loading is equal to half of its final value as predicted by Wager's function.

2. The (C_L) converges towards one value as the mesh is refined, however, with minor differences, indicating that the selected panel resolutions are adequate for computation of steady vane forces. However, the coarse panel resolution shows a very flat asymptotic behaviour of the loading as the simulation progresses.

3. As consequence of initial wake shedding and roll up, a kink can be identified in the velocity components, past which, a steady value is reached. The kink corresponds to the convection time of the wake from the TE of the vane to the monitor point; i.e. $\approx \frac{1.5-0.3}{U_\infty} = \frac{1.2}{15} = 0.08$ [s]. As the wake roll-up moves past the monitor point, the flow reaches its steady state. To illustrate this, the instantaneous wake at $t = 0.07$ and $t = 0.10$ is shown Figure 6.7. The lowest peak of (u) corresponds to $t = 0.07$ [s]. At this instant in time, the wake is upstream of the monitor point, and has rolled up. After the rolled up wake passes the monitor point and convects downstream, the velocity recovers to free stream value as seen by the position of the wake at $t = 0.10$ [s]. A similar behaviour is seen in the (v) component. This behaviour is further shown by the corresponding instantaneous velocity components contours in the xy-plane shown in Figures 6.8 and 6.9. The schematic of vane and wake circulation are overlaid on the horizontal velocity contours.

4. The wake shape is maintained the same in the near region, corresponding to the lift coefficient converging relatively close for the three selected panel resolutions. The finer panel resolution shows a better wake roll, explaining the more gradual increase of (C_L) for the finer panel resolution.
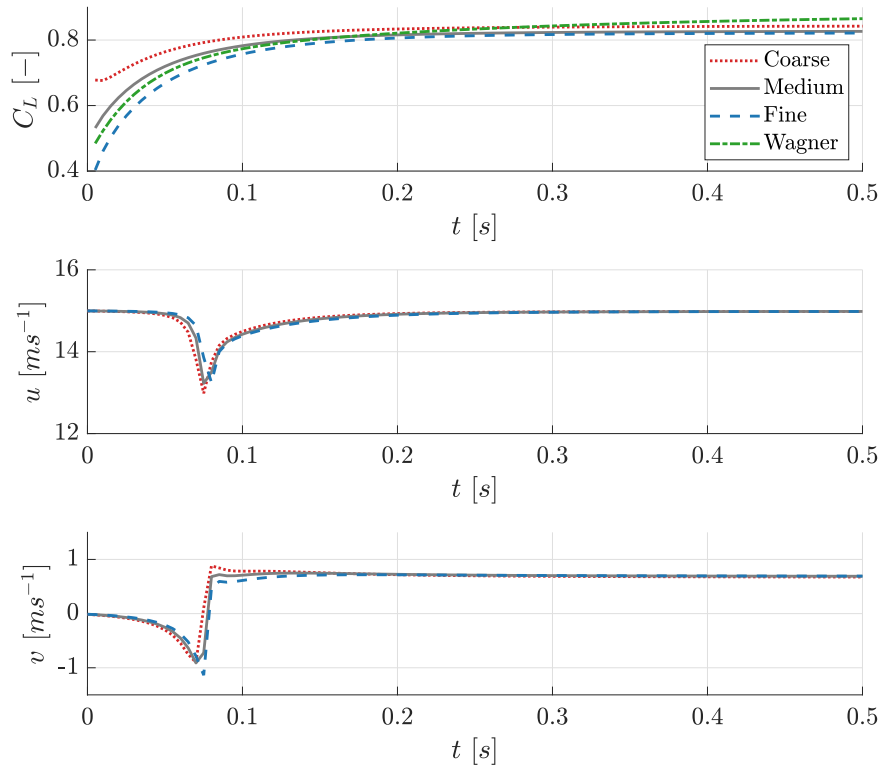
Figure 6.5: Lift coefficient and flow field velocity components at $\mathbf{x} = (1.5, 0, 0)$ [m] for various panel resolutions; coarse: $N = 10$, $M = 4$, medium: $N = 20$, $M = 8$, fine: $N = 30$, $M = 16$. Simulation carried out with a single vane with $c = 0.3$ [m], $b = 2.7$ [m], $U_\infty = 15$ [ms^{-1}], $\psi = 10$ [°].
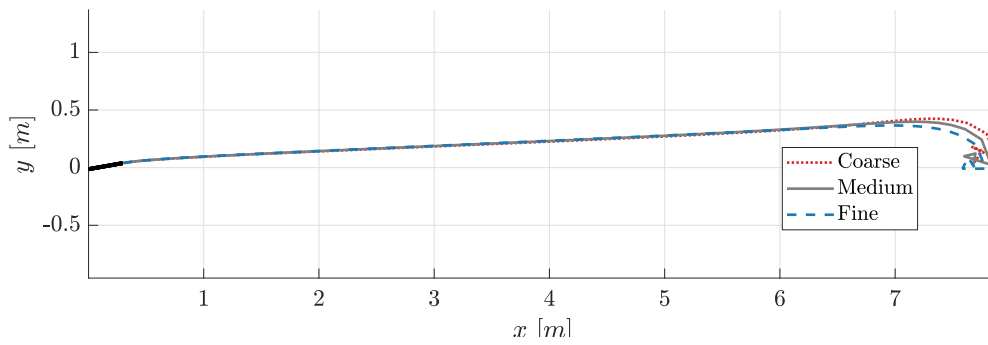
Figure 6.6: Corresponding mid span wake sheet lines for the results shown in Figure 6.5.
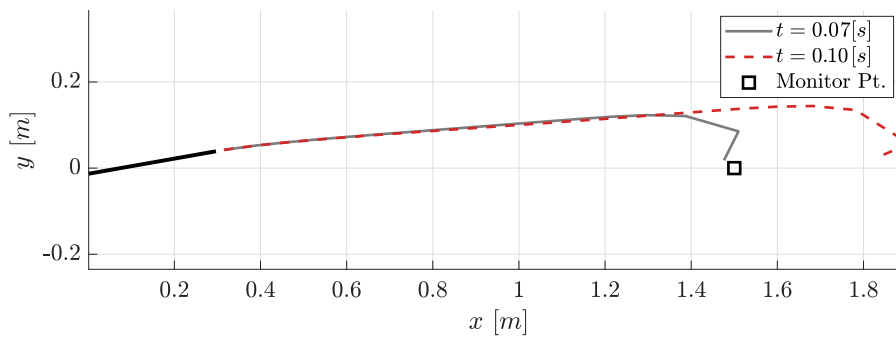
Figure 6.7: Instantaneous mid span wake sheet lines for the results shown in Figure 6.5 at $t = 0.07$ $[s]$ and $t = 0.10$ $[s]$. Black square shows the location of the monitor point where the velocity components were sampled. Results shown for a coarse mesh.
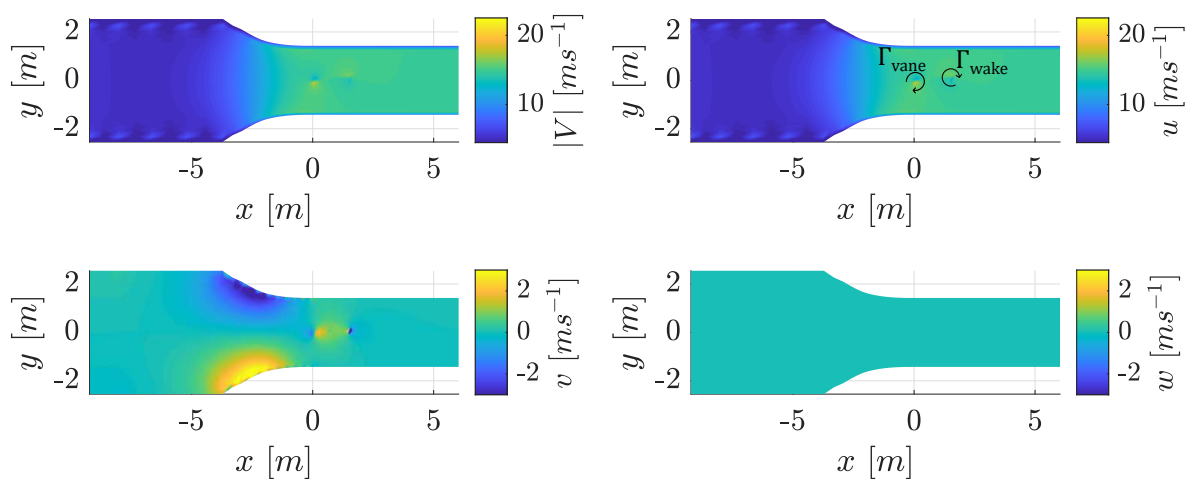
Figure 6.8: xy-plane velocity magnitude and components along the OJF centre plane at $t = 0.07$ $[s]$. Schematic of vane and wake circulation direction overlaid on (u) contour.
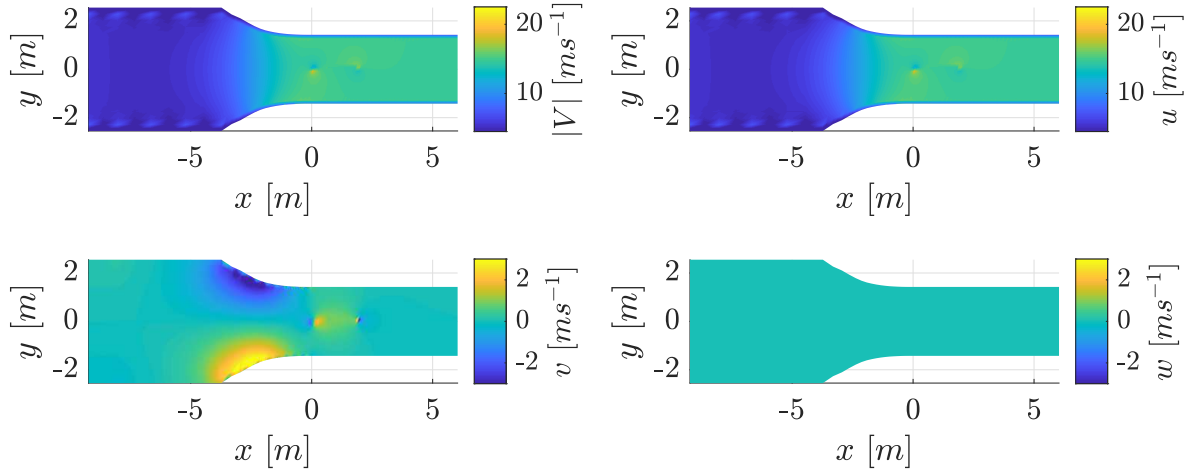
Figure 6.9: xy-plane velocity magnitude and components along the OJF centre plane at $t = 0.1$ $[s]$.

Table 6.3 shows the simulation times and end value of (C_L) for the three cases. The simulations are ran on a machine with CPU clock speed of 3.33 $[GHz]$ and 8 processors. Note is made that running on multiple processors is advantageous since some of the subroutines in the model run in parallel. Furthermore, the reported times are with the visual output turned on as the simulation progresses. A further reduction in computational time to 1.9 $[min]$ is seen when disabling per time step visual output, corresponding to the medium mesh; i.e. reduction of 53%. The solution is still saved at the end of the simulation and post processing can be applied. Based on the similarity in lift, monitored velocity and computational time, one would deem the medium mesh a reasonable compromise.

Table 6.3: Corresponding simulation times for the results in Figure 6.5.

Mesh	Sim. time $[min]$	%-time change	C_L $[-]$	%-C_L change
Coarse	3.0	-55	0.8424	2.6
Medium	4.0	-40	0.8265	0.6
Fine	6.7	-	0.8213	-

Single Vane, Sinusoidal Motion:

The panel resolution independence is further tested under an unsteady sinusoidal motion. The vanes were spaced 0.7 $[m]$ apart, centred about the centreline. The time step was decreased to $\frac{c}{8U_\infty} = 0.0025$ $[s]$ such that the maximum increment pitch change was ≤ 0.5 $[°]$. The unsteady lift coefficient is plotted against pitch angle in Figure 6.10. The analytical solution by Theodorsen for a pitching airfoil is overlaid for comparison Gordon Leishman (2006). Lift coefficient values are scaled by the same factor as in the previous analysis. Velocity components of the flow field at $\mathbf{x} = (1.5, 0, 0)$ $[m]$ are shown in Figure 6.11. Lastly, the corresponding wake of the vane is shown in Figure 6.12. The following observations are

made:

1. The results do not show mesh independence and the lift coefficient approaches the steady state curve as panel resolution is increased. The trend is seen on the upstroke of the vane; i.e. at the start of the simulation as pitch angle increases from 0 to 10 [°]. As the vane returns to 5 [°] pitch the three cases converge closely. As the vane continues its next upstroke in the opposite direction; i.e. pitch angle 5 to -10 [°], the results show mesh dependence again. The above is repeated upon the vane returning to -5 [°] pitch; i.e. pitch angle from -10 to -5 [°]. The explanation of the differences in lift coefficient stems from the use of a vortex core model. As the panels on the vanes get smaller, the influence coefficient matrix changes. This leads to variation in circulation distribution on the vanes and ultimately to a variation in lift coefficient. The true solution is approached as vortex core size decreases to zero, however, this led to the simulations exploding. The next section will seek quantification of influence of vortex core size and set limits on the vortex core size such that accuracy is preserved while maintaining numerical stability.

2. Small differences are seen in the velocity field as well, reflected by the slight change in wake shape for the medium and fine cases.
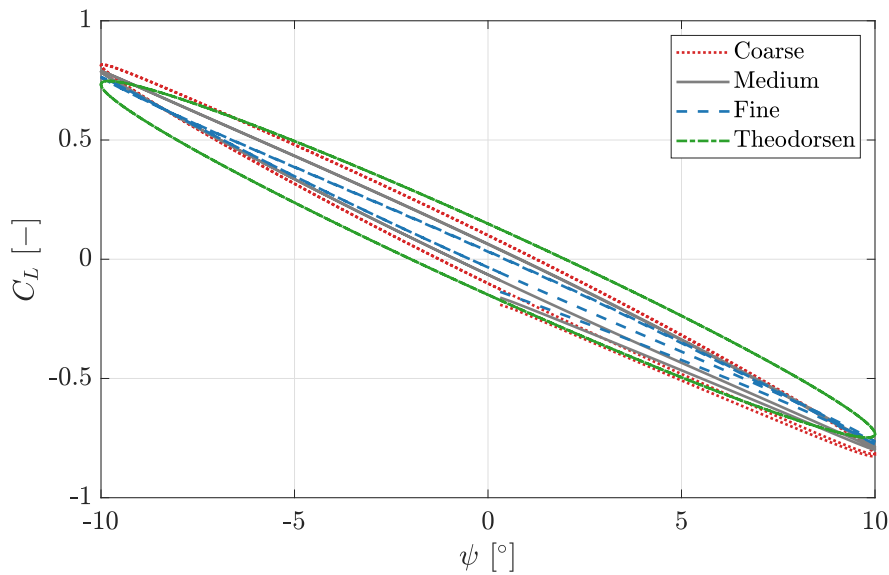
Figure 6.10: Lift coefficient as a function of pitch angle for various panel resolutions; coarse: $N = 10$, $M = 4$, medium: $N = 20$, $M = 8$, fine: $N = 30$, $M = 16$ and very fine: $N = 40$, $M = 24$. Simulation carried out on 1 vane with $c = 0.3$ $[m]$, $b = 2.7$ $[m]$, $U_\infty = 15$ $[ms^{-1}]$, $\psi = 10\sin(4\pi t)$ $[°]$, $k = 0.13$ $[-]$.
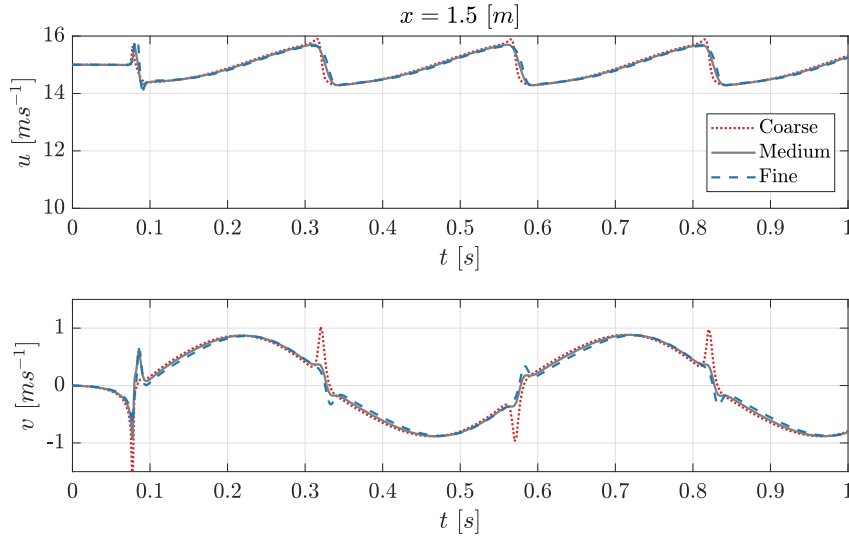
Figure 6.11: Flow field velocity components at $\mathbf{x} = (1.5, 0, 0)$ $[m]$ for various panel resolutions; coarse: $N = 10$, $M = 4$, medium: $N = 20$, $M = 8$, fine: $N = 30$, $M = 16$ and very fine: $N = 40$, $M = 24$. Simulation carried out on 1 vane with $c = 0.3$ $[m]$, $b = 2.7$ $[m]$, $U_\infty = 15$ $[ms^{-1}]$, $\psi = 10\sin(4\pi t)$ $[°]$, $k = 0.13$ $[-]$.
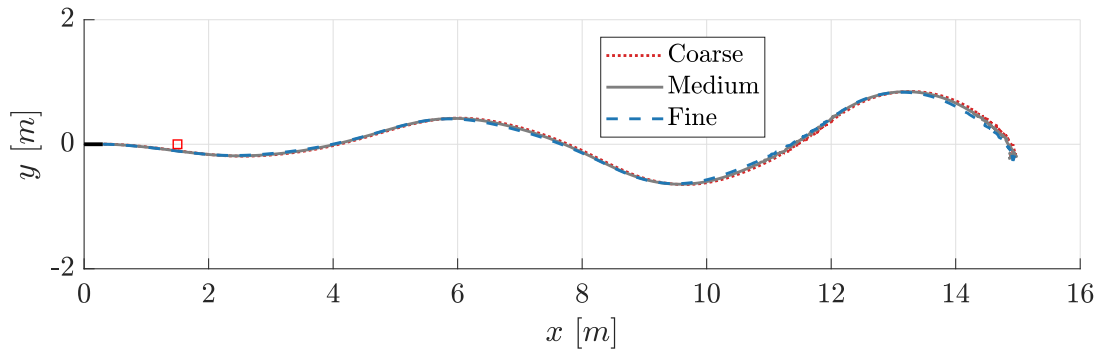
Figure 6.12: Corresponding mid span wake sheet lines for the results shown in Figure 6.10.

It is concluded that a penalty between panel resolution, vortex core size and lift coefficient accuracy is required to maintain the numerical stability of the algorithm. A panel resolution represented by the medium distribution ($N = 20, M = 8$) achieves this optimum.

6.1.2 Vortex Core Size

The simulations are ran for a step in pitch angle. The time step is set to $\Delta t = \frac{c}{4U_\infty} = 0.005$ $[s]$ and the panel resolution is $N = 20, M = 8$. The results from the variation of

vortex core sizes described in Table 6.1 were virtually identical (to 4 decimal places) and are summarised in Table 6.4. The range was varied further with the maximum $R = 0.1$ $[m]$ and the minimum being machine precision of 1×10^{-13} $[m]$. An additional case was run without a vortex core model. The results remained virtually identical for decreasing (R), however, an upper limit was identified, which, once exceeded resulted in the explosion of the numerical algorithm. The issue manifested due to a wrong influence coefficient matrix; the self influence of panels with width smaller than (R), no longer resembled the true value. This resulted in the computation of non-physical circulation values. Since the shed wake vortices have the same circulation as the TE vortices, the wake expanded past any resemblance to the physical situation. Furthermore, as this limit was approached (increasing values of R), the computed (C_L) increased past expected values (again, dependency of local panel circulation). The limit was identified to be on the order of the minimum panel width; for the present results being 0.0167 $[m]$. However, the user is advised to use an order lower to avoid erroneous results.

Table 6.4: Computed steady-state (C_L) values for various vortex core sizes under a step change in angle of attack.

$\mathbf{R}$ $[m]$	$\mathbf{C_L}$ $[-]$	%-$\mathbf{C_L}$ increase
≤ 0.005	0.8265	-
0.02	0.8529	3
0.03	0.9506	15
0.04	0.9305	13

Note is made that the panels at the tips were the first to get affected. This was due to the use of cosine spacing for the spanwise discretisation which resulted in smaller panels at the tips. These results were not replicated under a sinusoidal pitching motion, where a lower limit of the vortex core size existed as well. Crossing this limit lead to unphysical wake expansions and therefore no solution. Generally, values on the order of the smallest panel height/width result in stability of the algorithm. The value of 0.005 chosen as a mid value.

6.1.3 Time Step

The time step is expressed in convection time of chord length fractions; i.e. $\frac{c}{16U_\infty} = 0.00125$ $\leq \Delta t \leq \frac{c}{2U_\infty} = 0.01$ $[s]$. The wake is allowed to convect freely. The panel resolution is set to $N = 20$, $M = 8$ and the vortex core size to $R = 0.005$ $[m]$.

Single Vane, Ramp Motion:

The results for the ramp up and hold motion are shown in Figures 6.13 and 6.14. The pitching increments per time step are: $\frac{c}{2U_\infty}$, $\Delta\psi = 0.2$ $[°]$, $\frac{c}{4U_\infty}$, $\Delta\psi = 0.1$ $[°]$ and $\frac{c}{8U_\infty}$, $\Delta\psi = 0.05$ $[°]$. The following is observed:

1. The lift coefficients are similar for the three cases except for $\Delta t = \frac{c}{2U_\infty}$ $[s]$, which rises at a slower rate, however, reaching the same end value.

2. A similar but larger inconsistency is seen in the velocity components sampled down-
   stream.

To explain this, the instantaneous wakes at $t = 0.20$ $[s]$ for the cases with $\Delta t = \frac{c}{2U_\infty}$ and
$\frac{c}{4U_\infty}$ are plotted in Figure 6.15. It becomes clear that although the pitch increment for the
$\Delta t = \frac{c}{2U_\infty}$ case is low, the time step is too large for the wake to deform properly. As the
vane pitches, the tip vortices filaments cross over each other, lag behind and accumulate at
a point. This causes the vortex filaments to stretch. Since the developed model is not valid
for strong rollup, the excessive stretching of wake panels results in incorrect modelling; "*In
the case of a strong wake rollup the size of the wake vortex ring can increase (or be stretched)
and if a vortex line segment length increases its strength must be reduced (from the angular
momentum point of view).*" (Katz and Plotkin, 2001, p. 429). A remedy would be to lower
the circulation of the deformed wake panels proportionally to the increase in area, however,
this is not attempted in the thesis at hand and care must be taken to ensure wake elements
have not stretched excessively.
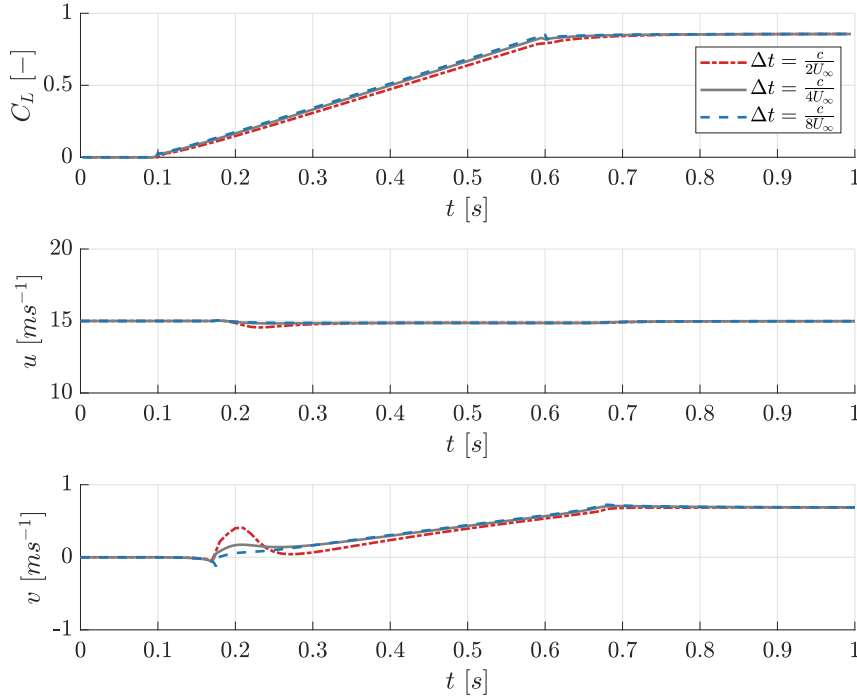
Figure 6.13: Lift coefficient and flow field velocity components at $\mathbf{x} = (1.5, 0, 0)$ $[m]$ for various
time steps; $\Delta t = \frac{c}{2U_\infty}$, $\Delta t = \frac{c}{4U_\infty}$, $\Delta t = \frac{c}{8U_\infty}$ $[s]$. Simulation carried out for a ramp up and
hold motion with a single vane with $c = 0.3$ $[m]$, $b = 2.7$ $[m]$, $U_\infty = 15$ $[ms^{-1}]$, $\psi_{max} = 10$ $[°]$,
$r = 20$ $[°/s^{-1}]$.
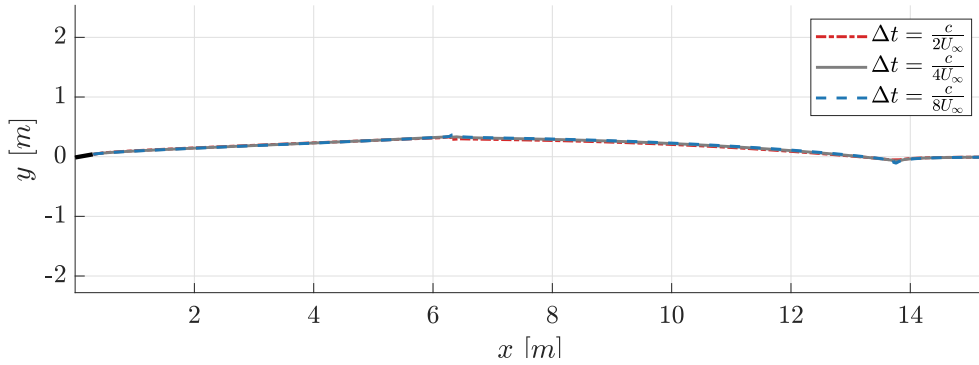
Figure 6.14: Corresponding mid span wake sheet lines for the results shown in Figure 6.13.
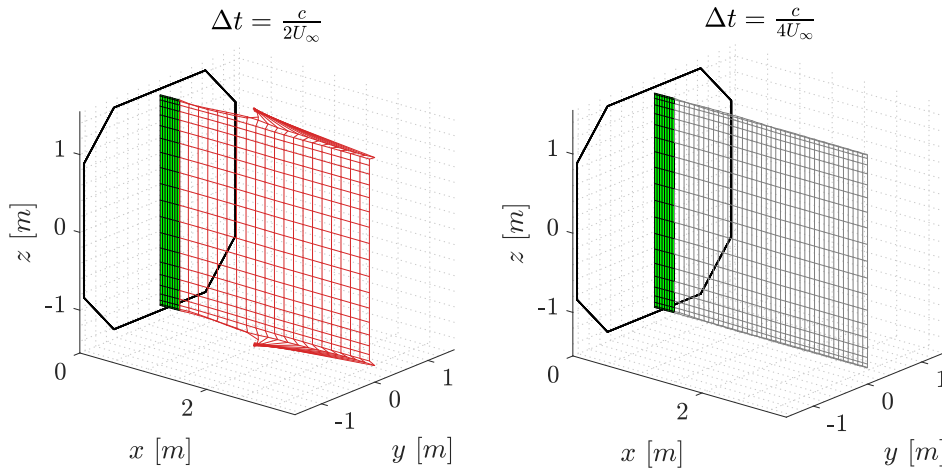
Figure 6.15: Instantaneous wakes at $t = 0.2$ [s] for the cases with $\Delta t = \frac{c}{2U_\infty}$ and $\Delta t = \frac{c}{4U_\infty}$ showcasing wrong wake deformation.

Single Vane, Sinusoidal Motion:

The results for the sinusoidal motion are shown in Figures 6.16 through 6.18. The maximum pitching increments per time step are: $\Delta t = \frac{c}{4U_\infty}$, $\Delta\psi = 0.63$ [°], $\Delta t = \frac{c}{8U_\infty}$, $\Delta\psi = 0.31$ [°] and $\Delta t = \frac{c}{16U_\infty}$, $\Delta\psi = 0.16$ [°]. The lift coefficient of the vane is plotted against the pitching angle of the vanes in Figure 6.16. The analytical solution by Theodorsen is overlaid for comparison. The unsteady lift variation is clearly described in the lower time steps cases ($\frac{c}{4U_\infty}$, $\frac{c}{8U_\infty}$), with minor differences at higher pitch angles. The highest time step case flattens at the extremities, resembling the steady state case. It is interesting to point out that this is accentuated on the upstroke of the vane; i.e. as the vane pitches away from 0 [°]. On the downstroke; i.e. as the vane returns to 0 [°] pitch the results coincide between $10 \leq \psi \leq 5$ [°]. The same behaviour was observed for increasing panel resolution.
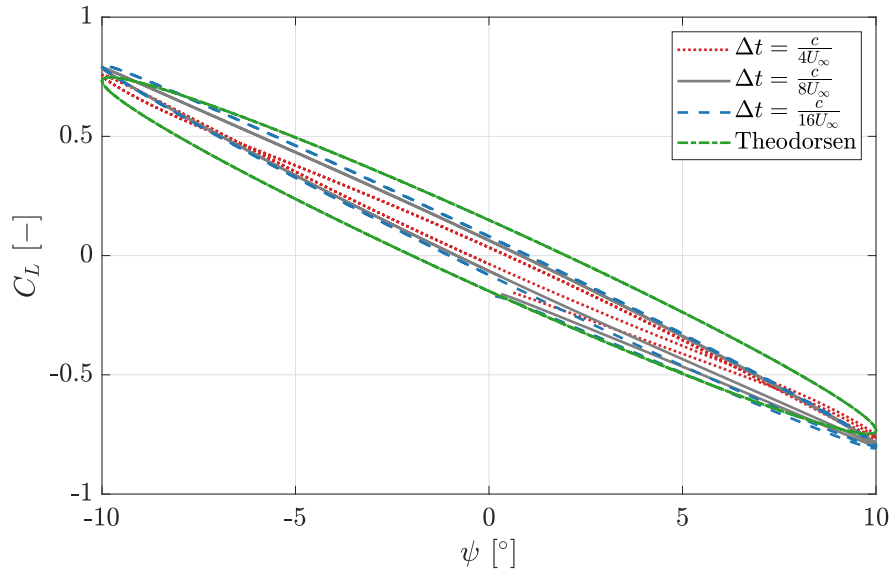
Figure 6.16: Lift coefficient as a function of pitch angle for various time steps; $\Delta t = \frac{c}{4U_\infty}$, $\Delta t = \frac{c}{8U_\infty}$, $\Delta t = \frac{c}{16U_\infty}$. Simulation carried out on 1 vane with $c = 0.3$ $[m]$, $b = 2.7$ $[m]$, $U_\infty = 15$ $[ms^{-1}]$, $\psi = 10\sin(4\pi t)$ $[°]$, $k = 0.13$ $[-]$.

The velocity components at 1.5 $[m]$ downstream of the nozzle is monitored.. The results are presented in Figures 6.17.
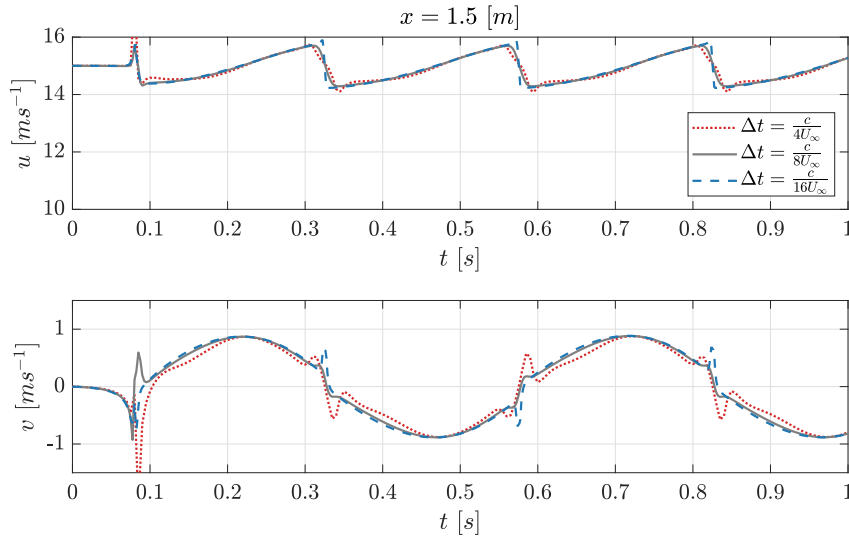
Figure 6.17: Flow field velocity components at $\mathbf{x} = (1.5, 0, 0)$ $[m]$ for various time steps; $\Delta t = \frac{c}{4U_\infty}$, $\Delta t = \frac{c}{8U_\infty}$, $\Delta t = \frac{c}{16U_\infty}$. Simulation carried out on 1 vane with $c = 0.3$ $[m]$, $b = 2.7$ $[m]$, $U_\infty = 15$ $[ms^{-1}]$, $\psi = 10\sin(4\pi t)$ $[°]$, $k = 0.13$ $[-]$.

The results are comparable for the lower time step cases $(\frac{c}{4U_\infty}, \frac{c}{8U_\infty})$ with negligible dif-

ferences. The highest time step case velocity field response lags behind the other cases, particularly on the upstoke of the vane; at $0.1 \leq t \leq 0.2$ $[s]$, $0.35 \leq t \leq 0.45$ $[s]$, $0.6 \leq t \leq 0.7$ $[s]$ and $0.85 \leq t \leq 0.95$ $[s]$. Viewing the mid-span wake line in Figure 6.18 mirrors the above explained trend. The highest time step case's wake lags behind the other cases on the up-stroke of the vane. Examination of the full wake did not reveal any excessive stretching of the wake panels filaments.
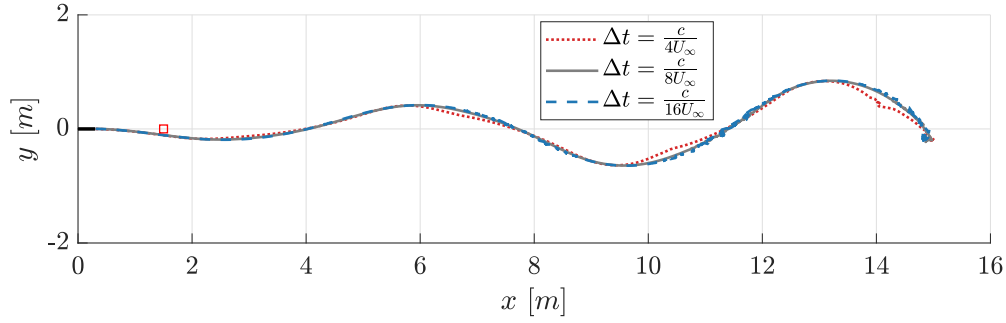
Figure 6.18: Corresponding mid span wake sheet lines for the results shown in Figure 6.16. Red squares represent monitor points for the velocity field.

Considering the results from the two motions the time step is governed by two considerations, of which, the minimum should be chosen:

1. A low enough value of the time step such that the wake can deform properly without excessive stretching; $\Delta t \approx \frac{c}{4U_\infty}$

2. A low enough time step for the simulated motion s.t. the maximum pitch angle increment between time steps is small; Δt s.t. $\Delta \psi \leq \approx 0.3$.

6.1.4   Free Wake Length

The appropriate length of the free wake in the near region is sought. The limitation of the free wake length is implemented for increased computational efficiency. The length should be selected appropriately as to not lead to wrong results. The panel resolution is set to $N = 20, M = 8$. The vortex core size was fixed at $R = 0.005$ $[m]$. The free wakes tested range in lengths of $b/2$ - $2b$; i.e. 1.4 - 5.4 $[m]$.

Single Vane, Step Motion:

The analysis is conducted with the time step is set to $\Delta t = \frac{c}{4U_\infty} = 0.005$ $[s]$. The lift coefficient of the single vane for various free wake lengths is shown in Figure 6.19. The results are virtually identical. Velocity components at various downstream locations are shown in

Figures 6.20 through 6.23. A visualisation of wake shape differences is shown in Figure 6.24. The following observations are made:

1. The results are identical close to the vane; i.e. $x = 1.5 \ [m]$. All free wakes extend past this point, therefore, it is expected that differences in the flow field are not present.

2. As the velocity field is sampled further downstream, differences are seen. These stem from the lack of wake deformation for the cases with a limited wake. At $x = 2.5 \ [m]$ the case with free wake length of $b/2$ shows differences from the other cases. Table 6.5 presents the corresponding free wake lengths and location downstream where they diverge from the fully free wake.

3. The above trend is supported by the shape differences of the wakes.
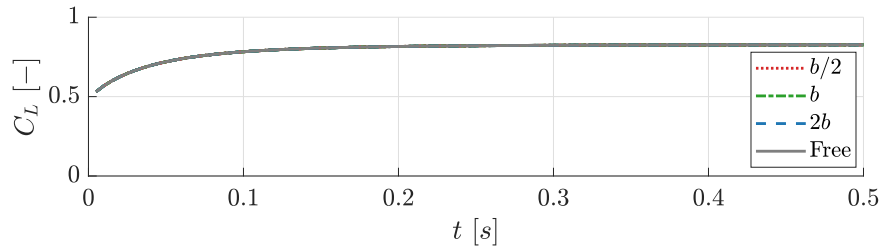
Figure 6.19: Lift coefficient for various free wake lengths; $b/2$, b, $2b$ $[m]$. Simulation carried out with a single vane with $c = 0.3 \ [m]$, $b = 2.7 \ [m]$, $U_\infty = 15 \ [ms^{-1}]$, $\psi = 10 \ [°]$.
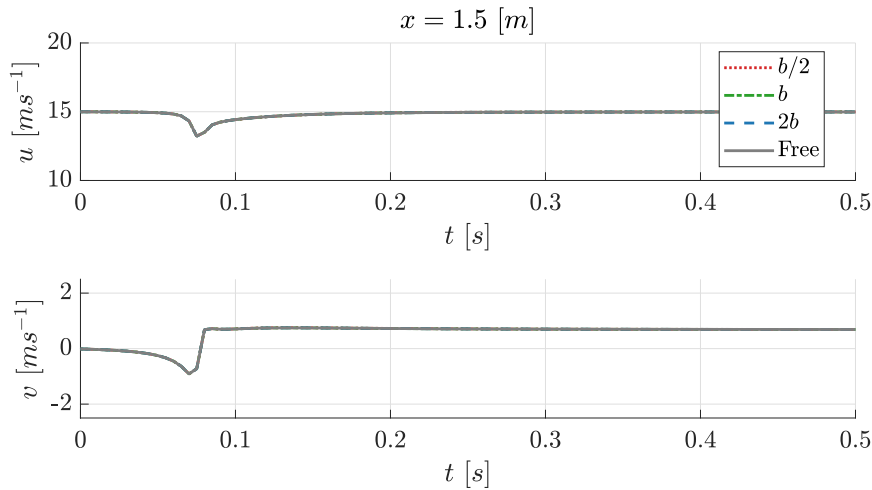
Figure 6.20: Flow field velocity components at $\mathbf{x} = (1.5, 0, 0) \ [m]$ for various free wake lengths; $b/2$, b, $2b$ $[m]$. Simulation carried out with a single vane with $c = 0.3 \ [m]$, $b = 2.7 \ [m]$, $U_\infty = 15 \ [ms^{-1}]$, $\psi = 10 \ [°]$.
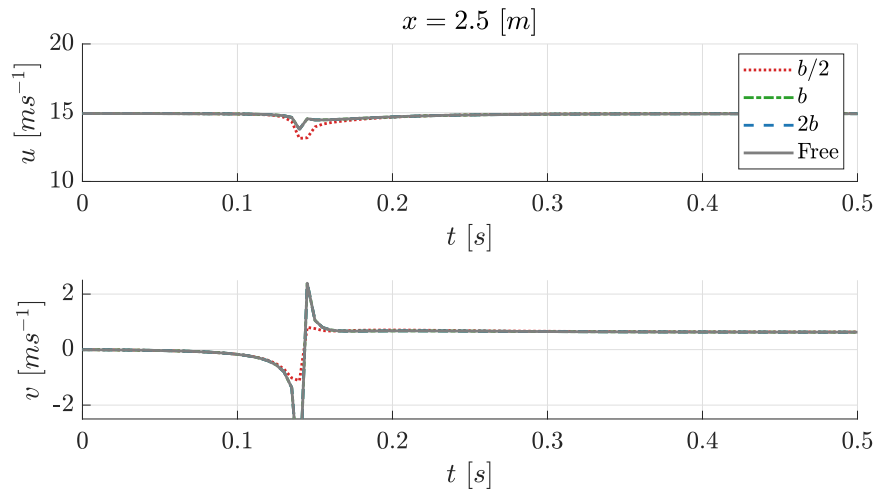
Figure 6.21: Flow field velocity components at $\mathbf{x} = (2.5, 0, 0)$ $[m]$ for various free wake lengths; $b/2$, b, $2b$ $[m]$. Simulation carried out with a single vane with $c = 0.3$ $[m]$, $b = 2.7$ $[m]$, $U_\infty = 15$ $[ms^{-1}]$, $\psi = 10$ $[°]$.
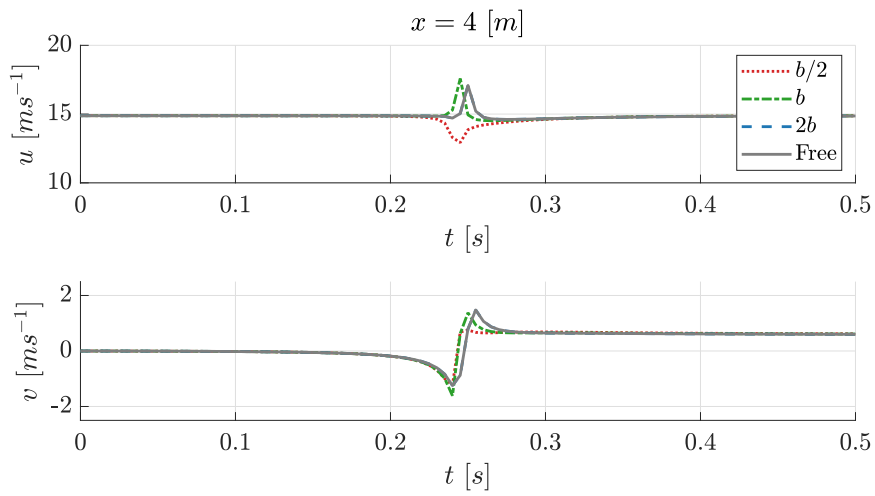
Figure 6.22: Flow field velocity components at $\mathbf{x} = (4, 0, 0)$ $[m]$ for various free wake lengths; $b/2$, b, $2b$ $[m]$. Simulation carried out with a single vane with $c = 0.3$ $[m]$, $b = 2.7$ $[m]$, $U_\infty = 15$ $[ms^{-1}]$, $\psi = 10$ $[°]$.
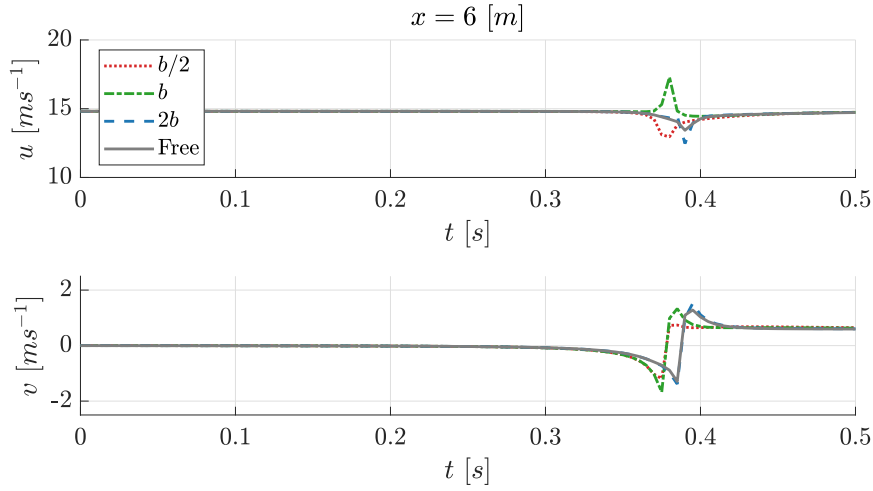
Figure 6.23: Flow field velocity components at $\mathbf{x} = (6, 0, 0)$ $[m]$ for free various wake lengths; $b/2$, b, $2b$ $[m]$. Simulation carried out with a single vane with $c = 0.3$ $[m]$, $b = 2.7$ $[m]$, $U_\infty = 15$ $[ms^{-1}]$, $\psi = 10$ $[°]$.

Table 6.5: Relation between end of free wakes, location of velocity sampling and divergence from the fully free case for the steady motion of a single vane.

Case	Loc. end $[m]$	Loc. divergence $[m]$	Gap $[m]$
$b/2$	≈ 1.7	≈ 2.5	≈ 0.8 or $0.3b$
b	≈ 3	≈ 4	≈ 1 or $0.4b$
$2b$	≈ 5.7	≈ 6	≈ 0.3 or $0.1b$
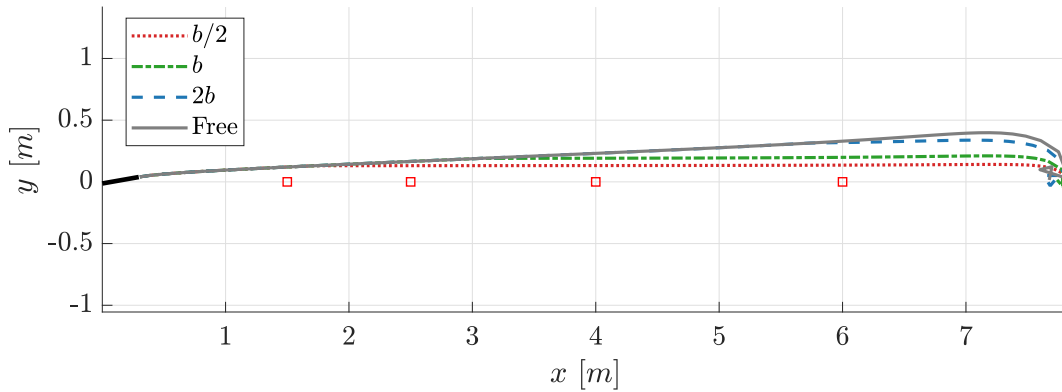
Figure 6.24: Corresponding mid span wake sheet lines for the results shown in Figure 6.20.

Table 6.6 shows the (C_L) at the end of the simulation and the total simulation time for the four cases. The differences in computational time with respect to the fully free wake are calculated. Considering the %-decrease in computational time, with relatively negligible difference in (C_L), a free wake of $b/2$ proves to be enough. However, note is made that based

on the vane dimensions and location of monitoring velocity (or generating the appropriate gust) the free wake would require further extension by half a span past the region of interest.

Table 6.6: Computed C_L for various wake length and the corresponding simulation time.

Wake length	C_L [$-$]	Sim. time [min]	%-time change
Free	0.8265	1.9	-
$b/2$	0.8266	1.2	-37
b	0.8265	1.4	-26
$2b$	0.8265	1.8	-5

Dual Vane, Sinusoidal Motion:

The same analysis is carried out for a sinusoidal motion of a vane pair. The time step is set to $\Delta t = \frac{c}{8U_\infty} = 0.0025$ [s] as concluded from the time step convergence study. The results are documented in Figures 6.25 through 6.30. Similarly, to the steady motion, the lift coefficient is not affected by the free wake length as see in Figure 6.25, with the results being virtually identical.
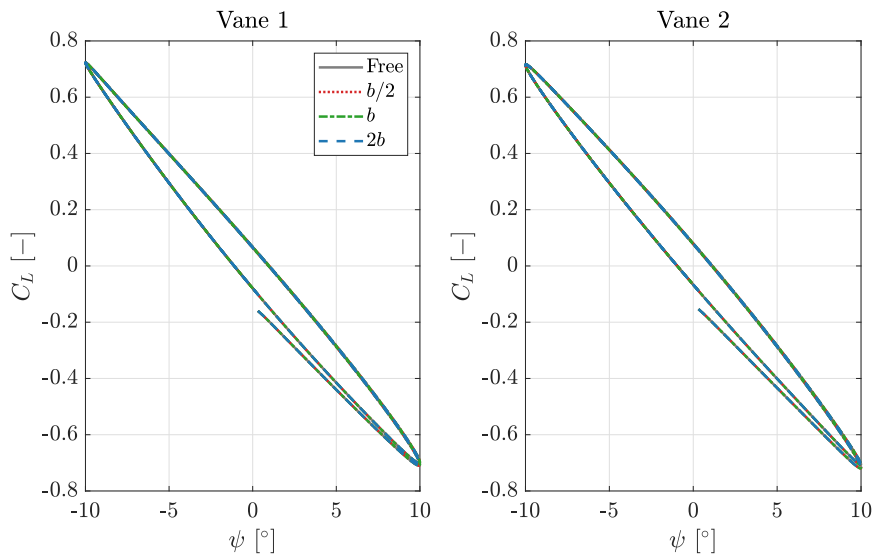
Figure 6.25: Lift coefficient of the two vanes for various wake lengths; $b/2$, b, $2b$ [m]. Simulation carried out on 2 vanes with $c = 0.3$ [m], $b = 2.7$ [m], $U_\infty = 15$ [ms^{-1}], $\psi = 10\sin(4\pi t)$ [°], $k = 0.13$ [$-$].

The three limited free wakes $b/2$, b and $2b$, correspond to a wake transition location from free to frozen of ≈ 1.7, 3 and 5.7 [m]. The velocity components at the centreline at a downstream location from the nozzle of 1.5, 2.5, 4 and 6 [m] are shown in Figures 6.26 through 6.29 respectively. The end of simulation mid span wake sheet line is shown in Figure 6.30, where the red squares indicate the above described monitor points. The results up to $x = 2.5$ [m] are virtually identical. Due to the lack of wake deformation, the results start varying at

$x = 4\ [m]$ in terms of horizontal velocity component. This is due to the frozen wakes not intersecting the monitor point and not inducing the step velocity defects as the free wake. This is repeated for the velocity components sampled at $x = 6\ [m]$. Table 6.7 summarises the findings. The tolerance for a shorter free wake length decreases downstream, where wake deformation plays a more important role.

Table 6.7: Relation between end of free wakes, location of velocity sampling and divergence from the fully free case for the sinusoidal motion of dual vanes.

Case	Loc. end $[m]$	Loc. divergence $[m]$	Gap $[m]$
$b/2$	≈ 1.7	≈ 4	≈ 2.3 or $0.8b$
b	≈ 3	≈ 4	≈ 1 or $0.4b$
$2b$	≈ 5.7	≈ 6	≈ 0.3 or $0.1b$
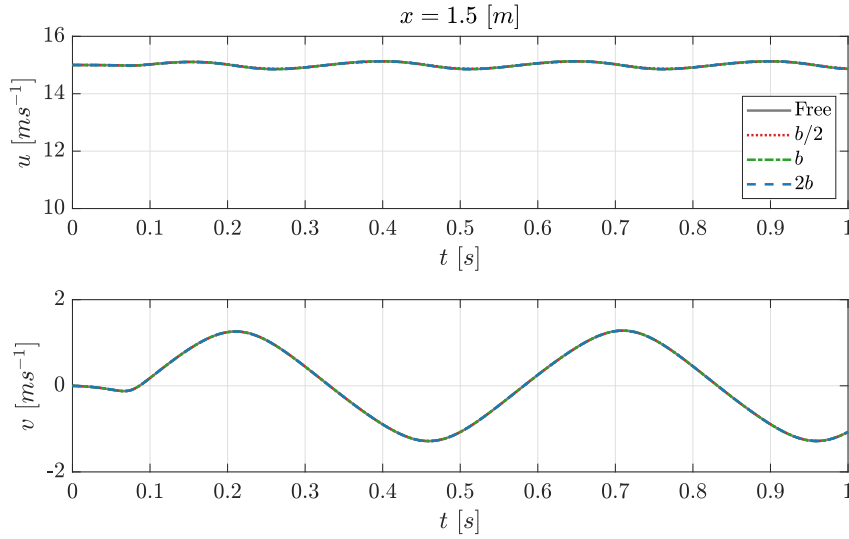
Figure 6.26: Flow field velocity components at $\mathbf{x} = (1.5, 0, 0)\ [m]$ for various free wake lengths; $5c$, $10c$, $20c\ [m]$. Simulation carried out on 2 vanes with $c = 0.3\ [m]$, $b = 2.7\ [m]$, $U_\infty = 15$ $[ms^{-1}]$, $\psi = 10\sin(4\pi t)\ [°]$, $k = 0.13\ [-]$.
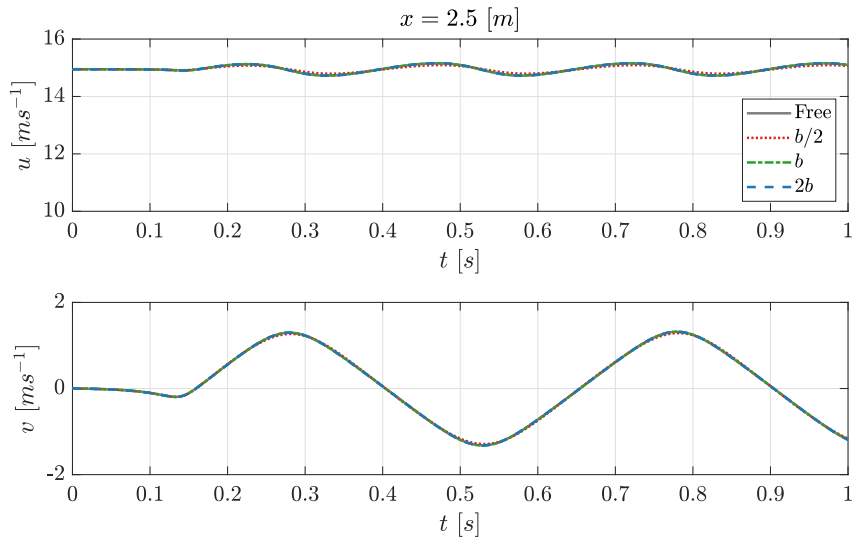
Figure 6.27: Flow field velocity components at $\mathbf{x} = (2.5, 0, 0)$ $[m]$ for various free wake lengths; $5c$, $10c$, $20c$ $[m]$. Simulation carried out on 2 vanes with $c = 0.3$ $[m]$, $b = 2.7$ $[m]$, $U_\infty = 15$ $[ms^{-1}]$, $\psi = 10\sin(4\pi t)$ $[°]$, $k = 0.13$ $[-]$.
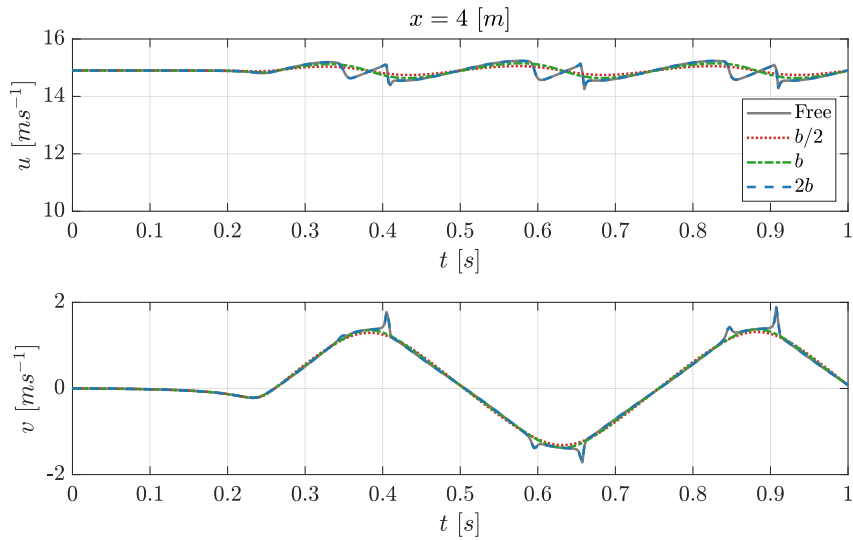
Figure 6.28: Flow field velocity components at $\mathbf{x} = (4, 0, 0)$ $[m]$ for various free wake lengths; $5c$, $10c$, $20c$ $[m]$. Simulation carried out on 2 vanes with $c = 0.3$ $[m]$, $b = 2.7$ $[m]$, $U_\infty = 15$ $[ms^{-1}]$, $\psi = 10\sin(4\pi t)$ $[°]$, $k = 0.13$ $[-]$.
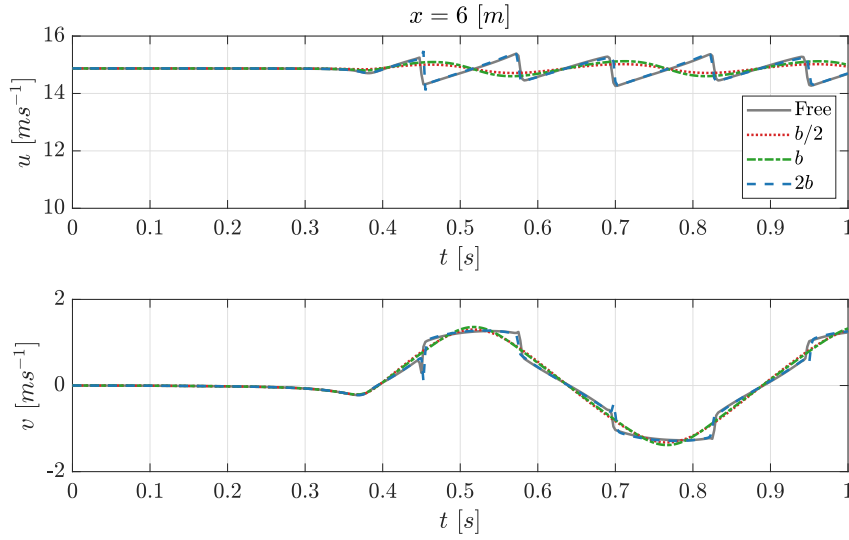
Figure 6.29: Flow field velocity components at $\mathbf{x} = (6, 0, 0)$ $[m]$ for various free wake lengths; $5c$, $10c$, $20c$ $[m]$. Simulation carried out on 2 vanes with $c = 0.3$ $[m]$, $b = 2.7$ $[m]$, $U_\infty = 15$ $[ms^{-1}]$, $\psi = 10\sin(4\pi t)$ $[°]$, $k = 0.13$ $[-]$.
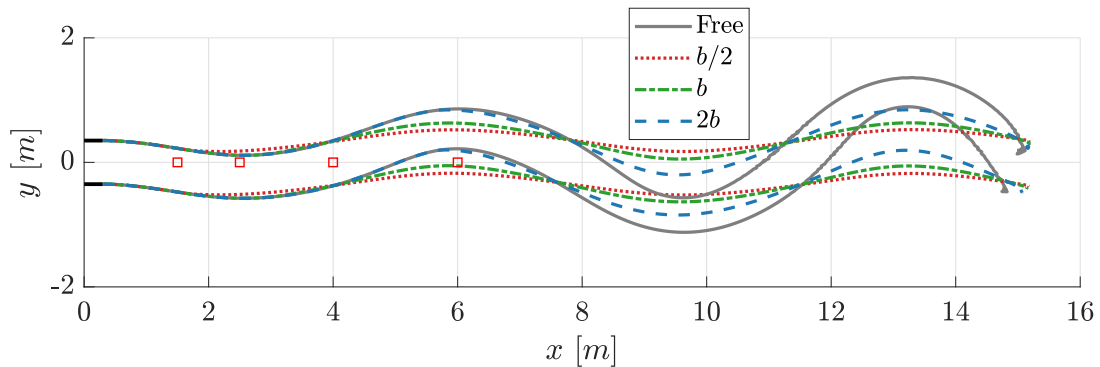
Figure 6.30: Corresponding mid span wake sheet lines for the results shown in Figure 6.25.

In summary, the wake length should be a minimum of $b/2$ in length. Furthermore, the free wake should extend at least until any region of interest in the flow domain. An additional extension of $b/2$ past set region is recommended. Table 6.8 summarises the results of the convergence analysis and recommended model parameters. The algorithm, however, also has short comings. The unsteady loading on the vane(s) is found to be questionable, not showing a convergent behaviour for panel resolution and time step refinement. Nevertheless, convergence behaviour is obtained for the velocity field and wake shape as panel resolution and time steps were refined.

Table 6.8: Recommended model parameter practices derived from the converge analysis.

Parameter	Recommendation
N	20
M	9
R	0.005 $[m]$ or an order of mag. smaller than $\min(\Delta b)$
Δt	$\mathcal{O}(\frac{c}{4U_\infty})$ or s.t. $\Delta \psi \leq 0.3$ $[°]$
Wake	$\mathcal{O}(b/2)$ or s.t. $b/2$ length past region of interest in the domain

6.2 Sensitivity Analysis

Subsequent to finalising the convergence analysis and drawing clear conclusions about the model inputs, the trends for varying gust generator parameters for a system of two vertical vanes are analysed. The results follow the same range of parameters as presented in Lancelot et al. (2015) such that the 2D, transient, CFD with moving mesh can be used for comparison. The free stream velocity is set to $U_\infty = 25$ $[ms^{-1}]$, corresponding to $Re = 494,722$ $[-]$. The main parameter compared is the gust angle achieved in the flow field (α_{gust}), which, is computed from (6.2). The velocity components are sampled at $\mathbf{x} = (1.5, 0, 0)$ $[m]$. The vanes are panelled by 20 and 8 panels in the spanwise and chordwise direction respectively. The vortex core size is fixed at 0.005 $[m]$. The time step is adjusted per reduced frequency to satisfy recommendations from Table 6.8. The free wake length is fixed to one span length. The vanes follow a sinusoidal pitching motion with various rotational speeds: $2\pi, 6\pi, 10\pi$ $[rads^{-1}]$.

$$\alpha_{gust} = \tan^{-1}\left(\frac{v}{u}\right) \tag{6.2}$$

Chord

The maximum gust angle, corresponding to the peaks in the sinusoidal gust, as a function of vane chord is shown in Figure 6.31. The obtained results follow the same trend as the CFD results, however, over predicting the gust angle by approximately 1.5 $[°]$ for all three cases. The trend is a linear variation in maximum gust angle w.r.t. the chord length of the vanes. Interestingly, the results from the developed model maintain the same slope relating the maximum achieved gust angle and vane chord as the CFD results. A linear fit to the results is described by (6.3).
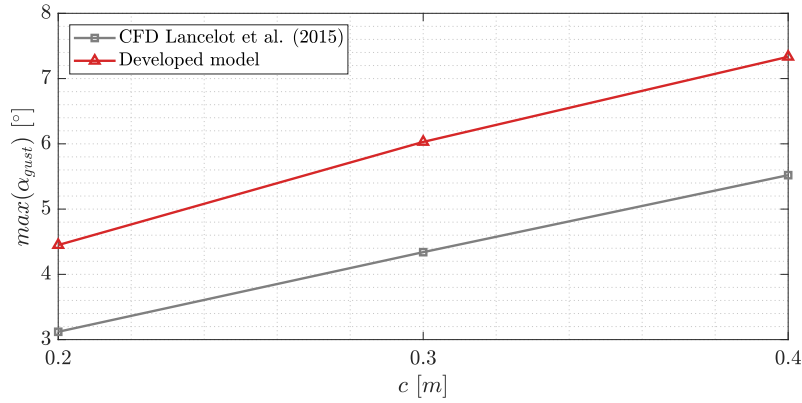
Figure 6.31: Maximum gust angle at $\mathbf{x} = (1.5, 0, 0)$ $[m]$ for varying chord length: $c = 0.2, 0.3, 0.4$ $[m]$. Simulation carried out for 2 vanes with $b = 2.7$ $[m]$, $U_\infty = 25$ $[ms^{-1}]$, $\psi(t) = 10\sin(10\pi t)$ $[°]$ and $dh = 0.5$ $[m]$. The three chord lengths correspond to $k = 0.1257, 0.1885, 0.2513$ $[-]$.

$$\max(\alpha_{gust}) = 13.75c + 1.75 \tag{6.3}$$

Vane Spacing

Figure 6.32 shows the gust angle for three vane spacings. For a larger spacing, the gust angle at the centreline is smooth and free of kinks, however, for the smaller spacing kinks can be seen as the gust angle approaches its maximum. This is due to the wake elements interacting with each other. Furthermore, the maximum gust angle increases for decreasing vane spacing. The middle case, shows an increase in maximum gust angle from the largest spacing case, however, unlike the smallest spacing case, it is free of kinks. The same conclusion is drawn as in Lancelot et al. (2015); i.e. vane spacing smaller than 0.5 $[m]$ can lead to interaction between vanes.
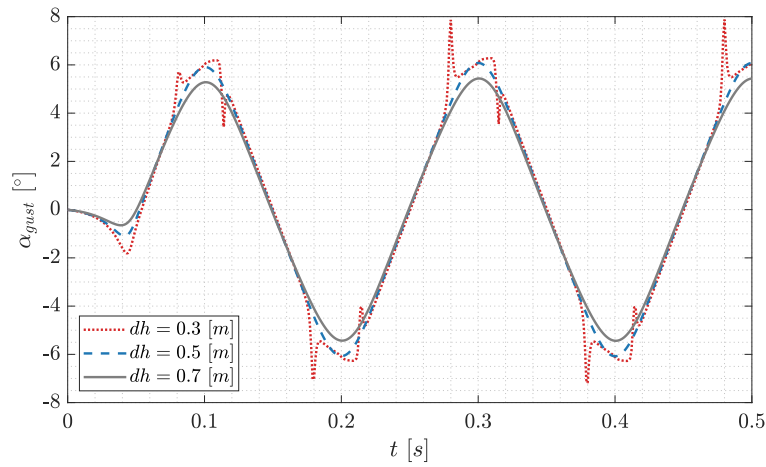
Figure 6.32: Gust angle at $\mathbf{x} = (1.5, 0, 0)$ $[m]$ for varying vane spacing: 0.3, 0.5 and 0.7 $[m]$. Simulation carried out for 2 vanes with $c = 0.3$ $[m]$, $b = 2.7$ $[m]$, $U_\infty = 25$ $[ms^{-1}]$, $\psi(t) = 10\sin(10\pi t)$ $[°]$ and $k = 0.1885$ $[-]$.

Additionally, the obtained results are compared to CFD results from Lancelot et al. (2015) in Figure 6.33. A similar vane interaction for the smallest spacing case is replicated by the CFD results, although to a much lesser extents than the obtained results. The developed model approachs the CFD results as the vane spacing increases, pointing towards difficulties in modelling the vane interaction.
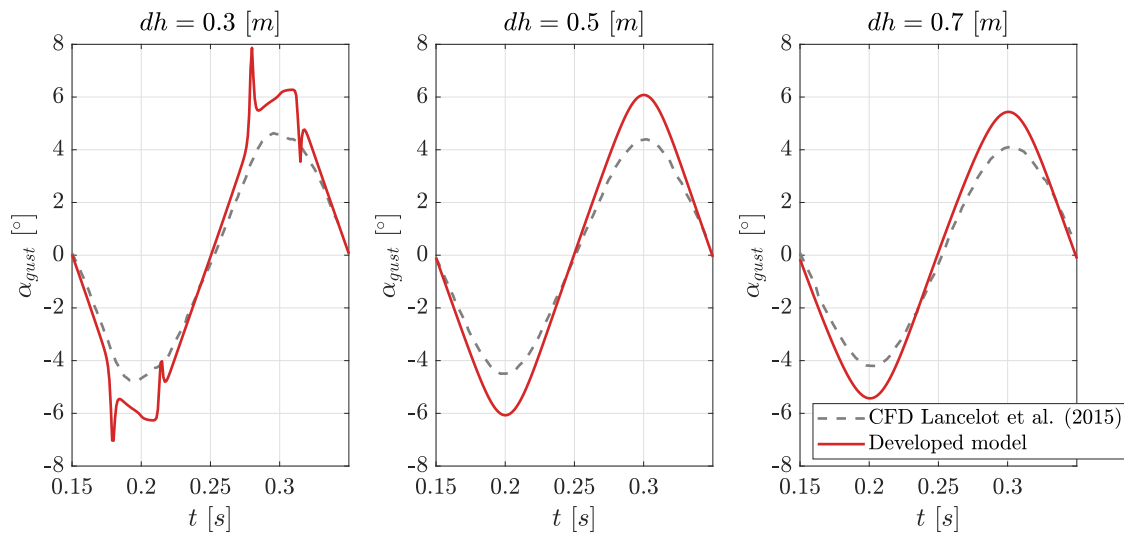
Figure 6.33: Comparison of vane spacing sensitivity obtained from the developed model with CFD results from Lancelot et al. (2015). Gust angle at $\mathbf{x} = (1.5, 0, 0)$ $[m]$ for varying vane spacing: 0.3, 0.5 and 0.7 $[m]$. Simulation carried out for 2 vanes with $c = 0.3$ $[m]$, $b = 2.7$ $[m]$, $U_\infty = 25$ $[ms^{-1}]$, $\psi(t) = 10\sin(10\pi t)$ $[°]$ and $k = 0.1885$ $[-]$.

Reduced Frequency

The maximum gust angle is shown as a function of reduced frequency and downstream location in Figure 6.34. The results vary linearly with reduced frequency, to a similar extent as the CFD results, although the generated results over predict the CFD. The over prediction is to a greater extent at lower reduced frequency. The maximum gust angle decreases downstream for lower reduced frequencies, while the opposite is true at the highest reduced frequency (0.1884 [−]). The former observation is mirrored in the CFD results, however, the latter is not, with the maximum gust angle being the same at the three downstream location for the CFD results at the highest reduced frequency (0.1884 [−]). Not accounting for the downstream variation, Equation 6.4 expressed the linear behaviour of the maximum gust angle as a function of reduced frequency. The positive slope is explained by the increased component of kinematic velocity by the vanes; i.e. as they oscillate at a higher frequency, the fluid feels a larger deflection.
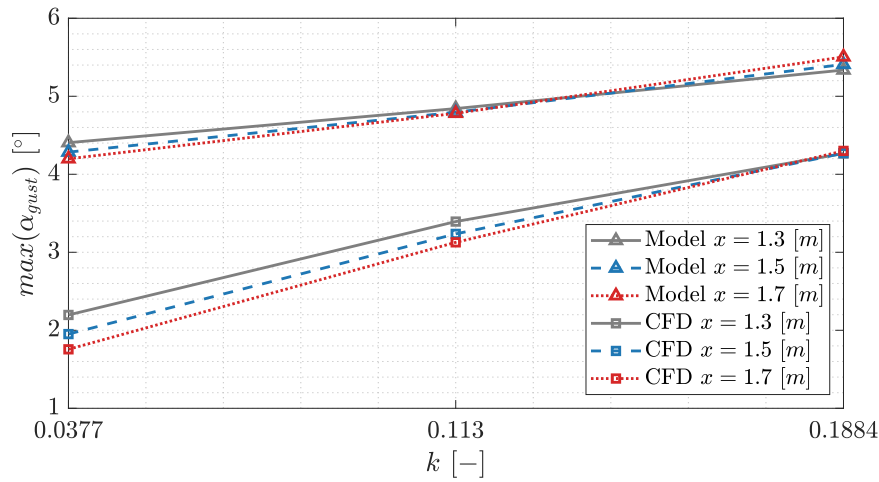
Figure 6.34: Maximum gust angle for varying reduced frequency and downstream location: $k = 0.0377, 0.1130, 0.1884$ and $x = 1.3, 1.5, 1.7$ $[m]$. Simulation carried out for 2 vanes with $c = 0.3$ $[m]$, $b = 2.7$ $[m]$, $dh = 0.7$ $[m]$ and $U_\infty = 25$ $[ms^{-1}]$, $\psi(t) = 10\sin(\omega t)$ $[°]$ and $\omega = 2\pi, 6\pi, 10\pi$ $[rads^{-1}]$.

$$\max(\alpha_{gust}) = 8.67k + 3.85 \tag{6.4}$$

Maximum Pitching Angle

The effect of maximum pitch angle on the achieved maximum gust angle is shown in Figure 6.35. The trend is linear, approaching the CFD results at lower maximum pitch angle. Equation 6.5 describes the trend.
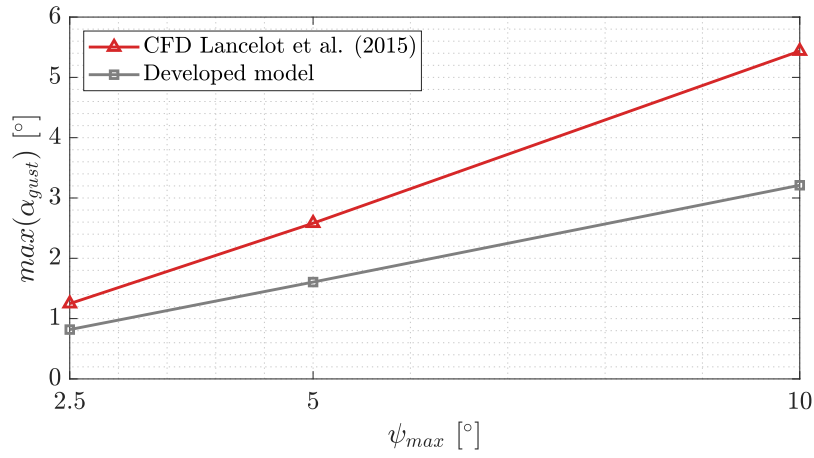
Figure 6.35: Maximum gust angle at $\mathbf{x} = (1.5, 0, 0)$ $[m]$ for varying maximum pitching angle: $\psi_{max} = 2.5, 5, 10$ $[°]$. Simulation carried out for 2 vanes with $c = 0.3$ $[m]$, $b = 2.7$ $[m]$, $dh = 0.7$ $[m]$, $U_\infty = 25$ $[ms^{-1}]$, $\psi(t) = 10 \sin(10\pi t)$ $[°]$ and $k = 0.1885$ $[-]$.

$$\max(\alpha_{gust}) = 0.56\psi_{max} - 0.18 \tag{6.5}$$

In summary, the chord, reduced frequency and maximum deflection angle all have a linear effect on the gust amplitude. The vane spacing influences the gust amplitude in two ways: as the vane spacing approaches the chord length of the vanes, interaction between the vanes can be seen resulting in a non-uniform gust generation. As the vane spacing increases towards two times the chord length the maximum gust amplitude decreases. This trend points toward a middle optimum where vane interaction is absent and maximum gust amplitude is maximised. A gust generator vanes configuration will be influenced by the formerly mention parameters.

Chapter 7

Conclusions

The presence of gusts introduce detrimental effects on wind turbine longevity, power generation quality and efficiency of wind farms. Counteractive measures such as active control strategies, remote sensing and load alleviating are becoming available and the need to test them in a controlled environment arises. As such, this research has explored the potential and limitations of wind tunnel gust generation relevant to wind turbines. The analysis was performed for Delft University of Technology Open Jet Facility wind tunnel, with focus on horizontal axis wind turbines. A literature survey identified and characterised four in-field gusts: (1) veer, (2) wind gusts (direction/speed change), (3) low-level jets and (4) shear. In their presence, wind turbines are exposed to significant differential loading, wake skewing, power delivery fluctuating, fatigue and unsteady loads. Furthermore, the survey classified experimental set-ups capable of generating gusts: circulation control, introduction of secondary flow, wind tunnel fan control, array of oscillating vanes, active turbulence grid and boundary layer wind tunnels. The analysis was performed assuming a gust generator employing an array of oscillating vanes. Veer (spatially varying) and wind gusts (temporally varying) were targeted for wind tunnel simulation.

A computationally efficient model employing 3D lifting surface represented by vortex rings and a free wake model was developed and validated against existing experimental measurements. Validation by PIV measurements showed errors of maximum 14% for high frequency gusts ($k = 0.2$ $[-]$), while less unsteady gusts were modelled with 5% accuracy ($k = 0.1$ $[-]$). An isolated case showed error of up to 30%, however, preserving general trends. A vane configuration search was performed, suggesting a candidate for each considered gust. Non-dimensional parameters such as tip-speed-ratio, Strouhal number and veer angle distribution across the rotor are matched when targeting in-field gusts.

In-field veer distributions measured in relatively flat terrain were successfully simulated for unstable, neutral and stable atmospheric conditions. A limit case with veer differential of 20 $[°]$ was demonstrated. Veer profile gradient was linked to the trailing vorticity of the vanes and thus the vanes' spanwise circulation. As such, the implementation of twist can be exploited

for tailoring user defined veer profiles.

The generation of unsteady wind gusts (streamwise speed variation) was demonstrated by a similar set-up as the current OJF gust generator. Doubling the number of vanes showed little improvement. The gust length scale is linked to vane spacing and as such is identified to limit the possibility of application to large scale wind turbines, leading to a compromise between gust length and time scales. Thus, targeted gust length scales were sacrificed in favour of time scale matching. The methodology, however, can apply for smaller wind turbines. Meaningful velocity variations of up to 28% of free stream values are simulated within 0.3 $[s]$, corresponding to vane reduced frequency $k \approx 0.15$ $[-]$.

Finally, it is concluded that with alterations to the current test set-up, its capabilities can be extended to wind turbine testing under veer and unsteady wind gusts. Applicability to vertical axis wind turbines is established due to their smaller geometric size, allowing for larger time scales ratio, hence better non-dimensional parameter matching. Assuming that the model wind turbine could be as large as half scale, wind tunnel tests would have the potential not only for aerodynamics load assessment but also for aeroelastic experimental simulations.

7.1 Recommendations

The study performed has proven the potential for in-field, horizontal axis wind turbine relevant wind gust generation. The analysis, however, did have limitations in its depth, modelling fidelity, case consideration and generalisation. To overcome the shortcomings of the performed study the author has prepared a list of recommendations that could contribute to future studies on the topic. They have been classified in three categories as follows:

- Developed model improvements
    1. The written code could further be optimised for computational efficiency. Parts lack parallelisation and quantities are computed twice at times. An overall optimisation could further speed up the code, which could be used in the conceptual design of vane configurations.
    2. The code could be implemented to run on graphics cards, which would results in drastic computational time reduction.

- Higher fidelity modelling
    1. Implementation of pressure field computation to provide insights into the reason of sharp velocity drop past maxima.
    2. The full aerofoil profile can be implemented in the unsteady panel method code, coupled with boundary layer equation solved for reliable viscous forces calculations.
    3. Aeroelastic coupling could be implemented as the code contains a placeholder for a surface deformation term.

4. The simulated force distribution could be used as input in a CFD model employing an actuator line model, facilitating a workbench for configuration evaluation at the detailed design phase for new gust generator configurations.

5. The tested pitching protocols could be simulated experimentally with the current gust generator set-up to provide validation data for the behaviour of the gust generator in targeting streamwise velocity variations.

- Further investigation

    1. An optimisation could be set up for determining the optimal vane configuration for a given target gust as well as for the pitching protocol of the gust vanes.

    2. Assessment of vertical axis wind turbine relevant gusts and repetition of the study.

Bibliography

M. Abkar, J. N. Sørensen, and F. Porté-Agel. An Analytical Model for the Effect of Vertical Wind Veer on Wind Turbine Wakes. *Energies*, 11(7):1–10, 2018. ISSN 19961073. doi: 10.3390/en11071838.

J. Arnqvist, A. Segalini, E. Dellwik, and H. Bergström. Wind Statistics from a Forested Landscape. *Boundary-Layer Meteorology*, 156(1):53–71, 2015. ISSN 15731472. doi: 10.1007/s10546-015-0016-x. URL http://dx.doi.org/10.1007/s10546-015-0016-x.

P Baas, F. C. Bosveld, H. K. Baltink, and A. A.M. Holtslag. A climatology of nocturnal low-level jets at Cabauw. *Journal of Applied Meteorology and Climatology*, 48(8):1627–1642, 2009. ISSN 15588424. doi: 10.1175/2009JAMC1965.1.

T. Bell, P. Klein, N. Wildmann, and R. Menke. Analysis of Flow in Complex Terrain Using Multi-Doppler Lidar Retrievals. *Atmospheric Measurement Techniques Discussions*, (January):1–21, 2019. doi: 10.5194/amt-2018-417. URL https://www.atmos-meas-tech-discuss.net/amt-2018-417/.

J. Berg, J. Mann, and E. G. Patton. Lidar-observed stress vectors and veer in the atmospheric boundary layer. *Journal of Atmospheric and Oceanic Technology*, 30(9):1961–1969, 2013. ISSN 07390572. doi: 10.1175/JTECH-D-12-00266.1.

W. Bierbooms, Po-Wen Cheng, G. Larsen, and Bo Juul Pedersen. Modelling of Extreme Gusts for Design Calculations. Publishable final report, European Commission, 2000. URL http://bit.ly/2czqs0k.

A. K. Blackadar. Boundary Layer Wind Maxima and Their Significance for the Growth of Nocturnal Inversions. *Bulletin of the American Meteorological Society*, 38(5):283–290, 1957. ISSN 0003-0007. doi: 10.1175/1520-0477-38.5.283.

R. Bos, A. Giyanani, and W. Bierbooms. Assessing the Severity of Wind Gusts with Lidar. *Remote Sensing*, 8(9), 2016. ISSN 20724292. doi: 10.3390/rs8090758.

T. Burton, D. Sharpe, N. Jenkins, and E. Bossanyi. *Wind Energy Handbook*. John Wiley & Sons, Ltd, second edition, 2011. ISBN 978-0-470-69975-1. URL http://doi.wiley.com/10.1002/0470846062.

R. B. Cal, J. Lebrón, L. Castillo, H. S. Kang, and C. Meneveau. Experimental study of the horizontally averaged flow structure in a model wind-turbine array boundary layer. *Journal of Renewable and Sustainable Energy*, 2(1), 2010. ISSN 19417012. doi: 10.1063/1.3289735.

F. Castellani, D. Astolfi, M. Becchetti, and F. Berno. Experimental and Numerical Analysis of the Dynamical Behavior of a Small Horizontal-Axis Wind Turbine under Unsteady Conditions: Part I. *Machines*, 6(4):52, 2018. ISSN 2075-1702. doi: 10.3390/machines6040052. URL http://www.mdpi.com/2075-1702/6/4/52.

M. J. Churchfield and S. Sirnivas. On the Effects of Wind Turbine Wake Skew Caused by Wind Veer. In *American Institute of Aeronautics and Astronautics SciTech*, Kissimmee, 2018. National Renewable Energy Laboratory. ISBN 978-1-62410-522-7. doi: 10.2514/6. 2018-0755. URL https://arc.aiaa.org/doi/10.2514/6.2018-0755.

U. Cordes, B. Lambie, K. Hufnagel, H. Spiegelberg, G. Kampers, and C. Tropea. The Adaptive Camber Concept—A passive approach for gust load alleviation on wind turbines. *Wind Energy*, 21(9):732–744, 2018. ISSN 10991824. doi: 10.1002/we.2190.

S. Emeis. *Wind Energy Meteorology*. Springer International Publishing AG, 2018. ISBN 978-3-319-72859-9.

J Gordon Leishman. *Principles of Helicopter Aerodynamics*. Cambridge University Press, second edition, 2006. ISBN 978-0-521-85860-1.

N. D. Ham, P. H. Bauer, and T. L. Lawrence. WIND TUNNEL GENERATION OF SlNU-SOlDAL LATERAL AND LONGITUDINAL GUSTS BY CIRCULATION CONTROL. Technical report, NASA, 1974.

M. M. Hand, D. A. Simms, L. J. Fingersh, D. W. Jager, J. R. Cotrell, S. Schreck, and S. M. Larwood. Unsteady Aerodynamics Experiment Phase VI: Wind Tunnel Test Configurations and Available Data Campaigns. Technical report, NREL, Golden, 2001.

A. A.M. Holtslag. Estimates of Diabatic Wind Speed Profiles From Near-Surface Weather Observations. *Boundary-Layer Meteorology*, 29:225–250, 1984.

A. A.M. Holtslag. Estimation of Atmospheric Boundary Layer Parameters for Diffusion Applications. *Journal of Climate and Applied Meteorology*, 24:1196–1207, 1985.

A. A.M. Holtslag and H. A. R. De Bruin. Applied Modeling of the Nighttime Surface Energy Balance over Land. *Journal of Applied Meteorology*, 27:689–704, 1988.

J. R. Hotlon. The diurnal boundary layer wind oscillation above sloping terrain. *Tellus*, 19 (2):199–205, 1967. ISSN 00402826. doi: 10.1111/j.2153-3490.1967.tb01473.x. URL http://tellusa.net/index.php/tellusa/article/view/9766.

K. B. Howard and M. Guala. Upwind preview to a horizontal axis wind turbine: a wind tunnel and field-scale study. *Wind Energy*, 19:1371–1389, 2016. ISSN 11283602.

W. Hu, F. Letson, R. J. Barthelmie, and S. C. Pryor. Wind Gust Characterization at Wind Turbine Relevant Heights in Moderately Complex Terrain. *Journal of Applied Meteorology and Climatology*, 57(7):1459–1476, 2018. ISSN 15588432. doi: 10.1175/JAMC-D-18-0040.1. URL https://doi.org/10.1175/JAMC-D-18-0040.1.

IEC. Wind turbines - Part 1: Design requirements. International standard, International Electrotechnical Commission, Geneva, 2005.

IRENA. Renewable Capacity Statistics 2018. Statistical report, International Renewable Energy Agency, Abu Dhabi, 2018.

M. S. Jeong, S. W. Kim, I. Lee, and S. J. Yoo. Wake impacts on aerodynamic and aeroelastic behaviors of a horizontal axis wind turbine blade for sheared and turbulent flow conditions. *Journal of Fluids and Structures*, 50:66–78, 2014. ISSN 10958622. doi: 10.1016/j.jfluidstructs.2014.06.016. URL http://dx.doi.org/10.1016/j.jfluidstructs.2014.06.016.

J. C. Kaimal and J. J. Finnigan. *Atmospheric Boundary Layer Flows: Their Structure and Measurement*. Oxford University Press, 1994.

P. C. Kalverla, G. J. Steeneveld, R. J. Ronda, and A. A.M. Holtslag. An observational climatology of anomalous wind events at offshore meteomast IJmuiden (North Sea). *Journal of Wind Engineering and Industrial Aerodynamics*, 165:86–99, 2017. ISSN 0167-6105. doi: 10.1016/j.jweia.2017.03.008.

J. Katz and A. Plotkin. *Low-Speed Aerodynamics*. Cambridge University Press, 2nd ed. edition, 2001. ISBN 0-521-66219-2.

N. Kelley, M. Shirazi, D. Jager, S. Wilde, J. Adams, M. Buhl, E Patton, and P Sullivan. Lamar Low-Level Jet Project Interim Report. Technical Report NREL/TP-500-34593, NREL, Golden, CO, 2004.

T. Kim, M. M. Petersen, and T. J. Larsen. A comparison study of the two-bladed partial pitch turbine during normal operation and an extreme gust conditions. *Journal of Physics: Conference Series (Online)*, 524(1):012065, 2014. ISSN 17426596. doi: 10.1088/1742-6596/524/1/012065. URL https://doi.org/10.1088/1742-6596/524/1/012065.

H. Kobayahi and A. Hatanaka. Active Generation of Wind Gust in a Two-Dimensional Wind Tunnel. *Jounal of Wind Engineering and Industrial Aerodynamics*, 41-44:959–970, 1992.

V. Kotroni and K. Lagouvardos. Low-Level Jet Streams Associated with Atmospheric Cold Fronts: Seven Case Studies from the Fronts 87 Experiment. *Geophysical Research Letters*, 20(13):1371–1374, 1993.

L. Kröger, J. Frederik, J. W. Van Wingerden, J. Peinke, and M. Hölling. Generation of user defined turbulent inflow conditions by an active grid for validation experiments. *Journal of Physics: Conference Series*, 1037:052002, 2018. ISSN 17426596. doi: 10.1088/1742-6596/1037/5/052002. URL https://doi.org/10.1088/1742-6596/1037/5/052002.

P. Lancelot, J. Sodja, N. Werter, and R. Breuker. DESIGN AND TESTING OF A LOW SUBSONIC WIND TUNNEL GUST GENERATOR. In *International Forum on Aeroelasticity and Structural Dynamics*, 124, 2015.

P. Lancelot, J. Sodja, and R. De Breuker. Investigation of the Unsteady Flow Over a Wing Under Gust Excitation. In *International Forum on Aeroelasticity and Structural Dynamics*, 2017. ISBN 9788897576280.

F. Letson, R. J. Barthelmie, W. Hu, and S. C. Pryor. Characterizing Wind Gusts in Complex Terrain. *Atmospheric Chemistry and Physics Discussions*, (September):1–27, 2018. doi: 10.5194/acp-2018-906. URL https://doi.org/10.5194/acp-2018-906.

H. Makita. Realization of a large-scale turbulence field in a small wind tunnel. *Fluid Dynamics Research*, 8(1-4):53–64, 1991. ISSN 01695983. doi: 10.1016/0169-5983(91)90030-M.

L. Menegozzo, A. Dal Monte, E. Benini, and A. Benato. Small wind turbines: A numerical study for aerodynamic performance assessment under gust conditions. *Renewable Energy*, 121:123–132, 2018. ISSN 18790682. doi: 10.1016/j.renene.2017.12.086. URL https://doi.org/10.1016/j.renene.2017.12.086.

L. Mydlarski. A turbulent quarter century of active grids: From Makita (1991) to the present. *Fluid Dynamics Research*, 49(6):061401, 2017. ISSN 01695983. doi: 10.1088/1873-7005/aa7786. URL http://dx.doi.org/10.1088/1873-7005/aa7786.

S. Norris, R. C. Storey, K. Stol, and J. Cater. Modeling Gusts Moving Through Wind Farms. In *50th AIAA Aerospace Sciences Meeting including the New Horizons Forum and Aerospace Exposition*, number 0536. American Institute of Aeronautics and Astronautics, 2012. ISBN 978-1-60086-936-5. doi: 10.2514/6.2012-536. URL http://www.scopus.com/inward/record.url?eid=2-s2.0-84873864384{&}partnerID=tZOtx3y1.

Y. Ohya, R. Nakamura, and T. Uchida. Intermittent Bursting of Turbulence in a Stable Boundary Layer with Low-level Jet. *Boundary-Layer Meteorology*, 126(3):349–363, 2008. ISSN 00068314. doi: 10.1007/s10546-007-9245-y.

C. A. Paulson. The Mathematical Representation of Wind Speed and Temperature Profiles in the Unstable Atmospheric Surface Layer, 1970. ISSN 0021-8952. URL http://journals.ametsoc.org/doi/abs/10.1175/1520-0450{%}281970{%}29009{%}3C0857{%}3ATMROWS{%}3E2.0.CO{%}3B2.

A. Peña, R. Floors, A. Sathe, S. E. Gryning, R. Wagner, M. S. Courtney, X. G. Larsén, A. N. Hahmann, and C. B. Hasager. Ten Years of Boundary-Layer and Wind-Power Meteorology at Høvsøre, Denmark. *Boundary-Layer Meteorology*, 158(1):1–26, 2016. ISSN 15731472. doi: 10.1007/s10546-015-0079-8.

S. B. Pope. *Turbulent Flows*. Cambridge University Press, 2000. ISBN 9780521598866. URL https://books.google.nl/books?id=HZsTw9SMx-0C.

Y. X. Qiu, X. D. Wang, S. Kang, M. Zhao, and J. Y. Liang. Predictions of unsteady HAWT aerodynamics in yawing and pitching using the free vortex method. *Renewable Energy*, 70:93–106, 2014. ISSN 09601481. doi: 10.1016/j.renene.2014.03.071. URL http://dx.doi.org/10.1016/j.renene.2014.03.071.

A. J. Saddington, M. V. Finnis, and K. Knowles. The characterisation of a gust generator for aerodynamic testing. *Proceedings of the Institution of Mechanical Engineers, Part G: Journal of Aerospace Engineering*, 229(7):1214–1225, 2015. ISSN 20413025. doi: 10.1177/0954410014548237.

Y. Sakagami, P. A. A. Santos, R. Haas, J. C. Passos, and F. F. Taves. Wind shear assessment using wind LiDAR profiler and sonic 3D anemometer for wind energy applications - Preliminary Results. In *World Renewable Energy Congress*, London, 2014.

T Sarpkaya. Computational Methods With Vortices — The 1988 Freeman Scholar Lecture. *Journal of Fluids Engineering*, 111(1):5–52, 1989.

H. Snel and J. G. Schepers. Joint Investigation of Dynamic Inflow Effects and Implementation of an Engineering Method. Technical report, Commision of the European Communities, 1995.

R. C. Storey, S. E. Norris, and J. E. Cater. Modelling Turbine Loads during an Extreme Coherent Gust using Large Eddy Simulation. *Journal of Physics: Conference Series*, 524: 012177, 2014. ISSN 17426596. doi: 10.1088/1742-6596/524/1/012177.

B. Storm, J. Dudhia, S. Basu, A. Swift, and I. Giammanco. Evaluation of the Weather Research and Forecasting Model on Forecasting Low-level Jets: Implications for Wind Energy. *Wind Energy*, 12(1):81–90, 2009. ISSN 10954244. doi: 10.1002/we.288.

I. Suomi, S. E. Gryning, R. Floors, T. Vihma, and C. Fortelius. On the vertical structure of wind gusts. *Quarterly Journal of the Royal Meteorological Society*, 141(690):1658–1670, 2015. ISSN 1477870X. doi: 10.1002/qj.2468.

G. Svensson and A. A. M. Holtslag. Analysis of Model Results for the Turning of the Wind and Related Momentum Fluxes in the Stable Boundary Layer. *Boundary-Layer Meteorology*, 132(2):261–277, 2009. ISSN 00068314. doi: 10.1007/s10546-009-9395-1.

D. M. Tang, P. G. A. Cizmas, and E. H. Dowell. Experiments and analysis for a gust generator in a wind tunnel. *Journal of Aircraft*, 33(1):139–148, jan 1996. ISSN 0021-8669. doi: 10.2514/3.46914. URL http://arc.aiaa.org/doi/10.2514/3.46914.

G. van Kuik. *The Fluid Dynamic Basis for Actuator Disc and Rotor Theories*. IOS Press BV, Delft, 2018. ISBN 1614998663. doi: 10.3233/978-1-61499-866-2-i.

R. Volpe, A. Da Silva, V. Ferrand, and L. Le Moyne. Experimental and Numerical Validation of a Wind Gust Facility. *Journal of Fluids Engineering*, 135(1):011106, 2013. ISSN 0098-2202. doi: 10.1115/1.4023194. URL http://fluidsengineering.asmedigitalcollection.asme.org/article.aspx?doi=10.1115/1.4023194.

M. Wächter, H. Heißelmann, M. Hölling, A. Morales, P. Milan, T. Mücke, J. Peinke, N. Reinke, and P. Rinn. The Turbulent Nature of the Atmospheric Boundary Layer and its Impact on the Wind Energy Conversion Process. *Journal of Turbulence*, 13, 2012. doi: 10.1080/14685248.2012.696118.

Appendix A

Verification

The key subroutine of the developed model is subjected to four unit tests. The subroutine in questions involves the computation of induced velocity due to a vortex ring made up of four connected vortex filaments with the same circulation at a user specified point. This subroutine is called in the model for each lifting-surface and wake surface panel. Furthermore, the vortex core model implemented is tested as well. Note is made that various other unit tests have been performed but not documented since their output was purely visual. This would have extended the document size past sensible page count. These included: co-ordinate transformation, wind tunnel and gust vanes discretisation, normal and tangential vectors computation. Furthermore, the subroutines computing influence coefficients were not subjected to a verification procedure. Nor was the subroutine computing the lift coefficient. The correctness of these subroutines was evaluated directly through validation process by comparison to experimental measurements of lift coefficient and chordwise pressure distribution. The results showed small errors ($\leq 5\%$) as long as the simulation was ran within the limitations of the model assumptions.

Unit Test 1: Evaluation point at centreline

The first unit test involves a square vortex ring, with sides measuring 2 $[m]$ and unit circulation. The point of induced velocity evaluation is located at the centreline. This means that all vortex filaments will contribute to the total induced velocity equally. The subroutine output was $\boldsymbol{u} = $ **(-0.4502,0,0)** $[ms^{-1}]$. Figure A.1 described the case visually.
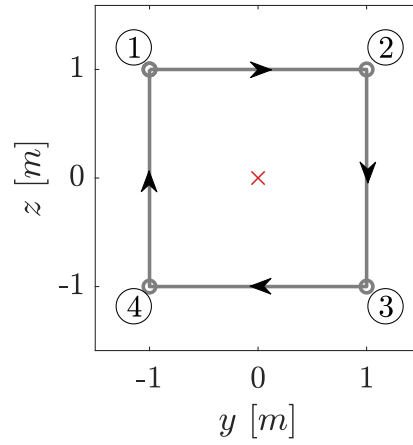
Figure A.1: Unit test 1 nomenclature. Arrows show direction of circulation, circles are vortex filaments ends and red cross is the point at which the induced velocity is computed.

The position vectors, vortex filament length vector and the position vector of the point of interest to the filament for segment 1,2 are:

$$\boldsymbol{r_1} = \begin{pmatrix} 0 \\ 0 \\ 0 \end{pmatrix} + \begin{pmatrix} 0 \\ -1 \\ 1 \end{pmatrix} = \begin{pmatrix} 0 \\ -1 \\ 1 \end{pmatrix} \qquad |\boldsymbol{r_1}| = \sqrt{2}$$

$$\boldsymbol{r_2} = \begin{pmatrix} 0 \\ 0 \\ 0 \end{pmatrix} + \begin{pmatrix} 0 \\ 1 \\ 1 \end{pmatrix} = \begin{pmatrix} 0 \\ 1 \\ 1 \end{pmatrix} \qquad |\boldsymbol{r_2}| = \sqrt{2}$$

$$\boldsymbol{r_0} = \boldsymbol{r_1} - \boldsymbol{r_2} = \begin{pmatrix} 0 \\ -1 \\ 1 \end{pmatrix} - \begin{pmatrix} 0 \\ 1 \\ 1 \end{pmatrix} = \begin{pmatrix} 0 \\ -2 \\ 0 \end{pmatrix} \qquad |\boldsymbol{r_0}| = 2$$

$$\boldsymbol{r_1} \times \boldsymbol{r_2} = \begin{Vmatrix} 0 & -1 & 1 \\ 0 & 1 & 1 \end{Vmatrix} = \begin{pmatrix} -2 \\ 0 \\ 0 \end{pmatrix} \qquad |\boldsymbol{r_1} \times \boldsymbol{r_2}| = 2$$

And the induced velocity at the centreline by vortex filament 1,2 is:

$$\boldsymbol{u_{1,2}} = \frac{\Gamma}{4\pi} \frac{\mathbf{r}_1 \times \mathbf{r}_2}{|\mathbf{r}_1 \times \mathbf{r}_2|^2} \mathbf{r}_0 \cdot \left(\frac{\mathbf{r}_1}{|\mathbf{r}_1|} - \frac{\mathbf{r}_2}{|\mathbf{r}_2|} \right)$$

$$= \frac{1}{\pi \cdot 4 \cdot 4} \begin{pmatrix} -2 \\ 0 \\ 0 \end{pmatrix} \begin{pmatrix} 0 \\ -2 \\ 0 \end{pmatrix} \cdot \begin{pmatrix} 0 - 0 \\ -\frac{1}{\sqrt{2}} - \frac{1}{\sqrt{2}} \\ \frac{1}{\sqrt{2}} - \frac{1}{\sqrt{2}} \end{pmatrix}$$

$$= \frac{1}{16\pi} \begin{pmatrix} -2 \\ 0 \\ 0 \end{pmatrix} \left(0 + \frac{4}{\sqrt{2}} + 0 \right)$$

$$= \begin{pmatrix} -0.1125 \\ 0 \\ 0 \end{pmatrix}$$

$$\therefore \boldsymbol{u} = 4 \cdot \boldsymbol{u_{1,2}} = \begin{pmatrix} -0.4502 \\ 0 \\ 0 \end{pmatrix}$$

The subroutine is therefore deemed verified and correct for the computation of induced velocity for a point far from the vortex filaments.

Unit Test 2: Evaluation point on segment 1,2

The second unit test was repeated with the same vortex ring, however, the point of interest has been moved at the midpoint of segment 1,2. No vortex core model was implement. The purpose of this test was to seek whether the subroutine had singular behaviour when the point of interest laid on a vortex filament. The procedure is as above. Quantifies for segment 1,2 are not computed. The subroutine output was $\boldsymbol{u} = \textbf{(-0.1779,0,0)}$ $[ms^{-1}]$. The case is summarised in Figure A.2.
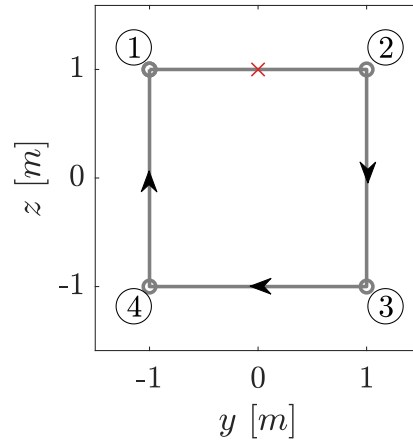
Figure A.2: Unit test 2 nomenclature.

Quantities related to segment 2,3:

$$\boldsymbol{r_1} = \begin{pmatrix} 0 \\ 1 \\ 1 \end{pmatrix} - \begin{pmatrix} 0 \\ 0 \\ 1 \end{pmatrix} = \begin{pmatrix} 0 \\ 1 \\ 0 \end{pmatrix} \qquad |\boldsymbol{r_1}| = 1$$

$$\boldsymbol{r_2} = \begin{pmatrix} 0 \\ 1 \\ -1 \end{pmatrix} - \begin{pmatrix} 0 \\ 0 \\ 1 \end{pmatrix} = \begin{pmatrix} 0 \\ 1 \\ -2 \end{pmatrix} \qquad |\boldsymbol{r_2}| = \sqrt{5}$$

$$\boldsymbol{r_0} = \boldsymbol{r_1} - \boldsymbol{r_2} = \begin{pmatrix} 0 \\ 1 \\ 0 \end{pmatrix} - \begin{pmatrix} 0 \\ 1 \\ -2 \end{pmatrix} = \begin{pmatrix} 0 \\ 0 \\ 2 \end{pmatrix} \qquad |\boldsymbol{r_0}| = 2$$

$$\boldsymbol{r_1} \times \boldsymbol{r_2} = \begin{Vmatrix} 0 & 1 & 0 \\ 0 & 1 & -2 \end{Vmatrix} = \begin{pmatrix} -2 \\ 0 \\ 0 \end{pmatrix} \qquad |\boldsymbol{r_1} \times \boldsymbol{r_2}| = 2$$

And the induced velocity at the point of interest by vortex filament 2,3 is:

$$\boldsymbol{u_{2,3}} = \frac{\Gamma}{4\pi} \frac{\mathbf{r}_1 \times \mathbf{r}_2}{|\mathbf{r}_1 \times \mathbf{r}_2|^2} \mathbf{r}_0 \cdot \left(\frac{\mathbf{r}_1}{|\mathbf{r}_1|} - \frac{\mathbf{r}_2}{|\mathbf{r}_2|} \right)$$

$$= \frac{1}{\pi \cdot 4 \cdot 4} \begin{pmatrix} -2 \\ 0 \\ 0 \end{pmatrix} \begin{pmatrix} 0 \\ 0 \\ 2 \end{pmatrix} \cdot \begin{pmatrix} 0 - 0 \\ 1 - \frac{1}{\sqrt{5}} \\ 0 - \frac{2}{\sqrt{5}} \end{pmatrix}$$

$$= \frac{1}{16\pi} \begin{pmatrix} -2 \\ 0 \\ 0 \end{pmatrix} \left(0 + 0 + \frac{4}{\sqrt{5}} \right)$$

$$= \begin{pmatrix} -0.0712 \\ 0 \\ 0 \end{pmatrix}$$

Vortex filament 3,4:

$$\boldsymbol{r_1} = \begin{pmatrix} 0 \\ 1 \\ -1 \end{pmatrix} - \begin{pmatrix} 0 \\ 0 \\ 1 \end{pmatrix} = \begin{pmatrix} 0 \\ 1 \\ -2 \end{pmatrix} \qquad |\boldsymbol{r_1}| = \sqrt{5}$$

$$\boldsymbol{r_2} = \begin{pmatrix} 0 \\ -1 \\ -1 \end{pmatrix} - \begin{pmatrix} 0 \\ 0 \\ 1 \end{pmatrix} = \begin{pmatrix} 0 \\ -1 \\ -2 \end{pmatrix} \qquad |\boldsymbol{r_2}| = \sqrt{5}$$

$$\boldsymbol{r_0} = \boldsymbol{r_1} - \boldsymbol{r_2} = \begin{pmatrix} 0 \\ 1 \\ -2 \end{pmatrix} - \begin{pmatrix} 0 \\ -1 \\ -2 \end{pmatrix} = \begin{pmatrix} 0 \\ 2 \\ 0 \end{pmatrix} \qquad |\boldsymbol{r_0}| = 2$$

$$\boldsymbol{r_1} \times \boldsymbol{r_2} = \begin{Vmatrix} 0 & 1 & -2 \\ 0 & -1 & -2 \end{Vmatrix} = \begin{pmatrix} -4 \\ 0 \\ 0 \end{pmatrix} \qquad |\boldsymbol{r_1} \times \boldsymbol{r_2}| = 4$$

$$\boldsymbol{u_{3,4}} = \frac{\Gamma}{4\pi} \frac{\mathbf{r}_1 \times \mathbf{r}_2}{|\mathbf{r}_1 \times \mathbf{r}_2|^2} \mathbf{r}_0 \cdot \left(\frac{\mathbf{r}_1}{|\mathbf{r}_1|} - \frac{\mathbf{r}_2}{|\mathbf{r}_2|} \right)$$

$$= \frac{1}{\pi \cdot 4 \cdot 16} \begin{pmatrix} -4 \\ 0 \\ 0 \end{pmatrix} \begin{pmatrix} 0 \\ 2 \\ 0 \end{pmatrix} \cdot \begin{pmatrix} 0 - 0 \\ \frac{1}{\sqrt{5}} + \frac{1}{\sqrt{5}} \\ -\frac{2}{\sqrt{5}} + \frac{2}{\sqrt{5}} \end{pmatrix}$$

$$= \frac{1}{64\pi} \begin{pmatrix} -4 \\ 0 \\ 0 \end{pmatrix} \left(0 + \frac{4}{\sqrt{5}} + 0 \right)$$

$$= \begin{pmatrix} -0.0356 \\ 0 \\ 0 \end{pmatrix}$$

Vortex filament 4,1:

$$\boldsymbol{r_1} = \begin{pmatrix} 0 \\ -1 \\ -1 \end{pmatrix} - \begin{pmatrix} 0 \\ 0 \\ 1 \end{pmatrix} = \begin{pmatrix} 0 \\ -1 \\ -2 \end{pmatrix} \qquad |\boldsymbol{r_1}| = \sqrt{5}$$

$$\boldsymbol{r_2} = \begin{pmatrix} 0 \\ -1 \\ 1 \end{pmatrix} - \begin{pmatrix} 0 \\ 0 \\ 1 \end{pmatrix} = \begin{pmatrix} 0 \\ -1 \\ 0 \end{pmatrix} \qquad |\boldsymbol{r_2}| = 1$$

$$\boldsymbol{r_0} = \boldsymbol{r_1} - \boldsymbol{r_2} = \begin{pmatrix} 0 \\ -1 \\ -2 \end{pmatrix} - \begin{pmatrix} 0 \\ -1 \\ 0 \end{pmatrix} = \begin{pmatrix} 0 \\ 0 \\ -2 \end{pmatrix} \qquad |\boldsymbol{r_0}| = 2$$

$$\boldsymbol{r_1} \times \boldsymbol{r_2} = \begin{Vmatrix} 0 & -1 & -2 \\ 0 & -1 & 0 \end{Vmatrix} = \begin{pmatrix} -2 \\ 0 \\ 0 \end{pmatrix} \qquad |\boldsymbol{r_1} \times \boldsymbol{r_2}| = 2$$

$$\boldsymbol{u_{4,1}} = \frac{\Gamma}{4\pi} \frac{\mathbf{r}_1 \times \mathbf{r}_2}{|\mathbf{r}_1 \times \mathbf{r}_2|^2} \mathbf{r}_0 \cdot \left(\frac{\mathbf{r}_1}{|\mathbf{r}_1|} - \frac{\mathbf{r}_2}{|\mathbf{r}_2|} \right)$$

$$= \frac{1}{\pi \cdot 4 \cdot 4} \begin{pmatrix} -2 \\ 0 \\ 0 \end{pmatrix} \begin{pmatrix} 0 \\ 0 \\ -2 \end{pmatrix} \cdot \begin{pmatrix} 0 - 0 \\ -\frac{1}{\sqrt{5}} + 1 \\ -\frac{2}{\sqrt{5}} - 0 \end{pmatrix}$$

$$= \frac{1}{16\pi} \begin{pmatrix} -2 \\ 0 \\ 0 \end{pmatrix} \left(0 + 0 + \frac{4}{\sqrt{5}} \right)$$

$$= \begin{pmatrix} -0.0712 \\ 0 \\ 0 \end{pmatrix}$$

$$\therefore \boldsymbol{u} = \boldsymbol{u_{2,3}} + \boldsymbol{u_{3,4}} + \boldsymbol{u_{4,1}}$$

$$= \begin{pmatrix} -0.0712 \\ 0 \\ 0 \end{pmatrix} + \begin{pmatrix} -0.0356 \\ 0 \\ 0 \end{pmatrix} + \begin{pmatrix} -0.0712 \\ 0 \\ 0 \end{pmatrix}$$

$$= \begin{pmatrix} -0.1780 \\ 0 \\ 0 \end{pmatrix}$$

Unit Test 3: Evaluation point coinciding with point 4

The last unit test involving a vortex ring is the with the point of interest at the the connection point of two vortex filaments, point 4 as shown in Figure A.3. This leaves only segments 1,2 and 2,3 contributing to the induced velocity, with equal contribution. The subroutine output was $\boldsymbol{u} = \textbf{(-0.0563,0,0)}$ $[ms^{-1}]$.
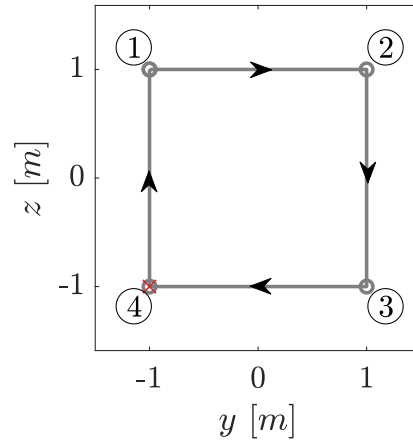
Figure A.3: Unit test 3 nomenclature.

The induced velocity due to segment 1,2:

$$\boldsymbol{r_1} = \begin{pmatrix} 0 \\ -1 \\ 1 \end{pmatrix} - \begin{pmatrix} 0 \\ -1 \\ -1 \end{pmatrix} = \begin{pmatrix} 0 \\ 0 \\ 2 \end{pmatrix} \qquad |\boldsymbol{r_1}| = 2$$

$$\boldsymbol{r_2} = \begin{pmatrix} 0 \\ 1 \\ 1 \end{pmatrix} - \begin{pmatrix} 0 \\ -1 \\ -1 \end{pmatrix} = \begin{pmatrix} 0 \\ 2 \\ 2 \end{pmatrix} \qquad |\boldsymbol{r_2}| = \sqrt{8}$$

$$\boldsymbol{r_0} = \boldsymbol{r_1} - \boldsymbol{r_2} = \begin{pmatrix} 0 \\ 0 \\ 2 \end{pmatrix} - \begin{pmatrix} 0 \\ 2 \\ 2 \end{pmatrix} = \begin{pmatrix} 0 \\ -2 \\ 0 \end{pmatrix} \qquad |\boldsymbol{r_0}| = 2$$

$$\boldsymbol{r_1} \times \boldsymbol{r_2} = \begin{Vmatrix} 0 & 0 & 2 \\ 0 & 2 & 2 \end{Vmatrix} = \begin{pmatrix} -4 \\ 0 \\ 0 \end{pmatrix} \qquad |\boldsymbol{r_1} \times \boldsymbol{r_2}| = 4$$

$$\boldsymbol{u_{1,2}} = \frac{\Gamma}{4\pi} \frac{\mathbf{r}_1 \times \mathbf{r}_2}{|\mathbf{r}_1 \times \mathbf{r}_2|^2} \mathbf{r}_0 \cdot \left(\frac{\mathbf{r}_1}{|\mathbf{r}_1|} - \frac{\mathbf{r}_2}{|\mathbf{r}_2|} \right)$$

$$= \frac{1}{\pi \cdot 4 \cdot 16} \begin{pmatrix} -4 \\ 0 \\ 0 \end{pmatrix} \begin{pmatrix} 0 \\ -2 \\ 0 \end{pmatrix} \cdot \begin{pmatrix} 0 - 0 \\ 0 - \frac{2}{\sqrt{8}} \\ 1 - \frac{2}{\sqrt{8}} \end{pmatrix}$$

$$= \frac{1}{64\pi} \begin{pmatrix} -4 \\ 0 \\ 0 \end{pmatrix} \left(0 + \frac{4}{\sqrt{8}} + 0 \right)$$

$$= \begin{pmatrix} -0.0281 \\ 0 \\ 0 \end{pmatrix}$$

$$\therefore \boldsymbol{u} = 2 \cdot \boldsymbol{u_{1,2}} = \begin{pmatrix} -0.0562 \\ 0 \\ 0 \end{pmatrix}$$

Unit Test 4: Vortex filament with vortex core

A single vortex filament is tested in the presence of a vortex core model. The segment is along the z-axis with starting point at $z = -10$ [m] and end at $z = 10$ [m]. The point of interested is situated at $\boldsymbol{x} = (0.0001, 0, 0)$ [m], while the vortex core radius is set to $R = 0.001$ [m]. The subroutine output for the induced velocity at this point was $\boldsymbol{u} = \textbf{(0,15.925,0)}$ [ms^{-1}].

The analytically computed induced velocity is:

$$\boldsymbol{r_1} = \begin{pmatrix} 0 \\ 0 \\ -10 \end{pmatrix} - \begin{pmatrix} 0.0001 \\ 0 \\ -10 \end{pmatrix} = \begin{pmatrix} -0.0001 \\ 0 \\ -10 \end{pmatrix} \qquad |\boldsymbol{r_1}| = 10$$

$$\boldsymbol{r_2} = \begin{pmatrix} 0 \\ 0 \\ 10 \end{pmatrix} - \begin{pmatrix} 0.0001 \\ 0 \\ 0 \end{pmatrix} = \begin{pmatrix} -0.0001 \\ 0 \\ 10 \end{pmatrix} \qquad |\boldsymbol{r_2}| = 10$$

$$\boldsymbol{r_0} = \boldsymbol{r_1} - \boldsymbol{r_2} = \begin{pmatrix} -0.0001 \\ 0 \\ -10 \end{pmatrix} - \begin{pmatrix} -0.0001 \\ 0 \\ 10 \end{pmatrix} = \begin{pmatrix} 0 \\ 0 \\ -20 \end{pmatrix} \qquad |\boldsymbol{r_0}| = 20$$

$$\boldsymbol{r_1} \times \boldsymbol{r_2} = \begin{Vmatrix} -0.0001 & 0 & -10 \\ -0.0001 & 0 & 10 \end{Vmatrix} = \begin{pmatrix} 0 \\ 0.002 \\ 0 \end{pmatrix} \qquad |\boldsymbol{r_1} \times \boldsymbol{r_2}| = 0.002$$

$$d = \frac{|\boldsymbol{r_1} \times \boldsymbol{r_2}|}{|\boldsymbol{r_0}|} = \frac{0.002}{20} = 0.0001$$

If one of the following conditions is met, the vortex core will be enabled:

1. $|\boldsymbol{r_1}| \leq R \rightarrow 10 \leq 0.001 \rightarrow False$

2. $|\boldsymbol{r_2}| \leq R \rightarrow 10 \leq 0.001 \rightarrow False$

3. $d \leq R \rightarrow 0.0001 \leq 0.001 \rightarrow True$

Since one of the conditions is met, the point of interest is within the radius of the vortex core and the induced velocity will be:

$$
\begin{aligned}
\boldsymbol{u_{1,2}} &= \frac{\Gamma}{4\pi} \frac{\mathbf{r_1} \times \mathbf{r_2}}{R^2 |\mathbf{r_0}|^2} \mathbf{r_0} \cdot \left(\frac{\mathbf{r_1}}{|\mathbf{r_1}|} - \frac{\mathbf{r_2}}{|\mathbf{r_2}|} \right) \\
&= \frac{1}{\pi \cdot 4 \cdot 0.001^2} \begin{pmatrix} 0 \\ 0.002 \\ 0 \end{pmatrix} \begin{pmatrix} 0 \\ 0 \\ -\frac{1}{20} \end{pmatrix} \cdot \begin{pmatrix} -0.00001 + 0.00001 \\ 0 - 0 \\ -1 - 1 \end{pmatrix} \\
&= \frac{1}{4\mathrm{e}{-}6\pi} \begin{pmatrix} 0 \\ 0.002 \\ 0 \end{pmatrix} \left(0 + 0 + \frac{2}{20} \right) \\
&= \begin{pmatrix} 0 \\ 15.925 \\ 0 \end{pmatrix}
\end{aligned}
$$